In situ spectroscopy to probe catalytic interfaces during electrochemical CO_2 reduction

by

Yuval Fishler

B.Sc. Technion - Israel Institute of Technology, 2018

M.S. University of Colorado Boulder, 2021

A thesis submitted to the

Department of Chemical & Biological engineering

In partial fulfillment of the requirements for the degree of

Doctor of philosophy

2024

Doctoral Committee:

Dr. Wilson A. Smith

Dr. Adam Holewinski

Dr. J. Will Medlin

Dr. Tanja Cuk

Dr. Michael F. Toney

Abstract

With the rise in the average global temperature due to human intervention, there is a need to reduce its increase to 1.5-2.0 ^{0}C to achieve carbon neutral society by the end of the century.[1–3] One major contributor to this issue, is atmospheric CO_2 which is emitted as a greenhouse gas from currently used fossil fuel dependent processes.[4] Therefore, there is a need to improve the current state of the art CO_2 capture, conversion and storage technologies.[5,6] *In-situ* spectroscopy techniques are a powerful tool for electrochemical reactions characterization under operating conditions. Vibrational spectroscopy, such as attenuated total reflection – surface enhanced infrared absorption spectroscopy (ATR-SEIRAS), allows the detection of species at the microenvironment of the catalyst surface.[7,8] Using ATR-SEIRAS supplies meaningful fundamental insights for the optimization of the electrocatalytic system by monitoring changes at the catalyst-electrolyte interface in real time.

Currently, the most promising approaches for electrochemical CO_2 capture and conversion are electrolyzer technology and acid-base electrodialysis.[9–11] Electrolyzer technology consists of an electrolytic electrochemical cell that when coupled with renewable energy sources as a driving force, can produce viable chemicals that can contribute to multiple industries (e.g. chemical fuels, feedstock and additives) while minimizing CO_2 emissions from the energy source. The state-of-the-art configuration for a CO_2 reduction electrolyzer consists of a membrane electrode assembly (MEA), with components in the following order: CO_2 stream/cathode/catholyte/membrane/anolyte/anode.[12] The electrolyte used within the electrolyzer as catholyte or anolyte could be either in a solid, or liquid state.[12–14] Lastly, it is suggested that decoupling the process into two steps, CO_2 reduction to CO and CO reduction to

products, results in a more promising approach relative to a direct CO2 reduction to products.[15] However, one limiting factor for the improvement of CO2 reduction electrolyzer technology is related to the choice of catalyst and its synthesis as different electrocatalysts and their synthesis route could affect their product distribution and activity. Therefore, there is a need for interfacial *in-situ* characterization techniques to probe the catalyst-electrolyte microenvironment. Doing so can support better understanding of these microenvironments to improve catalytic performance. This research project aims to advance ATR-SEIRAS systems to gain fundamental insights on electrochemical CO2 reduction in various conditions. Moreover, this work could contribute to a wide variety of fields and applications, as the main focus is on technique development demonstrated on CO2 reduction and this approach could be used for other electrocatalytic systems.

In this project we worked with the following objectives in mind:

Objective 1: Understanding of Spectro-electrochemical fundamentals while proposing an approach for the usage of ATR-SEIRAS for electrochemical CO_2 reduction.

Objective 2: Support an experimental-computational feedback loop with either experimentally guided simulations, or validation of models with experiments.

Objective 3: Advance the capabilities of in-situ Spectro-electrochemical ATR-SEIRAS towards bridging the gap between bench scale experiments and industrial needs.

Dedication

This work is dedicated to the Chemical & Biological Engineering

Department at the University of Colorado Boulder,

My father's wellbeing and longevity,

My family and friends,

And anyone who finds it beneficial.

Acknowledgments

I would like to thank my advisor, Dr. Wilson A. Smith, for his guidance, support, and encouragement throughout the course of my doctoral studies. His expertise, mentorship, and commitment have been important for completion of this work. I am also appreciative of the members of my doctoral committee, Dr. Adam Holewinski, Dr. Tanja Ćuk, Dr. Michael F. Toney and Dr. J. Will Medlin for their insights, constructive feedback, and guidance, which significantly contributed to the direction and quality of this research.

This research was made possible by the support and resources provided by the National Renewable Energy Laboratory in Golden Colorado, the Renewable and Sustainable Energy Institute, and the COSINC facilities at the University of Colorado Boulder, whose personnel offered critical assistance. I am grateful for the collaborations and intellectual contributions of the ElectroBuffs and Holewinski research groups and the Liquid Sunlight Alliance. In addition to the listed above, I would like to thank all the collaborators who participated in the works presented in this thesis which have not yet been listed: Dr. Noemi Leick, Dr. Glenn Teeter, Todd N. Whittaker, Jacob M. Clary, Paige Brimley, Charles B. Musgrave, Carrie A. Farberow, Derek Vigil-Fowler, Shaoyang Lin, Soonho Kwon, Annette E. Böhme, Weixuan Nie, Matthias H. Richter, Moon Young Yang, Jesse E. Matthews, Zachery WB. Iton, Brian C. Lee, Thomas F. Jaramillo, Harry A. Atwater, William A. Goddard III and Kimberly A. See. On top of that, I would like to thank all other collaborators that were involved in this work in any shape and form. Finally, I would like to give my sincere thanks to the Department of Chemical & Biological Engineering at the University of Colorado Boulder for fostering an environment conducive to academic and professional growth.

Table of Contents

List of Tables

List of Figures

Chapter 1: Introduction

1.1 Fundamentals of electrochemical systems

The introduction of the galvanic electrochemical cell design dates back to 1836, where John Frederik Daniell finalized the concept of the electrochemical battery by using a copper/zinc-mercury cell to generate electricity. The cell was used to demonstrate the operation of a lightbulb using this stack. Three years later (1839), the first fuel cell was produced by William Grove. Unlike previous batteries, a fuel cell requires a continuous source of fuel and oxygen. In addition, that specific fuel cell was used to demonstrate water recombination. The opposite case, where electricity is used to drive a chemical reaction, is called an electrolytic cell. In the context of the original fuel cell, electrons can be supplied in order to split water molecules to generate its constituents (Hydrogen and Oxygen).

A typical electrochemical cell consists of the following: a potentiostat, a cathode which is immersed in an electrolyte (catholyte), a salt bridge, and an anode which is also immersed in an electrolyte (anolyte), as can be seen in the following illustration:

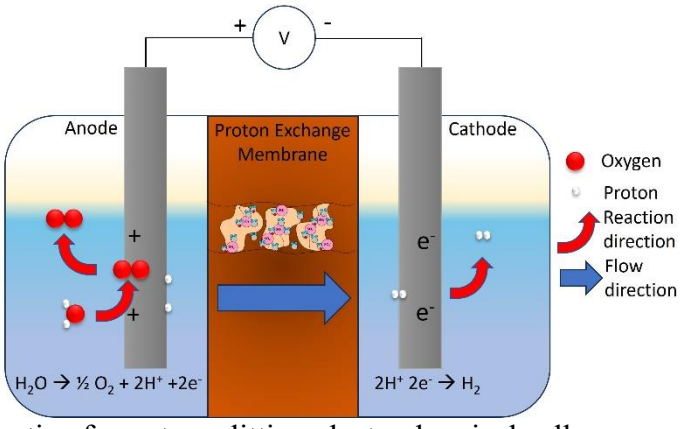

Figure 1.1: Schematic of a water splitting electrochemical cell.

When electric potential bias is applied on the system, electrons can flow from the anode to the cathode. This results in two electrochemical reactions, reduction at the cathode and oxidation at the anode. In the case of charge accumulation, counter ions (ions with opposite charge to the charge built at the electrode surface) can flow within the electrolyte (and through the membrane) to the electrode surface to maintain electroneutrality.[25] In this project, we focus on the cathode as we are interested in gaining insights on electrochemical reduction reactions, namely, CO2 reduction reaction (CO2RR). In the next subsection I will discuss specifically on electrochemical CO_2RR in more detail.

1.2 Electrochemical CO_2RR

Modern understanding of electrochemical CO2RR stems from works done by Yoshio Hori in the 1980s, which demonstrated selectivity and activity trends on various metallic electrodes.[26] Since then, major advances have been made in understanding CO2RR reaction pathways for various products, and selectivity trends for monometallic electrodes have been fairly characterized.[27] Interestingly, among all monometallic electrodes, copper is the only one known to form multi-carbon (C2+) products.[27–29] However, the contribution of different effects on CO2RR activity and selectivity, such as electrode reconstruction, degradation and the electrolyte composition, or more broadly, the characteristic of the catalyst-electrolyte microenvironment remains unclear. Therefore, to further understand CO2RR fundamentally, an active and selective system is needed. In addition, untangling these contributing effects remains an unresolved challenge. To elucidate reaction mechanisms, a collaborative approach using a combined experimental and computational analysis is needed. This approach can contribute to enhancing both experimental and computational research. On one hand, computational analysis can support

validating experimental results and elucidate mechanistic pathways. On one hand, computational analysis can support the validation of experimental analysis and elucidate mechanistic pathways. On the other hand, experimental analysis can support the validation and improvement of existing models.

In this work, we have taken another step towards developing methods to probe CO_2RR under operating conditions. First, we have used an active and selective system for formate (Sn based electrocatalysts) to gain mechanistic insights on CO_2RR to formate as a 2-electron transfer reaction, following **Chem. eq. 1.**

$$CO_2 + 2e^- + H_2O \rightarrow HCOO^- + OH^-; \textbf{(Chem. Eq. 1)}$$

Second, we employed a collaborative approach to gain insights on CO_2RR selectivity ratio between ethylene (**Chem. eq. 2**) and carbon monoxide (**Chem. eq. 3**) on copper-based electrodes in highly concentrated electrolytes, namely, 1 M HCOOK and 7.1 M HCOOK. This was done to gain a deeper understanding of the contribution of various components affecting the catalyst-electrolyte microenvironment.

$$2CO_2 + 12e^- + 8H_2O \rightarrow C_2H_4 + 12OH^-; \textbf{(Chem. Eq. 2)}$$

$$CO_2 + 2e^- + H_2O \rightarrow CO + 2OH^-; \textbf{(Chem. Eq. 3)}$$

1.3 FTIR spectroscopy background for using ATR-SEIRAS

Fourier Transformed Infra-Red (FTIR) spectroscopy was commercialized in the 1940s.[30] Since then, significant developments have been made to FTIR spectrometers. One mode that is relevant to electrochemistry is attenuated total reflectance (ATR). This mode leverages Snell's law of refraction at an interface between media with different refractive indices, as described in **eq. 1.1**:

$$n_1 \sin(\theta_1) = n_2 \sin(\theta_2)\ ;\ \textbf{(eq 1.1)}$$

Where n_i represents the refractive index of medium i and θ_i represents the angle of incidence relative to the normal to the interface.

Therefore, when considering the equation as a function of $\sin(\theta 1)$, and given an inequality between the refractive indices, there must be an angle at which the solution becomes a complex number. The threshold for this transition is called the critical angle (θc).

$$\theta_c = \sin^{-1}\left(\frac{n_2}{n_1}\right), \sin(\theta_2) = 1\ ;\ \textbf{(eq 1.2)}$$

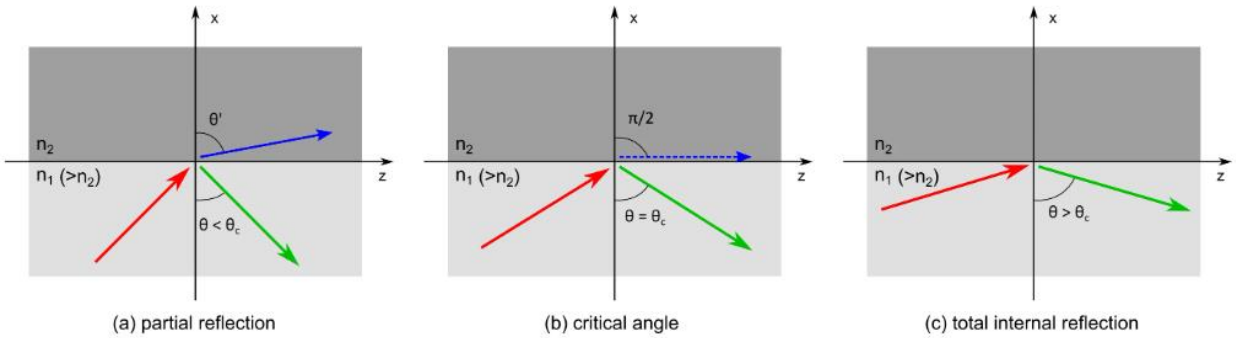

Figure 1.2: Illustration of reflection from an interface between media with difference in refractive index. (a) Partial reflection, (b) critical angle reflection and (c) total internal reflection.

The physical interpretation of this mathematical case is that when photons are incident on the system, total internal reflection occurs. However, this reflection of photons induces an electric field that interacts with the low refractive index medium following an exponential decay, namely, an evanescent wave as shown in **eq. 1.3**:

$$E \propto e^{\frac{z}{d_p}}\ ;\ \textbf{(eq 1.3)}$$

The evanescent wave depth of penetration, which is the characteristic length scale over which the exponential decay (dz) reaches a value of $1/e$ (~36.8%), is shown in **eq. 1.4**:

$$d_p = \frac{\lambda}{2\pi n_1 \sqrt{\sin^2(\theta) - (\frac{n_2}{n_1})^2}} \text{ ; (eq 1.4)}$$

Where d_p is the depth of penetration, λ is the wavelength of the incident ray in vacuum, n_1 is the refractive index of the medium through which the beam travels, θ is the angle of incidence and n_2 is the refractive index of the medium from which the beam is reflected.[31]

When measuring a differential spectrum between an initial state and a final state in the lower refractive index medium, attenuation of specific wavelengths that correspond to changes in vibrational modes within the medium can be detected.

ATR-SEIRAS was first formulated by Masatoshi Osawa, who suggested that when incorporating nanoparticles of a material with a plasma frequency (Resonant frequency) at the visible light, the evanescent wave induces plasmonic resonances both within the particles (Plasmon) and at their skin (Surface plasmon). The surface plasmon induces a resonance within the dielectric medium (i.e., a polariton). These effects combined are called "Surface Plasmon Polariton" (SPP) which takes the form of an additional evanescent wave.[32]

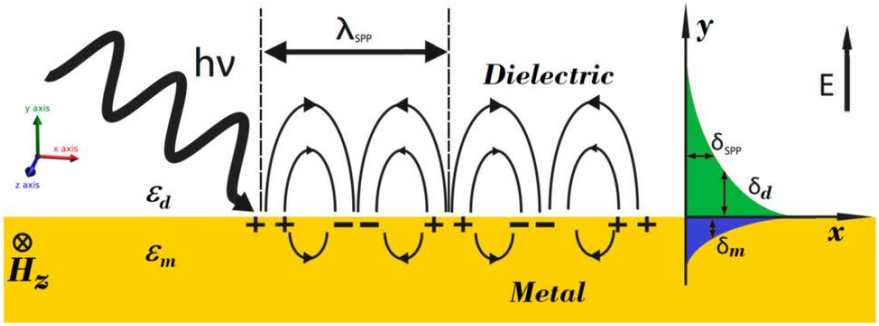

Figure 1.3: Surface plasmon polariton illustration.[16]

Such evanescent wave has a much shorter depth of penetration, and it follows an alternative set of physical equations according to SPP wave theory:

$$k_{z,d} = \sqrt{k_{SPP}^2 - \varepsilon_d k^2} \text{ ; (eq 1.5a)}$$

Where $k_{z,d}$ is the wavevector in the z direction, k_{SPP} is the wavevector of the surface plasmon polariton, ε_d is the permittivity of the dielectric and k is the wavevector at the speed of light.

$$k = \frac{\omega}{c}\text{; (eq 1.5b)}$$

Where ω is the incident light frequency and c is the speed of light.

$$\text{and } k_{SPP} = k\sqrt{\frac{\varepsilon_d\varepsilon_m}{\varepsilon_d+\varepsilon_m}}\text{; (eq 1.5c)}$$

Where ε_m is the permittivity in the metal.

$$\text{Therefore: } k_{z,d} = \sqrt{\frac{\varepsilon_d\varepsilon_m}{\varepsilon_d+\varepsilon_m} * k^2 - \varepsilon_d k^2} = k\sqrt{\frac{\varepsilon_d\varepsilon_m}{\varepsilon_d+\varepsilon_m} - \varepsilon_d} = k\sqrt{\frac{\varepsilon_d\varepsilon_m}{\varepsilon_d+\varepsilon_m} - \frac{\varepsilon_d(\varepsilon_d+\varepsilon_m)}{\varepsilon_d+\varepsilon_m}} = k\sqrt{-\frac{\varepsilon_d^2}{\varepsilon_d+\varepsilon_m}};$$

(eq 1.5d)

Finally, the SPP electric field component in the z direction is proportional to an exponential decay as well.

$$E_{SPP,d} \propto e^{-k_{z,d}z}\text{; (eq 1.6)}$$

Where $E_{SPP,d}$ is the electric field strength at a given distance from the metal-dielectric interface into the dielectric medium and z is the distance from the surface-dielectric interface in the dielectric medium.

1.4 Spectro-electrochemical *in-situ* ATR-SEIRAS

Investigating electrochemical reactions requires a closed electrochemical circuit. Therefore, to achieve electrical contact on the ATR crystal, a roughened thin conductive film is required as an alternative to plasmonic nanoparticles. However, when using roughened surfaces rather than plasmonic particles, a different model needs to be applied to simulate the SEIRA effect. Two highly relevant models have been developed and proposed by Stefan Franzen and Ian J.

Burgess, and a practical guide was formalized by Kas et al.[8,33,34] However, there is still room for further optimization to capture the effects of a continuous thin film as a substrate, especially when the film consists of multiple layers.

Using *in-situ* spectro-electrochemical ATR-SEIRAS allows the detection of changes at the catalyst-electrolyte microenvironment during reaction (e.g., CO2RR). Multiple factors can contribute to changes in signal response, such as materials composition, film thickness, nanostructure, etc. These effects result in a complex nature of the system's physics and optics, which is still under debate. However, using experimental approaches, empirical signal evaluation and estimation are meaningful for comparing ATR-SEIRAS performance. Therefore, in this work, we have proposed an empirical approach for estimating the SEIRA signal response using a set of two consecutive measurements. First, we estimate the total signal response, which provides an estimation of the overall evanescent wave profile. Second, the deposition of a self-assembled monolayer as a proxy for adsorbate signal response provides an estimate of the width of the evanescent wave base at the catalyst-electrolyte interface.

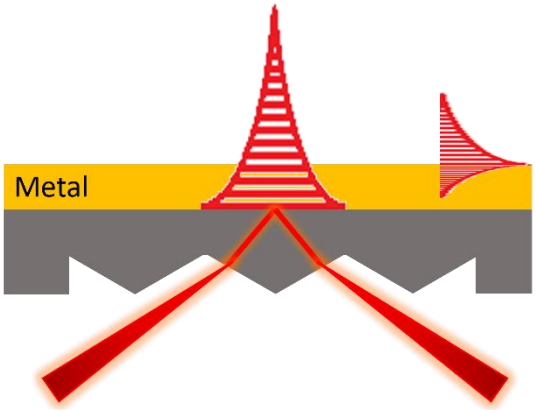

Figure 1.4: EC ATR-SEIRAS illustration showing the totally reflected IR broadband and evanescent waves on a silicon (100) micromachined ATR element.

To summarize, EC ATR-SEIRAS is a powerful tool for characterizing electrocatalytic processes. However, although major advancements have been made, further investigation is needed to improve its capabilities, especially for electrocatalytic systems is needed.

1.5 Significance and chapters content

In the second chapter, we focused on establishing electrosynthesis routes for ATR-SEIRAS Spectro-electrochemical measurements, devising an approach for signal profile estimation (Quality of catalyst for this type of measurement), and applying it to a renewable energy relevant problem (CO_2RR).

In the third chapter, we worked on resolving plausible mechanisms for CO_2 reduction on Sn based electrocatalysts while validating computational models using ATR-SEIRAS.

In the fourth chapter, we worked on understanding the different effects contributing to CO_2 reduction product selectivity at the catalyst-electrolyte microenvironment while validating experimental results with computational models.

The fifth chapter serves as a summary of the project, including concluding remarks and ideas for future direction.

1.6 Introduction summary, conclusions and outlook

In summary, electrochemical CO_2RR powered by renewable energy presents a promising approach to reduce greenhouse gas emissions. Spectro-electrochemical methods such as ATR-SEIRAS can be used *in-situ* to gain fundamental insights into CO_2RR. In a collaborative approach involving computational researchers, density functional theory (DFT) and *ab-initio* molecular dynamics (AIMD) simulations can provide more accurate insights on CO_2RR.

With this work, one could gain an understanding of how to use vibrational characterization methods to obtain fundamental insights when studying electrocatalytic systems. In addition, one could get up to date on the current state of CO_2RR. However, while this work may be applicable and translatable to multiple systems, additional efforts may be needed to make this approach general and broad enough. Therefore, there is still a lot of room to work in this domain, and there is a need for passionate individuals to contribute to improving and optimizing this approach.

Chapter 2: Layered Sn-Au thin films for increased electrochemical ATR-SEIRAS enhancement

Reprint with permission from: ACS Applied Materials & Interfaces. 2024, 16, 15, 19780-19791, https://doi.org/10.1021/acsami.4c01525.

2.1 Abstract

Operando electrochemical attenuated total reflection surface enhanced infrared absorption spectroscopy (EC ATR-SEIRAS) is a valuable method for fundamental understanding of electrochemical interfaces under real operating conditions. The applicability of this method depends on the ability to tune the optical and catalytic properties of an electrode film, and it thus requires unique optimization for any given material. Motivated by the growing interest in Sn-based electrocatalysts for selective reduction of CO_2 to formate species, we here investigate several Sn thin film synthesis routes for their resulting SEIRA signal response. We compare the SEIRA performance of thermally evaporated metallic Sn to a series of Sn-based films on top of a SEIRA-active Au substrate (metallic Sn, oxide-derived metallic Sn and metal oxide SnO_x). Using alkanethiol self-assembled monolayers as a probe, we find that electrodepositing metallic catalyst films on top of SEIRA-active Au substrates yields higher signal relative to thermal evaporation as well as higher signal than the independent SEIRA-active Au underlayer. These observations come despite the fact that thermally evaporated Sn has a significantly higher surface roughness (and thus higher adsorbate population), suggesting specific SEIRA-magnifying effects for the

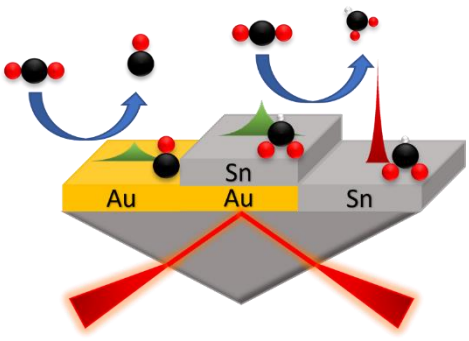

stacked films. Finally, we apply these films to observe the electrochemical conversion of CO_2. Differences are observed in spectral features based on the composition of the electrode being either metallic or oxide-derived metallic Sn, implying differences in their respective reaction pathways.

2.2 Introduction

The growth of renewable electricity generation has improved prospects for electrosynthesis of chemicals and fuels from renewable resources and/or waste products including water, carbon dioxide, and bio-derived organic molecules.[27,35–40] In order to accelerate the development and deployment of these technologies, fundamental insights are needed to understand how various reactions proceed at the electrochemical interface, defined within a few nanometers of an electrocatalyst surface. This microenvironment can be very different than the bulk environment of the electrolyte, and thus there is a need for continued development of characterization techniques that can probe this region without disturbing the catalytic reaction. Vibrational spectroscopies such as Fourier transform infrared (FTIR) and Raman are powerful, noninvasive techniques for mechanistic studies, but they must be adapted in surface-sensitive modalities that are not always readily transferrable between materials and reactions of interest. For example, EC ATR-SEIRAS can amplify signals by 2-3 orders of magnitude and be used to probe both surface-bound reactive intermediates and near-surface speciation of molecules. However, the range of materials that can promote the phenomenon of SEIRA is limited, and with a few notable exceptions (mainly noble metals), there are neither well-established structural parameters to target for optimal enhancement, nor standard synthetic procedures to reproducibly achieve those structures. An important example can be seen in using EC ATR-SEIRAS to understand reaction mechanisms for electrochemical CO_2 reduction (CO_2RR), which involves numerous elementary steps and can yield a wide range of products. Au, Ag, and Cu electrocatalysts have been studied in great detail using EC ATR-SEIRAS,

while Sn—which is of growing interest for its uniquely high selectivity towards formate[41]—is not as readily implemented for ATR-SEIRAS, with very modest signal enhancements achieved in documented electrochemical ATR-FTIR studies.[42]

The most common method of fabricating SEIRA-active electrodes (developed mainly for Au, Ag, Cu and Pt) is an electroless deposition approach first demonstrated by Osawa in the early 2000s.[43–45] While sputtering and thermal evaporation methods are also commonly implemented,[7,42,46–52] it has been shown that electroless deposition tends to provide better signal response relative to other methods (without intensive parameter optimization). This is suggested to be due to more optimal nanoparticle size distributions that promote appropriate optical resonances.[33,49,53–57] In addition, it has been suggested that electroless deposition provides better mechanical stability due to simultaneous etching reactions on the ATR crystal surface allowing better adhesion.[32,43] While the exact structures needed for broad spectrum signal enhancement are hard to predict due to the complex optical properties of rough films, efforts to transfer the SEIRA effect between materials have also been explored through stacking catalytically-active films on top of established SEIRA-active surfaces.[54,58,59] There are nonetheless still large gaps in understanding the optics of these systems due to their heterogeneous composition, as well as limited synthesis methodologies for precise and reproducible fabrication.

Since many reports in electrocatalysis have pointed to Sn as a promising CO_2 reduction catalyst—and these have further suggested that variation in reaction pathways/reactivity can stem from the origin of the material (metallic vs. oxide-derived)—we explore here the impact on SEIRA characteristics and resulting spectra using a variety of Sn-film electrosynthesis methods. We focus mainly on direct electrodeposition and indirect electrosynthesis via oxide deposition, examining each of these using a SEIRA-active Au substrate for deposition of Sn and measuring the relative

signal intensities using alkane self-assembled monolayers (SAMs) on the final films. These Sn/Au stacked films are further compared to the ATR-SEIRAS performance of pure thermally evaporated Sn. We find that when optimized, Sn/Au stacked films promote higher signal response than Sn or Au layers alone. Since the signal response from the Sn/Au stack is higher than that of either constituent, it suggests that surface plasmon resonance (SPR) in the IR regime is enhanced by interactions between the layers. Lastly, we demonstrate the SEIRA performance of the electro-synthesized metallic and oxide-derived Sn electrodes under CO_2RR conditions, highlighting differences in their catalytic reaction chemistry. This work may support mechanistic insights in the electrocatalysis field for CO_2RR while also providing a simple and general synthesis approach for active films in diverse ATR-SEIRAS applications.

2.3 Methods

2.3.1 Materials

All materials were used as purchased without further purification. For thermal evaporation, Au (Kurt J. Lesker, 99.999% 1/8" Diameter -1/8" long pellets) and Sn (1 mm shots, 99.99995%) were used. For Au electroless deposition, $NaAuCl_4$ (Premion Sodium tetrachloroaurate dihydrate 99.99% - metal basis Au 49-50%), NH_4F (99.99%, trace metals basis, Sigma-Aldrich), NH4Cl (99.99%, ACS Grade, Sigma-Aldrich), HF (Suprapur 40%, Merck), Na2S2O3 (98%, ACS Grade, Sigma-Aldrich) and Na2SO3 (99.5%, ACS Grade, Sigma-Aldrich) were used. For electrosynthesis, Tin(II) sulfate (Sigma-Aldrich, ≥ 95% metal salt), H2SO4 (Merck, Suprapur 96%) and HNO3 (Merck, Suprapur 65%) were used. For thiolate self-assembled monolayer deposition, 1-Decanethiol (96% Alfa Aesar) and 200 proof EtOH (Decon Laboratories inc.) were used. For phosphonic acid self-assembled monolayer deposition, 1-Decylphosphonic acid (98% Thermo Scientific) was used. CO_2 (Instrument grade, CD I200), O_2 (Ultra High Purity, Ox UHP

300) and Ar (Ultra High Purity, Ar UHP 300) gas cylinders were used in this work and were supplied by Airgas.

Throughout this work, MilliQ ≥ 18.2 MΩ was used as a water source.

2.3.2 Electrosynthesis

Sn based electrodes synthesis was conducted within the same PTFE and PEEK cell housing from the ATR-FTIR apparatus was used with a custom acrylic cap, which includes three ports. The ports serve as housing for a bubbler, a reference electrode, and a counter electrode. A graphite rod counter electrode was held in parallel to the working electrode in a vertical configuration. A KCl saturated Ag/AgCl electrode was used as the reference electrode. Metallic derived Sn based electrode was deposited at -0.467 V vs Ag/AgCl in 0.1 M H_2SO_4 with 10 mM $SnSO_4$, and oxide derived Sn based electrode was deposited at -0.6 V vs Ag/AgCl in 1.5 M HNO_3 with 30 mM $SnSO_4$ via chrono-coulometry.

2.3.3 Thermal evaporation

A CVC thermal evaporator was used for physical vapor depositions. The evaporation chamber was pumped down to a pressure of ~$5x10^{-7}$ torr prior to deposition. For Au thermal evaporation, a deposition rate of 0.2 Å/s was used to a thickness of 5 nm followed by a deposition rate of 1.0 Å/s to a total thickness of 30 nm. For Sn thermal evaporation, initial deposition rate of 1.0 Å/s for the first 10 nm, followed by a deposition rate of 2.0 Å/s for an additional 90 nm. Thicknesses were measured in-situ using an Au quartz crystal microbalance. All samples were introduced to a reductive electrochemical treatment prior to FTIR experiments equivalent to thin films synthesized via chemical, or electrosynthesis methods.

2.3.4 Characterization methods

XRD: X-ray diffractograms were acquired on a Rigaku Smartlab 9kW rotating anode utilizing Cu K-alpha radiation (1.54 Angstrom). Nickel metal foils were used to filter Kβ radiation. The instrument was operated in parallel beam grazing incidence mode with a HyPix3000-SE detector set to 0D continuous acquisition. The beam profile was set to 0.1 mm tall x 5 mm wide, and the axial divergence was reduced with symmetric 2.5 degree Soller slits on the incident and receiving optics path. An additional 0.5 degree parallel slit analyzer was used to reduce vertical divergence of the diffracted X-rays. The detector two-theta range and source incidence angles were varied as reported in the main text. All data was acquired and reduced using the Rigaku SmartLab Studio II software.

LEIS: For high-sensitivity low-energy ion scattering (HS-LEIS) characterization, an IONTOF Qtac100 spectrometer was used. Samples were first inserted into a high vacuum chamber. For metallic Sn sample, Ar sputtering was used for surface cleaning. Sputtering was done at 500 eV for a dose density of 2.04×10^{16} ions/cm^2. For SnO_2, atomic oxygen cleaning was performed for 10 min prior to the measurement. Post cleaning, a spectrum was collected using He^+ ion gun with 3keV energy, averaging 10 rounds of measurements (Dose density of 2.43×10^{13} ions/cm^2 and 5.01×10^{13} ions/cm^2 for ED-Sn and ED-SnO_2 respectively) in an energy range that accommodates oxygen, tin and gold (500-3000eV).

Profilometry: To characterize the thickness profile of the different layers of the stack, we used a Bruker Dektak XT with contact stylus profilometer, measuring a 40 μm line over 3 sec, applying 2×10^{-5} N of force on the sample. We measured Sn/Au step profile and Au/Si step profile separately for each sample to measure the height of each thin film layer. Films were synthesized similarly to spectroscopically tested electrocatalysts. We created a well-defined step using PTFE

tweezers, exposing the underlying silicon layer without damaging it. Finally, we probed a line including the step using a Dektak contact stylus profilometer.

FIB: An FEI NOVA Nanolab 600 FIB was used for SEM imaging. A current of 93 pA was used for secondary electrons, and the working distance was set to 5 mm. Images were taken at an angle of either 0º or 52º.

SEM: Scanning electron microscopy (SEM) micrographs were acquired using a backscattered electron detector in a through-lens configuration on a FEI Nova NanoSEM 630 operating at 8 keV accelerating voltage and 2.3 nA beam current at a working distance of 5 mm. Energy-dispersive X-ray spectroscopy (EDS) was performed using an Oxford Instruments Ultim Max detector.

XPS: data sets were acquired using a Physical Electronics VersaProbe III instrument. High-resolution XPS spectra were acquired at 55 eV pass energy, using monochromatic Al-ka x-rays (hn = 1486.7 eV). Measurements were calibrated using the Au $4f_{7/2}$ (83.96 eV) and Cu $2p_{3/2}$ (932.62 eV) core levels measured on sputter-cleaned metal foils.

Ellipsometry: The thickness and optical properties of the Au and Sn samples were determined through ex situ spectroscopic ellipsometry, employing a J.A. Woollam Co. M-2000® variable angle ellipsometer. To enhance measurement sensitivity, three angles near the Brewster angle of Si were selected for the Au-containing samples 65˚, 70˚, and 75˚. Similarly, angles of 72˚, 77˚, and 82˚, close to the Brewster angle of Sn, were chosen for the Sn-containing samples. The analysis used the CompleteEASE software (version 6.1), employing the built-in general oscillator parameterization to model data from TE-Au and TE-Sn.

2.3.5 ATR-FTIR

For *in-situ* ATR-FTIR experiments, a Nicolet 6700 FTIR spectrometer (Thermo Fisher Scientific) with VeeMAX^{TM} III (PIKE Technologies) ATR configuration chamber was used. The photoelectrochemical experiments were performed in a J1W Jackfish spectro-electrochemical cell (PIKE Technologies) with a PTFE/PEEK base, and IRUBIS Si(100) specialized 1 ATR element (single-bounce ATR crystal). Polycrystalline Au electrode was chemically deposited (electroless deposition) from. based on previous work by Osawa.[43] Each electrode was first deaerated with argon for at least 2 minutes per ml of electrolyte, then cycled between 0.2 V – 1.75 V vs. RHE for 20 cycles at 50m V/s for surface cleaning and SEIRA activation.

Alkane SAM deposition: The ATR-SEIRAS experiments on gold were performed by taking background spectra in MilliQ water, followed by solution exchange to 10 mM 1-Decanethiol in 200 proof EtOH for SAM deposition. Next, the solution was rinsed with ultrapure water, with spectrum taken after each rinse without purging until no more changes were noticeable.

In the case of Sn/Au electrodes, prior to ATR-SEIRAS experiments, a CV was conducted, followed by polarization for 5 min using the SnO_2 reduction peak potential bias prior to SAM deposition. For decanethiols deposition on Sn based electrodes, a reducing bias was held until no change in IR signal response was observed.

For decyl phosphonic acid (deposited on ED-SnO_2), we followed a similar procedure to thiol SAM deposition on gold but dissolved 10 mM 1-Decylphosphonic acid in ultrapure milliQ water rather than ethanol.

2.4 Results and discussion

2.4.1 Synthesis of Sn ATR-SEIRAS films

Different synthesis methods were used to generate metallic and oxide-derived Sn films for assessment of SEIRA activity (Figure 2.1). For clarity, electrodeposited Sn and SnO_2 electrodes

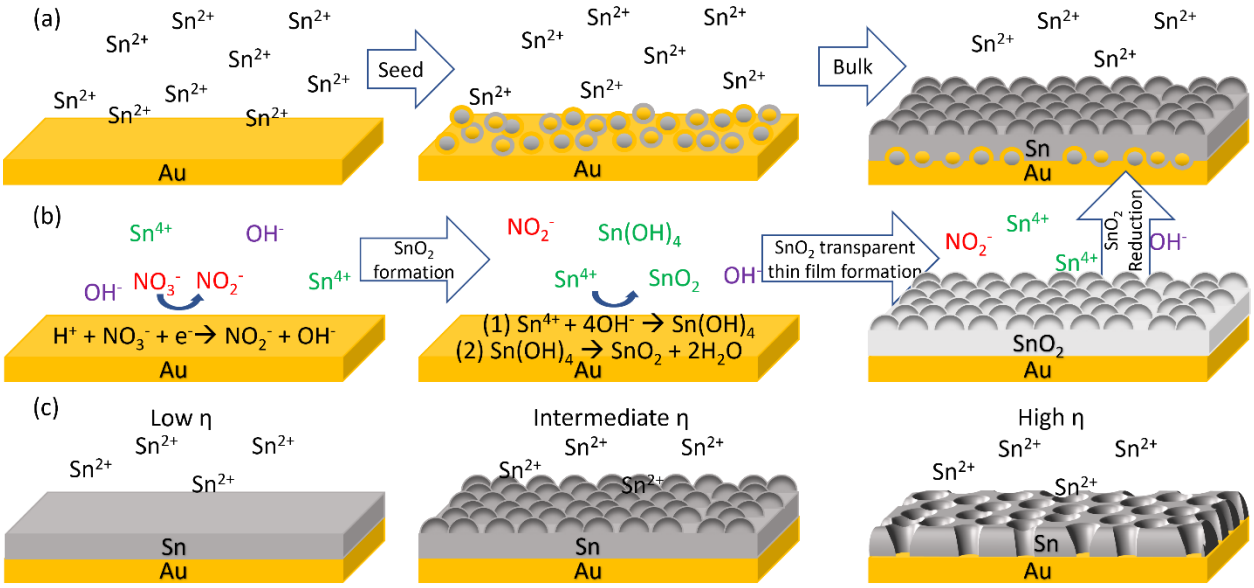

Figure 2.1: Illustration of (a) metallic Sn and (b) oxide derived Sn via SnO_2 electrosynthesis routes. (c) Illustration of electrodeposited film topography as a function of applied reducing overpotential (η).

are hereby referred to as ED-Sn and ED-SnO_2, while the thermally evaporated Sn electrodes are denoted as TE-Sn. Oxide-derived Sn, created from reduction of SnO_2, will be referred to as OD-ED-Sn. For bare Au, electroless chemically deposited Au electrodes are denoted as CD-Au while thermally evaporated electrodes are denoted TE-Au.

The deposition methods for each film were designed with consideration of the Pourbaix diagram of Sn in H_2O (Figure S2.1). Inspecting this diagram, it can be seen that Sn^{2+} ($E^0_{Sn/Sn2+}$ = -0.14 vs. NHE) is only soluble in a narrow potential window below pH ~4. Conversion to Sn^{4+} ($E^0_{Sn2+/Sn4+}$ above ~0.15 vs. RHE) results in SnO_2 precipitation over a wide range of conditions—SnO_2 is effectively insoluble from roughly pH 0-13. Thus, to maintain solubility for a controlled deposition rate, the electrodepositions were carried out in a plating solution of 0.1 M H_2SO_4 + 10 mM $SnSO_4$ (pH~1). The sulfate precursor was chosen to avoid halide species that can specifically

adsorb (e.g. from $SnCl_2$), and the solution was deaerated with argon prior to salt addition and throughout the synthesis to avoid promotion of alternate oxide formation paths (e.g., $Sn^{2+} + \frac{1}{2}O_2 + 2H_2O \rightarrow SnO_2 + H_2O + 2H^+$). The low pH also aids to avoid Sn hydrolysis to Sn-hydroxide species.[60–62]

Electrodeposition conditions such as potential bias, current density, Sn salt concentration, and total charge passage dictate the roughness, thickness, and porosity of the resulting electrodes (Figure 2.1.c).[22,63] Depositing Sn at a high negative bias can result in a porous electrode due to bubble formation from the hydrogen evolution reaction (HER), which occurs simultaneously with the electrodeposition.[64] In order to decide on the potential biases for plating, cyclic voltammetry experiments were conducted to locate the Sn underpotential deposition (Sn-UPD) peak, seen at ~0.1 V vs. RHE, and Sn overpotential deposition (Sn-OPD), with peaks at roughly –0.2 V and –0.3 V vs. RHE. These are followed by oxidation and dissolution on the reverse sweep, as can be seen in Figure S2.2.a.[60] The first Sn-OPD peak potential was chosen for electrodeposition to minimize generation of porosity from the HER while still being able to deposit Sn. ED-Sn films were deposited to 38 mC/cm^2_{geo} (After testing a series between 3.16mC/cm^2_{geo} and 47.4mC/cm^2_{geo}) via chronocoulometric electroreduction of Sn onto Au (Figure S2.2.b). Using the Van der Waals radius of Sn to estimate a cross-sectional area, we approximate—assuming conformal growth, negligible HER, and average roughness factor of 9 (measured separately)—the charge transfer required to fill a complete monolayer would be ~574 μC. This equates to an estimated film thickness of 9.1 nm for the conditions used. Calculation examples can be found in the Supplementary Information. Although, additional pH/concentration dependent synthesis routes may exist and will require further investigation beyond the scope of this work.

For metal oxide film synthesis, it is challenging to precipitate a nanoscale thin film because pH adjustment creates conditions of bulk insolubility. Therefore, rapid electroreduction of the electrolyte was used to alter the local pH near the electrode surface, promoting amorphous SnO_2 growth only in that region. Films formed by this method are thus still referred to as "electrodeposited" SnO_2 (ED-SnO_2). The method developed was based on a work by Vequizo et. al., who deposited amorphous SnO_2 on an indium doped tin oxide (ITO) substrate.[65] 1.5 M HNO_3 (pH~ -0.17) was chosen as the electrolyte because solubilizing Sn^{4+} requires very acidic conditions (pH<0).[61] Rapid reduction of protons and NO_3^- was then utilized to raise the local pH (Figure 2.1.b). A characteristic cyclic voltammogram (CV) is shown in Figure S2.3.a. Based on this CV, a deposition potential of –0.6 V vs. Ag/AgCl was chosen for film synthesis. Film deposition was additionally carried out with O_2 purging in order to enhance SnO_2 formation by converting Sn in the bulk solution to the +4 state as well as possible additional reaction through the redox process: $Sn^{4+} + O_2 + 4e^- \rightarrow SnO_2$.[65] Deposition conditions such as potential bias and charge transfer that were tested for suitable deposition conditions: 1.58 – 6.32 C/cm^2_{geo} total charge transfer and -0.6, -0.8 V vs Ag/AgCl potential biases. Films were deposited up to 3.16 C/cm^2_{geo} (Figure S2.3.b) and then the reaction was quenched by replacing the plating solution with MilliQ water to avoid dissolution from the original low bulk pH.

2.4.2 Physical characterization of deposited films

To observe morphological properties that may correlate with performance of the different films, scanning electron microscopy (SEM) and atomic force microscopy (AFM) were performed. Samples were analyzed both as-deposited as well as after a reductive treatment, required to convert ED-SnO_2 to OD-ED-Sn and applied to other Sn samples for consistency. For as-synthesized ED-Sn, the surface was relatively smooth and uniform (SEM Figure S2.4.a). After reductive treatment,

the average particle height according to AFM was ~7 nm (1 μm^2 geometric area), although wider survey images showed a low density of large (~50 nm) particles (Figure S2.4.d). For ED-SnO_2, after reductive treatment to form metallic Sn (OD-ED-Sn), SEM and AFM images suggest a comparable surface topography between both the ED-Sn and OD-ED-Sn, as shown in Figure 2.2.a-

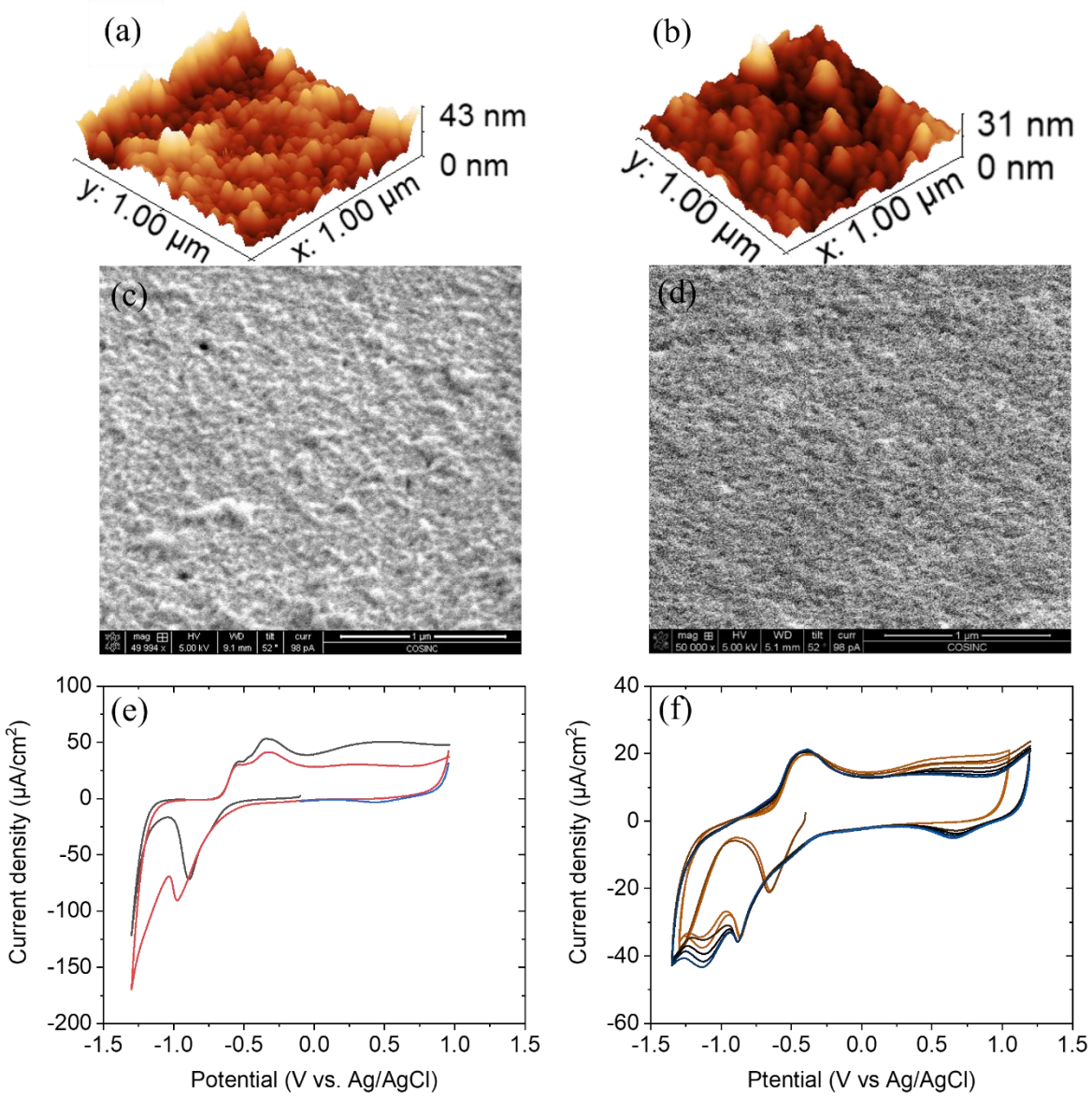

Figure 2.2: AFM topography of pretreated (a) OD-ED-Sn and (b) ED-Sn. SEM images of pretreated (c) OD-ED-Sn and (d) ED-Sn. (e) Characteristic CVs of as-synthesized ED-SnO2 in 0.1 M NaClO4 (scan rate of 100 mV/s). Black line corresponds to first cycle, red line to second cycle, and blue line to third cycle. (f) CVs of ED-Sn in 0.1 M NaClO4 (scan rate of 50 mV/s). Cycle evolution follows brown (1st) to blue (7th) line color.

d. Unlike ED-Sn and OD-ED-Sn, TE-Sn maintains its roughness, topography and broad particle height distribution (Table S2.1, Figure S2.4 and Figure S2.5). Unlike ED-Sn and OD-ED-Sn, TE-Sn exhibits much different surface structure (SEM and AFM images in Figure S2.4.c,f). The TE-Sn shows large, isolated particles sitting atop relatively smoother domains. Topological metrics (average and RMS roughness) for all samples are compiled in Table S2.1. To further characterize the electrodeposited films interface, cross-section SEM was performed on CD-Au, ED-Sn, ED-SnO_2 and OD-ED-Sn (Figure S2.6). According to cross-section SEM measurements, the film thickness of the bare CD-Au layer is approximately 30 nm (Figure S2.6.a). In the case of ED-Sn, a gradient within the layered film is noticeable (Figure S2.6.b), which we suspect to be the result of intermetallic alloying between the gold and the tin layers. Unlike ED-Sn, ED-SnO_2 synthesis results in two distinct layers of Au and SnO_2, with SnO_2 being relatively rough and irregular (Figure S2.6.c). Upon electrochemical reductive treatment (Conversion of ED-SnO2 to OD-ED-Sn), it is noticeable that the composite film's nature appears more similar to ED-Sn (Figure S2.6.d).

To estimate the thickness of the thin films, profilometry was used (representative profile shown in Figure S2.7). For the ED-Sn films, a thickness of approximately 12-30 nm was observed for the top (Sn) layer, measured at multiple locations. As-synthesized ED-SnO_2 showed an approximate thickness of 20-35 nm (Figure S2.8.a), while reductively treated OD-ED-Sn (Figure S2.8.b) showed an approximate thickness of 10-30nm. Unlike electrodeposited Sn based films, TE-Sn showed a thickness of approximately 20-40 nm at the edge of the film (Figure S2.8.c) and 100-160 nm at the center (Figure S2.8.d), showing this technique leads to a less homogeneous deposition. CD-Au and TE-Au had thicknesses of approximately 35-45 nm and 20-35 nm respectively (Figure S2.8.e,f).

Although the optical properties of Sn will mainly be tuned by its morphology and thickness, we additionally characterized each film by a variety of other *ex situ* techniques. The thin film crystallinity and bulk composition was analyzed by X-ray diffraction (XRD, Figure S2.9). ED-Sn (Figure S2.9.a) showed a pure thin film Sn body centered tetragonal (BCT) phase[66] with trace amounts of a SnAu alloy originating from a mixed phase that is known to form at the interface between bulk Au and bulk Sn layers.[66–68] A lack of well-defined diffraction peaks for ED-SnO_2 implies an amorphous film structure (Figure S2.9.b).[65] The Sn and SnO_2 surfaces were found to be pinhole-free with respect to exposure of the Au underlayer, confirmed by high-sensitivity low energy ion scattering (HS-LEIS)[69] to assay the top atomic layer of each surface (Figure S2.10). X-ray photoelectron spectroscopy (XPS) was further used to analyze Sn 3d (Figure S2.11) and Au 4f (Figure S2.12) states. From the Sn $3d_{5/2}$ binding energy, due to the presence of a doublet peak with binding energies of ~485eV and ~486.7eV, ED-Sn, OD-ED-Sn and TE-Sn result in a mixture of Sn^0 and SnO_x (Figure S2.11.a,b,c),[70,71] which is consistent with a small degree of surface oxidation from air exposure. Unlike the former cases, ED-SnO_2 is comprised of SnO_x solely, due to the presence of a singlet peak with binding energy of ~487.5eV (Figure S2.11.d). The high binding energy for tin oxide in the case of ED-SnO_2 relative to the standard value (~486.7eV – $3d_{5/2}$) is most likely related to the presence of carbon on the surface, being an ex-situ measurement. To test this hypothesis, we conducted depth profiling XPS measurements (Figure S2.11.e). According to the analysis, upon surface sputter cleaning, the SnO_x peak position appears at a binding energy of 486.7eV. Sputter etching through the SnO_2 layer reviles traces of metallic Sn following binding energy of 485eV for Sn $3d_{5/2}$. The Au 4f signal is more intense for ED-Sn (Figure S2.12.b) relative to ED-SnO_2 (Figure S2.12.c), suggesting that ED-SnO_2 is thicker than ED-Sn. It also implies that some regions of the pure Sn phase in the stacked films may be less than ~10 nm thick in some

locations (information depth for XPS). In addition to inhomogeneities in the Sn layer thickness, a shift in Au $4f_{7/2}$ binding energy from ~84eV closer to ~85eV for ED-Sn and OD-ED-Sn (Figure S2.12.b,d),[68,71] but not for ED-SnO_2 (Figure S2.12.c), Suggests that SnAu intermetallic alloys layer has formed at the interface of Sn and Au. This shift in Au $4f_{7/2}$ binding energy in the case of OD-ED-Sn strengthens the elemental mixing hypothesis between Au and Sn and that it occurs upon reductive treatment in addition to direct cathodic reduction. To try and qualitatively discuss the elemental composition of the electro-synthesized thin films, we took additional XPS depth profiling measurements (Figure S2.13 and figure S2.14). Interestingly, Au 4f electrons are sensitive to both film thickness and intermixing with Sn.[68,70–72] As can be seen in figure S2.13 and S14, in the case of ED-Sn and OD-ED-Sn, the Au $4f_{7/2}$ binding energy is initially ~85eV. This is in agreement with Sn rich intermixed layer. Unlike the formers, ED-SnO_2 Au $4f_{7/2}$ electrons have binding energy of ~84eV. This suggests minimal mixing between the metals. Finally, in all cases when etching through the gold layer its 4f electrons binding energies shift towards 85eV. In agreement with previous works in literature regarding Au 4f electrons binding energy as a function of film thickness .[72] Spectroscopic ellipsometry was employed to compare the optical properties of various thin film systems. For the isolated Au (TE-Au) and Sn (TE-Sn) films, with thicknesses of ~ 30 nm and ~39 nm, respectively, their dielectric functions were parameterized using Drude-Lorentz oscillators (Table S2.2). Typically, strongly absorbing metallic films exhibit bulk-like optical properties ~50 nm, rendering ellipsometry less sensitive to thickness. Nevertheless, a pseudo-transform from psi and delta yields a representative dielectric function, denoted as $<\varepsilon_r>$ = $<\varepsilon_1>$ + i$<\varepsilon_2>$ ~ ε_r, where ε_r is the dielectric function and $<\varepsilon_r>$ is its pseudo counterpart.

This transformation is illustrated in Figure S2.15 for TE-Au and TE-Sn, where ε_1 and ε_2 obtained from the general oscillator model align closely with the pseudo-transforms $<\varepsilon_1>$ and

$<\varepsilon_2>$. In Figure S2.15, the pseudo dielectric functions of the treated samples are compared with those of the pristine TE-Au and TE-Sn samples. All thin films display a pseudo dielectric function comparable to that of TE-Au, with CD-Au nearly indistinguishable from TE-Au. However, subtle yet notable differences are observed in the Sn and SnO_2-containing films.

The pseudo dielectric constants for both Sn samples, ED-Sn and OD-ED-Sn, are very similar, with only a slight shift in $<\varepsilon_2>$. The low-energy "dip" in $<\varepsilon_1>$ is likely attributable to Sn's feature ~ 1.2 eV, evident in TE-Sn's $<\varepsilon_1>$, confirming the presence of Sn in these samples. In the low eV region, it is intriguing to note that $<\varepsilon_2>$ is more intense for these Au-Sn samples compared to the Au-only samples. This region signifies characteristics of free carriers, suggesting a potentially higher electrical conductivity than that of pristine Au films. Finally, the SnO_2-containing sample displays dielectric constants consistent with semiconducting behavior: $<\varepsilon_2>$ approaches 0 from ~3.6 eV, corresponding to SnO_2's bandgap, and the intensity in the low-energy region indicates lower free-carrier absorption than in metallic samples.

2.4.3 Electrochemical characterization

To test the electrochemical characteristics of ED-Sn and OD-ED-Sn electrodes, CV scans were taken in 0.1 M $NaClO_4$. Figure S2.16.a shows the CV of the as-deposited ED-Sn electrode, which shows reduction features, indicating that some surface oxides still initially co-exist with metallic Sn, followed by oxidation on the reverse sweep. The ED-Sn CVs were stable to atmospheric exposure and comparable to the as-synthesized CV, with negligible changes after testing the electrode again after 48 hours storage in air. The characteristic CV of as-deposited ED-SnO_2 (Figure S2.16.b) showed two cathodic reduction features which can be attributed to SnO_2 → SnO (C_1) and SnO → Sn^0 (C_2) transitions, followed by two anodic oxidation peaks (A_1 and A_2) related to the reverse processes.[60] Unlike ED-Sn, OD-ED-Sn turned back to its transparent oxide

form (ED-SnO_2) within 24 hours of air exposure. No Au redox features appeared in either case, validating that the Sn phases are sufficiently thick to not expose Au (Figure 2.2.e-f). Upon extending cycling to oxidative potentials, Sn dissolution and readsorption occurs on both ED-Sn and OD-ED-Sn. The growth in Au features after oxidation cycles suggests that leaching and/or readsorption of Sn is favored on Sn surfaces, causing agglomeration and exposing the gold substrate (Figure 2.2.e-f). Due to this behavior, oxidative bias should be avoided.

To estimate the electrochemically active surface area (ECSA), capacitance measurements were used. For electro synthesized Sn based electrodes, the double layer capacitance was found in organic electrolyte (0.15 M KPF_6 in acetonitrile) (Figure S2.17) because the specific capacitance in water is ill-defined for easily oxidized metals. From this method, ED-Sn and OD-ED-Sn both had roughness factors (RFs) of ~6.0 based on an established capacitance of 11 $\mu F/cm^2$.[73] For Au based electrodes, we estimated ECSA in aqueous electrolyte using a specific capacitance value of 8 $\mu F/cm^2$.[73] These approximations yielded an RF (ratio of real to geometric area) of 9.0 (Figure S2.18).

For TE-Sn (films deposited directly on silicon wafers), an RF was calculated using the average roughness height root mean square (RMS) value (Table S2.1). This was done by taking the RMS ratio between TE-Sn and ED-Sn and multiplying by the ED-Sn double layer capacitance roughness factor (calculation example can be seen in the SI). The relative RF ratio was estimated to be ~10 in this manner, with RF values of 61.1 and 6.0 for TE-Sn and ED-Sn respectively.

2.4.4 ATR-SEIRAS signal response

The EC ATR-SEIRAS performance of electrodes made by each fabrication technique was experimentally examined next. To probe SEIRAS signals of adsorbates, we deposited C_{10} alkane SAMs onto the electrode surfaces (procedure described in the SI), as they can organize to have

similar dense coverages on all the materials.[74–78] Decanethiol was used for Au and Sn-based electrodes (including OD-ED-Sn),[74–78] while on the as-is SnO_2 electrode, decyl phosphonic acid was used to form the SAM (Figure S2.19).[79] Having a hydrocarbon chain, these SAMs are characterized by strong vibrational signals at frequencies in the 2850 cm^{-1}–3000 cm^{-1} range, attributed to various CH_2 and CH_3 stretching modes.[80] The raw signals from the SAMs in ATR-SEIRAS are compared in Figure 2.3.a and Figure S2.19. Following the CH_2 antisymmetric stretch

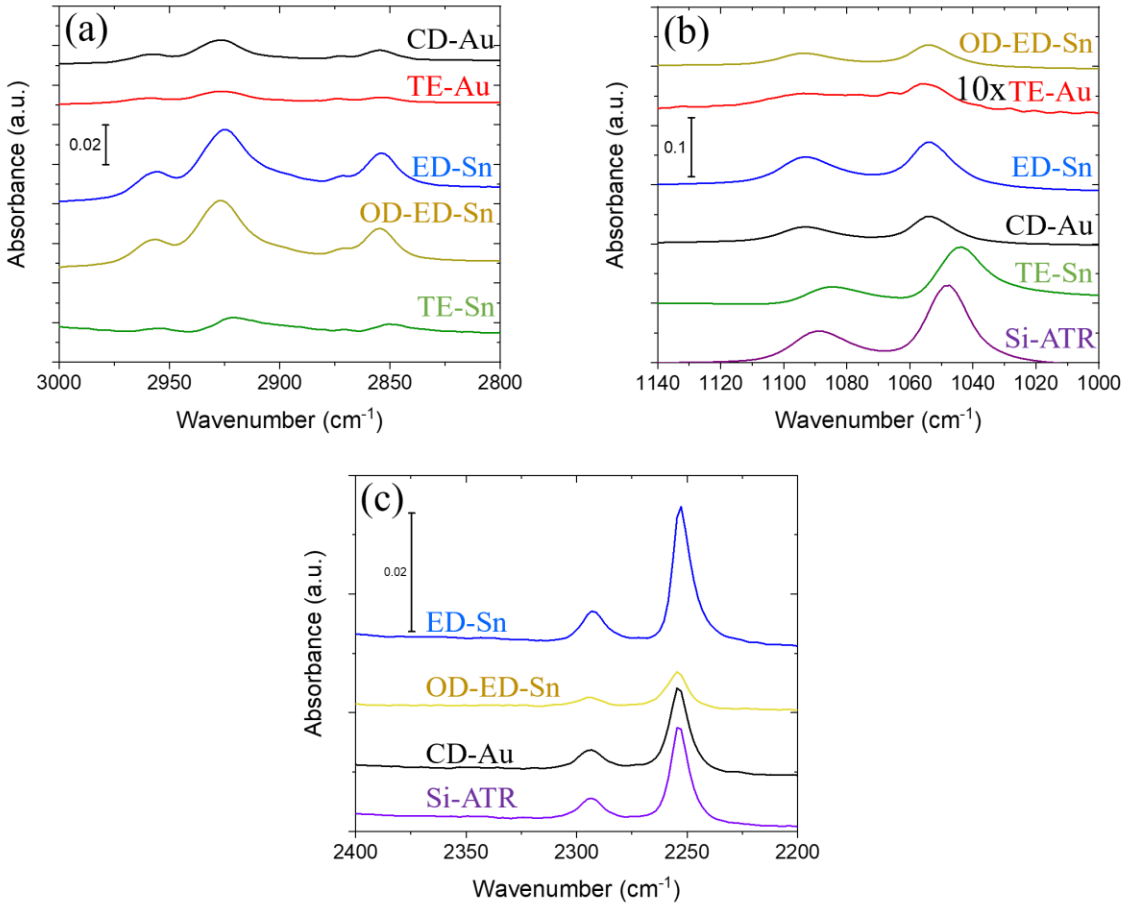

Figure 2.3: (a) CH_3 and CH_2 stretches signal response, depositing decanethiols under Sn reducing conditions. (b) EtOH νC-O ATR-FTIR spectra. (c) Acetonitrile νC-N ATR-FTIR spectra.

around ~2927 cm^{-1} (the most intense peak) as a benchmark, signal intensities are also reported in Table 2.1 (representative CH-stretches peaks deconvolution in Figure S2.20).

Table 2.1: Signal response for SAM's CH_2 asymmetric stretch (~2927cm^{-1}) and roughness factor for electrocatalysts

Electrode	Raw peak intensity (x10^{-3}) [a.u.]	Roughness Factor	Area-normalized peak intensity (x10^{-3}) [a.u.]	Peak area (x10^{-3}) [a.u.]	Area-normalized peak area (x10^{-3}) [a.u.]	Peak frequency [cm^{-1}]	FWHM [cm^{-1}]
CD-Au	10.8*	9.0	1.2	239	26.6	2928	22.2
TE-Au	5.7*	9.0	0.63	130	14.5	2926	24.1
ED-SnO_2/ OD-ED-Sn	5.6$^{\wedge}$ / 31.7**	32.6$^{\#}$ / 6.0	0.17 / 5.3	149 / 659	124	2927 / 2927	24.2 / 22.1
ED-Sn	32.5**	6.0	5.4	685	127	2926	22.8
TE-Sn	7.1**	61.1$^{\#}$	0.12	202	3.3	2922	30.0

* Decanethiol signal response deposited at OCP. ** Decanethiol signal response deposited under reducing conditions. $^{\wedge}$ Decyl-phosphonate signal response deposited at OCP. $^{\#}$ Estimated via AFM average roughness height RMS relative to pretreated EDSn^0 RF (Calculation example in SI).

First, comparing the different deposition methods for the Au underlayer revealed that the CD-Au electrode shows a ~1.8 times higher signal relative to TE-Au electrode. Next, the ratios for both ED-Sn and OD-ED-Sn relative to TE-Sn were ~3.4. Comparing signal enhancements between the most active films, we observe that the signal ratio for both ED-Sn and OD-ED-Sn, relative to CD-Au alone, is ~2.8 higher for the Sn-coated electrodes. Lastly, the ED-SnO_2 electrode showed comparable signal response with the TE-Au electrode (Table 2.1) but had a lower response than any of the various metallic Sn electrodes.

To eliminate contribution from difference in surface population as a result of differences in surface area, we also normalized signals by RF. First, we observed that the CD-Au and TE-Au electrodes had comparable surface roughness and CV profiles (Figure S2.21). Thus, we attribute most of the difference in signal between the Au electrodes to differences in plasmonic effects, which emanate from differences in morphology and topography between the electrode (As can be

seen for Sn based electrodes in table 2.1). Unlike single crystal metallic electrodes which have a well-defined surface plasmon frequency (ω_{SP}) that is much higher than the IR frequency regime, polycrystallinity can support extension of plasmon polariton evanescent wave (SPP-EW) contributions to a much lower and broader distribution of frequencies spanning the IR. This results in giving corresponding signal enhancements to surface species.[81] Although crystallinity of the electrocatalysts may affect the peak shape, or intensity, these deviations are minor relative to the differences observed in this work. Looking at Sn-based electrodes and accounting for differences in ECSA, signals for ED-Sn and OD-ED-Sn electrodes were roughly 38x relative to TE-Sn. Compared to CD-Au, signals for ED-Sn and OD-ED-Sn were greater by ~4x, highlighting that the Sn/Au stacked films were more enhancing than either constituent. Interestingly, comparing CH_2 stretch frequency and full width half max (FWHM) between all cases, it is noticeable that every electrode except for TE-Sn have comparable results. Thus, we suspect that the main contribution to deviation for TE-Sn is a result of film topography which affects the absorption/dispersion ratio.[8] The dispersive nature of TE-Sn can be seen in figure 2.3 by the asymmetric nature of the peaks.

To further attempt a qualitative understanding of the SEIRAS signal response in terms of the total evanescent wave shape, we devised a complementary method for comparing adsorbate to bulk signal response. Specifically, solvent signals were used to characterize the total intensity of the evanescent wave that penetrates into the dielectric medium. Unlike adsorbate signals—which only correspond to the evanescent wave intensity at the metal-dielectric interface—measuring bulk electrolyte can gauge the total signal response captured with ATR-SEIRAS. In other words, a wider base to the evanescent wave increases surface signal, while a low penetration depth results in reduced signal coming from the solution near the surface. For electrochemical reactions, it is of

interest to enhance signals from both adsorbates as well as near-surface electrolyte for estimation of characteristics such as local pH.

Since water gives quite diffuse IR responses, the solution was changed from MilliQ-H_2O to 200proof EtOH (Figure S2.22), and sensitivity between the electrodes was compared for the C-O stretching modes at 1045 cm^{-1} and 1090 cm^{-1} (Figure 2.3.b). For this total signal intensity, we found the following trend: TE-Sn > ED-Sn > OD-ED-Sn ~ CD-Au > TE-Au. It is worth also noting that the exact frequency for EtOH C-O stretches is different between the electrodes. This is most likely a result of the spectral shift that can occur when the IR beam interacts with different optical density media. We illustrate this further in Figure S2.23 by following a series of ED-Sn electrodes with increasing thickness. A change in both signal as well as C-O stretch vibrational frequencies can be seen, with red shifts from frequencies comparable to pure Au (on Si wafer) films to those of pure Sn (on Si) for thicker Sn films. Finally, it should be emphasized that the ratio of adsorbate to bulk signal response is not proportional. The signal intensity for adsorbates on ED-Sn, OD-ED-Sn and CD-Au is higher than TE-Sn, while the total signal response to EtOH is lower than TE-Sn on all of these surfaces. Since plasmonic surface enhancement has a short penetration depth, we propose total evanescent wave shapes as illustrated in Figure 2.4, where the SPP contribution is

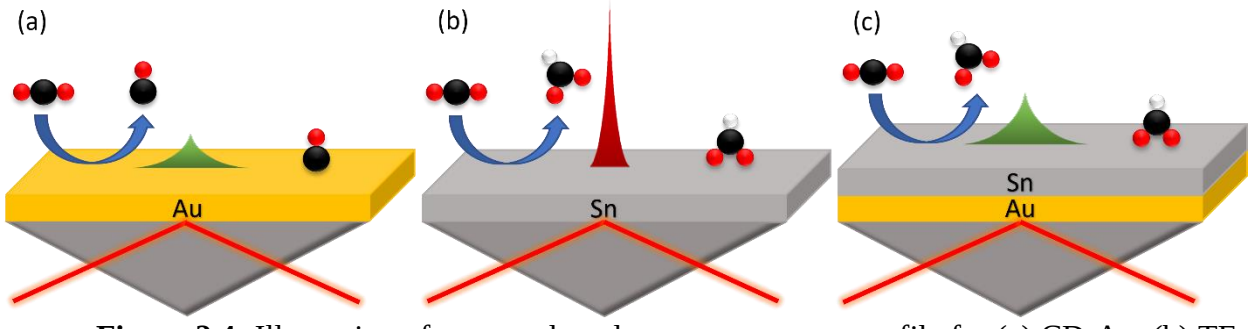

Figure 2.4: Illustration of proposed total evanescent wave profile for (a) CD-Au, (b) TE-Sn, (c) ED-Sn/OD-ED-Sn. * Illustration is not to scale.

much greater on Au and stacked Sn/Au films and the attenuation length of the ATR wave is much longer on pure Sn. Thiolate stability under reducing conditions was not directly evaluated in this work. But, following previous reports in literature, on Au based electrocatalysts, decanethiols drop below 75% of a monolayer above the theoretical HER onset potential,[82] while in the case of Sn based electrocatalysts decanethiols were proposed to desorb reductively around the SnOx reduction potential.[75] As an attempt to compare penetration and propagation lengths, while considering a simplified set of equations (Equations can be found in the supporting information), we calculated a ratio of ~1.41 for Sn/Au penetration depth (Normal to the surface) and a ratio of ~0.07 for Sn/Au lateral propagation depth (Parallel to the surface). This is in line with the proposed evanescent wave profile in Figure 2.4.

To further assess the signal response for solution phase species, we conducted a series of dilution experiments starting with 1 M EtOH, exposing the detection limit. For the detection limit estimation, we followed Agilent's definition of "three times the noise peak to peak value".[83] According to this analysis, we found that the detection limits of ethanol over ED-Sn, OD-ED-Sn and CD-Au are 0.118 M, 0.143 M and 0.167 M respectively (Figure S2.24 and table S2.3). Similarly, to test the generality of this approach beyond protic solvents, we extended the sensitivity analysis to another class of solvents (Aprotic) using acetonitrile (ACN) as the probe molecule (Figure 2.3.c). Albeit the fact that the trend between ED-Sn, OD-ED-Sn and CD-Au is maintained, in the case of aprotic solvents ED-Sn shows signal enhancement relative to the bare Si-ATR element. This is also validated by testing signal response to acetone (Figure S2.25). The detection limit to ACN for ED-Sn, OD-ED-Sn and CD-Au were 0.400 M, 0.794 M and 0.537 M respectively (Figure S2.26 and table S2.3). Due to the low signal response in the case of TE-Au, this sample was excluded from the analysis.

The above approach comparing surface and bulk signals of ATR-SEIRAS provides a simple method to probe complex interconnected effects that may contribute to differences in evanescent wave shapes between differently synthesized films. Given the differences between ED-Sn and TE-Sn, the observations could indicate a change in ω_{SP} of ED-Sn due to deposition on the Au thin film, since it maintains similar surface topography to the SEIRA-active Au underlayer.[84,85] In addition, according to the modified Fresnel equations (Reflection coefficient and SPP penetration depth into the dielectric medium equations can be found in the Supplementary Information), the thickness of the metal layer plays a role in reflection efficiency. However, according to physical and electrochemical characterization, the OD-ED-Sn films show similar characteristics and thickness to the ED-Sn films. Since our system is composed of complex multilayered composite films with comparable total thicknesses (ED-Sn and OD-ED-Sn), we assume a similar reflection coefficient between these cases.

While a deeper explanation is beyond the current scope, it is clear that using Au as a support underlayer for Sn based electrodes yields better enhancement that allows EC ATR-SEIRAS measurements with signal response that is at least on par with gold. Based on this work and corroboration with prior literature, it is possible to gain better signal response of an electrocatalyst by pairing it with a conductive support layer with optimal optical properties, but this approach is strongly material dependent and may not be generalizable.

2.4.5 Application to CO_2 reduction

Additional EC ATR-SEIRAS experiments were performed on the ED-Sn and OD-ED-Sn electrodes to test their ability to reveal surface species and features of the catalyst microenvironment during electrochemical CO_2RR. Both surfaces were first reduced under 0.1 M $NaClO_4$ electrolyte, then saturated with CO_2 gas, and continuously purged throughout the

experiment. Figure 2.5.a-b shows that there are major differences in spectra between ED-Sn and OD-ED-Sn, suggesting differences in their electrocatalytic nature.

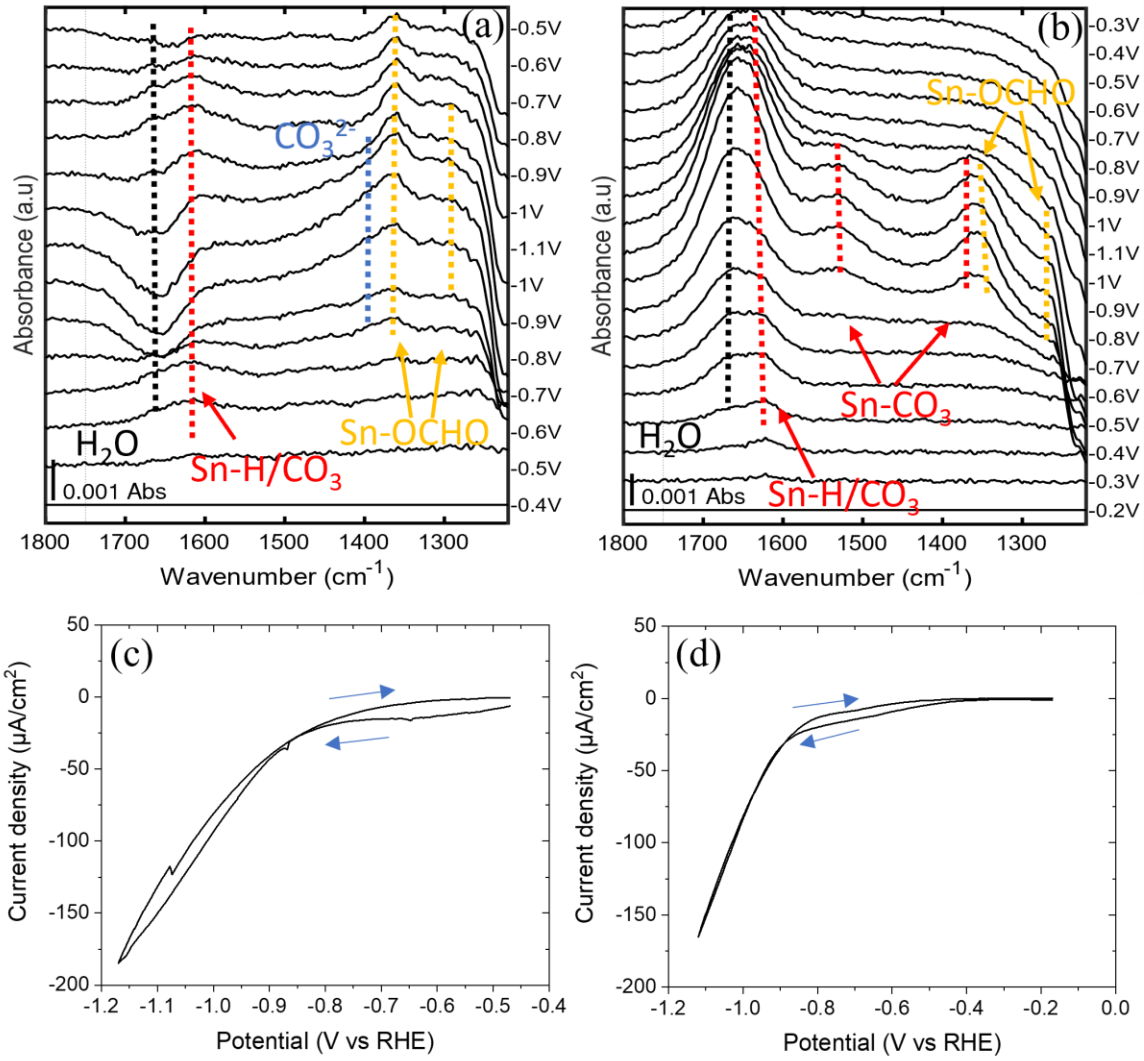

Figure 2.5: CO_2RR ATR-SEIRAS on (a) ED-Sn (b) OD-ED-Sn using cyclic voltammetry at a scan rate of 1 mV/s in 0.1M-$NaClO_4$. Corresponding CVs for (c) ED-Sn and (d) OD-ED-Sn.

Focusing on the bands which are related to CO_2RR, there are several species that may be reactive intermediates, spectators, reaction products, or bi/carbonate species related to the solution phase equilibrium: $CO_{2,aq} \leftrightarrow HCO_{3,aq}^{-} \leftrightarrow CO_{3,aq}^{2-}$. In comparison to prior literature, the metallic

and oxide derived Sn based electrodes shared common peaks around 1366 cm^{-1} and 1260 cm^{-1} that relate to bidentate oxygen-bound formate derived from CO_2 reduction.[42,86,87]

However, the metallic Sn electrode had a peak around 1400 cm^{-1} that corresponds to solution phase carbonate (Figure S2.27), caused by bicarbonate-carbonate equilibrium shifting from an increase in local pH under reducing conditions.[88] The detection of changes in solution phase species only in the metallic derived case could reflect on the difference in increase of local pH near the electrocatalytic surfaces.[7] Unlike ED-Sn electrode, OD-ED-Sn had a peak around 1520 cm^{-1} that may correspond to monodentate adsorbed carbonate. Monodentate adsorbed carbonate should also have a peak around 1380 cm^{-1}, although this overlaps with adsorbed formate and likely contributes to broadening of the band relative to ED-Sn.[42,87,89]

In addition, the peak around 1620 cm^{-1} that can be seen prior to CO_2RR onset (Figure 2.5.a,b) is suggested to be bidentate adsorbed carbonate,[42,87,89] under the assumption that bicarbonate deprotonates upon adsorption.[90] However, this peak could also be derived from adsorbed water.[91,92] According to the corresponding CVs, both metallic and oxide derived Sn electrodes hold similar current densities and onset potential for CO_2RR (Figure 2.5.c,d). Prior work by He et al. also showed that the activity and product distribution of CO_2RR on metallic and oxide derived Sn based catalysts is comparable.[93] Therefore, we suspect that there is a difference in the electrocatalysts microenvironment between metallic and oxide derived Sn based electrodes during CO_2RR. To reconcile further mechanistic insights and reveal potential reaction pathways, additional analysis beyond the scope of this work, such as quantum chemical calculations, will be needed.

2.5 Conclusions

In this work we have demonstrated a general, simple electrosynthesis route of either direct electrodeposition (metals) and indirect electrosynthesis (metal oxides) for ATR-SEIRAS electrocatalyst films. It has been shown that using a layered electrodeposition design yields superior signal response to adsorbed phase species relative to thermal evaporation while reducing the total evanescent wave bulk signal response to a comparable magnitude as the substrate. It was observed that applying a thin film of Sn on top of a SEIRA active Au film results in surface enhancement which is at least on par with polycrystalline Au thin films, while the normalized signal showed further enhancement relative to other samples tested in this work. In addition, we found that the profile of the evanescent waves of ATR-FTIR and ATR-SEIRAS can be influenced by complex interfacial electromagnetic effects, although they are beyond the scope of this work. Finally, the EC ATR-SEIRAS response for CO_2RR was compared between the ED-Sn and OD-ED-Sn electrodes. Differences were found based on these synthesis methods. Therefore, care should be taken with regard to electrocatalysts synthesis method and history when using different metallic and oxide derived electrodes for SEIRAS experiments.

2.6 Supporting information

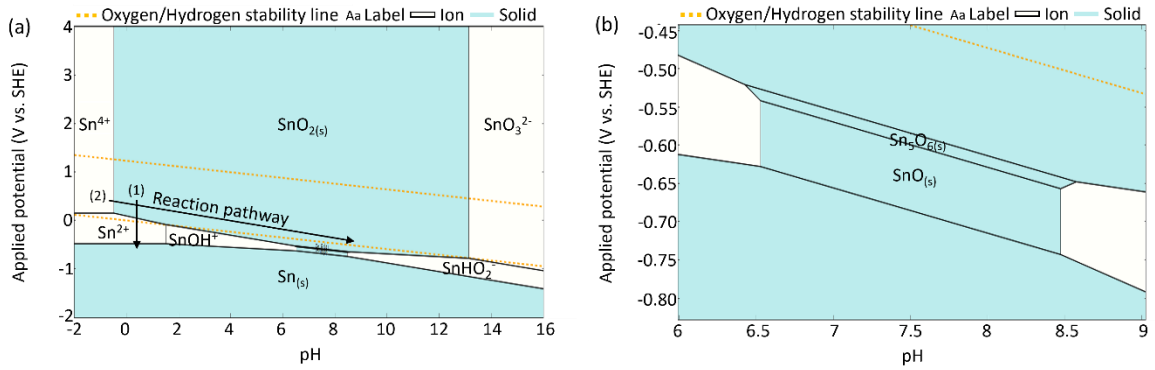

Figure S2.1: (a) E_H-pH Pourbaix diagram for Sn in H_2O with a dissolved Sn activity of 10^{-6} including reaction pathways for (1) Direct electrodeposition of ED-Sn and (2) Indirect electrodeposition of ED-SnO_2 via pH swing. (b) Blowup of the Pourbaix diagram exposing phases with narrow stability window. The diagrams were generated using materials project.[17–21]

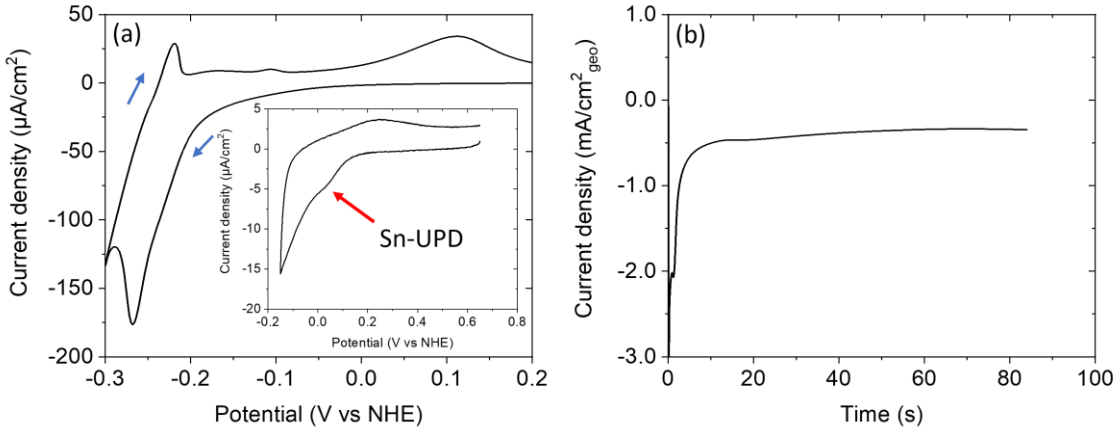

Figure S2.2: (a) Characteristic CV of 10 mM $SnSO_4$ in 0.1 M H_2SO_4 Ar-purged plating solution on Au electrode at a scan rate of 20mV/s (*Inset:* 1 mM $SnSO_4$ in 0.1 M H_2SO_4). (b) Chronocoulometric electrodeposition of 12 mC ED-Sn on Au electrode. Steady current changes after ~2.1 mC/cm^2_{geo} (~2 sec), which may be attributed to several phenomena including a transition between intermetallic alloy deposition and Sn deposition or a transition from nucleation to growth of the Sn layer.[22]

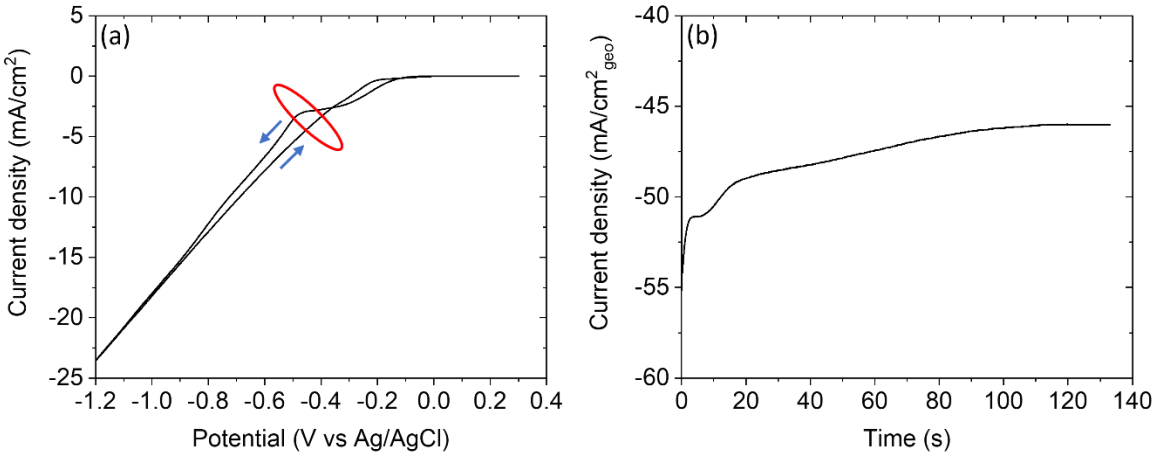

Figure S2.3: (a) Characteristic CV of 30 mM $SnSO_4$ in 1.5 M HNO_3 Ar-purged plating solution on Au electrode at a scan rate of 20 mV/s. A plateau on the cathodic sweep is due to mass transport limited conversion of Sn^{4+} to Sn^{2+} prior to the onset of HER and nitrate reduction. The existence of Sn^{4+} in solution is most likely due to homogeneous redox reactions with oxygen or nitrate, as they can be reduced with higher standard potential than Sn^{2+}/Sn^{4+} (e.g. $Sn^{2+} + NO_3^- + 2H^+ \rightarrow Sn^{4+} + NO_2^- + H_2O$). (b) Chronocoulometric electrodeposition passing 2 C to form ED-SnO_2 on Au electrode.

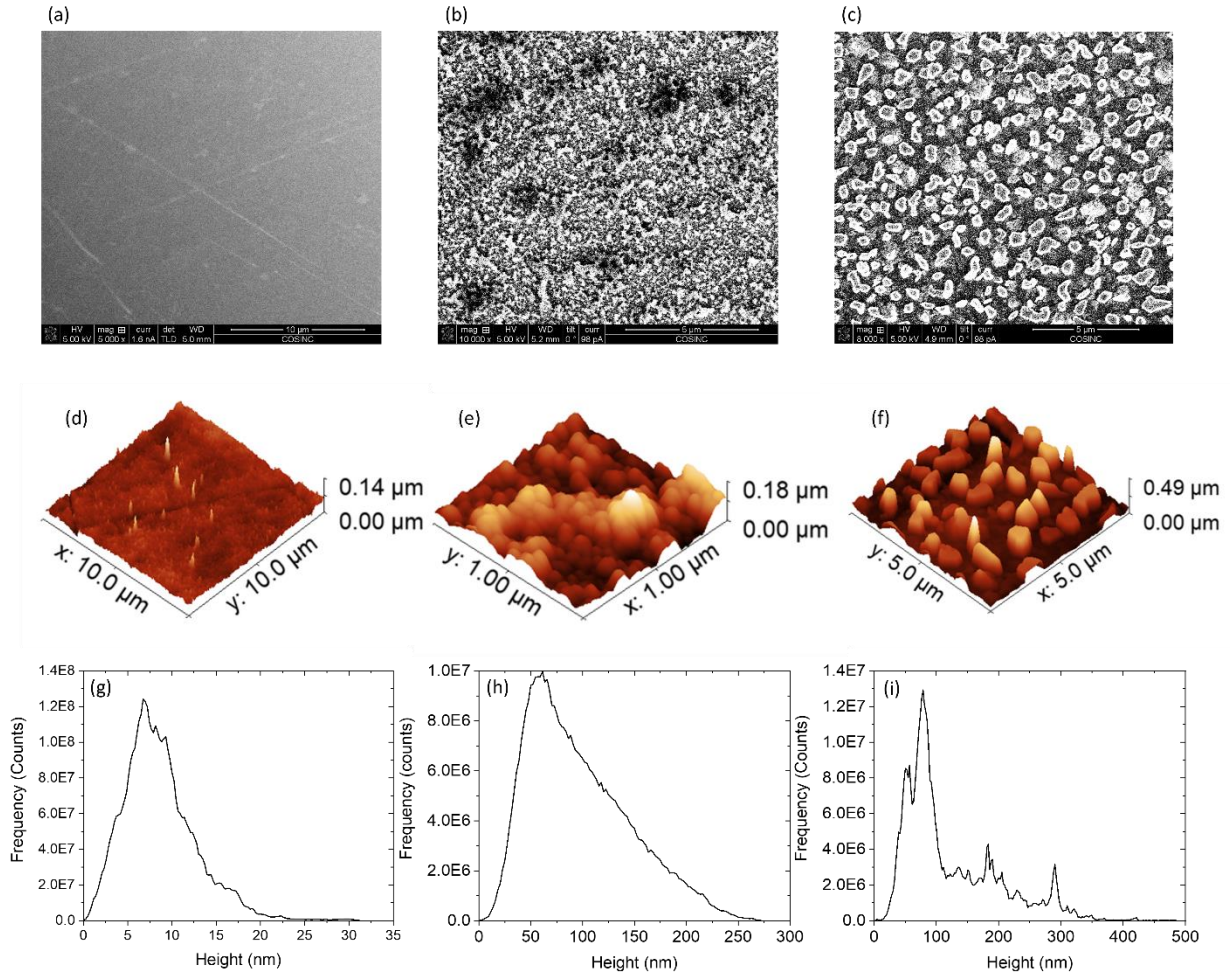

Figure S2.4: SEM images of as synthesized (a) ED-Sn, (b) ED-SnO_2 and (c) TE-Sn. AFM topography of as synthesized (d) ED-Sn, (e) ED-SnO_2 and (f) TE-Sn. Particle height distribution of as synthesized (g) ED-Sn (1 µm x 1 µm), (h) ED-SnO_2 (1 µm x 1 µm) and (i) TE-Sn (5 µm x 5 µm).

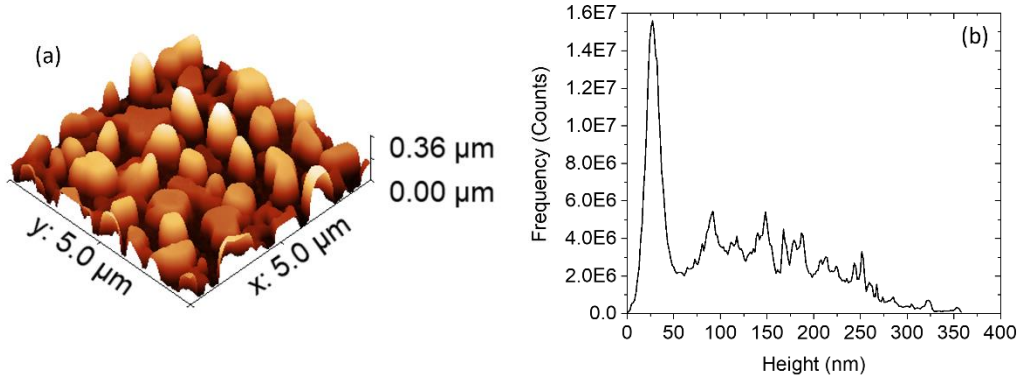

Figure S2.5: (a) AFM images (5µm x 5µm) of pretreated TE-Sn. (b) Particle height distribution of pretreated TE-Sn.

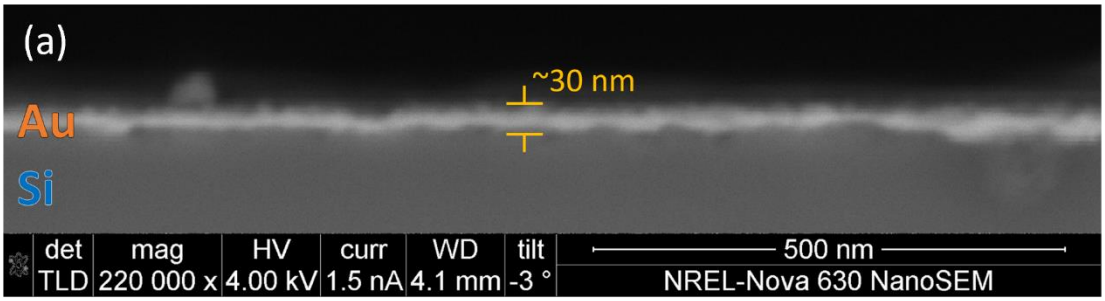

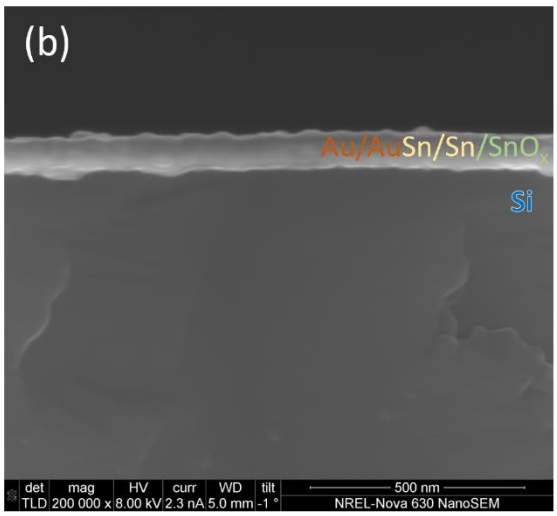

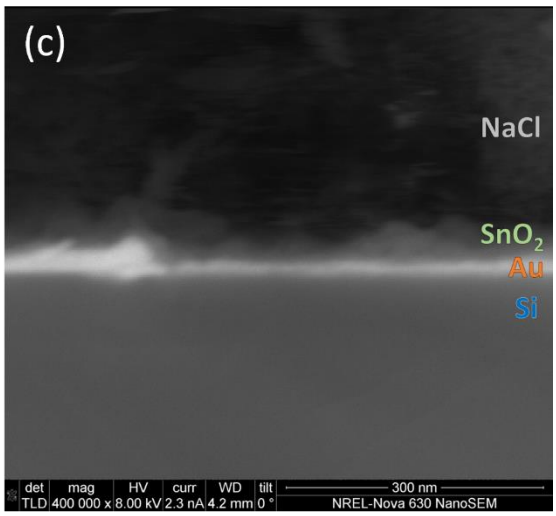

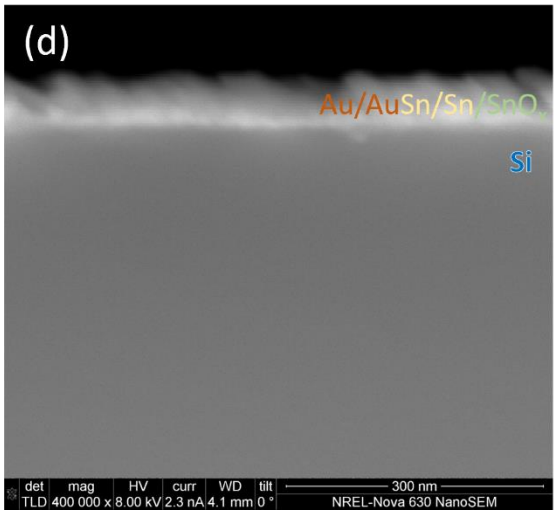

Figure S2.6: Cross-section SEM of (a) bare CD-Au, (b) ED-Sn, (c) ED-SnO_2 and (d) OD-ED-Sn. The gradient in the thin film region is represented by the layers in the composite films with the following interfaces from bottom to top: Au-AuSn, AuSn-Sn, Sn-SnO_x.

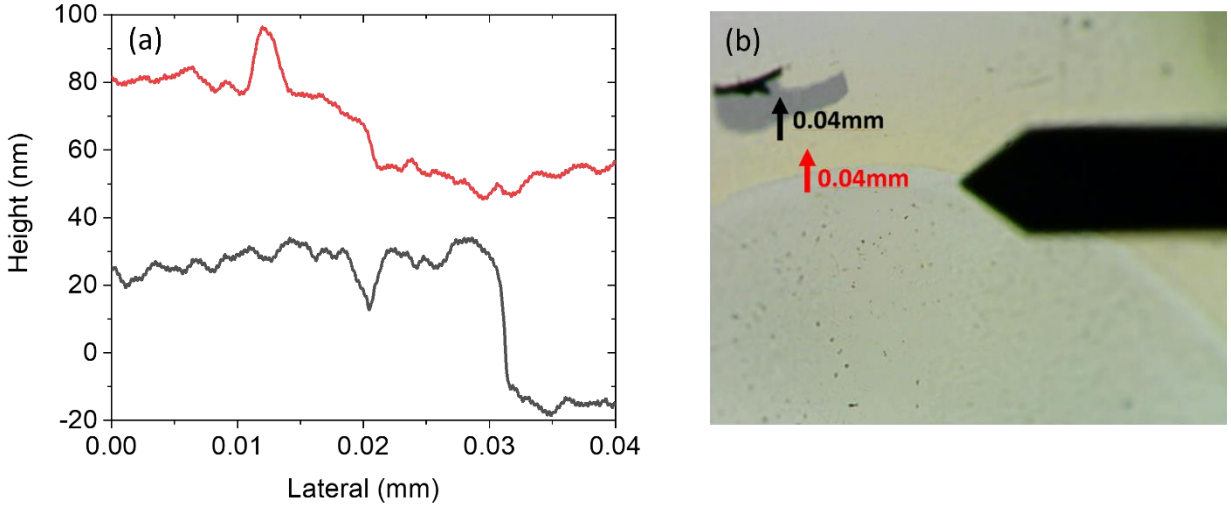

Figure S2.7: (a) Profilometer thickness profile of CD-Au (black line) and ED-Sn (red line) layers. (b) Optical microscope image of the profilometry measurement region. Red arrow represents the path to measure the Sn/Au step edge. Black arrow represents the path to measure the Au/Si step edge.

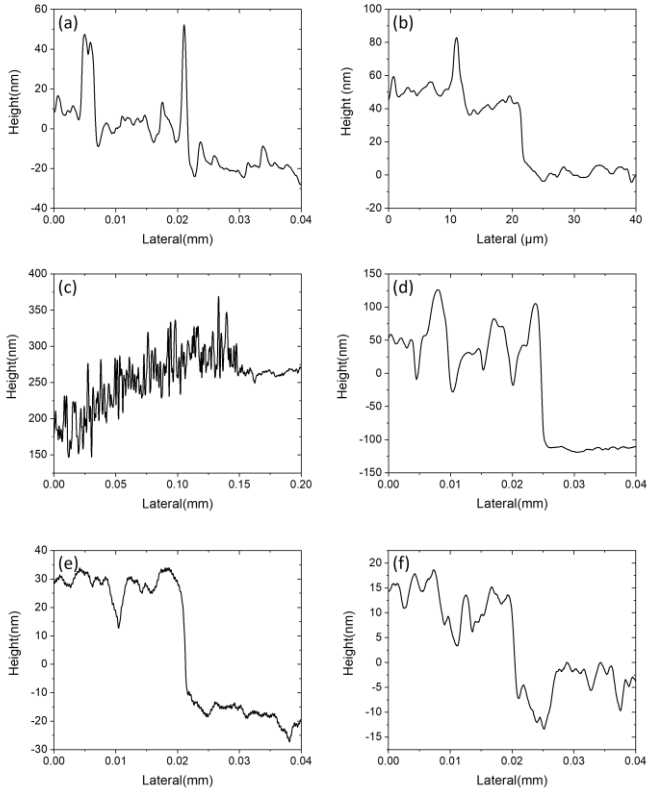

Figure S2.8: Profilometer thickness profiles of (a) ED-SnO_2, (b) OD-ED-Sn including Au layer, (c) TE-Sn sample edge, (d) TE-Sn sample center, (e) CD-Au and (f) TE-Au.

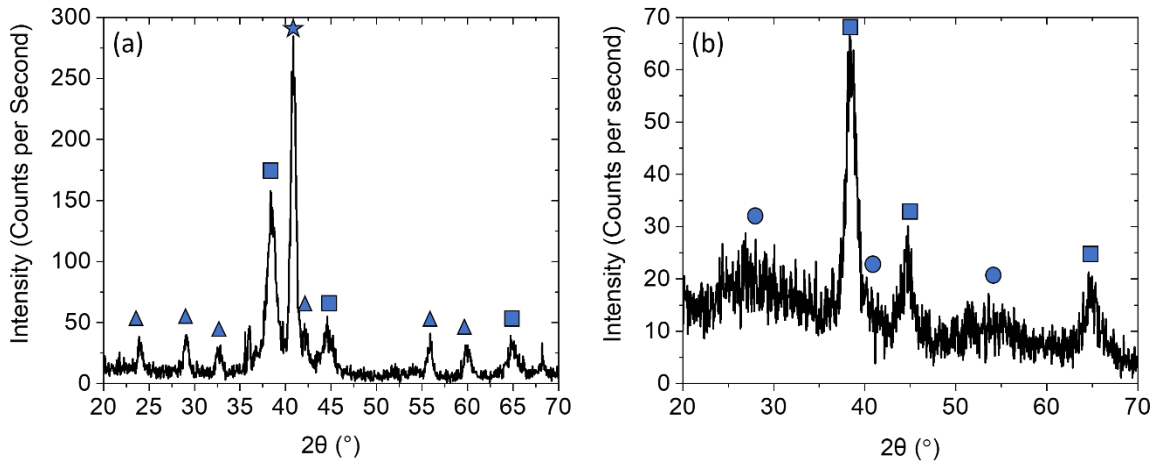

Figure S2.9: XRD patterns of (a) EDSn. Stars correspond to Sn^0, squares correspond to Au^0, and triangles correspond to SnAu. And (b) ED-SnO_2. Circles correspond to SnO_2 and squares correspond to Au^0.

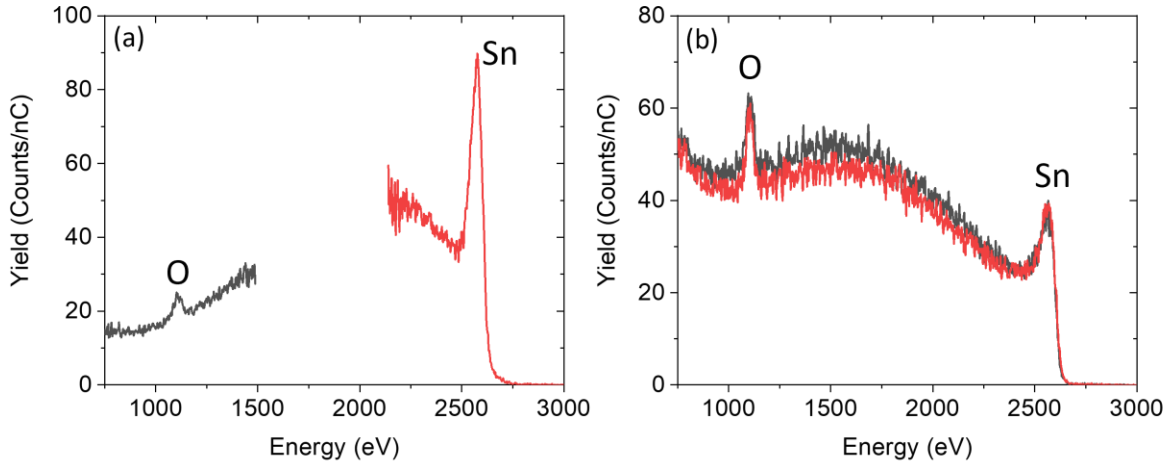

Figure S2.10: HS-LEIS spectrum of as synthesized (a) ED-Sn and (b) ED-SnO_2 showing only Sn and O elements on the surface. In the case of ED-Sn, measurement was taken between 750-1500eV and 2300-3000eV to avoid collection in blank region.

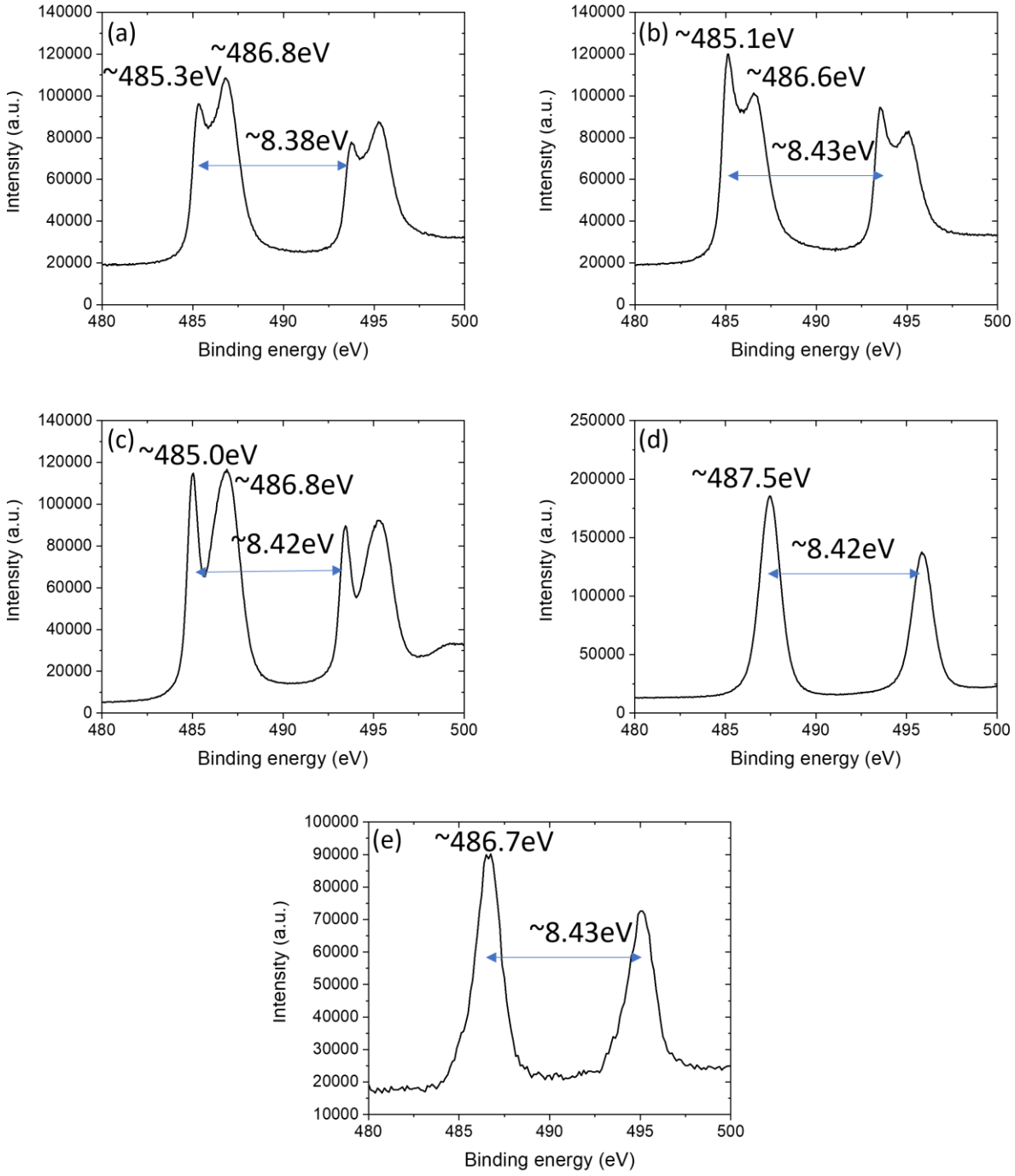

Figure S2.11: High resolution XPS Sn 3d spectra of (a) ED-Sn, (b) OD-ED-Sn, (c) TE-Sn and (d) ED-SnO_2 as is and (e) ED-SnO_2 post initial sputter etch.

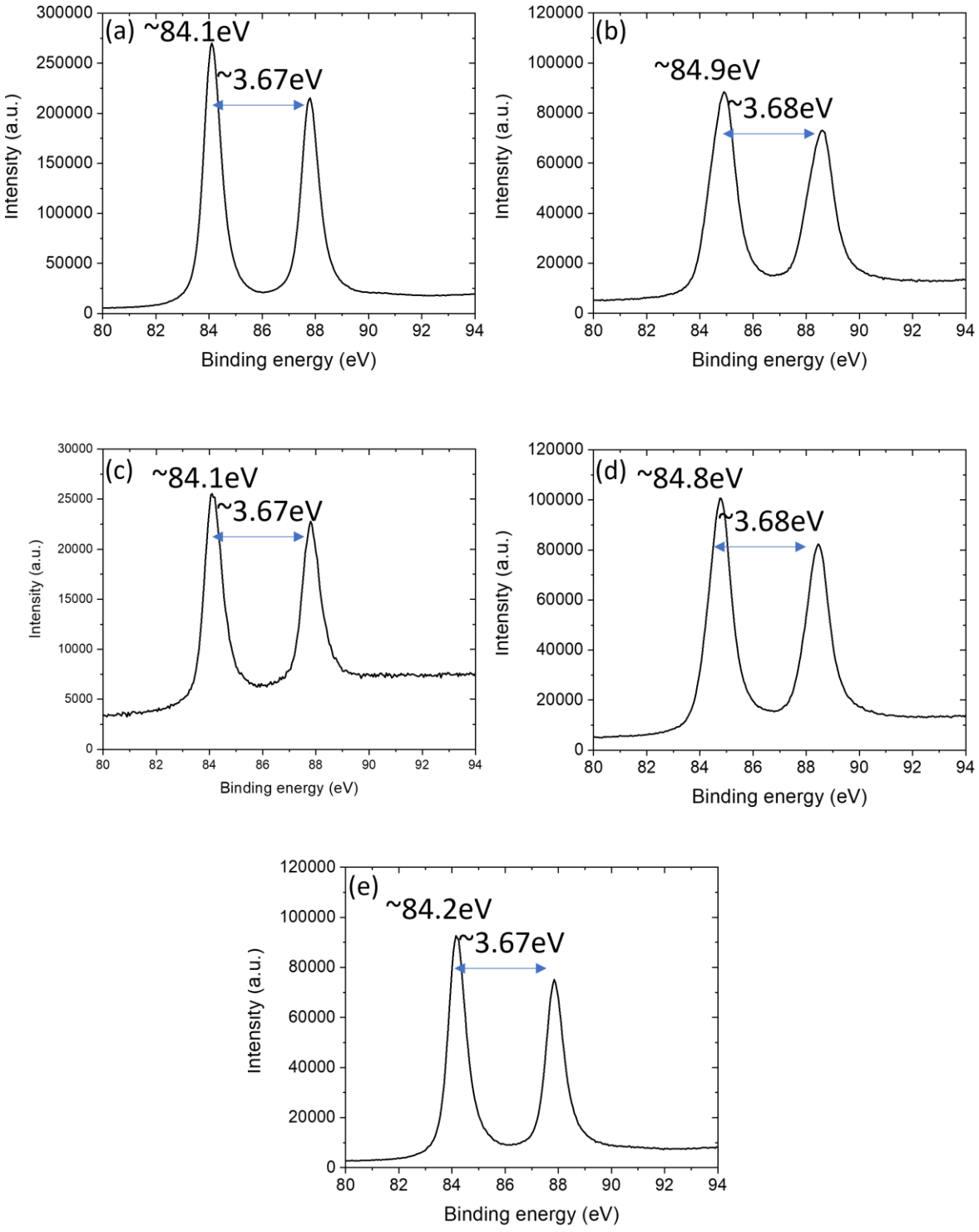

Figure S2.12: High resolution XPS Au 4f spectra of (a) CD-Au, (b) ED-Sn, (c) ED-SnO_2, (d) OD-ED-Sn and (e) TE-Au.

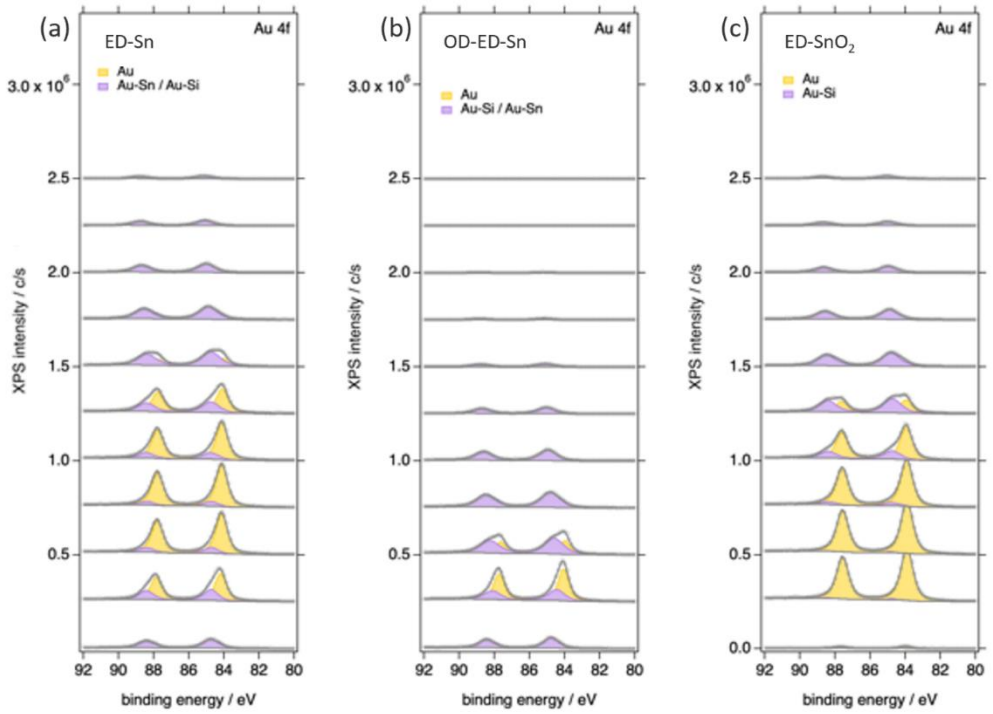

Figure S2.13: Depth profiling XPS spectra of $4f_{7/2}$ and $4f_{5/2}$ peaks position as a function of sputter time on (a) ED-Sn, (b) OD-ED-Sn and (c) ED-SnO_2.

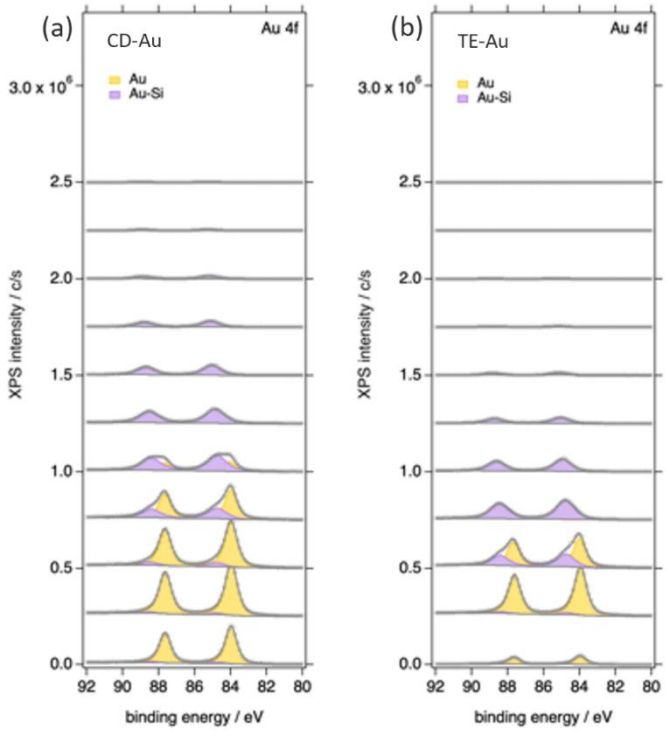

Figure S2.14: Depth profiling XPS spectra of Au $4f_{7/2}$ and $4f_{5/2}$ peaks position as a function of sputter time on (a) CD-Au and (b) TE-Au.

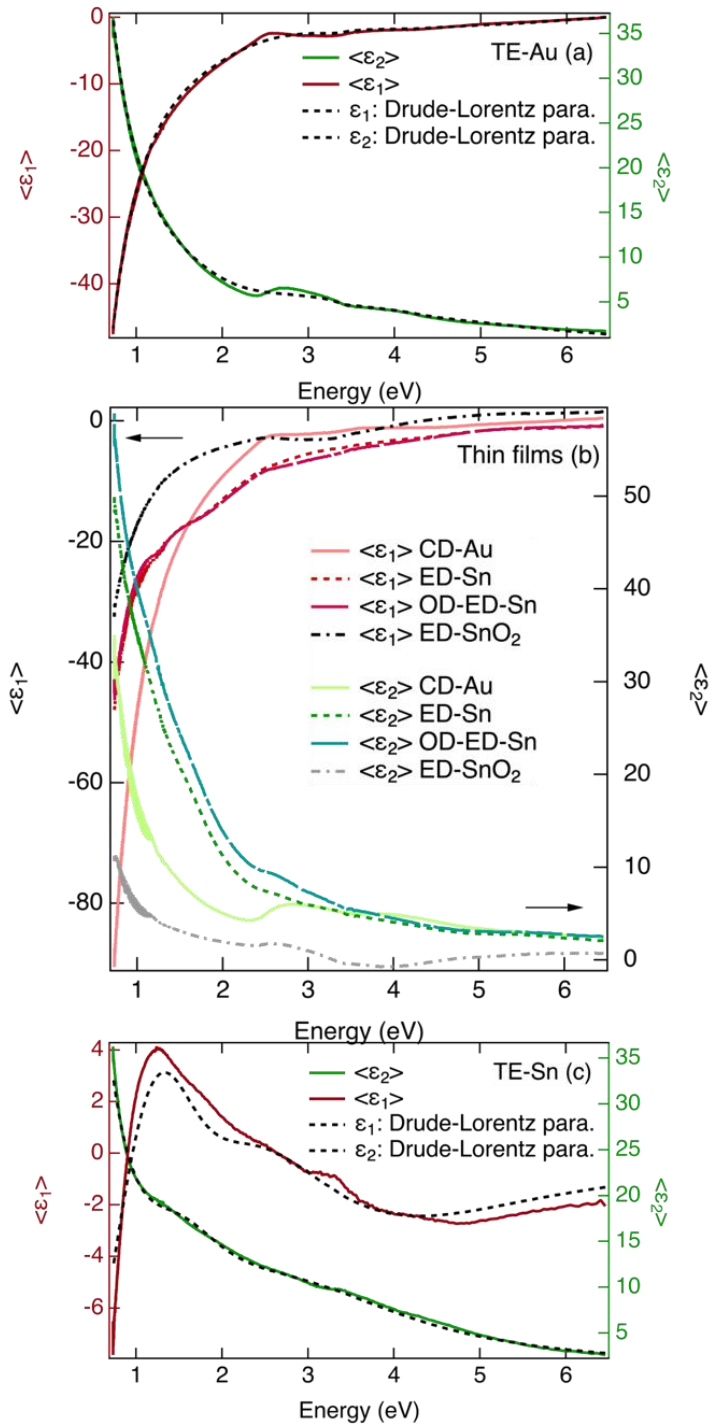

Figure S2.15: Pseudo dielectric function $<\varepsilon_1>$ and $<\varepsilon_2>$ for all thin film systems considered in this study: a) TE-Au, b) CD-Au, ED-Sn, OD-ED-Sn, ED-SnO_2, c) TE-Sn. For the pristine metals, TE-Au and TE-Sn, the actual dielectric function, ε_1 and ε_2, obtained from a general oscillator model is added in the dashed line.

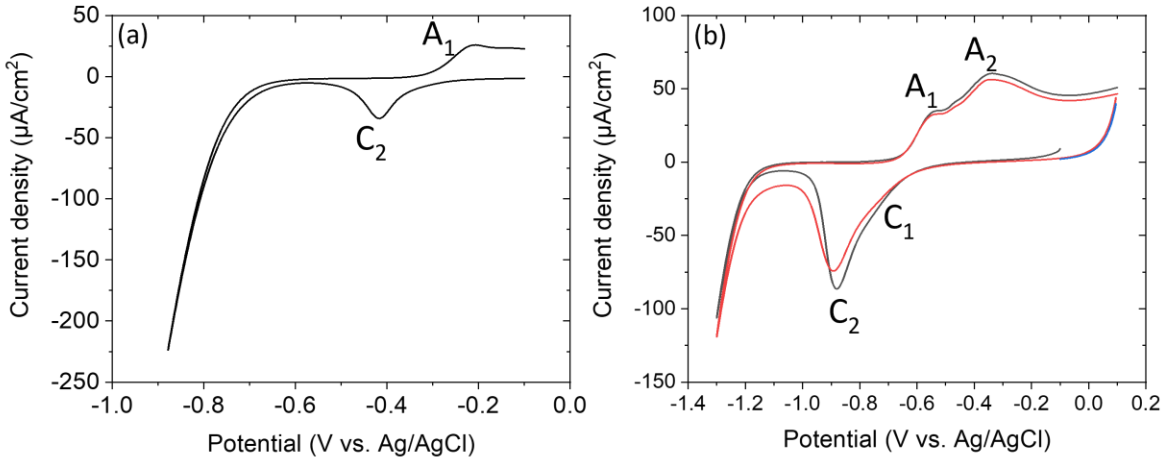

Figure S2.16: As deposited CV cycling within Sn/SnO_x redox region for (a) ED-Sn (on Au) in 0.1 M-$HClO_4$ and (b) ED-SnO_2 (on Au) in 0.1 M-$NaClO_4$. Black curve corresponds to first cycle and red curve corresponds to second cycle.

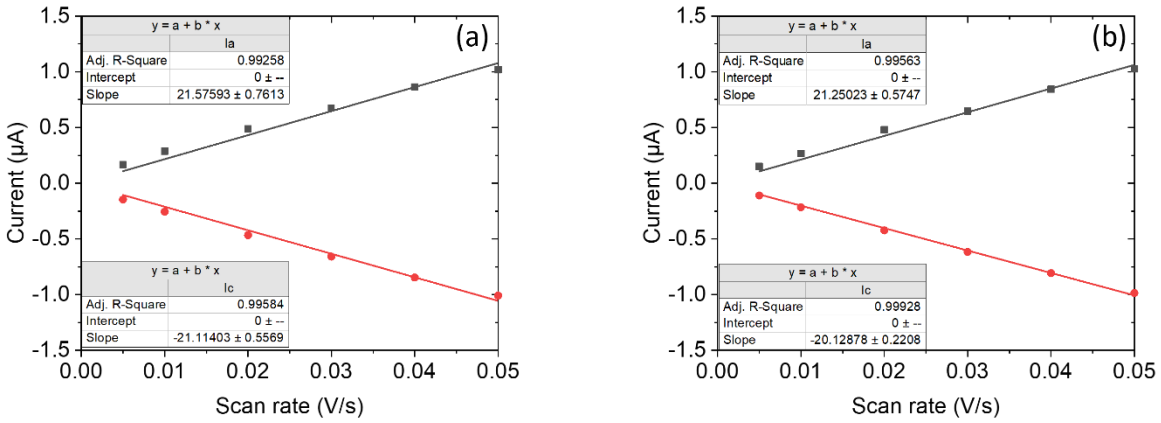

Figure S2.17: ECSA by double layer capacitance in 0.15 M-KF_6P in acetonitrile of (a) ED-Sn electrode. Black squares correspond to anodic current and red circles correspond to cathodic current, and (b) OD-ED-Sn electrode. Black squares correspond to anodic current and red circles correspond to cathodic current.

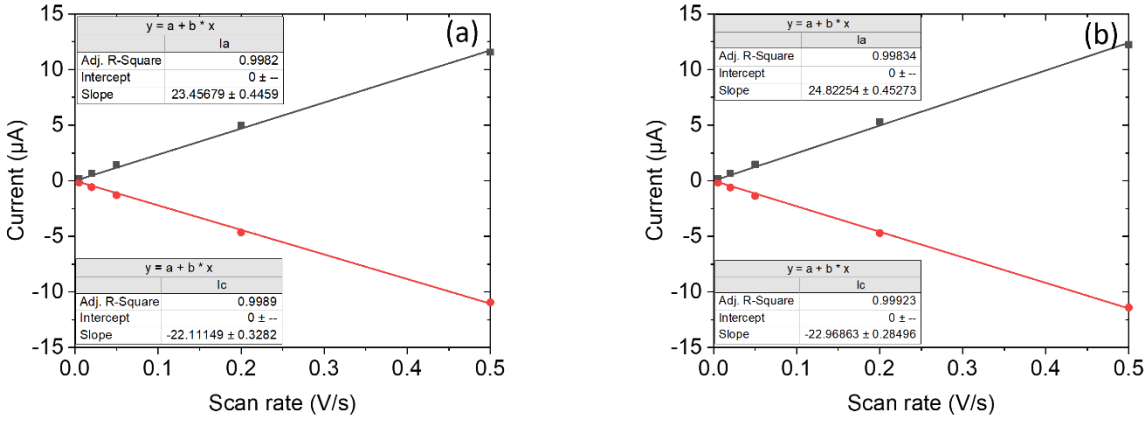

Figure S2.18: (a) ECSA of CD-Au estimation by double layer capacitance in 0.1 M $HClO_4$. Black squares correspond to anodic current and red circles correspond to cathodic current. (b) ECSA of TE-Au estimated by double layer capacitance in 0.1 M-$HClO_4$. Black squares correspond to anodic current and red circles correspond to cathodic current.

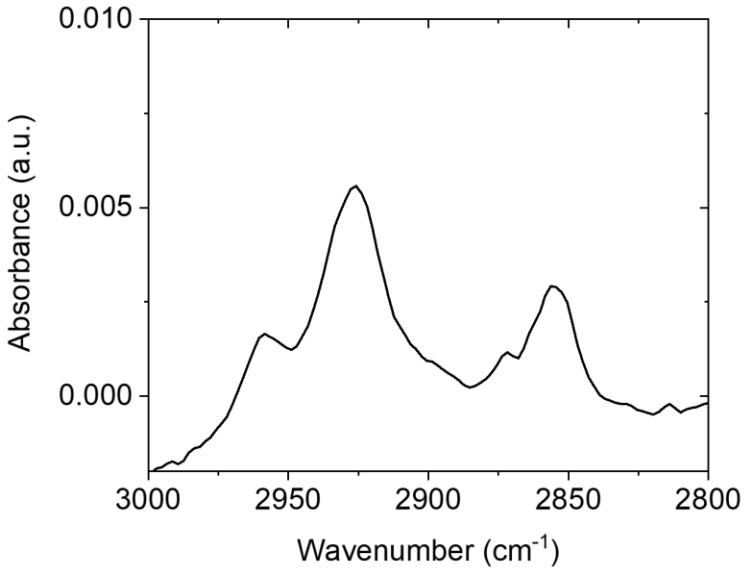

Figure S2.19: ATR-FTIR spectrum of decyl phosphonic acid self-assembled monolayer on as synthesized ED-SnO_2

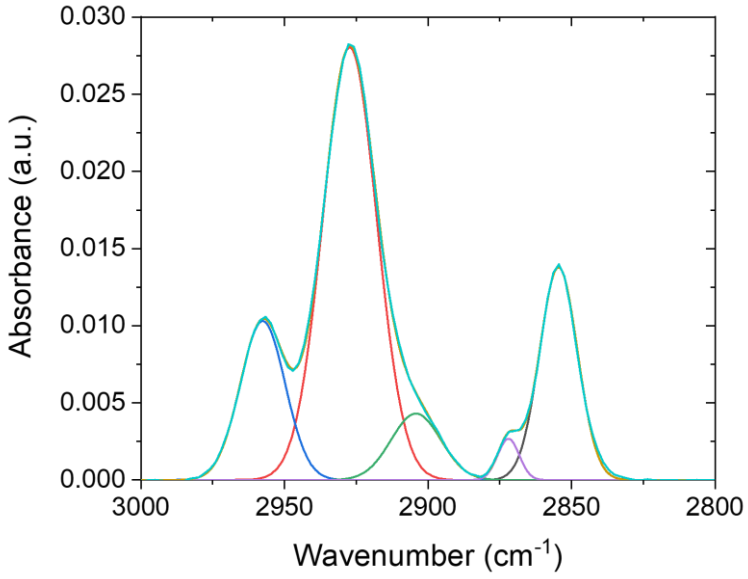

Figure S2.20: Representative fit of CH_2 and CH_3 stretches region for signal response analysis

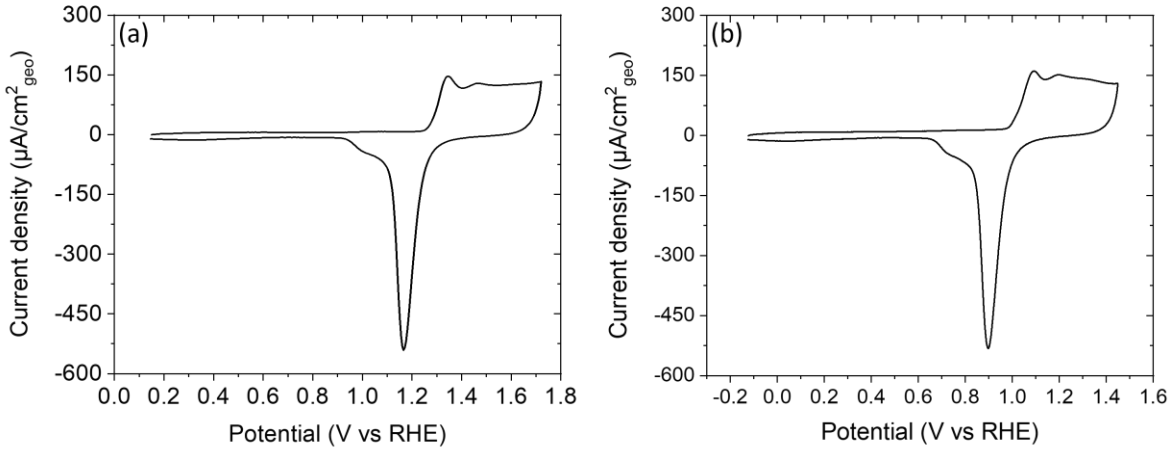

Figure S2.21: Characteristic CV profile of (a) CD-Au and (b) TE-Au in 0.1 M $HClO_4$ at a scan rate of 50 mV/s.

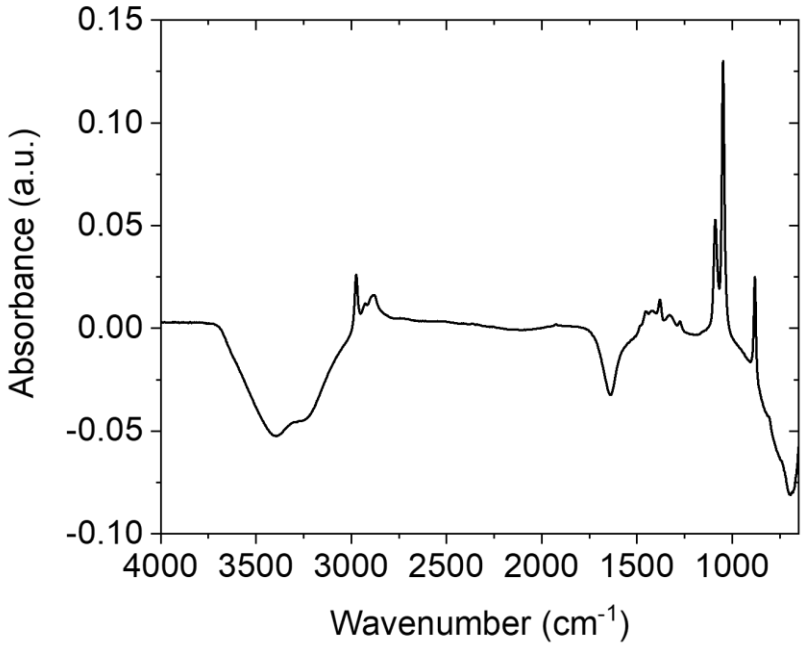

Figure S2.22: ATR-FTIR spectrum of 200 proof ethanol over silicon uATR element. Background taken in DI water.

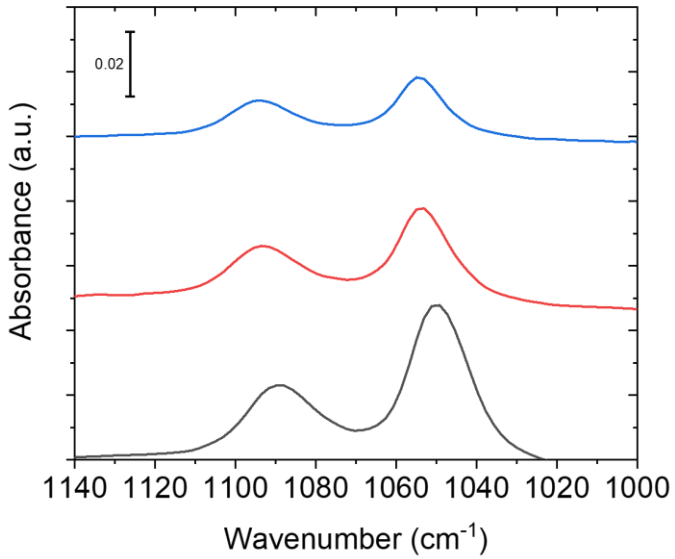

Figure S2.23: ATR-FTIR spectra of C-O stretch in EtOH signal response as a function of electrodeposited Sn electrode thickness by charge. Blue line corresponds to 1 mC ED-Sn, red line corresponds to 6 mC ED-Sn and black line corresponds to 12 mC ED-Sn.

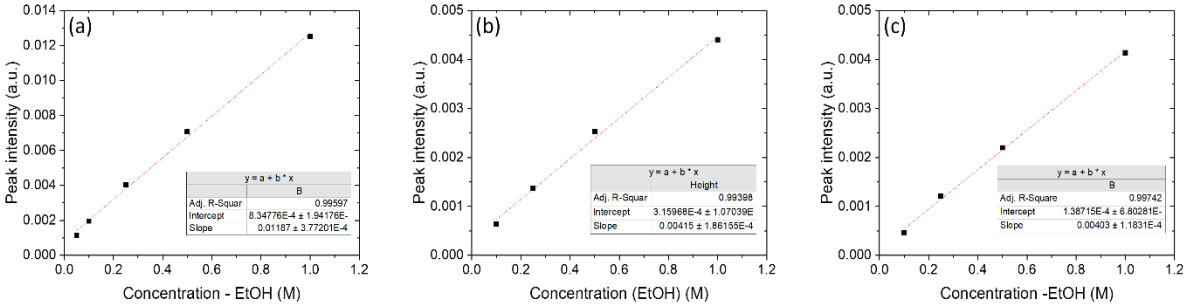

Figure S2.24: Ethanol detection limit dilution series above: (a) ED-Sn, (b) OD-ED-Sn and (c) CD-Au electrocatalysts.

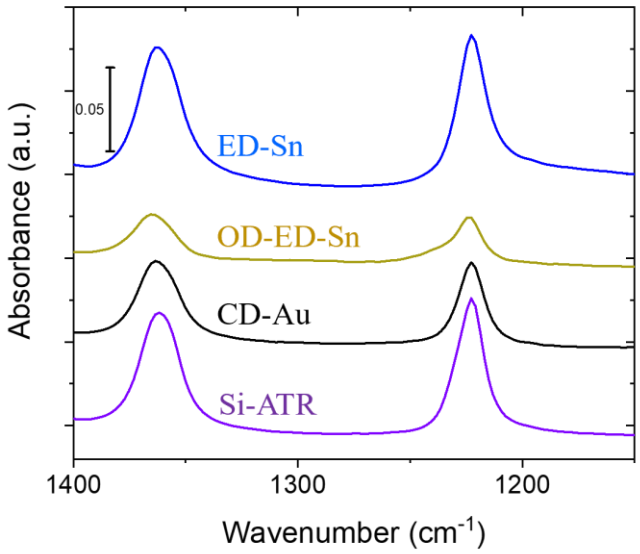

Figure S2.25: Acetone ATR-FTIR spectra above: ED-Sn, OD-ED-Sn, CD-Au and bare silicon.

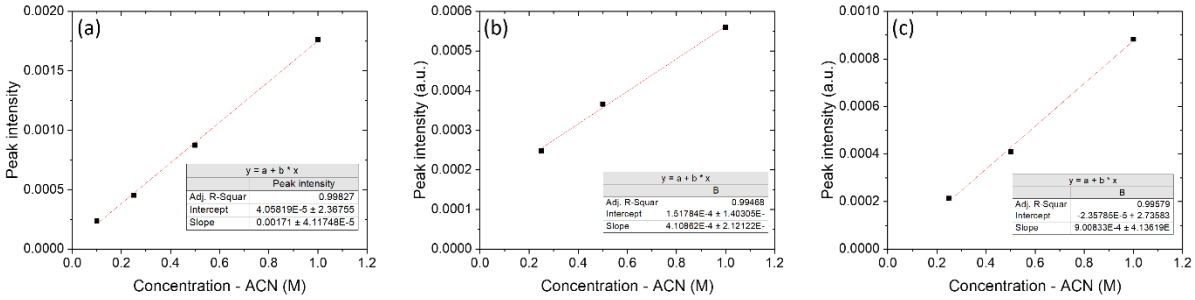

Figure S2.26: Acetonitrile detection limit dilution series above: (a) ED-Sn, (b) OD-ED-Sn and (c) CD-Au thin films.

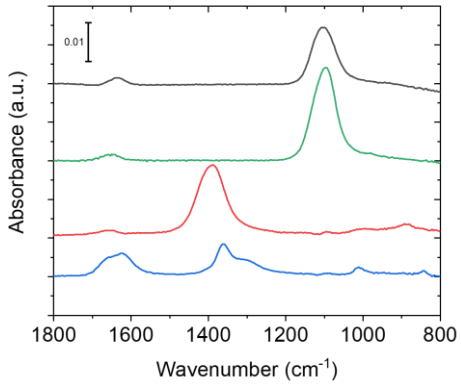

Figure S2.27: Characteristic ATR-FTIR spectrum of solution phase electrolytes. Black line corresponds to ClO_4^- , Green line corresponds to SO_4^{2-}, red line corresponds to CO_3^{2-} and blue line corresponds to HCO_3^-.

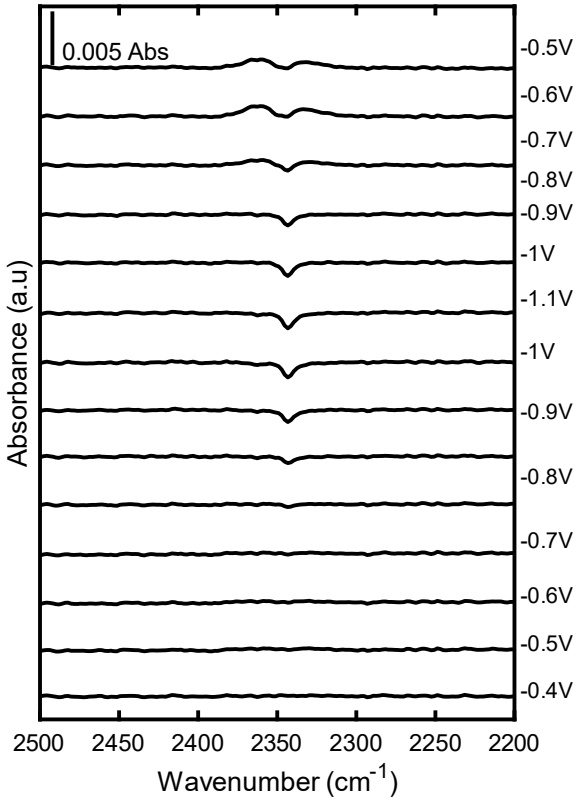

Figure S2.28: ATR-FTIR spectrum of $CO_{2,aq}$ consumption upon reduction. A negative band at 2343 cm^{-1} is commonly attributed to $CO_{2,aq}$.[23] Apart from these peak assignments unrelated to the surface or reaction, the band around 1650 cm^{-1} is associated with the water in-plane H-O-H bending mode (Figure 5a.b).[24] These results yield lower signal likely due to the fact that we are not reaching high surface coverage or there is a difference in dipole moment orientation or absorption cross section.

Table S2.1: Average roughness height and RMS for EDSnO$_2$, EDSn and TESn

	As is ED-SnO$_2$	OD-ED-Sn	As is TE-Sn	Pretreated TE-Sn	Pretreated ED-Sn
Average roughness	33.4nm	4.7nm	57.1nm	66.4nm	5.6nm
RMS	41.8nm	6.1nm	70.4nm	78.4nm	7.7nm
Average particle height	61.0nm	16.8nm	124.0nm	116.9nm	8.77nm

Table S2.2: Results from the Drude-Lorentz oscillators used to model TE-Au and TE-Sn, where the error bars give the 90% confidence interval

Thin film system	Metal thickness (nm)	Drude parameters [a]	Lorentz parameters [b]	Surface roughness [c] (nm)	Overall fit quality – mean squared error (MSE)
TE-Au	30.28 $\pm$ 0.15	R = 2.66x10^{-5} $\pm$ 6x10^{-7} $\Omega.cm$ τ = 4.06 $\pm$ 0.08 fs	Amp = 3.77 $\pm$ 0.02 eV Br = 4.59 $\pm$ 0.04 eV En = 4.14 $\pm$ 0.01 eV	--	15.88
TE-Sn	38.96 $\pm$ 0.21	R = 1.10x10^{-4} $\pm$ 8x10^{-6} $\Omega.cm$ τ = 1.17 $\pm$ 0.01 fs	Amp = 27.30 $\pm$ 0.34 eV Br = 3.65 $\pm$ 0.04 eV En = 3.63 $\pm$ 0.01 eV	14.85 $\pm$ 0.14	13.91

[a:] R and τ represent the modeled resistivity and scattering time of free carriers responsible for the Drude intraband absorption (free carriers). B: The interband absorption (bound carriers) can be parametrized using a Lorentz oscillator characterized by amplitude (Amp), broadening (Br), and energy position (En). [c]: The surface roughness is modeled using an EMA where the void fraction and the fraction of the top layer is modeled.

Table S2.3: Solvents detection limit

	ED-Sn	OD-ED-Sn	CD-Au	TE-Sn	TE-Au
Ethanol	0.118 M	0.143 M	0.167 M	-	-
Acetonitrile	0.400 M	0.794 M	0.537 M	-	-

Table S2.4: Optical properties of Si, Au and Sn

	α(@3400nm) [cm^{-1}]	ε'(@3400nm)	ε''(@3400nm)	n
Si[94]	0.0083862	12.040	1.5746*10^{-6}	3.4699
Au[95]	8.5750*10^5	-537.82	31.508	0.67903
Sn[96]	7.3772*10^5	-372.27	204.07	5.1120

RF estimation by average roughness height RMS

Example: $Pretreated\ TESn_{RF} = \frac{Pretreated\ TESn_{RMS}}{EDSn^0_{RMS}} * EDSn^0_{RF} = \frac{78.4}{7.7} * 6 = 61.1$

Electrode thickness calculation

For the electrode thickness calculation, as first approximation, we assume that the gold underlayer is a smooth and flat surface (Geometric area=ECSA). Second, we use the Van Der Waals tin ion cross-sectional area per tin atom deposited. Working electrode window cross-sectional area: 0.3167cm^2; Sn ionic cross-sectional area: 1.5904x10^{-15}[cm^2/atom]. This results in 1.9913x10^{14} atoms per atomic layer, ignoring the packing factor. Assuming 2 electron transfer per Sn atom → 3.982x10^{14} [electrons/layer].

(1) $3.982x10-14\ [electrons/layer]\ *\ 1.6022x10-19\ [C/electron]\ =\ 6.3808x10-5\ [C/layer]\ =\ 0.063808\ [mC/layer]$.

(2) $12[mC]\ /0.063808\ [mC/layer]\ =\ 188layers \sim 84.6\ [nm]$

Under the assumption of depositing the same amount of Sn atoms per layer.
Considering experimental roughness factor, the charge per layer comes to:

(3) $0.063808\ \left[\frac{mC}{layer}\right] * 9 =\ 0.5743\ \left[\frac{mC}{layer}\right]$

Therefore, the electrodeposited layer thickness turns to:

(4) $12[mC]\ /0.5743\ [mC/layer]\ =\ 20.9layers \sim 9.1\ [nm]$

Surface plasmon polariton penetration depth

$$L_{pd} = \frac{1}{Re\{\gamma_d\}}\ ;\ \gamma_d = ik\frac{\varepsilon_d}{\sqrt{\varepsilon_m+\varepsilon_d}}\ ;k = \frac{2\pi}{\lambda}$$

With L_{pd} being the penetration depth into the dielectric medium of a surface plasmon polariton, γ_d being the propagation constant, k being the wave vector and ε being the permittivity of the material. Since L_{pd} is formed at the metal-dielectric interface, the thickness of the metal layer does not affect its value.

$$L_{px} = \frac{1}{2 * k''_x}\ ;k''_x = \frac{2\pi}{\lambda}\left(\frac{\varepsilon'_m * \varepsilon_d}{\varepsilon'_m + \varepsilon_d}\right)^{\frac{3}{2}}\left(\frac{\varepsilon''_m}{2\varepsilon''^2_m}\right)$$

With L_{px} being the propagation length (1/e decay) along the interfacial surface, k''_x being the imaginary component of the propagation vector, ε'_m and ε''_m being the real and imaginary components of the metal permittivity and e_d being the dielectric permittivity. Since L_{px} is formed at the metal-dielectric interface, the thickness of the metal layer does not affect its value.

Fresnel reflection coefficient for prism-metal-dielectric system

$$r_{pmd} = \frac{r_{pm}+r_{md}e^{2ik_{mx}q}}{1+r_{pm}r_{md}e^{2ik_{mx}q}}\ ;\ k_{mx} = \frac{2\pi n_m}{\lambda} * \cos(\theta)$$

With r_{pmd} being the total reflection coefficient from both the prism-metal and the metal-dielectric interfaces, r_{pm} being the reflection coefficient from the prism-metal interface, r_{md} being the reflection coefficient from the metal-dielectric interface, k_{mx} being the perpendicular component of the wave vector within the metal layer and q being the metal layer thickness.

Chapter 3: Insights into Electrochemical CO_2 Reduction on Metallic and Oxidized Tin Using Grand-Canonical DFT and In Situ ATR-SEIRA Spectroscopy

Reprint with permission from: ACS Catal. 2024, 14, 8353-8365, https://doi.org/10.1021/acscatal.4c01290. The full-text version of this article may be viewed at: https://pubs.acs.org/doi/full/10.1021/acscatal.4c01290

In this work, I was in charge of the ATR-SEIRAS methodology, measurements acquisition, processing and analysis, and manuscript editing.

3.1 Abstract

Electrochemical CO_2 reduction (CO_2R) to formate is an attractive carbon emissions mitigation strategy due to the existing market and attractive price for formic acid. Tin is an effective electrocatalyst for CO_2R to formate, but the underlying reaction mechanism and whether the active phase of tin is metallic or oxidized during reduction is openly debated. In this report, we used grand-canonical density functional theory and attenuated total reflection surface-enhanced infrared absorption spectroscopy to identify differences in the vibrational signatures of surface species during CO_2R on fully metallic and oxidized tin surfaces. Our results show that CO_2R is feasible on both metallic and oxidized tin. We propose that the key difference between each surface termination is that CO_2R catalyzed by metallic tin surfaces is limited by the electrochemical activation of CO_2, whereas CO_2R catalyzed by oxidized tin surfaces is limited by the slow reductive desorption of formate. While the exact degree of oxidation of tin surfaces during CO_2R is unlikely to be either fully metallic or fully oxidized, this study highlights the limiting behavior of these two surfaces and lays out the key features of each that our results predict will promote rapid CO_2R catalysis. Additionally, we highlight the power of integrating high-fidelity quantum

mechanical modeling and spectroscopic measurements to elucidate intricate electrocatalytic reaction pathways.

3.2 Introduction

Electrochemical CO_2 reduction (CO_2R) is a potential strategy to lessen the impact of anthropogenic climate change and has been studied extensively across a variety of electrode materials over the last few decades.[97] Copper has received the most attention in the CO_2R literature due to its seemingly unique ability to produce C_{2+} products such as ethylene and ethanol with appreciable Faradaic efficiency, while gold and silver have also been studied for their high selectivity to CO.[27,98,99] However, a recent technoeconomic analysis showed that under 2019 market conditions, formic acid was the CO_2R product with a production cost closest to break-even.[100] Formic acid, which has an annual global demand of ~800 kilotons and is used mostly as a food preservative and in the production of rubber and leather, is produced at scale via the hydrolysis of formamide, which has undesirable environmental impacts.[101] Therefore, CO_2R to produce formic acid is not only a promising climate solution but can potentially reduce dependence on a nonideal existing industrial process.

CO_2R catalysts that are selective toward formate are generally characterized by having a weak affinity for CO. Most are p-block metals, and, among these, tin (Sn) is the most attractive because it has higher electrochemical stability than zinc and indium, is more environmentally benign than cadmium or lead, and is more abundant than bismuth.[102,103] There have been many reports of using Sn-based electrocatalysts for CO_2R, generally showing that at potentials more negative than −0.6 V_{RHE}, Faradaic efficiencies of >70% toward formic acid can be achieved with state-of-the-art current densities reaching 500 mA/cm^2.[93,104–106] However, several reports have shown differing interpretations of the precise nature of the active phase of Sn during CO_2R. Based

on the Pourbaix diagram for Sn, the purely metallic phase is expected to be present at potentials more negative than −0.5 V_{RHE}. However, numerous reports have invoked oxide phases of Sn as the active phase,[104,107–114] with some going as far as to say that CO_2R does not proceed on metallic Sn at all.[42,115,116] In direct opposition to this conclusion, many other reports claim that the metallic phase is the active phase and that in situ reduction of the oxide material to a more active metallic Sn phase is responsible for the high observed CO_2R activity and selectivity.[93,117,118] Clearly, neither the true surface state nor the mechanism of CO_2R on Sn-based electrocatalysts has been firmly established, and this lack of clarity has limited the development of improved catalysts and reactor systems.

In this report, we use a combined computational chemistry and in situ spectroscopic approach to examine CO_2R on both metallic and oxidized Sn electrodes. While a number of metastable Sn phases exist between the fully metallic Sn^0 and fully oxidized SnO_2 phases that could be responsible for CO_2R activity,[42,107] we chose these end points as useful limiting cases to examine. We use grand-canonical density functional theory (GC-DFT) to investigate the CO_2R mechanism under conditions relevant to the in situ experimental measurements. This approach poses several advantages compared to simpler methods such as the computational hydrogen electrode (CHE) method developed by Nørskov and co-workers almost 20 years ago. While the CHE is elegantly simple and has led to valuable insights into electrocatalytic mechanisms,[119] it also suffers from key limitations, namely that all molecular geometries, including the catalyst adsorbate structures, are relaxed at the potential of zero charge (PZC), that all electron transfers must be charge neutral (e.g., proton-coupled electron transfer, PCET, rather than sequential proton/electron transfer), and that it neglects the potential dependence on energetics of chemical steps.[120–123] GC-DFT accurately describes electrochemical mechanisms due to its self-consistent

treatment of the electrified interface under an applied potential and its ability to capture decoupled charge transfer, widely believed to be a relevant elementary step in CO_2R ($CO_2 + * + e^- \rightarrow CO_2^-$ *, where * represents a surface active site).[99,123,124] We also use attenuated total reflection surface-enhanced infrared absorption spectroscopy (ATR-SEIRAS) to investigate metallic and oxidized Sn surfaces during electrocatalysis. We recently developed a method of preparing Sn-based films that exhibit excellent surface enhancement in ATR-SEIRAS.[125] Much of the ongoing debate in the community regarding CO_2R on Sn originates from the lack of reliability in preparing and characterizing model Sn surfaces for spectroscopic investigation, as well as ambiguous frequency assignment.[42,104] By carefully comparing our observations from the GC-DFT and ATR-SEIRAS studies, we show that CO_2R is feasible on both metallic and oxidized Sn through a combination of pathways that lead to adsorbed formate. Based on these results, metallic Sn is expected to show stronger competition from the hydrogen evolution reaction (HER) because of its lower affinity for CO_2R intermediates, whereas oxidized Sn is hindered by overbound formate and competition with molecularly adsorbed water and electrolyte ions.

3.3 Methods

3.3.1 Materials

All solutions were prepared in 18.2 MΩ deionized water (Elga PURELAB flex 1). CO_2 (4.0, Airgas), Ar (5.0, Airgas), 96% sulfuric acid (Suprapur, Merck), 65% nitric acid (Suprapur, Merck), tin(II) sulfate (≥95%, Sigma-Aldrich), and potassium bicarbonate (Certified ACS Crystalline, Fisher Chemical) were used as received.

3.3.2 ATR-SEIRAS

In situ ATR-SEIRAS experiments were performed on a Nicolet 6700 FTIR spectrometer (Thermo Fisher Scientific) with a VeeMAX III ATR chamber (PIKE Technologies). The spectro-electrochemical experiments were performed in a J1W Jackfish spectro-electrochemical cell (PIKE Technologies) with a PTFE/PEEK base. The synthesis and characterization of ATR-SEIRAS-active Sn-based films have been described in detail elsewhere.[125] Other reports have also detailed the synthesis of electrodeposited metal films for SEIRAS, but not films of metal oxides.[126,127] Briefly, a polycrystalline Au underlayer was chemically deposited onto a Si(100) specialized 1 ATR element (single-bounce ATR crystal, IRUBIS) according to the procedure reported by Osawa.[43] This underlayer was electrochemically cycled between 0.2 and 1.75 V_{RHE} at 50 mV/s for 20 cycles with a Au counter electrode to achieve a clean, SEIRAS-active film. Metallic Sn was electrodeposited onto the Au underlayer at −0.467 $V_{Ag/AgCl}$ in 0.1 M H_2SO_4 until the total charge passed was 37.9 mC/cm_{geo}^2, which corresponds to a ∼10 nm thick Sn film. Oxidized Sn was deposited onto the Au underlayer by precipitating SnO_2 directly at the electrode surface by controlling the local pH via nitrate reduction to nitrite. The nitrate reduction was performed at −0.6 $V_{Ag/AgCl}$ in 1.5 M HNO_3 until the total charge passed was 3.16 C/cm_{geo}^2, which corresponds to a ∼20 nm thick SnO_2 film. The oxidized Sn film was reductively pretreated at −0.4 V_{RHE} for 5 min in 0.1 M $KHCO_3$ to improve the film's conductivity. Both Sn film deposition procedures used a graphite counter electrode. A non-Pt counter electrode was used during the Au underlayer and Sn film preparation was to avoid Pt dissolution and electrodeposition on the working electrode surface, which can cause erroneous SEIRAS features.[128,129] Once the Sn film was synthesized, spectroscopy was acquired using a Pt counter electrode which only experienced a linear anodic current sweep. Pt dissolution has been shown to be initiated during the oxide reduction process when switching from high anodic potentials back toward cathodic potentials.[130,131] Therefore, the

use of a Pt counter electrode should not convolute the SEIRAS features on Sn electrodes. CO_2R experiments were performed on metallic or oxidized Sn electrodes by sparging the electrolyte (0.1 M $KHCO_3$) with CO_2 for 20 min before starting the experiment. Cyclic voltammograms were collected using a Gamry Interface 1010 potentiostat at a sweep rate of 1 mV/s from −0.25 to −1 V_{RHE}. The uncompensated resistance was corrected using the current interrupt compensation feature of the potentiostat. Control experiments were also performed, where the electrolyte was sparged/blanketed with Ar rather than CO_2. All electrochemical experiments were performed using a homemade Ag/AgCl reference electrode, calibrated, and subsequently converted to the RHE potential scale.

3.3.3 Computational Details

GC-DFT calculations were performed using the open-source JDFTx software.[132] The generalized-gradient approximation PBE DFT functional with Grimme's D3 dispersion corrections was used for all calculations.[133,134] The Brillouin zone was sampled using a γ-centered 4 × 4 × 1 folded *k*-point mesh. The core electrons were modeled with GBRV v1.5 ultrasoft pseudopotentials with an energy cutoff of 20 hartree (544 eV) and a charge density cutoff of 100 hartree (2721 eV).[135] Charge neutrality was ensured by the inclusion of the CANDLE implicit solvation model.[136] The fluid solvent was water with 0.5 M NaF and was chosen as a noninteracting electrolyte. The constant potential calculations were performed by setting the electron chemical potential, μ_{calc}, to the desired potential via eq 3.1

$$\mu calc = -(Ve + VRHE - 0.059 * pH)\mu calc = -(Ve + VRHE - 0.059 * pH)\ ; \textbf{(eq 3.1)}$$

where V_e is the absolute electron potential (taken to be 4.66 eV, calibrated using the CANDLE solvation model[136]), V_{RHE} is the desired potential on the RHE scale, and pH is the solution pH

being modeled. Our calculations were performed at 0, −0.5, and −1 V_{RHE} and a pH of 8 to match the experimental conditions (energies were linearly interpolated between potentials to find equilibrium potentials reported in Results and Discussion). Bulk body-centered tetragonal (bct) Sn and rutile SnO_2 structures, acquired from the Materials Project,[21] were first relaxed and reproduced the experimental lattice parameters within 2% accuracy (calculated a = 5.958 Å, c = 3.157 Å and experimental a = 5.838 Å, c = 3.180 Å for bct Sn;[137] calculated a = 4.811 Å, c = 3.232 Å and experimental a = 4.741 Å, c = 3.187 Å for rutile SnO_2[138,139]). The lowest energy surfaces of each material were taken to be the 200 and 110 surface termination for bct Sn and SnO_2, respectively.[140,141] These surfaces were created using the Pymatgen python package.[142] Both surface unit cells, shown in Figure 3.1, contained 48 atoms (16 Sn and 32 O atoms for SnO_2(110)),

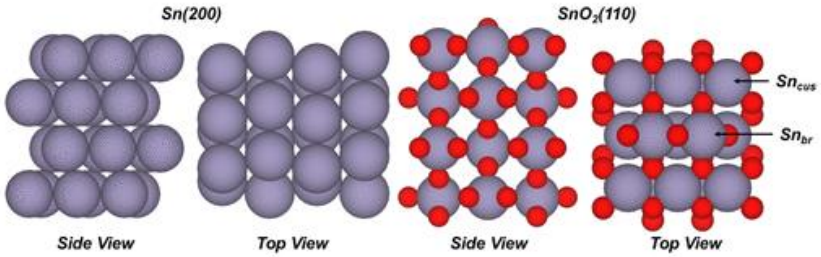

Figure 3.1: Side and top views of Sn(200) and SnO_2(110) surfaces.

and were 4 atomic layers thick, with at least 30 Å separating the slabs to ensure adequate potential screening. The bottom two atomic layers were frozen to their bulk coordinates. Geometry optimizations were performed using the Atomic Simulation Environment (ASE) python package.[143] Geometry optimizations were considered converged when the net force on the atoms was lower than 0.05 eV/Å. Vibrational frequencies for relevant adsorbates were calculated within JDFTx, with all atoms frozen aside from the adsorbate atoms and surface atoms directly bound to the adsorbate. Grand free energy was calculated according to eq 3.2

$$\Omega = EDFT - \mu Ne + EZPE + \int T0CpdT - TS\Omega = EDFT - \mu Ne + EZPE + \int 0TCpdT - TS \text{ ; } \textbf{(eq 3.2)}$$

where E_{DFT} is the electronic energy, μ is the potential of the calculation, N_e is the number of electrons in the calculation, E_{ZPE} is the zero-point energy, C_p is the heat capacity, T is the temperature, and S is the total entropy (sum of translational, vibrational, rotational and electronic). For molecules, the free energy corrections were determined from the ideal gas partition function using ASE's thermochemistry IdealGasThermo package. To investigate the vibrational frequency dependence on potential (Stark shift), we also computed the vibrational frequencies (at 298 K) as a function of potential. All converged geometries are shown in Figure S3.1.

3.4 Results and Discussion

3.4.1 Sn Surface Speciation Under Relevant Electrochemical Conditions

Before examining the thermodynamics of CO_2R intermediates on Sn surfaces, we first evaluated the potential-dependent interactions of both metallic and oxidized Sn with water in the absence of CO_2 across the range of potentials used in experiments. We performed this analysis because it is commonly claimed that surface hydroxylation is a key element for effective CO_2R catalysis on Sn-based electrodes.[42,104,107] For metallic Sn, we examined the oxidative adsorption of hydroxyl ($Sn + OH^- \rightarrow Sn - OH + e^-$) as well as associative adsorption of water molecules. We found that water spontaneously desorbed at all potentials on the Sn(200) surface. Figure 3.2 shows the coverage of hydroxyls on Sn(200) using a potential-dependent Langmuir adsorption isotherm, shown in eq 3.3

$$Keq,i = e - \Delta\Omega i(V)/RT; \theta i = Keq,iai1 + Keq,iaiKeq,i = e - \Delta\Omega i(V)/RT; \theta i = Keq,iai1 + Keq,iai \text{ ; } \textbf{(eq 3.3)}$$

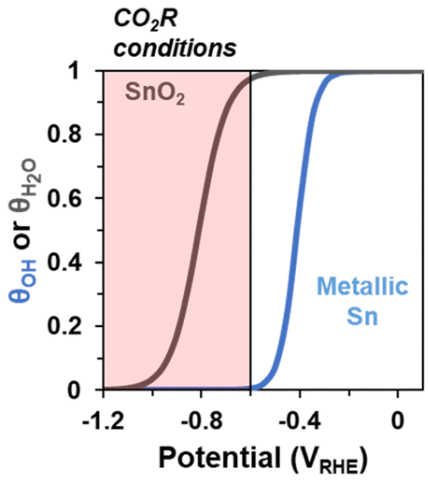

Figure 3.2. Coverage of OH* on Sn(200) and cus-water on SnO_2(110) as a function of potential, as derived from the potential-dependent change in grand free energy and Langmuir isotherm (eq 3.3, temperature = 298.15 K, pH = 8 and a_{H2O} = 1).

The coverage of hydroxyls on Sn(200) approaches zero for potentials more negative than −0.6 V_{RHE}. Therefore, for potentials more negative than −0.6 V_{RHE} on fully metallic Sn surfaces, we do not expect surface hydroxyls to make a significant contribution to CO_2R.

Oxidized Sn has a more complex surface speciation, summarized in Figure S3.2. Stoichiometric metal oxides are known to spontaneously dissociate water to form surface hydroxyls.[144–146] These surface hydroxyls are also known to have different Brønsted acid–base properties, namely that the hydroxyls bound to 5-fold coordinate metal sites (coordinatively unsaturated, or cus-) are more basic than those bound to 6-fold coordinate metal sites (bridge-bound, or br-).[147] We used the stoichiometric SnO_2(110) surface as our model starting point. The results of our calculations agree that stoichiometric SnO_2(110) spontaneously dissociates water to form cus- and br-hydroxyls at all potentials studied (more positive than −1 V_{RHE}). We also calculated the energy of protonating the cus-hydroxyls and found that, at potentials more negative than −0.5 V_{RHE}, the formation of cus-water groups is also spontaneous. Lastly, we considered the molecular desorption of water from cus- sites and found that it became favorable at potentials more

negative than −0.8 V_{RHE}. We found that br-hydroxyls could not be protonated; if a neighboring cus-hydroxyl site was available, the proton was spontaneously transferred to form the more stable cus-water, and if no cus-hydroxyl sites were available, the change in grand free energy was greater than 2 eV at all potentials.

CO_2R on Sn-based electrodes is generally carried out at potentials more negative than −0.5 V_{RHE}, so we considered the starting oxidized surface to be fully hydroxylated/protonated (where all br- sites are br-hydroxyl and all cus- sites are cus-water). Figure 3.2 also shows the coverage of cus-water as a function of potential. The coverage remains much higher than fully metallic Sn, only approaching zero at potentials more negative than −1.1 V_{RHE}. Therefore, in the potential regime relevant to CO_2R (−0.5 to −1 V_{RHE}), a non-negligible coverage of cus-water and br-hydroxyl is present. Consequently, we considered the clean Sn(200) (that is, no surface hydroxyls) and a SnO_2(110) surface with partial cus-water coverage (one cus-water and one cus-Sn with two br-hydroxyls), as well as with no cus-water groups (two cus-Sn and two br-hydroxyls). The other consequence of this finding is that a CO_2R mechanism that invokes the formation of surface bicarbonate/carbonate via nucleophilic attack of hydroxyls to CO_2 is unlikely to substantially contribute to the CO_2R activity of Sn-based electrodes.

3.4.2 Activation of CO_2

It has been proposed that the origin of selectivity toward formate over CO in CO_2R relates to bifurcation in pathways during CO_2 activation. One pathway creates OCHO* adsorbed via surface-oxygen(s) bonds, while the other creates COOH* adsorbed via a surface-carbon bond.[117] However, it is also often proposed that the first elementary step of CO_2R (to either product) is the single-electron reductive adsorption $CO_2 + * + e^- \rightarrow CO_2^{-*}$.[104,107,110,148] The CO_2^{-*} intermediate can be bound through the carbon atom or the oxygen atom(s), which can be

protonated to form COOH* or OCHO*, respectively. We therefore considered both the single-electron reductive adsorption and each of the PCET pathways to activate CO_2. We hypothesize that selectivity toward formate originates with the preference of Sn to activate CO_2 through the oxygen atoms rather than the carbon atom. We calculated the adsorption energy of CO_2 in both carbon-bound and oxygen-bound geometries as well as COOH* and OCHO* on the clean metallic Sn(200), SnO_2(110) with 1 cus-water, and SnO_2(110) with no cus-water surfaces as a function of potential, shown in Figure 3.3. It is immediately apparent however that the selective formation of

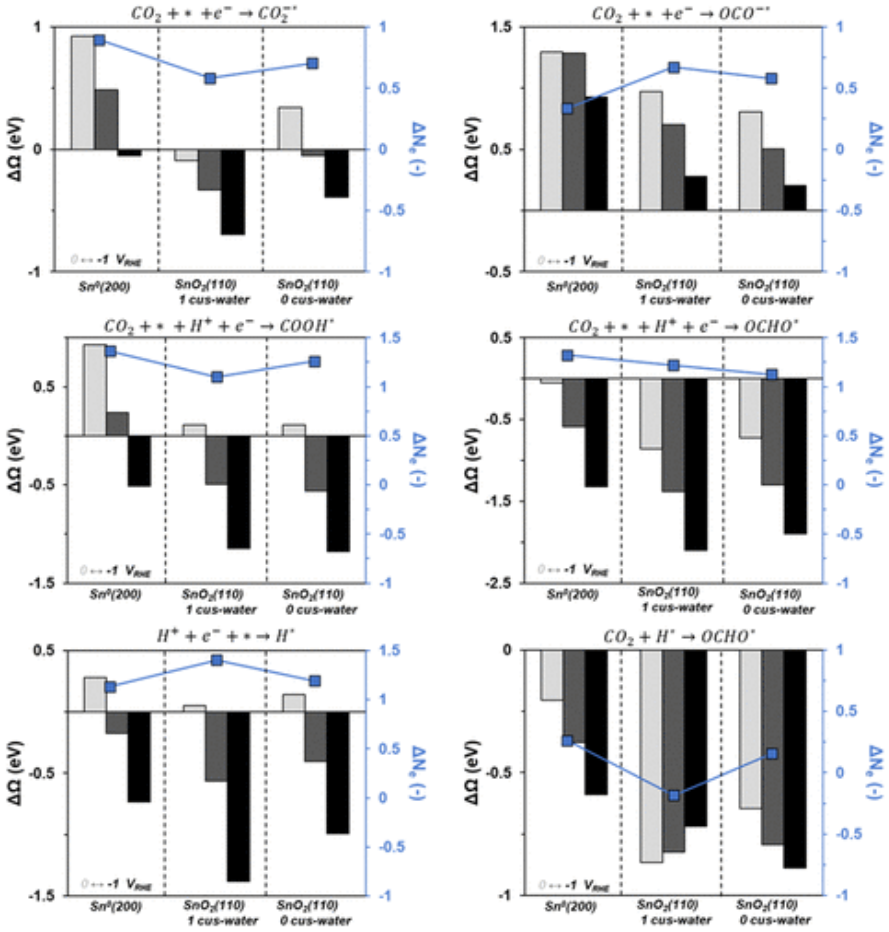

Figure 3.3: Change in grand free energy as a function of potential for different CO_2 adsorption elementary steps. The potentials are 0 (light gray), −0.5 (dark gray), and −1 (black) V_{RHE}. The reactions represented are reductive adsorption of CO_2 through the carbon atom (top left) and oxygen atom(s) (top right), proton-coupled electron transfer adsorption to form COOH* (middle left) and bidentate OCHO* (middle right), and proton adsorption (bottom left) and CO_2 insertion into a metal-hydride bond to form monodentate OCHO* (bottom right). The average number of electrons transferred across the three potentials is also shown (in blue).

OCO^{-*} vs CO_2^{-*} is not a reasonable explanation for the selectivity to formate vs CO, on metallic or oxidized Sn, regardless of potential. Reductive adsorption of CO_2 to form OCO^{-*} is not favorable at any potential more positive than −1 V_{RHE}—in fact, CO_2 spontaneously desorbs during geometry optimization at 0 and sometimes −0.5 V_{RHE}, see the Supporting Information, Figures S3.3 and S3.4 for a more detailed discussion of this point. In contrast, the formation of CO_2^{-*} becomes favorable at −0.99 and −0.45 V_{RHE} on metallic Sn and SnO_2 with no cus-water, respectively, while the formation of CO_2^{-*} is favorable at all examined potentials on the SnO_2 surface with one cus-water. Therefore, OCO^{-*} is not expected to play a substantial role in CO_2R toward formate. We note that in either case, the number of electrons transferred determined from the GC-DFT is not exactly one, but rather in the range of 0.4–0.9, depending on the surface and binding geometry. This demonstrates the utility of GC-DFT's ability to determine, rather than assume, the extent of charge transfer.

The formation of OCHO* is more favorable than COOH* across all potentials and surfaces, which is consistent with the experimentally observed selectivity trend. We did not calculate any transition state energies in the current study, and while a large kinetic barrier to forming OCHO* (or COOH*) via the PCET mechanism may exist, we expect the more exothermic step to also possess a lower activation barrier on the basis of Brønsted–Evans–Polanyi (BEP) scaling relationships.[149–151] Once again, we note that the number of electrons transferred in this step is not precisely what would be presumed from writing out the elementary steps, but in this case, more electrons (1.1–1.4) are transferred than expected. The consequence of this asymmetry in the degree of charge transfer is that the PCET adsorption of CO_2 to form either COOH* or OCHO* becomes more favorable at less reducing potentials than the reductive adsorption to form CO_2^{-*}.

We also considered the formation of monodentate OCHO* via CO_2 insertion into the Sn–H bond, known as the Eley–Rideal pathway, which has been suggested as a possible pathway for formate-selective CO_2R.[152] Figure 3.3 (bottom left) shows the energetics for proton reduction for the three different surfaces as a function of potential. The formation of H* becomes favorable at −0.29, 0.26, and −0.12 V_{RHE} on the metallic Sn(200), SnO_2(110) with one cus-water, and

SnO_2(110) with zero cus-water surfaces, respectively. Therefore, under potentials relevant for CO_2R, we expect a non-negligible coverage of H*, especially considering the adsorption energy is more favorable than for the adsorption of CO_2^{-*}. Figure 3.3 (bottom right) shows the energetics for insertion of CO_2 into the Sn–H bond. For all surfaces at all potentials, the formation of OCHO* in this fashion is favorable. There is less than a 0.1 eV difference in the formation energy for monodentate OCHO* and bidentate OCHO*. The potential dependence of the energetics of CO_2 insertion into the Sn–H bond is attenuated when compared to the Faradaic reactions in the other panels of Figure 3.3 because there is a lower, near-zero amount of electron transfer involved in this reaction, i.e., this is a chemical step. The origin of the potential dependence of this step may be due to second-order effects such as the interaction of the adsorbate dipole with the developing electric field, or changes in the stabilization of the electrolyte due to changes in the local concentration of electrolyte ions.[153]

3.4.3 Formation of Desorbed CO and Formate

The previous section compared the different pathways CO_2 may take to form an activated adsorbate on the surface of Sn-based catalysts. We now consider the next steps of CO_2R that involve the desorption of the products CO and formate. We started by calculating the adsorbate geometry of both CO and formic acid on the three Sn surfaces but found that they do not adsorb under any conditions considered (Figures S3.5 and S3.6). Therefore, moving forward we assume that any step that forms either CO or formic acid includes spontaneous desorption.

First, we considered reactions involving CO_2^{-*}. We note that the energetics presented in the previous section do not rule out the formation of CO_2^{-*} simply because the PCET adsorption to form COOH* or OCHO* is more downhill. The presence of a large kinetic barrier for the PCET steps and sufficiently low barrier for the direct reductive adsorption of CO_2^{-*} could lead to non-

negligible flux through this pathway, particularly on the oxide surfaces which bind CO_2^{-*} more strongly than metallic Sn. Both COOH* and OCHO* are accessible from CO_2^{-*}, the former likely coming from a proton transfer and the latter likely coming from a surface-catalyzed coupling of CO_2^{-*} with H*. The energetics for these reactions are depicted in Figure 3.4. Protonation of CO_2^{-*} is not purely a proton transfer—the GC-DFT calculation predicts that ~0.5 electrons are

Figure 3.4: Change in grand free energy as a function of potential for the protonation of CO_2^{-*} (top left), coupling of CO_2^{-*} and H* (top right), reduction of COOH* to form CO (bottom

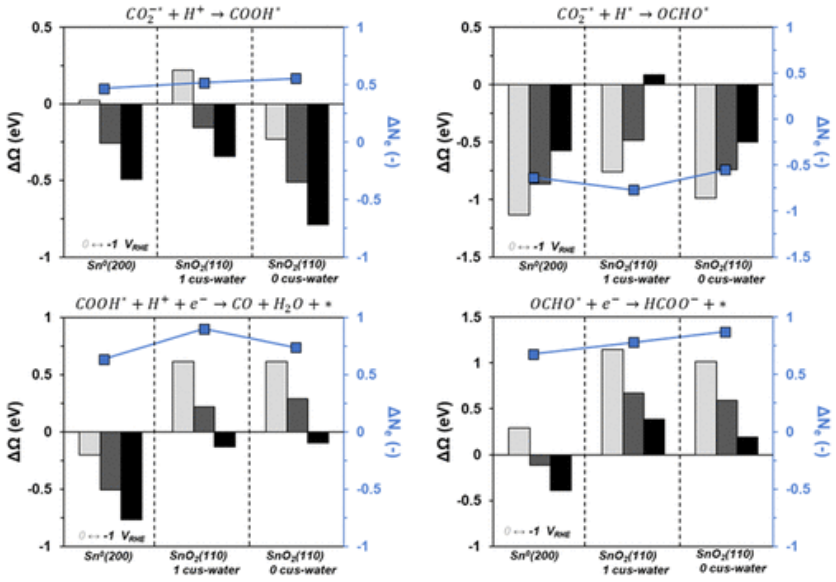

left), and reductive molecular desorption of OCHO* (bottom right). The potentials are 0 (light gray), −0.5 (dark gray), and −1 (black) V_{RHE}. The average number of electrons transferred across the three potentials is also shown (in blue).

transferred during this step as well. The formation of COOH* in this manner is mostly favorable across the three surfaces at all potentials considered. The Langmuir–Hinshelwood coupling between H* and CO_2^{-*} to form OCHO* is also mostly favorable across all potentials and surfaces studied, although interestingly the calculated electron transfer shows that this is an oxidation, with

~0.5 electrons transferred to, rather than from, the electrode. This step therefore becomes less favorable with more negative potential.

Next, we consider the reactions that form the CO or desorbed formate products (Figure 3.4). We examined a PCET reduction of COOH* to form CO and water as the pathway to CO and the reductive molecular desorption of OCHO* as the primary pathway to formate. We also considered the Langmuir–Hinshelwood coupling of COOH* and H* to form formic acid directly, but due to a less favorable change in grand free energy that becomes increasingly less favorable at more negative potential than the direct desorption, we do not consider it to be an active pathway (Figure S3.7). Interestingly, metallic Sn has a much larger driving force to form CO than either of the oxide surfaces, which only become favorable at potentials more negative than −0.8 V_{RHE}. This is somewhat expected based on the observation that COOH* is bound less strongly on the metallic Sn surface than on the SnO_2 surfaces. The same trend is observed when considering the reductive molecular desorption of OCHO*, where the desorption is more favorable on the metallic surface than the oxide. Without explicit calculation of transition state energetics, we cannot definitively say which of these steps will be kinetically faster, but molecular adsorption/desorption steps typically do not have significant activation barriers. Complex reaction coordinates such as reducing COOH* to CO and water may have an appreciable activation barrier, so the reductive desorption of OCHO* and formation of CO may be relatively competitive in rate.

3.4.4 Competition by HER and Carbonate Adsorption

The competition between cathodic reactions and HER is ubiquitous in electrocatalysis. An additional parasitic reaction that can lower the efficiency of CO_2R is the strong adsorption of bicarbonate and carbonate, which are present in CO_2R electrochemical cells either as supporting electrolyte or formed spontaneously from the equilibrium of CO_2 and water/hydroxide. To

holistically evaluate the performance of metallic and oxidized Sn catalysts for CO_2R, we also considered the competition from HER and bicarbonate/carbonate adsorption.

HER may follow two well-known mechanisms: the Volmer–Heyrovsky and Volmer–Tafel mechanisms.[154] HER on Sn is thought to mainly follow the Volmer–Heyrovsky mechanism due to low coverage of H* until larger overpotentials, by which time the rate of the Heyrovsky step becomes fast enough to scavenge H*.[155] We consider both mechanisms for the sake of completeness. Figure S3.8 shows the reaction coordinate diagrams for both the Volmer–Heyrovsky and Volmer–Tafel mechanisms on all three surfaces as a function of applied potential. The results agree with the existing literature that the Volmer–Heyrovsky mechanism is preferred on all Sn surfaces, with all steps being thermodynamically downhill at potentials more negative than −0.3 V_{RHE}. The presence of a large kinetic barrier for the Heyrovsky step could lead to non-negligible flux through the Volmer–Tafel mechanism on metallic Sn once an appreciable coverage of H* has accumulated. Each Volmer step transfers 1.1–1.4 electrons from the electrode, meaning that 0.2–0.8 electrons must be transferred back to the electrode during the Tafel step. Therefore, the Tafel step becomes less favorable at more negative potentials. This is more pronounced on the SnO_2 surfaces, so it is even more likely that the reaction proceeds through the Volmer–Heyrovsky mechanism on these surfaces. The most significant consequence of this is that, because the Volmer step is potential-determining on all three surfaces (for the Volmer–Heyrovsky mechanism), the surface coverage of H* is likely to be low (but not zero) because of the favorable reaction between either H^+ to from H_2 or CO_2 to form OCHO*. This will negatively impact the rate of CO_2R steps that involve H* unless there is a much lower kinetic barrier for these steps than the Heyrovsky step.

Next, we considered the competitive adsorption of bicarbonate/carbonate. Bicarbonate is often the supporting electrolyte of choice for CO_2R because it can retard the aqueous CO_2 equilibrium, which results in efficiency losses.[156,157] This aqueous CO_2 equilibrium means that bicarbonate will likely be present even in electrolytes that do not have intentionally added bicarbonate and therefore must be considered when evaluating the surface processes of CO_2R catalysts. Lastly, carbonate may begin to accumulate near the electrode interface due to the increase in pH that arises from the consumption of protons during cathodic reactions.[158] It is not unusual for the interfacial pH of a cathode to be 2–4 pH units higher than the bulk pH, meaning the interfacial pH could be greater than the pK_a of bicarbonate.[7] Figure 3.5 shows the energetics for

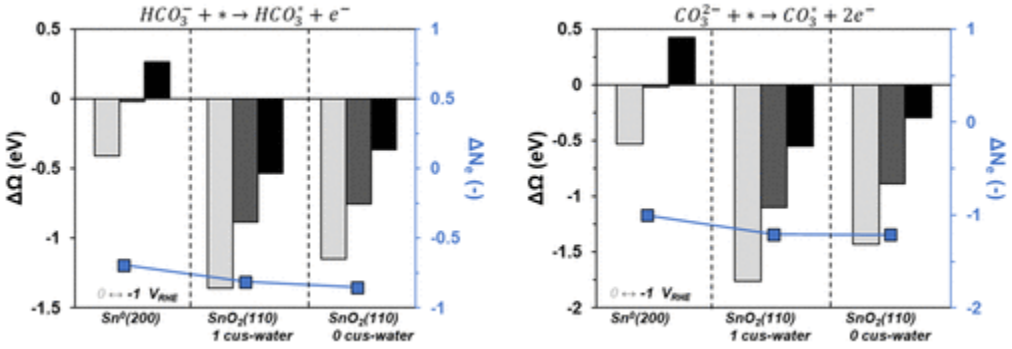

Figure 3.5: Change in grand free energy as a function of potential for the molecular adsorption of bicarbonate (left) and carbonate (right). The potentials are 0 (light gray), −0.5 (dark gray), and −1 (black) V_{RHE}. The average number of electrons transferred across the three potentials is shown (in blue).

the molecular adsorption of bicarbonate and carbonate on the three Sn surfaces as a function of potential. In line with the results described above for all previously discussed adsorbates, metallic Sn binds both bicarbonate and carbonate more weakly than either of the SnO_2 surfaces. The adsorption of bicarbonate and carbonate becomes less favorable at more negative potentials as expected due to the net oxidation during adsorption. The net electrons transferred for bicarbonate

is close to the expected value of 1, but the number of electrons transferred for carbonate is much lower than the expected value of 2, only slightly above 1. This means the carbonate adsorbate is partially charged and the adsorption energy is less sensitive to potential than expected. We also considered the energetics of the adsorption of bicarbonate with a simultaneous discharge of its proton to form adsorbed carbonate (Figure S3.9), but this process was less favorable than either of the two molecular adsorption processes and is therefore not expected to contribute significantly to the adsorption processes. This evidence suggests that molecular adsorption of bicarbonate and carbonate can compete with other intermediates for active sites at low potential, but will be driven off of the surface at more negative potentials.

Before discussing the results of the ATR-SEIRAS experiments, we summarize the observations from the preceding sections. First, metallic Sn is unlikely to have an appreciable coverage of hydroxyls during CO_2R, whereas oxidized Sn may have a non-negligible coverage of hydroxyls and water groups throughout the CO_2R relevant potential window. Next, CO_2 has four feasible activation pathways: direct reductive adsorption to form CO_2^{-*} bound through the carbon atoms, PCET adsorption to form either COOH* or OCHO*, and insertion of CO_2 into a Sn–H bond to form OCHO*. CO_2^{-*} can subsequently be protonated to form COOH*, which may react to form CO and H_2O in a final PCET, or react with H* to form OCHO*, which subsequently undergoes reductive molecular desorption to form solution-phase formate. A non-negligible competition may exist between CO_2R and (i) molecular adsorption of bicarbonate/carbonate at low overpotential and (ii) Volmer–Heyrovsky HER at higher overpotential.

3.4.5 ATR-SEIRAS on Metallic and Oxide-Derived Sn

With some degree of understanding of what might be present on the surface during CO_2R from the GC-DFT analysis described above, we performed ATR-SEIRAS experiments to validate

and refine this understanding. We previously reported a method to prepare both fully metallic and oxidized SEIRAS-active Sn films, which we used in the present study to discern differences in adsorbed species during CO_2R.[125] Before we begin the discussion of the SEIRAS results, we would like to point out that ex situ characterization of the two Sn films after the reductive treatment shows that they have similar degrees of oxidation. Both Sn films undergo spontaneous oxidation in air, which complicates the assignment of the exact oxidation state of the two films during CO_2R. Dutta et al. performed operando EXAFS experiments on SnO_2-based catalysts and found that metallic Sn coordination was not observed until −0.88 V_{RHE}, and SnO_2 and SnO features were still observed even at −1 V_{RHE}.[112] Therefore, while the oxidized Sn film undoubtedly partially reduces under the electrochemical conditions present in CO_2R, we do not necessarily expect it to resemble the fully metallic Sn film under the conditions examined and spectroscopic differences between the two Sn films may still appear. Figure 3.6 shows the ATR-SEIRAS spectra for both the metallic and

oxidized Sn film as a function of potential during CO_2R. We point out two common features for both samples, at ∼1200 and ∼1100 cm^{-1}. These features are attributed to the Si(100) phonon that comes from the wafer used to perform the ATR-SEIRAS experiment.[159] There may also be trace amounts of sulfate that remain from the electrosynthesis of the Sn films. Both features are present during blank experiments with no CO_2 or bicarbonate present and will not be discussed or interpreted further. The observed vibrational frequencies are collected in Table 3.1.

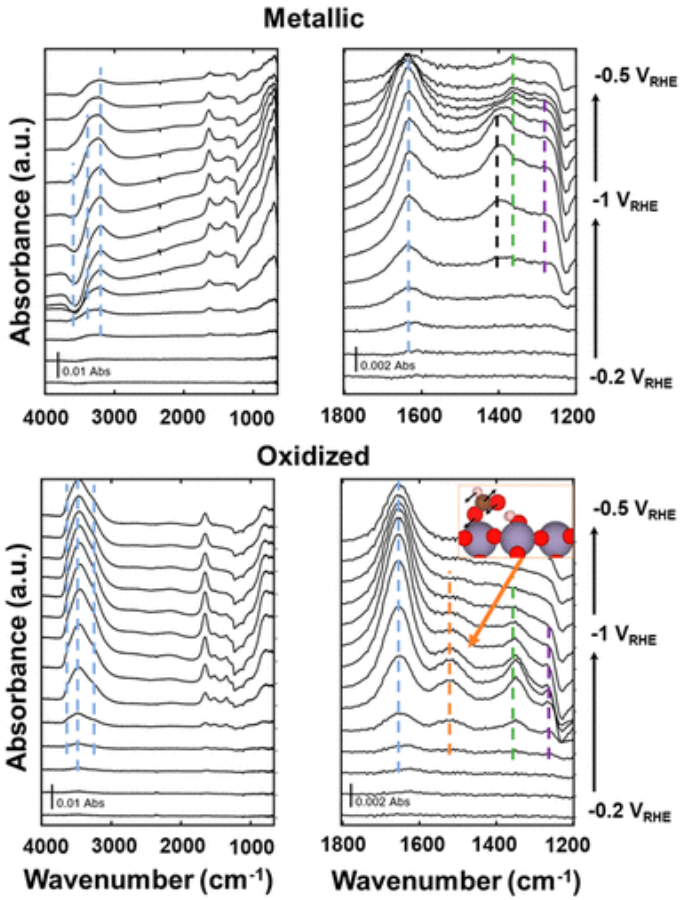

Figure 3.6: Full (4000–800 cm^{-1}, top left) and carbonaceous region (1800–1200 cm^{-1}, top right) ATR-SEIRAS spectra on the metallic Sn electrode during CO_2R. Full (4000–800 cm^{-1}, bottom left) and carbonaceous region (1800–1200 cm^{-1}, bottom right) ATR-SEIRAS spectra on the oxidized Sn electrode during CO_2R. Colored lines are drawn to guide the eye (spectra without these lines are available in the Supporting Information, Figures S3.34 and S3.35). Conditions: 0.1 M $KHCO_3$ (pH = 8) with bubbling CO_2, Sn, or SnO_x thin-film deposited on Au working electrode, Pt wire counter electrode and Ag/AgCl reference electrode. Inset: monodentate formate adsorbed on SnO_2(110) with no cus-waters with annotated vibration vectors for the calculated vibrational frequency of 1519 cm^{-1}.

Table 3.1. Observed Vibrational Frequencies (in cm^{-1}) for the Metallic and Oxidized Sn Films from Figure 3.6, along with the Corresponding Assignments

metallic Sn		**oxidized Sn**	
frequency (cm^{-1})	**assignment**	**frequency (cm^{-1})**	**assignment**
3562 (loss)	desorption of OH*	3644	interfacial water
3366	interfacial water	3486	interfacial water
3209	interfacial water	3256	interfacial water
~2400 (loss)	consumption of CO_2	~2400 (loss)	consumption of CO_2
1611	interfacial water	1635	interfacial water
1410	solution-phase carbonate	1524	monodentate formate
1363	monodentate formate	1349	monodentate formate
1282	monodentate formate	1267	monodentate formate

First, we observe positive bands in the 3200–3500 cm^{-1} region that could be assigned to changes in the interfacial water structure during electrode polarization.[160,161] The band at 1611 and 1635 cm^{-1} for metallic and oxidized Sn, respectively, is likely also related to changes in interfacial water structure. A difference between the two materials is seen in the high-frequency O–H stretch region, where metallic Sn has a negative band at 3562 cm^{-1} and oxidized Sn has a positive band at 3644 cm^{-1}. Given that the calculated PZC for Sn(200) is −0.52 V_{RHE} and the onset of the negative band is at −0.6 V_{RHE}, the O–H stretches might be attributed to shifts in the interfacial water structure. However, these high-frequency spectral features have also previously been assigned to "dangling" surface hydroxyls that have less hydrogen bonding than water.[147] Given that GC-DFT predicts that hydroxyls will desorb from metallic Sn at a similar potential, the negative IR peak is also consistent with the desorption of surface hydroxyls. This also explains why no such negative

peak appears for the oxidized Sn surface, where the cus-hydroxyls spontaneously form cus-water, and br-hydroxyls are not predicted to desorb at these potentials. Furthermore, the negative IR peak is fully reversible, which implies that as the potential is returned to the starting value, the vibrating species can return to their prior state.

Focusing now on the bands that may be associated with carbon-bearing species, both the metallic and oxidized Sn materials have loss bands at ~2400 cm^{-1} that appear between −0.5 and −0.6 V_{RHE} (although it is more apparent on the metallic Sn surface). These bands can be assigned to the consumption of CO_2 during electrolysis. However, it is not immediately obvious if this is simply due to the reactions of CO_2R, or if some of the CO_2 is converted to aqueous bicarbonate and carbonate at the electrode interface due to the cathodic pH increase. We refrain from interpreting the magnitude of these bands because of this ambiguity. Next, there is a band at 1524 cm^{-1} that is only present on the oxidized Sn surface and grows between −0.5 and −0.6 V_{RHE}, before mostly decreasing to the background level. A peak in this region has previously been interpreted as formate,[162] bicarbonate[42] and carbonate,[104] so we attempted to assign this band by calculating the vibrational frequencies. Table S3.1 shows the GC-DFT-calculated vibrational frequencies as a function of potential for the Sn(200), SnO_2(110) with 1 cus-water, and SnO_2(110) with no cus-waters. For the oxidized Sn surfaces, the observed vibrational frequency is most consistent with monodentate formate and bidentate bicarbonate adsorbates. However, due to the surface selection rule, only adsorbate vibrational modes with a change in dipole that is perpendicular to the surface will be IR active. Visualizations of the vibrational modes are provided in Figures S3.10–S3.33 (gif file animations are also available in the Supporting Information). For both monodentate formate and bidentate bicarbonate, the vibrational mode responsible for the frequency that is closest to the observed value is the OCO asymmetric stretch. The vibration coordinate, shown as an inset

in Figure 3.6, is more perpendicular for monodentate formate than for bidentate bicarbonate, so we assign this peak as monodentate formate. An additional clue that this is less likely to be bicarbonate and more likely to be formate is that we predicted the formation of formate to become increasingly favorable and the adsorption of bicarbonate to become decreasingly favorable at more negative potentials. Monodentate formate was assigned to a feature at 1680 cm^{-1} by Jiang et al. when studying CO_2R on Pd-based electrocatalysts.[162] They also assigned a peak at 1584 cm^{-1} to solution-phase, desorbed formate. This peak position differs significantly from both what we have observed in our own spectra and calculated using GC-DFT, but the difference could be explained by both differences in vibrational frequencies across different materials and under different electrochemical environments.

The next peak observed and used for mechanistic analysis is only present in the metallic Sn catalyst spectra as a reversible peak that appears at 1410 cm^{-1} at potentials more negative than −0.6 V_{RHE}. This feature is most consistent with either monodentate carbonate, or solution-phase carbonate which would arise from the increase in interfacial pH. GC-DFT calculations predict that carbonate will desorb from metallic Sn at these potentials, so it is more likely that solution-phase carbonate has accumulated at the electrode interface. The absence of this feature in the oxidized Sn spectra is of particular interest, as the *I–V* curves (Figure S3.36) show that oxidized Sn draws a higher current (as well as higher current density) than metallic Sn, which implies that the consumption of protons at the interface should be higher on oxidized Sn than metallic Sn. This may be explained by the presence of the cus-water and br-hydroxyl groups on the oxidized Sn surface playing a buffering role, that is, when solution-phase protons are consumed in cathodic reactions, protons on the surface may be released to neutralize the change at the interface. To evaluate the feasibility of this hypothesis, we determined the favorability of transferring a proton

from the SnO_2(110) surface to a carbonate ion (Figure S3.37), which was favorable at all potentials. Therefore, a complex equilibrium exists at the interface of the oxidized Sn surface that may be able to neutralize the expected pH increase upon cathodic polarization. Metallic Sn is unable to perform this interfacial buffering because its surface hydroxyls have been reduced off the surface at these potentials. Assigning the relative importance of the intrinsic electrode reactivity and the local pH on the activity and selectivity of Sn-based CO_2R catalysis would require a sophisticated coupled transport-kinetic model like Singh et al. developed for CO_2R on Ag catalysts.[99] Cao et al. assigned this feature to monodentate formate in their investigation of CO_2R to formate over two-dimensional Bi catalysts.[163] They measured this peak in the absence of CO_2 without quantifying or detecting any formate production, so it is more likely that this peak is also due to the formation of carbonate once the pH increases from the cathodic consumption of protons.

The remaining bands, at 1363/1282 and 1349/1267 cm^{-1} for metallic and oxidized Sn, respectively, likely belong to monodentate formate. This is consistent with the calculated vibrational frequencies from GC-DFT for both surfaces. The peaks at 1363 and 1349 cm^{-1} are assigned to the combination mode of C–H wagging and OCO bending, and the peaks at 1282 and 1267 cm^{-1} are assigned to the OCO symmetric stretch. As with the formate peak at 1524 cm^{-1}, this assignment is strengthened by the reversible appearance of these features at potentials more negative than −0.6 V_{RHE}. One difference between the metallic and oxidized Sn spectra is that the peak at 1363 cm^{-1} is not fully reversible on metallic Sn, and a small peak is still present at −0.5 V_{RHE} on the backsweep. We assign this as readsorbed formate, but the GC-DFT calculations predict that formate is bound more strongly to oxidized Sn than metallic, so we expected that this feature would be present in the oxidized case too. However, there is also a larger driving force to readsorb hydroxyls at more positive potentials on oxidized Sn. Therefore, because a much weaker

driving force exists for hydroxyl adsorption on metallic Sn, formate may only be displaced from metallic Sn at more positive potentials.

Finally, to assist with the assignments of the features in Figure 3.6, we repeated the SEIRAS experiment without CO_2 present in the electrochemical cell. Figure S3.38 (nonannotated versions in Figures S3.39 and S3.40) shows the SEIRAS spectra for both the metallic and oxidized Sn materials. For the metallic Sn electrode, only the signals corresponding to the changes in interfacial water and the solution-phase carbonate persist in the absence of CO_2. The solution-phase carbonate arises due to the pH increase from HER. This supports the assignment of the other peaks at 1363 and 1282 cm^{-1} as formate (or at least intermediates from CO_2R) and not molecular adsorption of bicarbonate/carbonate present in the electrolyte. Similarly, most of the SEIRAS features disappear for the oxidized Sn electrode when CO_2 is removed from the electrolyte. The features that arise from changes in the interfacial water remain, and a new negative feature appears at 1450 cm^{-1}. This peak is most consistent with bidentate carbonate. This shows that there may be carbonate adsorption from the electrolyte on the oxidized Sn surface that can be reduced off of the surface, which is supported by the results of calculations reported in Figure 3.5. The disappearance of the peaks at 1524, 1349, and 1267 cm^{-1} when CO_2 is absent confirms that these peaks originate from CO_2R intermediates that are most likely monodentate formate.

3.4.6 Proposed Mechanism and Strategies for Improved CO_2R

Through both the GC-DFT and ATR-SEIRAS analyses described above, we have identified CO_2R pathways that are feasible on both metallic and oxidized Sn surfaces. For metallic Sn, surface hydroxyls are reductively desorbed by −0.6 V_{RHE} (M.1). Direct reductive adsorption of CO_2 to form OCO^{-*} does not become favorable until potentials more negative than −1 V_{RHE}, which is more negative than the observed onset of peaks assigned to formate in the ATR-SEIRAS spectra.

Therefore, we believe that CO_2 is activated either by insertion into the Sn–H bond via an Eley–Rideal-like step (M.3a), preceded by Volmer proton adsorption (M.2), or PCET adsorption to OCHO* (M.3b). Only monodentate formate was detected using ATR-SEIRAS, which supports the Eley–Rideal activation of CO_2 on metallic Sn because there is a larger driving force for formate desorption than to rearrange into the bidentate configuration. Jiang et al. made a similar conclusion regarding the formation of monodentate formate when investigating CO_2R on Pd-based catalysts.[162] The potential limiting step for this mechanism is the reductive molecular desorption of formate (M.4), which becomes favorable at −0.39 V_{RHE}. The lack of IR bands associated with formate at this potential on metallic Sn is explained by the presence of hydroxyls, which are not predicted to completely vacate the surface until −0.6 V_{RHE}. This mechanism is summarized in Mechanism 1 and Figure 3.7, which also shows the free energy landscape for the pathways on metallic and oxidized Sn.

Mechanism 1. Proposed mechanism for CO_2R to formate on Sn-based catalysts

$$OH^* + e^- \rightarrow OH^- + * \ or \ H_2O^* \rightarrow H2O + * \text{ ; } \textbf{(M.1)}$$

$$H^+ + e^- + * \rightarrow H^* \text{ ; } \textbf{(M.2)}$$

$$CO_2 + H^* \rightarrow OCHO^* \text{ ; } \textbf{(M.3a)}$$

$$CO_2 + H^+ + e^- + * \rightarrow OCHO^* \text{; } \textbf{(M.3b)}$$

$$OCHO^* + e^- \rightarrow HCOO^- + * \text{ ; } \textbf{(M.4)}$$

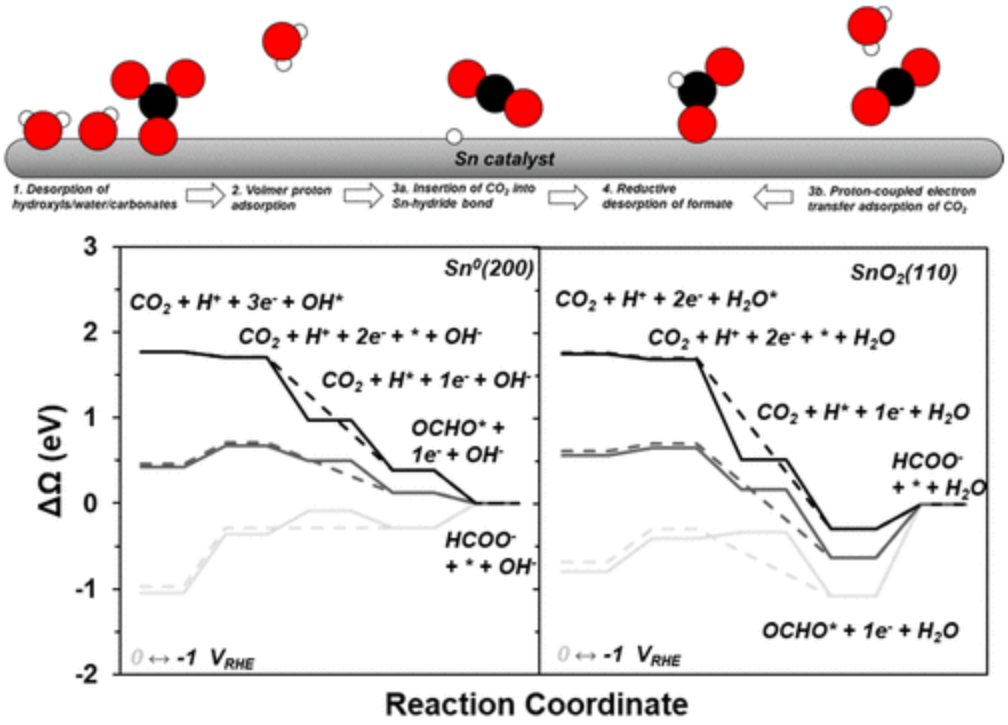

Figure 3.7: (Top) Schematic visualizing the proposed mechanism in Mechanism 1 and reaction coordinate diagram for metallic Sn (bottom left) and the average between oxidized Sn with one and no cus-waters (bottom right) for the proposed mechanism in Mechanism 1. The solid lines are for the Eley–Rideal pathway, and the dashed lines are for the PCET pathway.

For oxidized Sn, the mechanism is more similar to metallic Sn than expected based on the differences in the energetics predicted from GC-DFT. The surface is initially blocked by cus-water groups that begin to desorb at −0.6 V_{RHE} (M.1). Next, because the oxidized Sn surface has higher affinity for all intermediates than metallic Sn, it is possible that all of the proposed CO_2 activation pathways are accessible. However, unless there are substantial kinetic barriers for all of the steps except direct reductive adsorption of CO_2, there is a larger driving force to form H*, COOH*, and OCHO* at potentials more negative than −0.5 V_{RHE} due to the greater extent of charge transfer. We expect that any COOH* formed will go on to produce CO, so the same two CO_2 activation steps (Eley–Rideal reaction between CO_2 and H* and PCET adsorption to form OCHO*) are most

likely. Desorption of formate is again the potential-determining step, although for oxidized Sn it is predicted to be −1.22 V_{RHE}. This implies that the active phase of Sn during CO_2R is likely a partially reduced Sn oxide (or partially oxidized metallic Sn) such that the energetics of both activation and desorption steps are in between the two limiting cases examined in this study. We also considered the hydroxyl-mediated pathway proposed by Baruch et al.,[42] and cannot conclusively eliminate it as a possibility but believe that is likely only a minor contribution to the overall CO_2R rate (see the Supporting Information and Figures S3.41–S3.43). Metallic and oxidized Sn surfaces having different rate-limiting steps should manifest as different Tafel slopes. The electrochemical cell used for the SEIRAS experiments is not equipped to accurately determine the Tafel slope for CO_2R toward formate due to influences from mass transport and very low product concentrations, so more thorough kinetic measurements to determine the reaction orders, apparent activation barriers and the Tafel slope under a broader range of conditions will be necessary to fully resolve the mechanistic differences between metallic and oxidized Sn electrocatalysts.

The proposed mechanism, and data that lead to it, highlight the factors that limit CO_2R on Sn. On either metallic or oxidized Sn, GC-DFT predicts that the electrochemical activation of CO_2 becomes favorable at a less negative potential than the observed onset potential of −0.6 V_{RHE}, which coincides with the potential at which hydroxyls or molecular water groups are predicted to desorb from the surfaces. Therefore, lowering the overpotential of CO_2R on Sn will require decreasing the affinity of Sn surfaces toward hydroxyls/water. Doing so will be challenging to achieve because, due to adsorbate scaling relationships, surfaces that bind one class of adsorbates more weakly typically bind all classes of adsorbates more weakly, and as such lowering the potential for hydroxyl/water removal will also increase the potential for CO_2 activation. Some

strategies for decorrelating carbon-bound and oxygen-bound adsorbates have been proposed, such as alloying with distinct elements such as sulfur and taking advantage of interfaces between different materials like RuO_2 and CeO_2.[109,164–167] Controlling the near-electrode environment could also be a beneficial strategy. It has been demonstrated that the presence of electrolyte additives, such as self-assembled monolayers[160,161] and ionomer coatings[168] can modify the hydrophilicity of the electrode interface. Selectively destabilizing surface hydroxyls/water in this manner could lower the overpotential required to open active sites for CO_2R on Sn surfaces.

3.5 Conclusions

In this study, we used GC-DFT and ATR-SEIRAS to interrogate the differences in CO_2R mechanism toward formate on both metallic and oxidized Sn surfaces. While the computed energetics and observed IR features are distinct for both materials, we have proposed probable mechanistic steps that are common to both materials, with different limiting characteristics. The steps most consistent with our study are 1. Potential-driven desorption of hydroxyls/water/bicarbonate, 2. Volmer proton adsorption, 3a. Eley–Rideal insertion of CO_2 into a Sn–H bond, 3b. PCET adsorption of CO_2, and 4. Reductive desorption of formate. Metallic Sn is less likely to be limited by the desorption of formate or other spectator species such as bicarbonate, carbonate, and hydroxyls, but oxidized Sn is more able to facilely activate CO_2. In both cases, hydroxyls and molecular water must be driven off the surface to open active sites for CO_2R. This analysis ultimately supports the conclusion that Sn surfaces are in situ oxidized or reduced to achieve an intermediate oxidation state such as Sn_2O_3 or SnO, that is more optimally active for the CO_2R to formate than fully metallic or oxidized Sn. Future investigations of Sn-based electrocatalysts should focus on (1) Identifying the exact speciation of the operando Sn catalyst, (2) Calculating the explicit activation energies of the elementary steps identified here as

most relevant and (3) Experimentally determining the kinetic signatures like reaction orders, apparent activation barriers, and apparent transfer coefficients across a diverse set of experimental conditions to diagnose the mechanism with more confidence.

3.6 Supporting Information

CO_2R Adsorption Intermediate Geometries

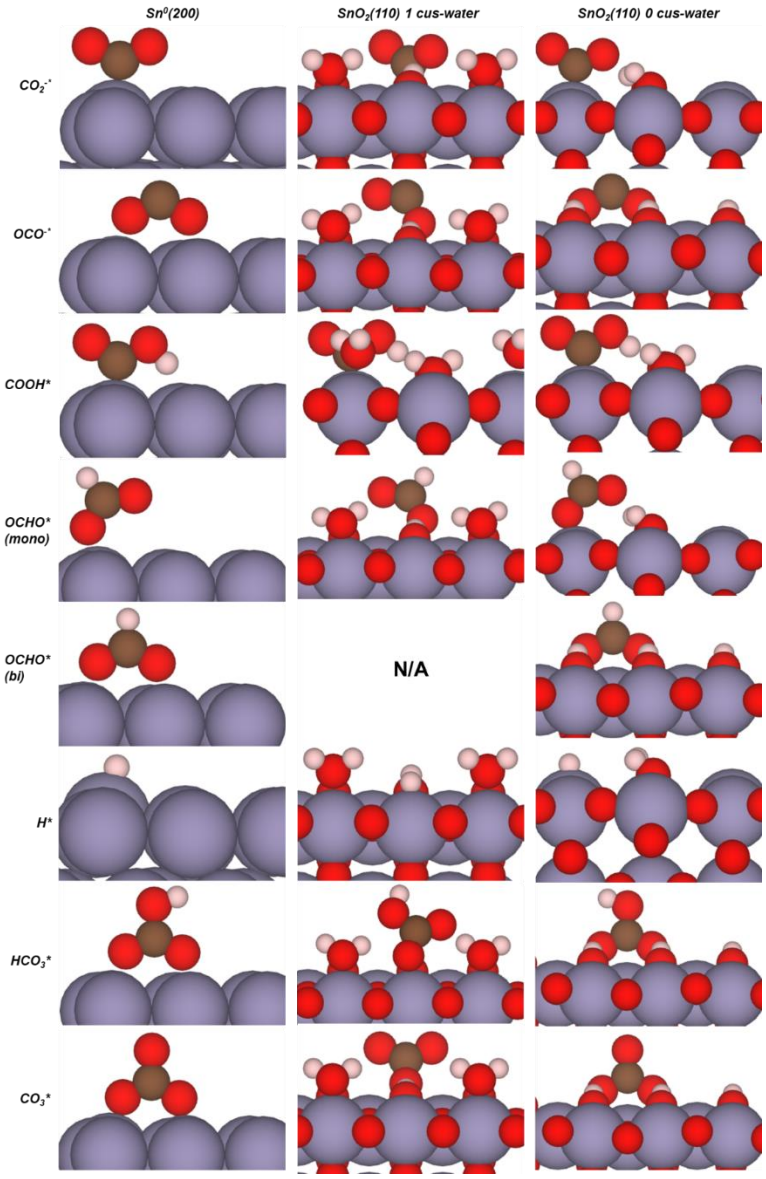

Figure S3.1: Converged geometries of the CO_2R intermediates considered at -0.5 V_{RHE} across the three Sn surface.

Energy landscape of SnO_2(110) in aqueous environment

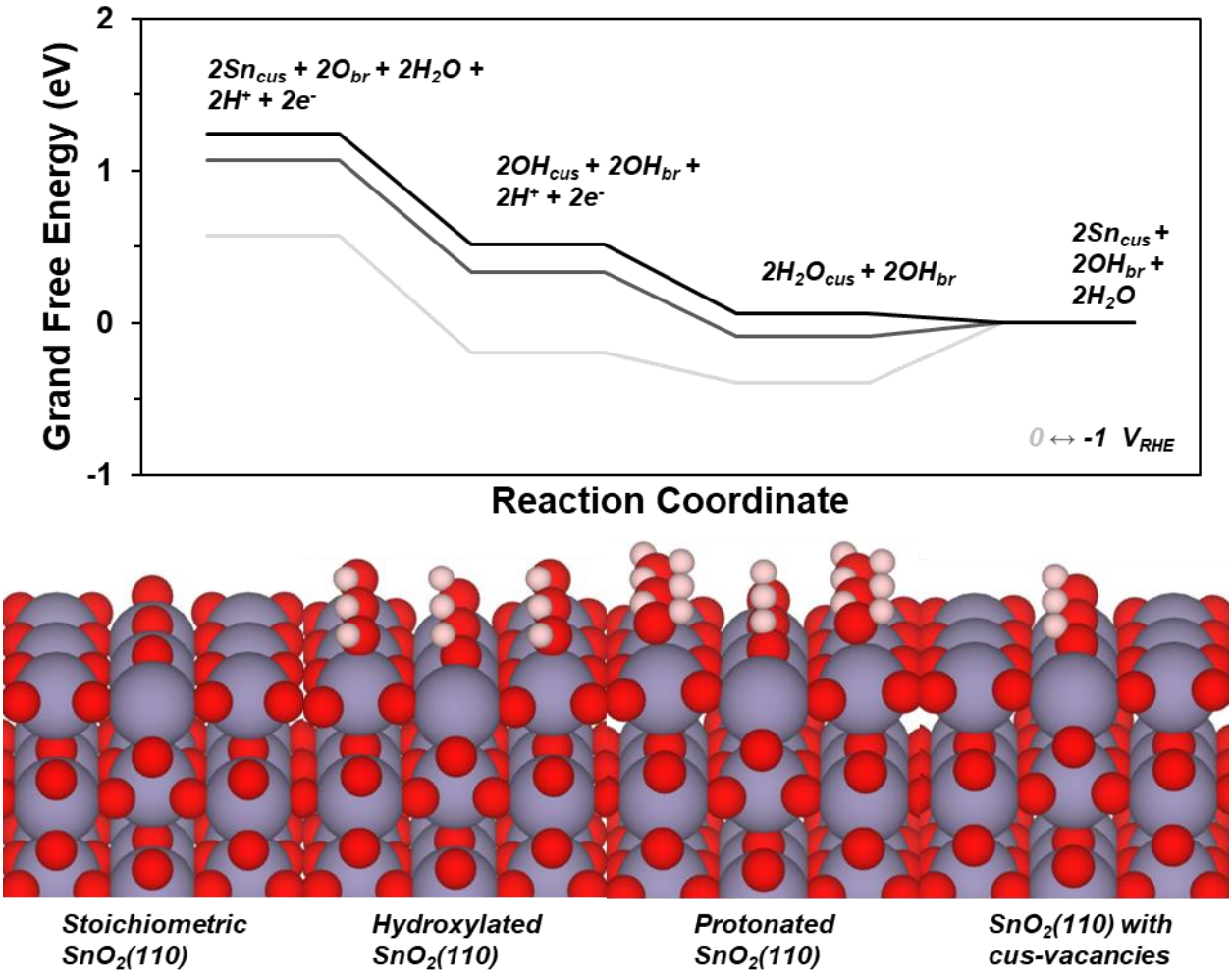

Figure S3.2: (top) Reaction coordinate diagram showing the energetics of different degrees of SnO_2(110) hydroxylation. (bottom) SnO_2(110) structures corresponding to the different states in the above reaction coordinate diagram.

Figure S3.2 shows the free energy landscape of SnO_2(110), specifically for the interaction with water. SnO_2(110) spontaneously dissociates water into cus-hydroxyls and br-hydroxyls at all potentials. Furthermore, the hydroxylated SnO_2(110) is spontaneously protonated at the cus-hydroxyl sites to form cus-water at all potentials. The cus-waters can be reductively desorbed at potentials more negative than -0.8 V_{RHE} to re-form the naked cus-Sn sites. For CO_2R, we

considered the SnO_2(110) with all br- sites as br-hydroxyls and either one cus-water and one cus-Sn or two cus-Sn sites (shown as the far right structure in **Figure S3.2**).

Importance of GC-DFT for adsorption energies

As we described in the introduction of the main text, GC-DFT is necessary to capture the energetics of partial charge transfer steps or decoupled electron/proton transfers. For CO_2R, the main step that this is relevant for is the reductive adsorption of CO_2 ($CO_2 + * + e^- \rightarrow CO_2^{-*}$). **Figure S3.3** and **Figure S3.4** show the initial structure for the adsorption of CO_2^{-*} and OCO^{-*} as well as the converged structures at 0, -0.5 and -1 V_{RHE} for all three Sn surfaces considered. The canonical, zero charge structure is also shown. First, It is apparent that, at low potential, the CO_2^{-*} spontaneously desorbs and there is no electron transfer. It is not until the potential is increased that the GC-DFT calculator adds an additional electron and the adsorption of CO_2^{-*} is an accessible state (even if it is still calculated to be uphill thermodynamically). This shows the importance of using GC-DFT for computational electrochemistry; without it the nuance of adsorption energetics as a function of potential may be lost. For the adsorption energetics shown in **Figure 3.3**, we constrained the Sn-C or Sn-O bonds to force the calculator to determine the energy of adsorption to accurately represent the potential dependence.

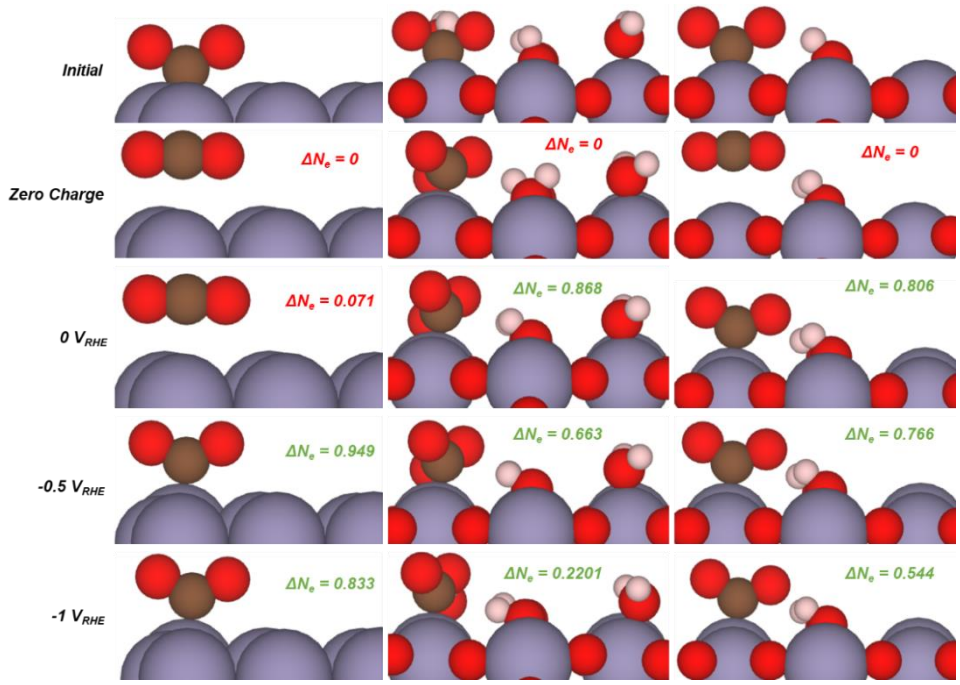

Figure S3.3: GC-DFT adsorption geometries for CO_2^{-*}. Top row is the initial guess for each calculation, second row is the converged canonical, zero-charge structure and the remaining rows are the converged grand-canonical structures at 0 (third row), -0.5 (fourth row) and -1 (fifth row) V_{RHE}. The change in the number of electrons is also shown.

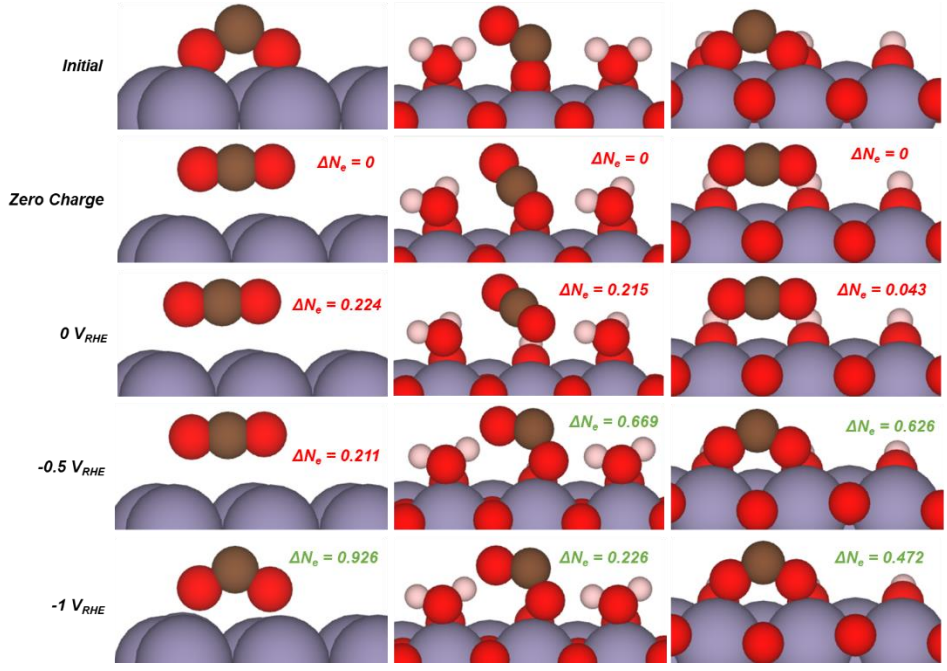

Figure S3.4: GC-DFT adsorption geometries for OCO^{-*}. Top row is the initial guess for each calculation, second row is the converged canonical, zero-charge structure and the remaining

rows are the converged grand-canonical structures at 0 (third row), -0.5 (fourth row) and -1 (fifth row) V_{RHE}. The change in the number of electrons is also shown.

Additional CO_2R intermediate considerations

We also considered the formation of surface bound CO and formic acid (HCOOH) as mechanistically relevant intermediates. However, as shown in **Figures S3.5** and **S3.6**, the calculator spontaneously elongates the surface bond to greater than 3 Å at all potentials on all three Sn surfaces considered, which is longer than what would typically be considered chemisorbed.

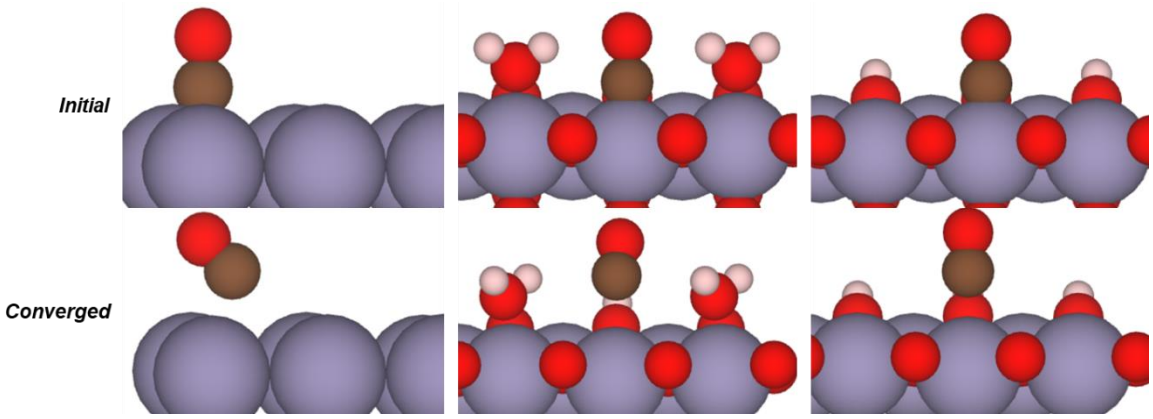

Figure S3.5: GC-DFT adsorption geometries for CO. Top row is the initial guess for each calculation, second row is the converged structure (all of the potentials converged to a similar desorbed state).

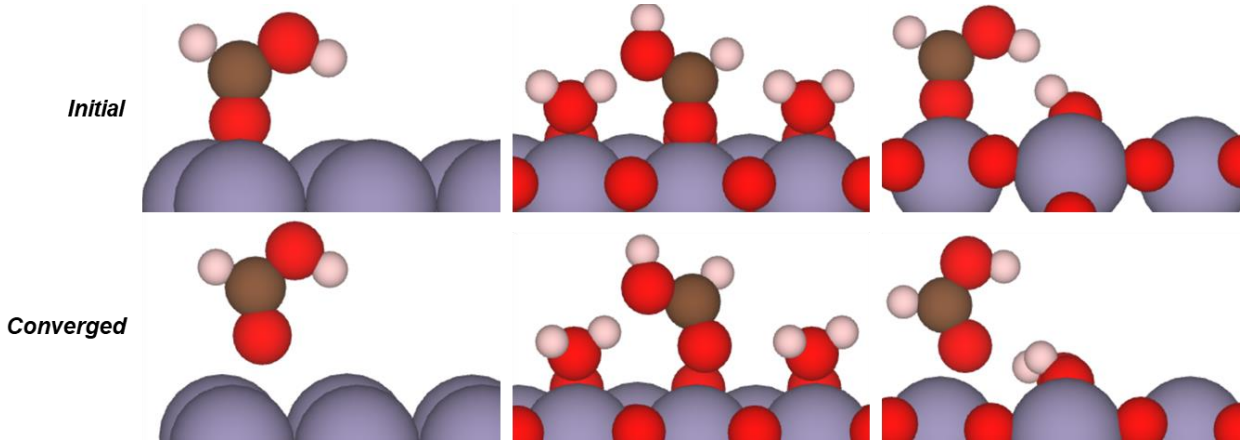

Figure S3.6: GC-DFT adsorption geometries for formic acid. Top row is the initial guess for each calculation, second row is the converged structure (all of the potentials converged to a similar desorbed state).

We considered the formation of HCOOH via Langmuir-Hinshelwood coupling of COOH* and H*. The energetics are shown in **Figure S3.7.** By looking at **Figure 3.3** in the main text, the number of electrons associated with the formation of COOH* and H* sums to greater than 2, which explains the net oxidation calculated for the step shown in **Figure S3.7**. Therefore, this step becomes less favorable as the potential is made more negative, and this step is not considered further as a relevant process.

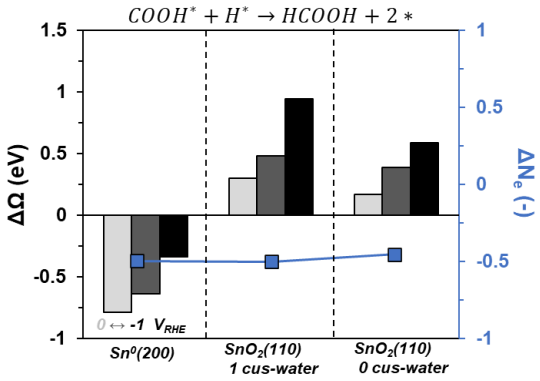

Figure S3.7: Change in grand free energy as a function of potential for the formation of formic acid via the Langmuir-Hinshelwood coupling of COOH* and H*. The potentials are 0 (light grey), -0.5 (dark grey) and -1 (black) V_{RHE}. In blue, the average number of electrons transferred across the three potentials is also shown.

As mentioned in the main text, we also considered the formation of carbonate on the surface via the simultaneous adsorption and discharge of proton from bicarbonate. The energetics for this process are shown in **Figure S3.8**. Comparing the energetics of this process to the energetics shown in the main text (**Figure 3.5**), this process is much less favorable than either molecular adsorption

of bicarbonate or carbonate, so it is more likely that surface-bound carbonate is formed via molecular adsorption of carbonate formed in solution from an increase in interfacial pH.

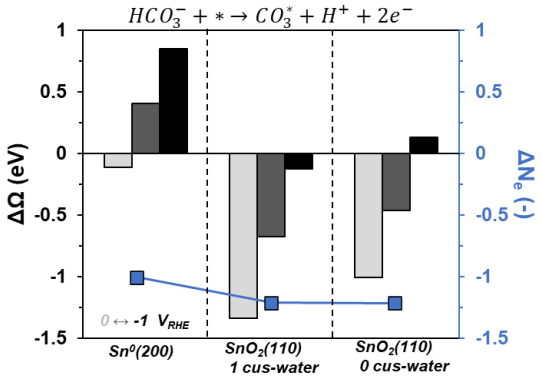

Figure S3.8: Change in grand free energy as a function of potential for the formation of surface-bound carbonate via simultaneous adsorption and discharge of proton from bicarbonate. The potentials are 0 (light grey), -0.5 (dark grey) and -1 (black) V_{RHE}. In blue, the average number of electrons transferred across the three potentials is also shown.

Hydroxyl-mediated CO_2R on SnO_2

We considered the formation of bicarbonate through the nucleophilic attack of CO_2 by br-hydroxyl, which has been suggested as a potential mechanism on oxidized Sn electrodes.[169] We do not consider the hydroxyl mediated mechanism on the metallic Sn surface or at the cus site of the SnO_2 surfaces, because the coverage of hydroxyls is expected to be very low in the potential range of CO_2R. In addition to the two SnO_2 surfaces considered for the other CO_2R intermediates (SnO_2(110) with 1 and 0 cus-water groups), we also considered the surface with 2 cus-water groups because the hydroxyl-mediated mechanism doesn't require naked Sn sites. The intermediates are shown in **Figure S3.9**.

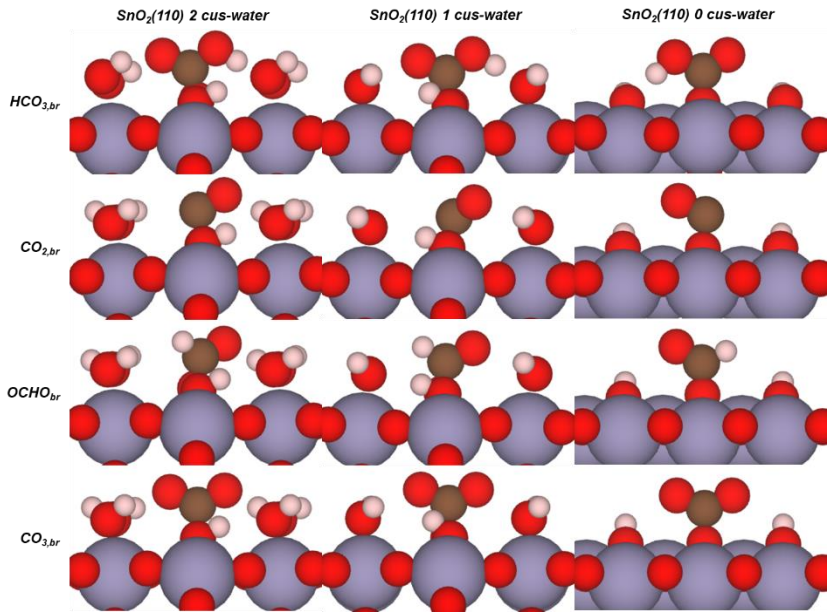

Figure S3.9: Converged geometries of the br-hydroxyl-mediated CO_2R intermediates considered at -0.5 V_{RHE} across the three SnO_2 surface.

Before discussing the energetics of the hydroxyl-mediated pathway, it is worth noting that the $CO_{2,br}$ intermediate spontaneously dissociates to CO and O_{br} during geometry optimization at potentials less than -1 V_{RHE}. This is shown in **Figure S3.10**. In order to determine the energetics of this intermediate to evaluate the hydroxyl-mediated pathway, we ran single-points at the lower potentials.

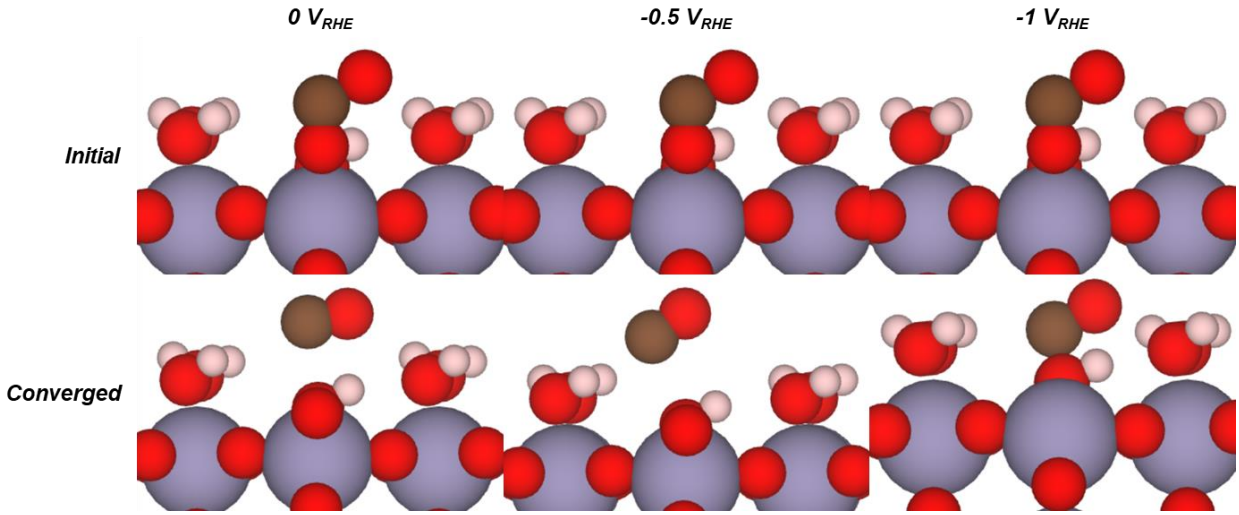

Figure S3.10: GC-DFT adsorption geometries for $CO_{2,br}$ on SnO_2(110) with 2 cus-water groups. Top row is the initial guess for each calculation, second row is the converged structure. The other SnO_2 surfaces with 1 and 0 cus-water groups showed the same behavior.

The energetics of the hydroxyl-mediated pathway are shown in **Figure S3.11**. The first step of the hydroxyl-mediated pathway is adsorption of CO_2 to form bicarbonate at the br-hydroxyl site. While this step is not formally electrochemical, the GC-DFT calculation predicts a partial charge transfer of ~0.5 electrons. As such, this step becomes more favorable at more negative potentials, but is still mildly uphill even at -1 V_{RHE}. Once bicarbonate is formed, we considered the reduction to $CO_{2,br}$ and H_2O_l via PCET as the next elementary step. This step is highly endothermic at low potential and becomes favorable at -1 V_{RHE}. This step has a much higher degree of charge transfer than would've been expected at ~1.5 electrons. We also considered the deprotonation of the bridge-bound bicarbonate to form adsorbed carbonate, which would be considered a parasitic reaction (that is, not yielding CO_2R products). This is a formal oxidation (calculated charge transfer of ~0.7 electrons), and as such becomes less favorable at more negative potentials. The deprotonation of bicarbonate is competitive with the reduction to $CO_{2,br}$ at -1 V_{RHE} on the SnO_2 surface with 2 cus-water groups, whereas it is much less favorable when cus-water groups are removed. This indicates that these groups may have lateral interactions that stabilize the carbonate adsorbate. We expect the coverage of these groups to decrease at more negative potentials, so we do not expect the flux of CO_2 to $CO_{3,br}$ to be large under CO_2R operating potentials, and because CO_2 adsorption to $HCO_{3,br}$ is unfavorable at low potential, the surface that would lead to $CO_{3,br}$ is unlikely to form $HCO_{3,br}$ in appreciable quantities.

Once $CO_{2,br}$ is formed, it can either be further reduced to form $OCHO_{br}$ or disproportionate to make CO and O_{br}. Formation of $OCHO_{br}$ is more favorable than CO and O_{br}, and because this is a ~0.5 electron reduction step and forming CO and O_{br} is a ~0.3 electron oxidation step, the gap in favorability grows at more negative potentials. However, because the formation of $CO_{2,br}$ isn't favorable until ~ -1 V_{RHE}, this pathway is only expected to from $OCHO_{br}$ (unless there is a much higher kinetic barrier for this step than the formation of CO). Once $OCHO_{br}$ is formed, the reductive desorption to release formate is the next step. Once again, this step is forced downhill at more negative potentials due to the transfer of ~1 electron upon desorption. Formate is bound slightly less strongly at the br-site when compared to the cus-sites in the main text, but the desorption only becomes favorable at reasonably negative potentials.

Once either formate or CO has been released, to close the catalytic cycle the br-hydroxyl must be regenerated. In the case of the formate pathway, this must be from the oxidative adsorption of hydroxyl in the solution. It is easily seen that this step must be an oxidation because the sum of the electrons transferred to form formate prior to this step is 2.9-3.2, and only two electrons are required to reduce CO_2 to formate. Indeed, GC-DFT predicts this step to be a ~1 electron oxidation, but because oxygen vacancies at the br-site are highly unstable, this step is still thermodynamically downhill even at -1 V_{RHE}. In the case of the CO pathway, O_{br} must be reduced back to br-hydroxyl via PCET. Interestingly, this step is less favorable on the SnO_2 surface with 2 cus-water groups than on the other two surfaces considered. However, as this is less likely to be the operant surface under the CO_2R potentials, and the reduction of O_{br} is favorable at all potentials on the other surfaces, we do not expect this step to be limiting in the hydroxyl-mediated pathway.

While this pathway is perfectly feasible and may even contribute to the overall CO_2R rate at large negative potentials, we considered it to be a minority pathway. This conclusion is mainly

derived from the fact that the steps that lead to formate (or CO) only become favorable at potentials approaching -1 V_{RHE}, while experimentally we, and many others, have shown that Sn based catalysts form CO_2R products at potentials as low as ~ -0.5 V_{RHE}. This analysis also does not include the presence of any potentially large kinetic barriers, which would only increase the overpotential required for measurable rates. Another reason why this mechanism is not expected to majorly contribute to the rate is because there is a narrow potential window where the CO_2R steps and the site regeneration (oxidative re-adsorption of br-hydroxyl) are simultaneously favorable. That is, if the potential is pushed too negative, it is expected that the coverage of br-hydroxyl would decrease and regeneration of this site would be rate limiting. Lastly, our SEIRAS experiments indicate that a stable formate adsorbate is measured in the CO_2R potential window on the oxidized, but not the metallic, Sn surface. The GC-DFT predicted binding energy of formate at the br-site is not quite as weak as on the metallic Sn(200) surface, but it is much weaker than on the cus-site. The presence of a peak assigned to formate in the SEIRAS spectra indicates that the rate of desorption of formate is slow enough to measure a steady coverage. Therefore, because the hydroxyl-mediated pathway forms formate at the br-site, which desorbs more readily than at the cus-site, we believe this pathway may only have a minority contribution to the rate. To authoritatively rule this out, more detailed kinetic measurements are required.

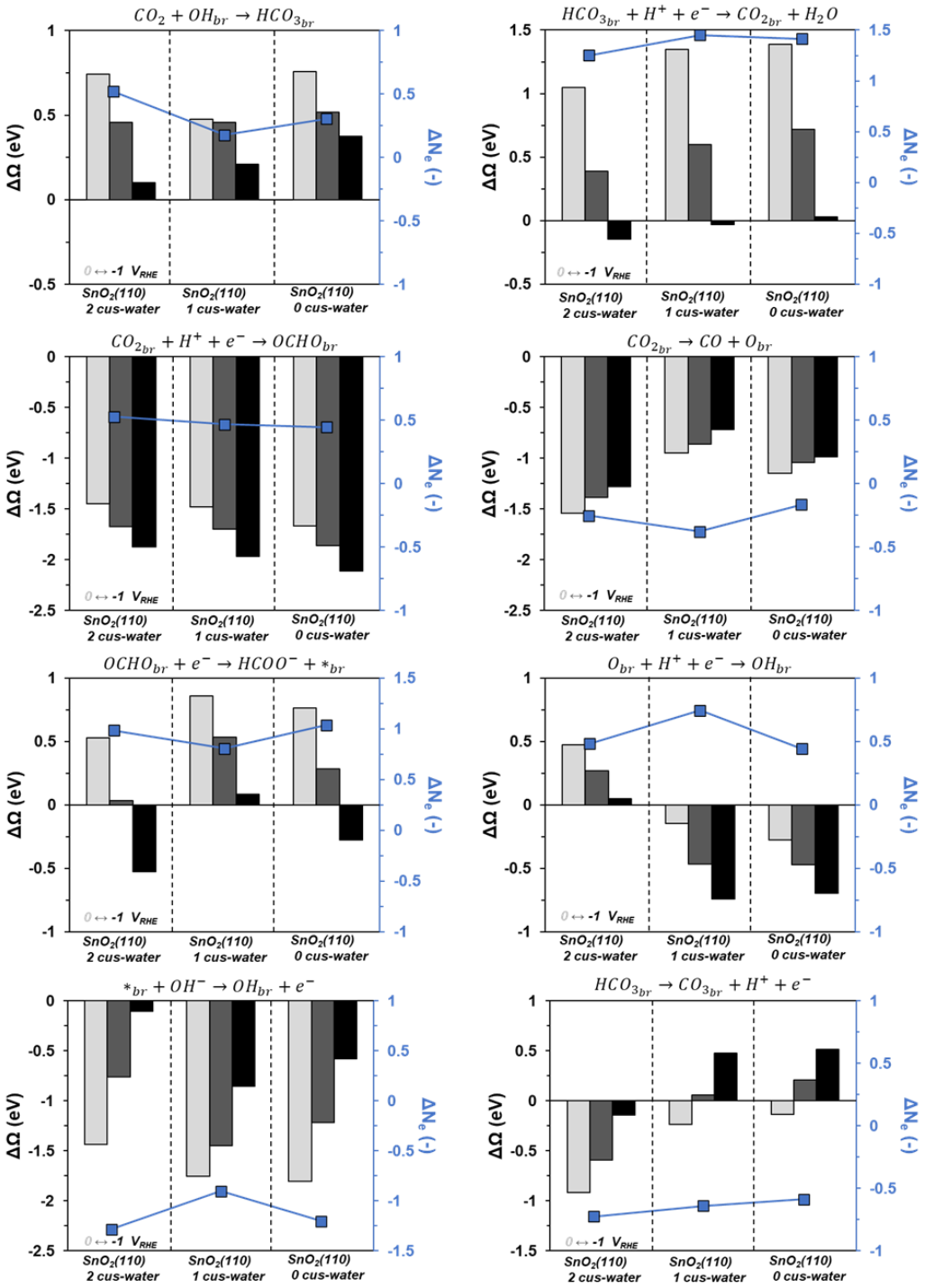

Figure S3.11: Change in grand free energy as a function of potential for CO_2R elementary steps on br-hydroxyl sites. The potentials are 0 (light grey), -0.5 (dark grey) and -1 (black) V_{RHE}. The reactions represented are formation of adsorbed bicarbonate via nucleophilic attack of CO_2 by br-hydroxyl (top left), reduction of bicarbonate to adsorbed CO_2 via PCET (top right), formation of adsorbed formate by PCET (upper middle left), formation of CO and br-O (upper middle right),

desorption of formate (lower bottom left) re-formation of br-hydroxyl by PCET (lower bottom right), re-formation of br-hydroxyl by adsorption of free hydroxyl (bottom left) and deprotonation of adsorbed bicarbonate to form adsorbed carbonate (bottom right). In blue, the average number of electrons transferred across the three potentials is also shown.

Hydrogen Evolution Reaction Energetics

We calculated the free energy changes for the two prominent hydrogen evolution reaction (HER) pathways to assess its competitiveness with CO_2R. In particular, we wanted to evaluate the driving force for CO_2R intermediates through the Eley-Rideal reaction between CO_2 and H* vs H* reacting to form H_2 (via a Heyrovsky or Tafel step). **Figure S3.12** shows the reaction coordinate diagrams for both the Volmer-Heyrovsky and Volmer-Tafel mechanism on all three Sn surfaces. The formation of H_2 via the Heyrovsky step is downhill at all potentials on all materials, so unless there is a significant kinetic barrier for this step, the coverage of H* is expected to be fairly low.

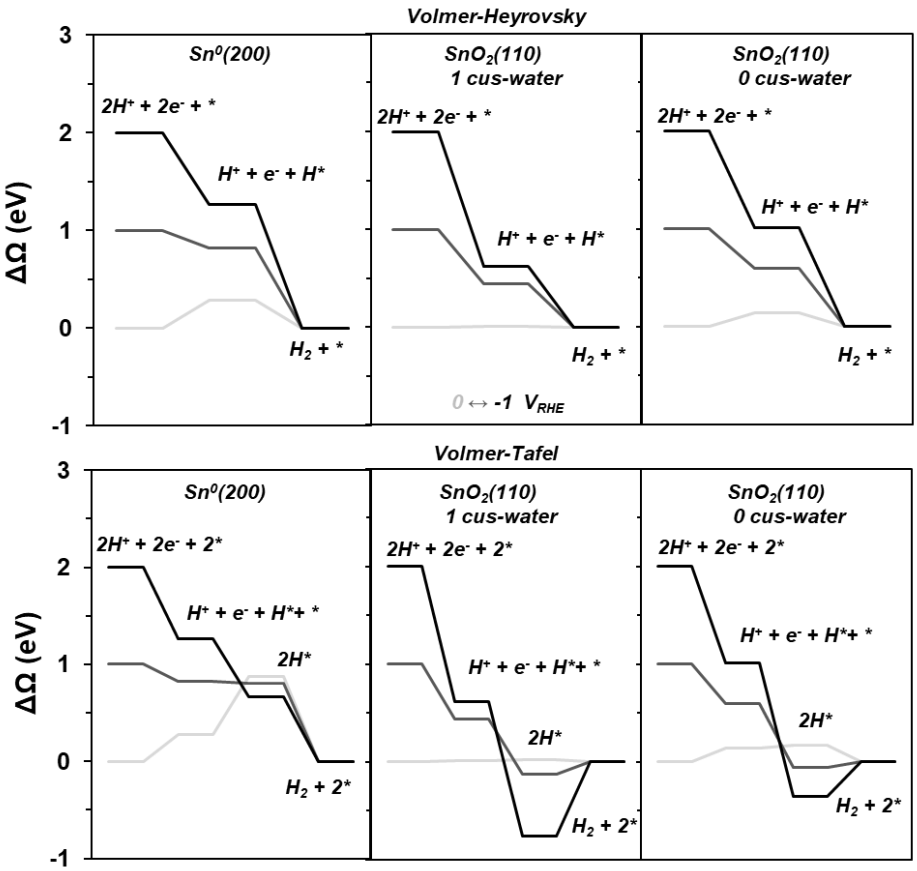

Figure S3.12: Reaction coordinate diagram for the Volmer-Heyrovsky (top) and Volmer-Tafel (bottom) mechanisms of HER on metallic Sn (left), SnO_2 with one cus-water (middle) and no cus-waters (right) as a functional of potential. The potentials are 0 (light grey), -0.5 (dark grey) and -1 (black) V_{RHE}.

Additional SEIRAS information

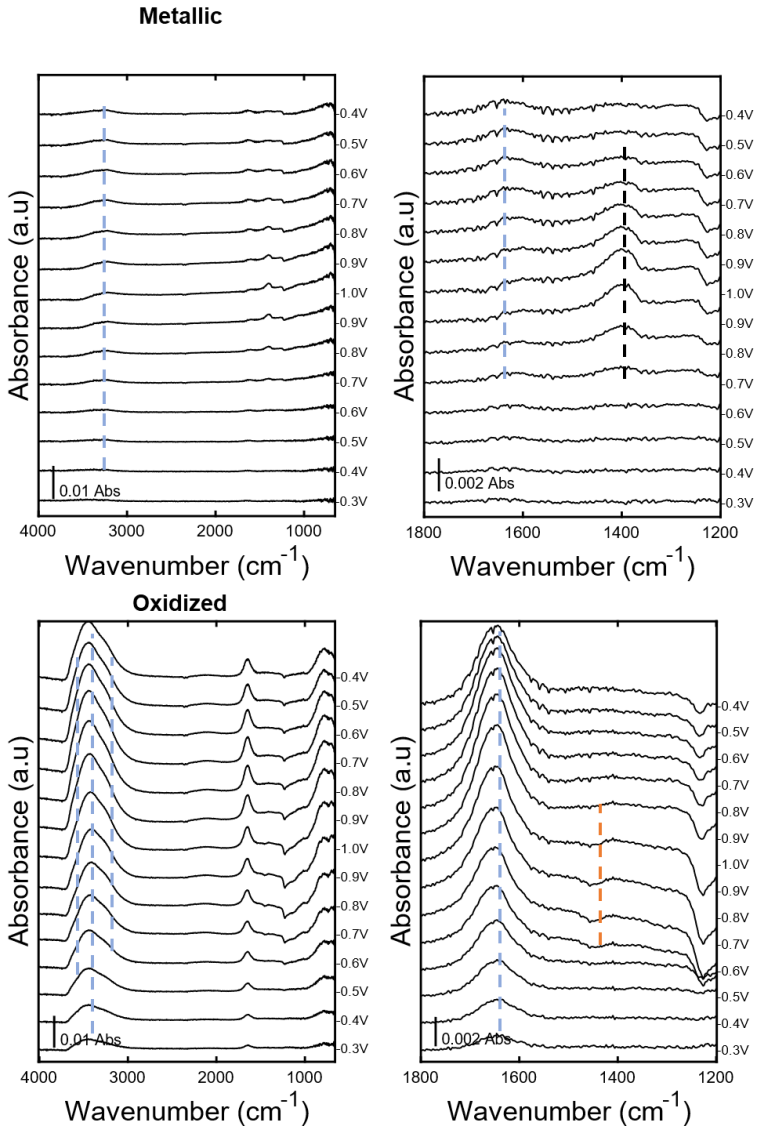

Figure S3.13: Full (4000-800 cm^{-1}, top left) and carbonaceous region (1800-1200 cm^{-1}, top right) ATR-SEIRAS spectra on the metallic Sn electrode with no CO_2 present (sparged with Ar). Full (4000-800 cm^{-1}, bottom left) and carbonaceous region (1800-1200 cm^{-1}, bottom right) ATR-SEIRAS spectra on the oxidized Sn electrode electrode with no CO_2 present (sparged with Ar). Colored lines are drawn to guide the eye (spectra without these lines are available in the supplementary information).

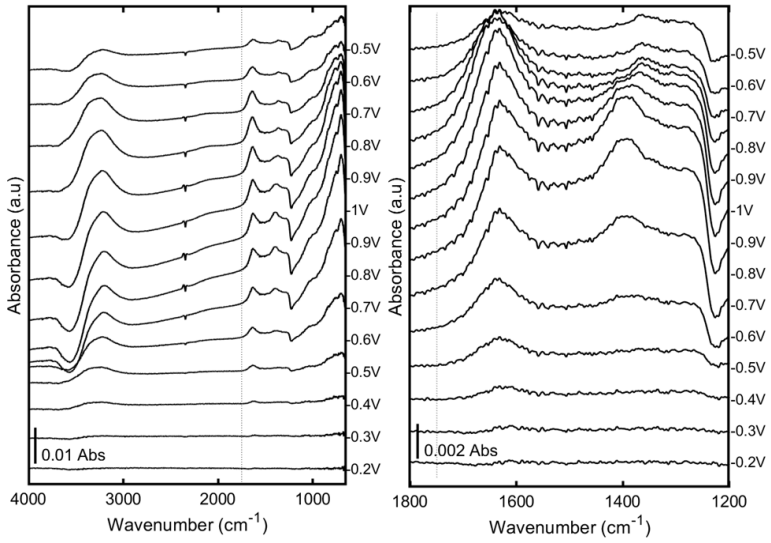

Figure S3.14: Full (4000-800 cm^{-1}, left) and carbonaceous region (1800-1200 cm^{-1}, right) ATR-SEIRAS spectra on the metallic Sn electrode during CO_2R.

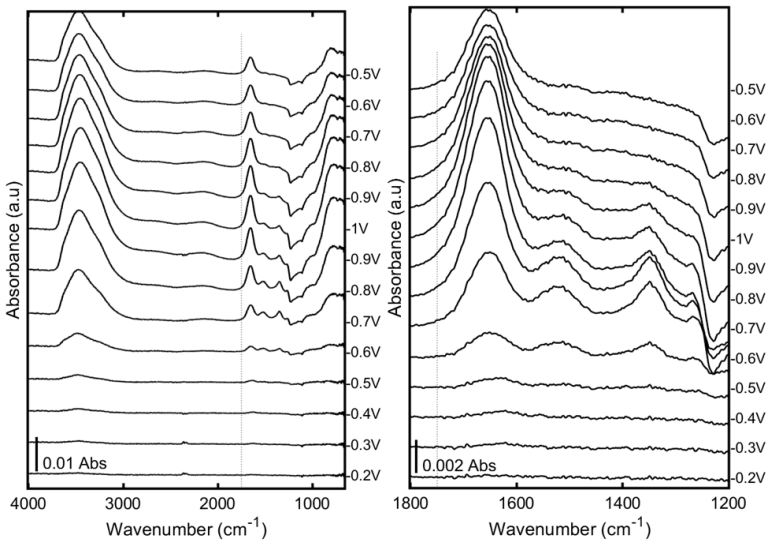

Figure S3.15: Full (4000-800 cm^{-1}, left) and carbonaceous region (1800-1200 cm^{-1}, right) ATR-SEIRAS spectra on the oxidized Sn electrode during CO_2R.

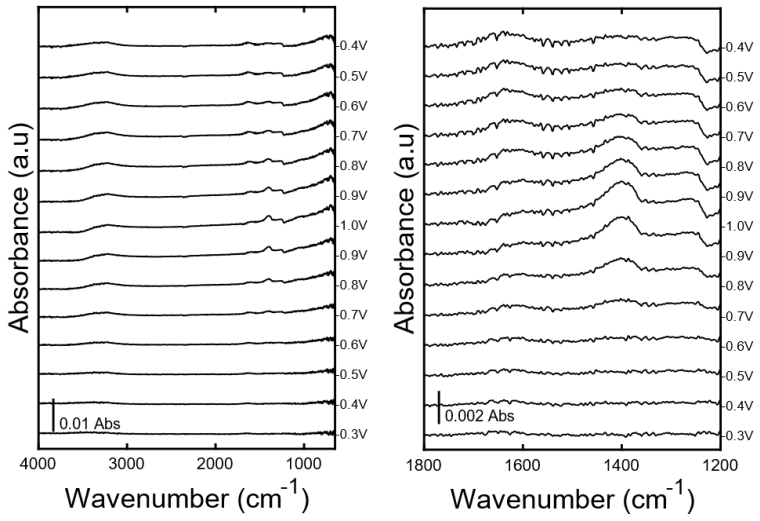

Figure S3.16: Full (4000-800 cm^{-1}, left) and carbonaceous region (1800-1200 cm^{-1}, right) ATR-SEIRAS spectra on the metallic Sn electrode with no CO_2 present (sparged with Ar).

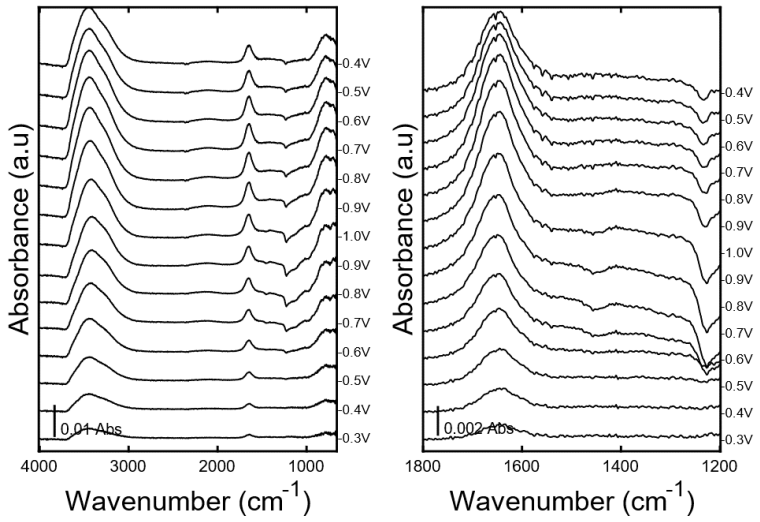

Figure S3.17: Full (4000-800 cm^{-1}, left) and carbonaceous region (1800-1200 cm^{-1}, right) ATR-SEIRAS spectra on the oxidized Sn electrode with no CO_2 present (sparged with Ar).

Figure S3.18 shows the cyclic voltammograms collected during the ATR-SEIRAS experiments above. The raw current and current densities are shown to compare the relative current pull and activity between the two different electrodes. The current drawn from the CO_2R experiment is greater than the Ar-sparged experiment on both materials, but the oxidized Sn has a

larger increase in current upon introduction of CO_2 relative to the metallic Sn. This is consistent with oxidized Sn's more facile activation of CO_2 than metallic Sn. We refrain from further interpretation of the electrochemical data due to the lack of quantification of products, which was outside the scope of the current study.

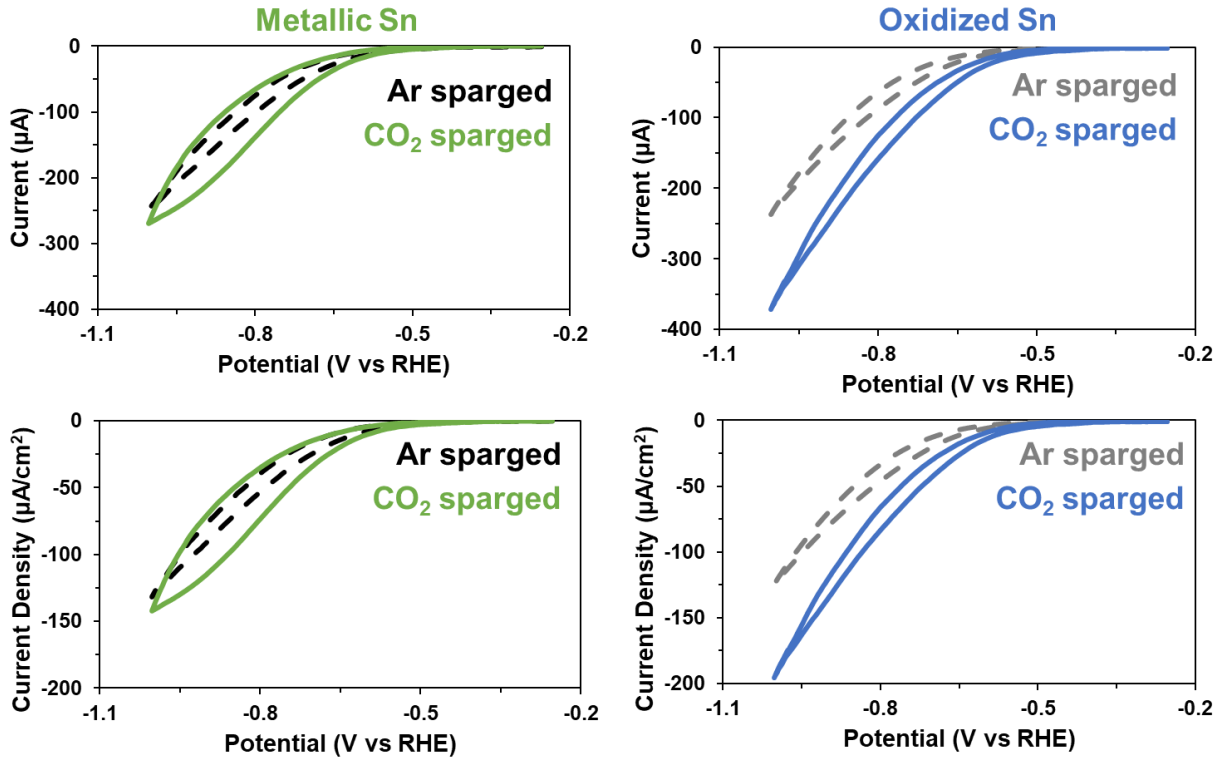

Figure S3.18: Cyclic voltammograms, showing current (top row) and current density (bottom row), for metallic Sn (left column) and oxidized Sn (right column) corresponding to CO_2R (solid colored lines) and Ar-sparged (broken greyscale lines) ATR-SEIRAS experiments from **Figure 3.6** and **Figure S3.13**.

Visualization of Vibrational Frequencies

Due to the surface selection rule, only vibrational modes that have a change in the dipole moment perpendicular to the surface will have a observable ATR-SEIRAS peak. Therefore, the vibrational modes need to be visualized to determine if they have a change in dipole in the z-direction. We chose to only visualize vibrational modes with frequencies above 900 cm^{-1} because the so-called fingerprint region (< 1000 cm^{-1}) is notoriously difficult to analyze with many

overlapping peaks. Additionally, we were most interested in explaining the difference in the observed peaks for metallic and oxidic Sn and consolidating that with the observed activity difference in the context of our computed reaction energetics. All reported vibrational frequencies in **Figures S3.19-42** are at -0.5 V_{RHE} (other potentials are reported below in **Table S3.1**). We also include animated gifs of the vibrations that are available for download to assist in visualization.

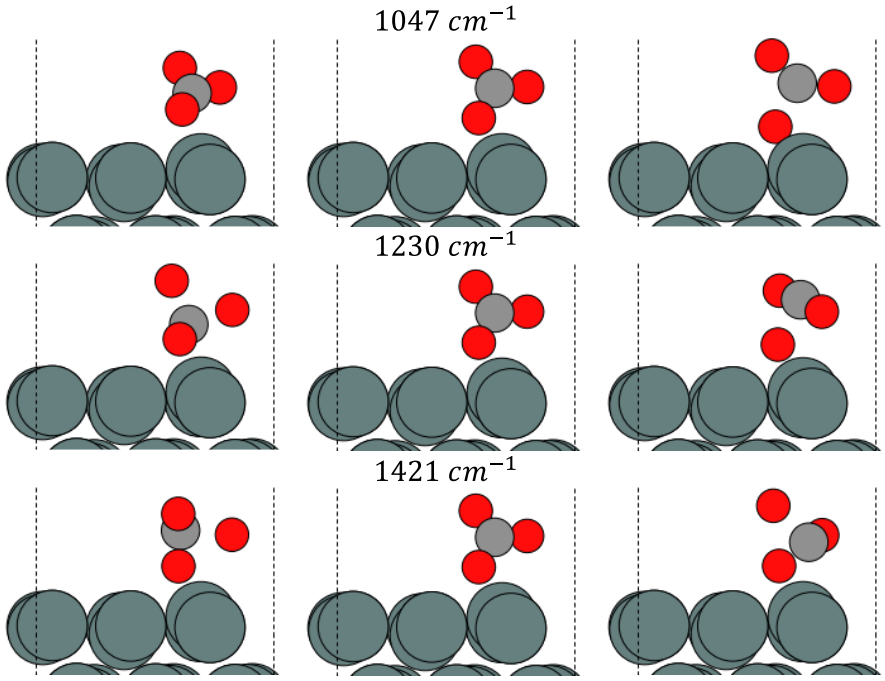

Figure S3.19: Visualization of vibrational modes for monodentate CO_3 on metallic Sn

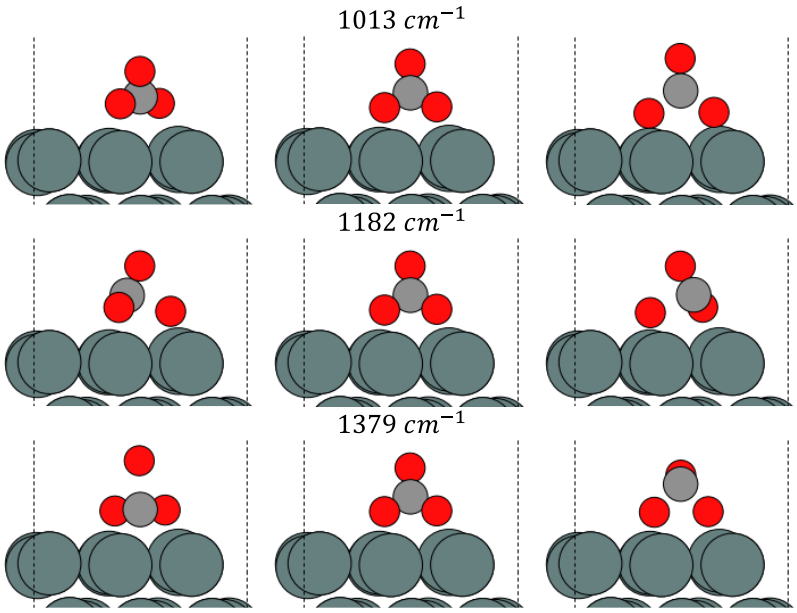

Figure S3.20: Visualization of vibrational modes for bidentate CO_3 on metallic Sn.

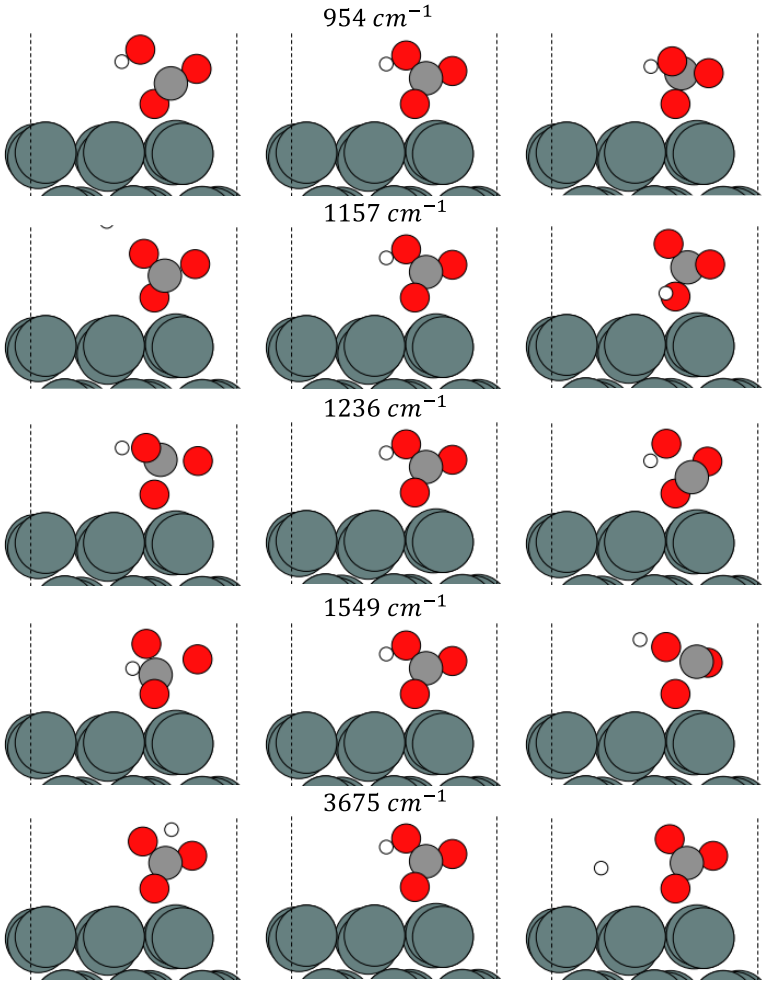

Figure S3.21: Visualization of vibrational modes for monodentate HCO_3 on metallic Sn

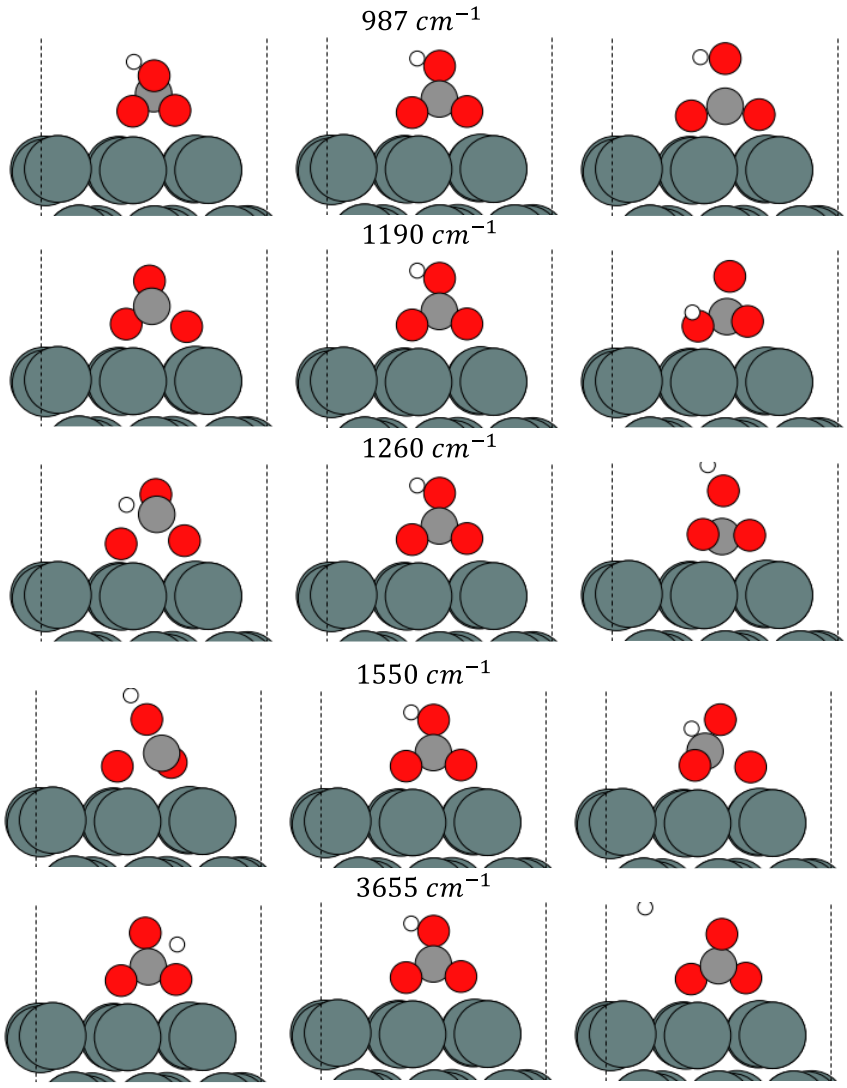

Figure S3.22: Visualization of vibrational modes for bidentate HCO_3 on metallic Sn

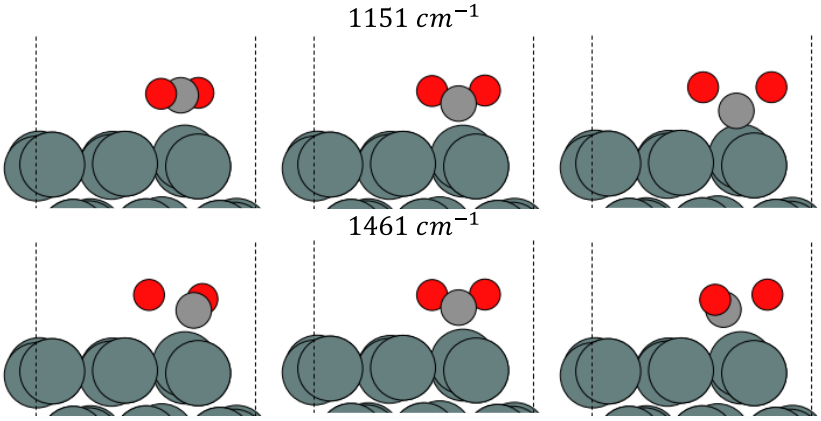

Figure S.23. Visualization of vibrational modes for CO_2 bound through carbon on metallic Sn

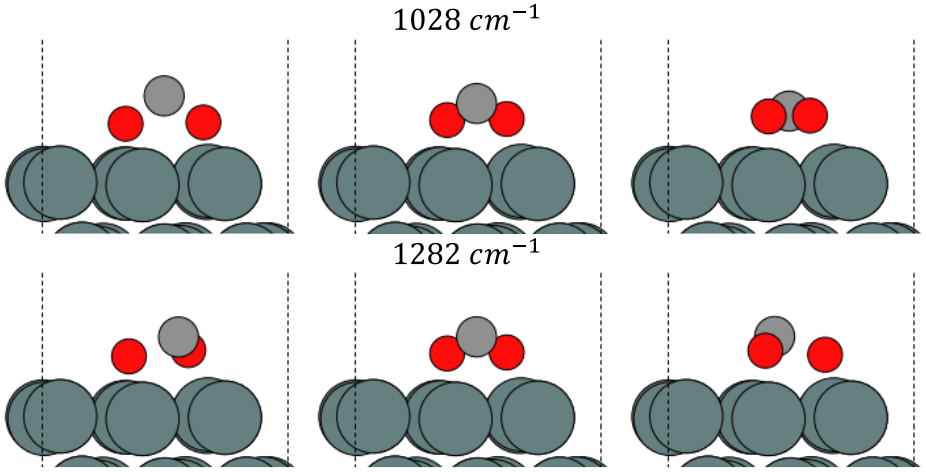

Figure S3.24: Visualization of vibrational modes for CO_2 bound through oxygens on metallic Sn. Note, these are the vibrations at -1 V_{RHE} due to CO_2 spontaneously desorbing at -0.5 V_{RHE} for this structure.

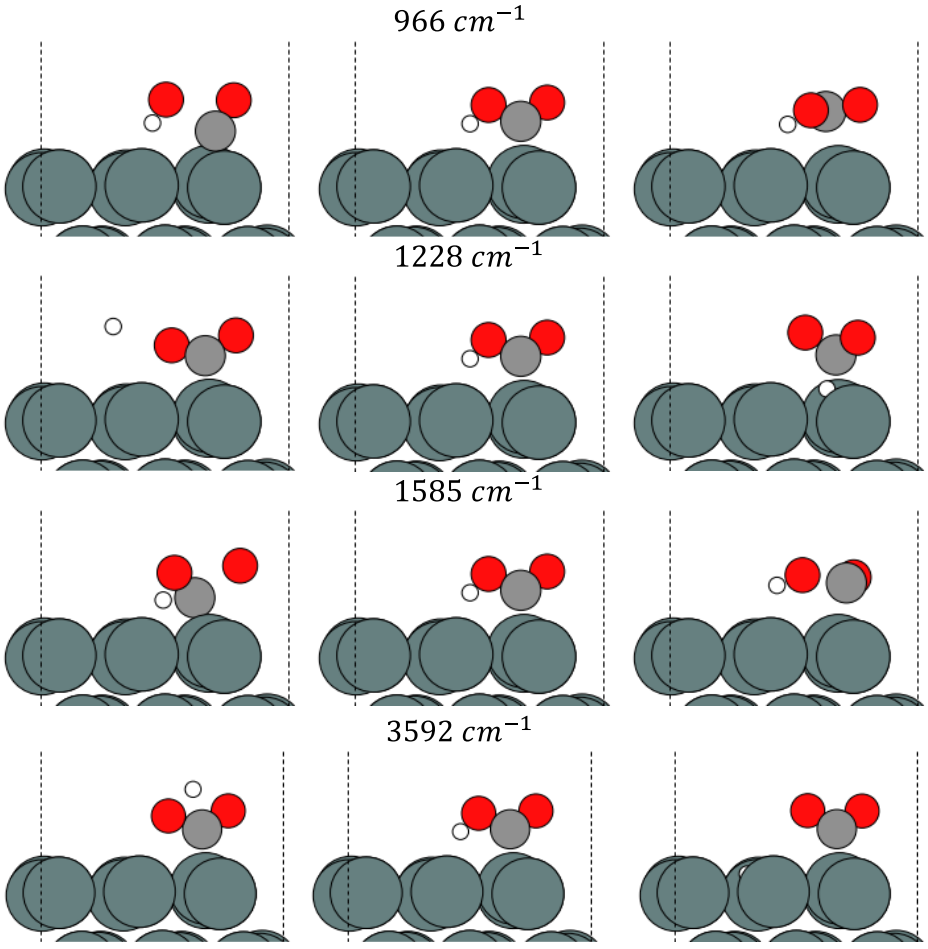

Figure S3.25: Visualization of vibrational modes for COOH on metallic Sn

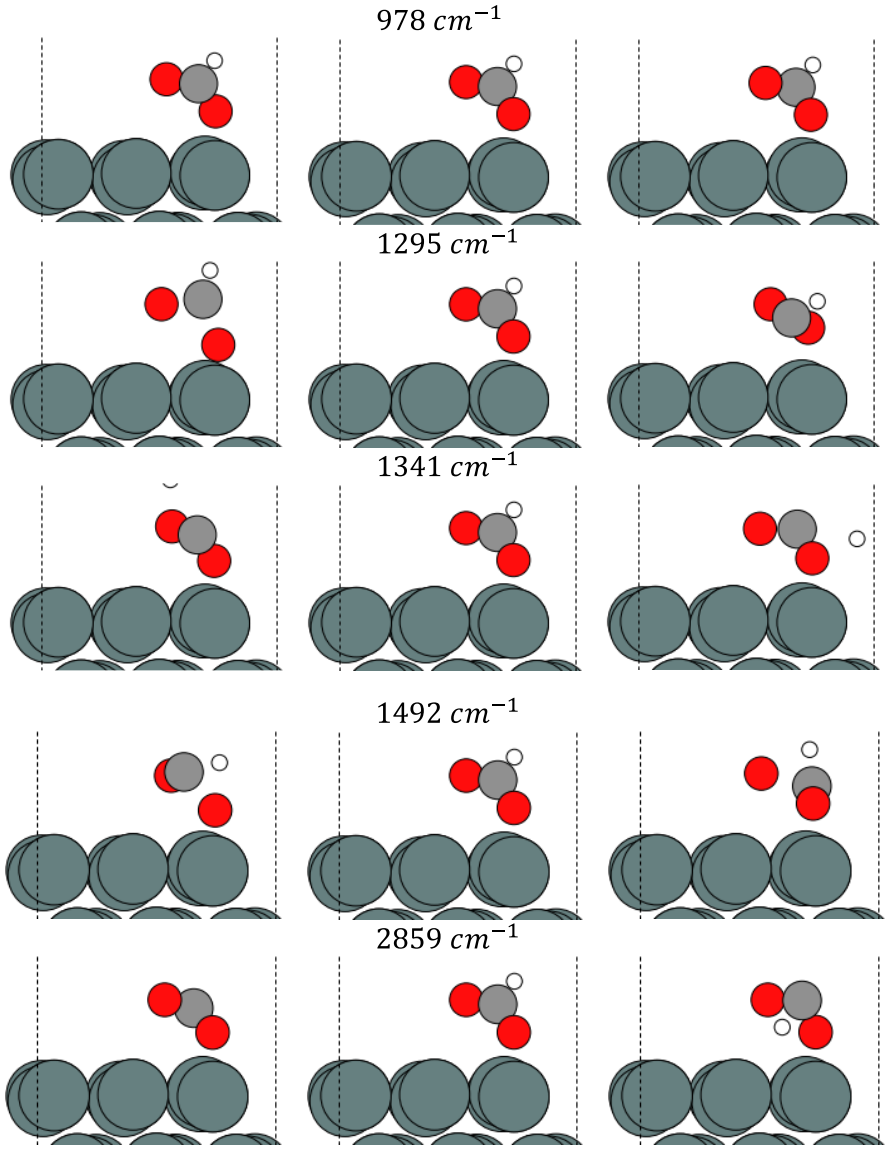

Figure S3.26: Visualization of vibrational modes for monodentate OCHO on metallic Sn

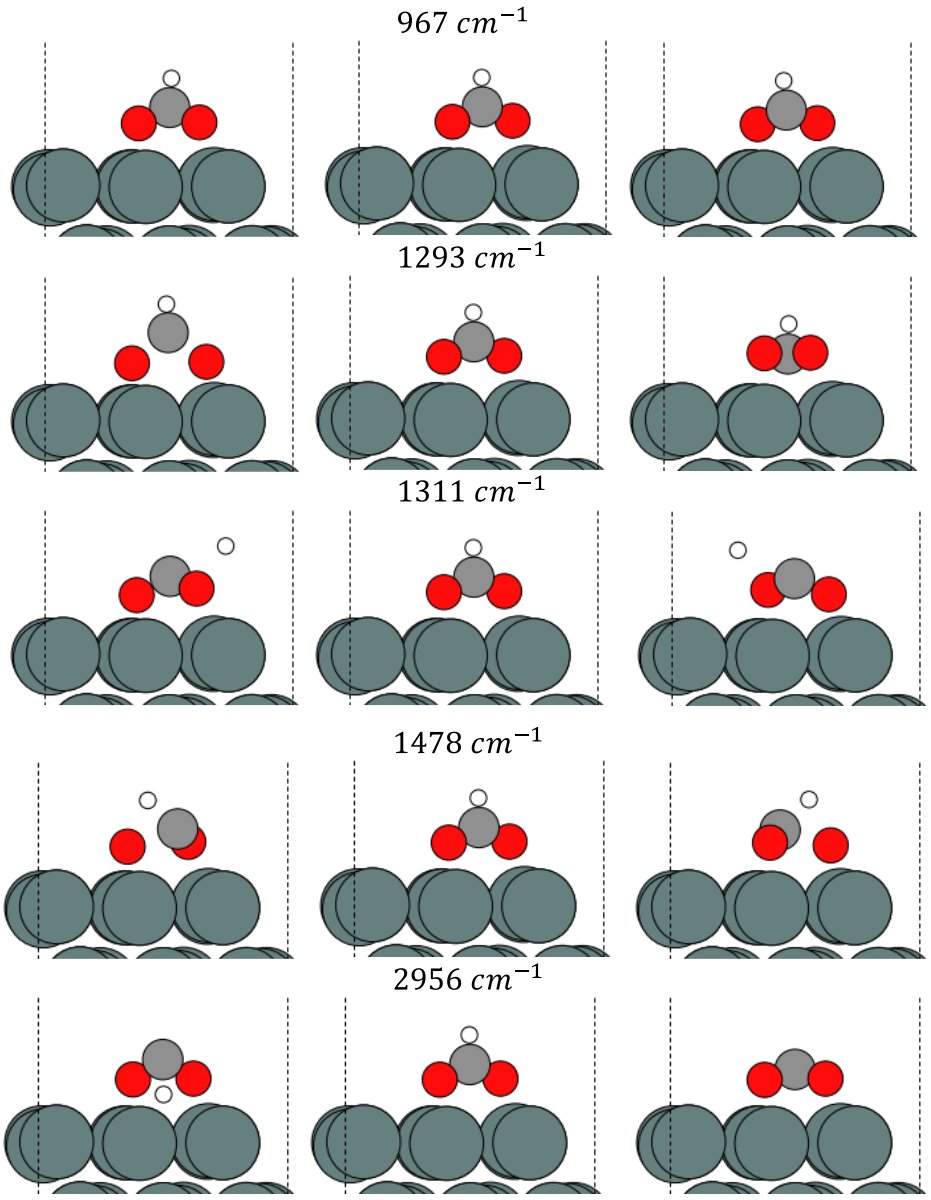

Figure S3.27: Visualization of vibrational modes for bidentate OCHO on metallic Sn

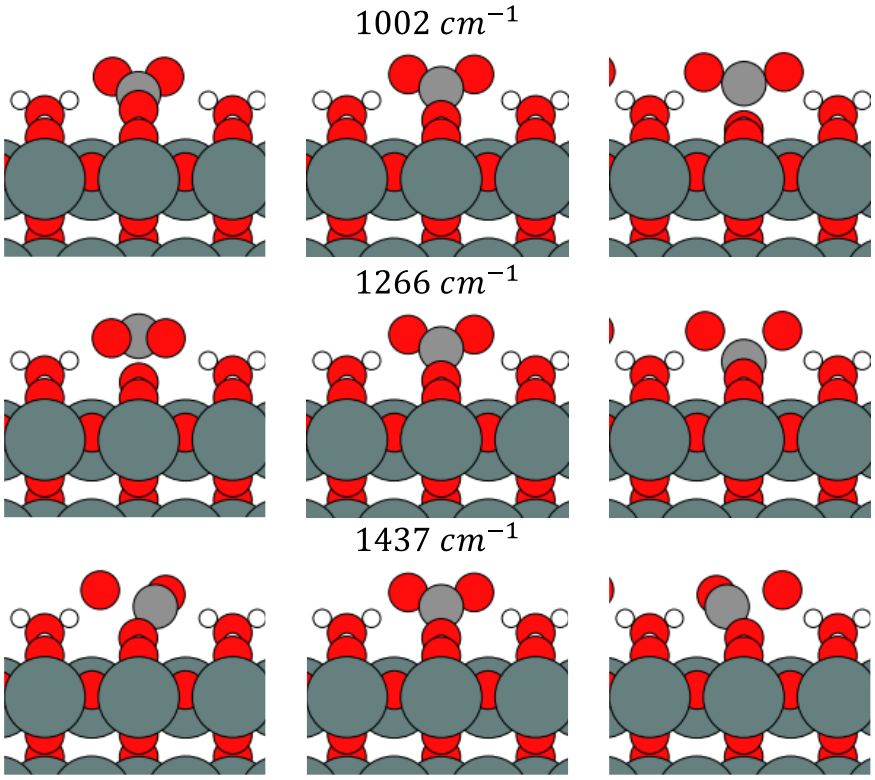

Figure S3.28: Visualization of vibrational modes for monodentate CO_3 on SnO_2 with one cus-water and one cus-vacancy

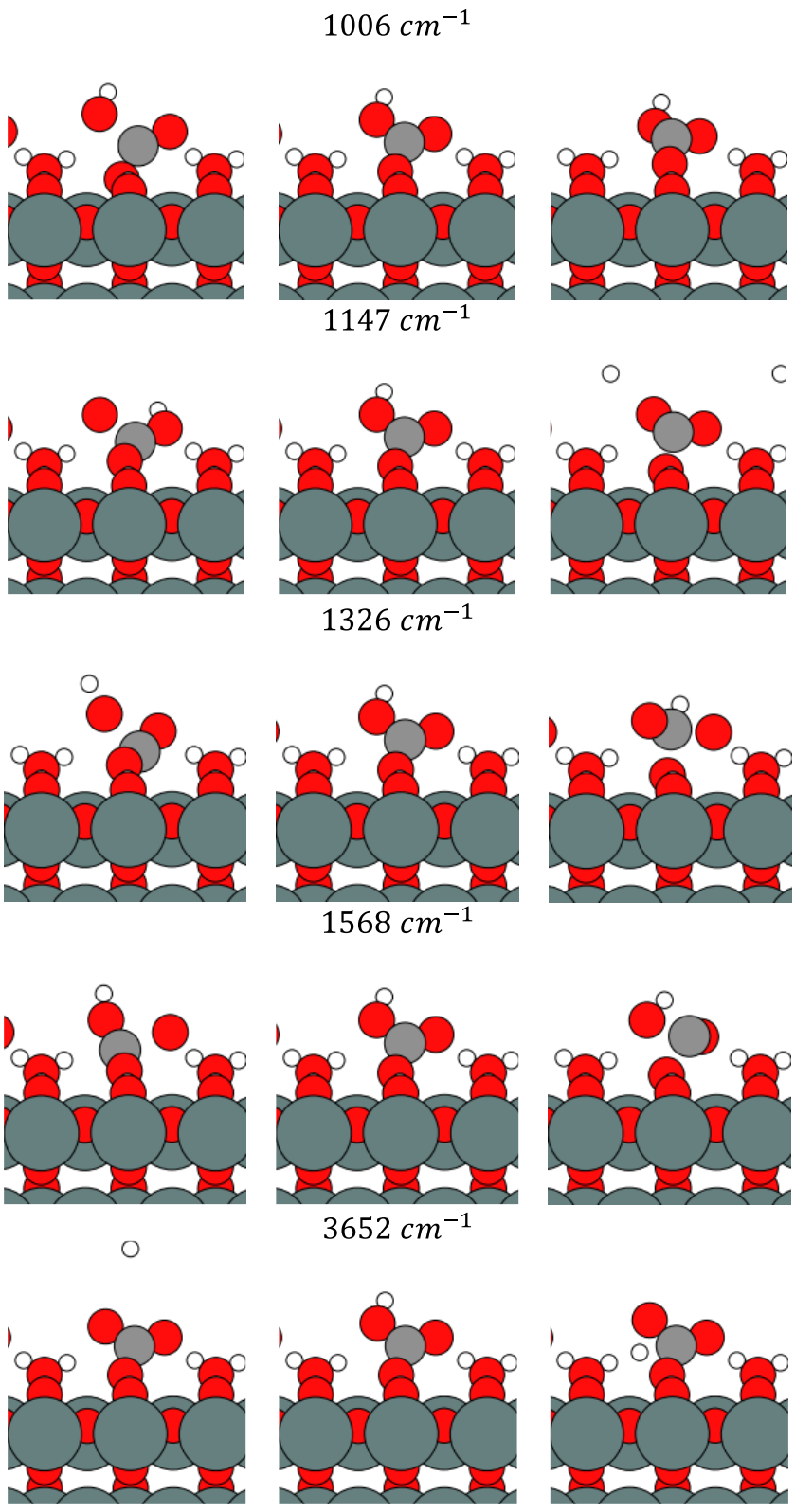

Figure S3.29: Visualization of vibrational modes for monodentate HCO_3 on SnO_2 with one cus-water and one cus-vacancy

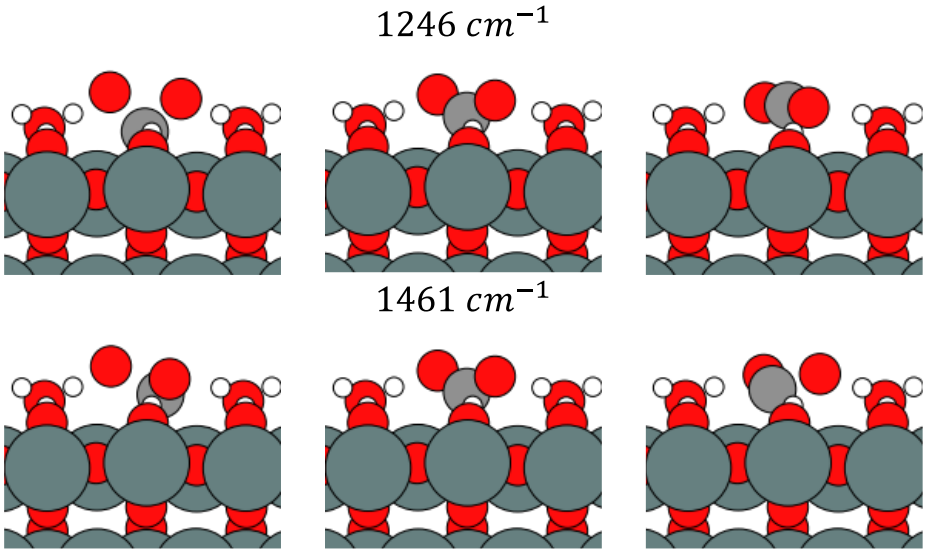

Figure S3.30: Visualization of vibrational modes for CO_2 bound through carbon on SnO_2 with one cus-water and one cus-vacancy

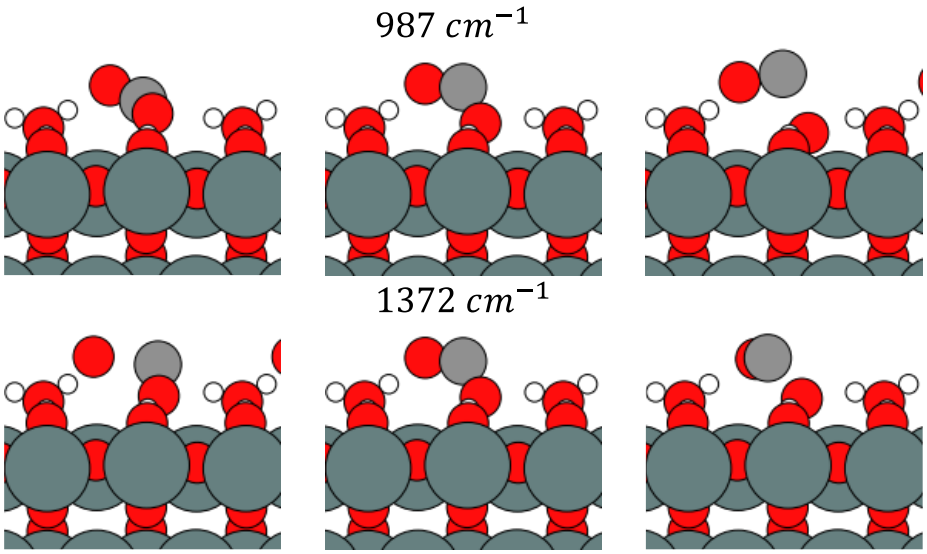

Figure S3.31: Visualization of vibrational modes for CO_2 bound through oxygen on SnO_2 with one cus-water and one cus-vacancy

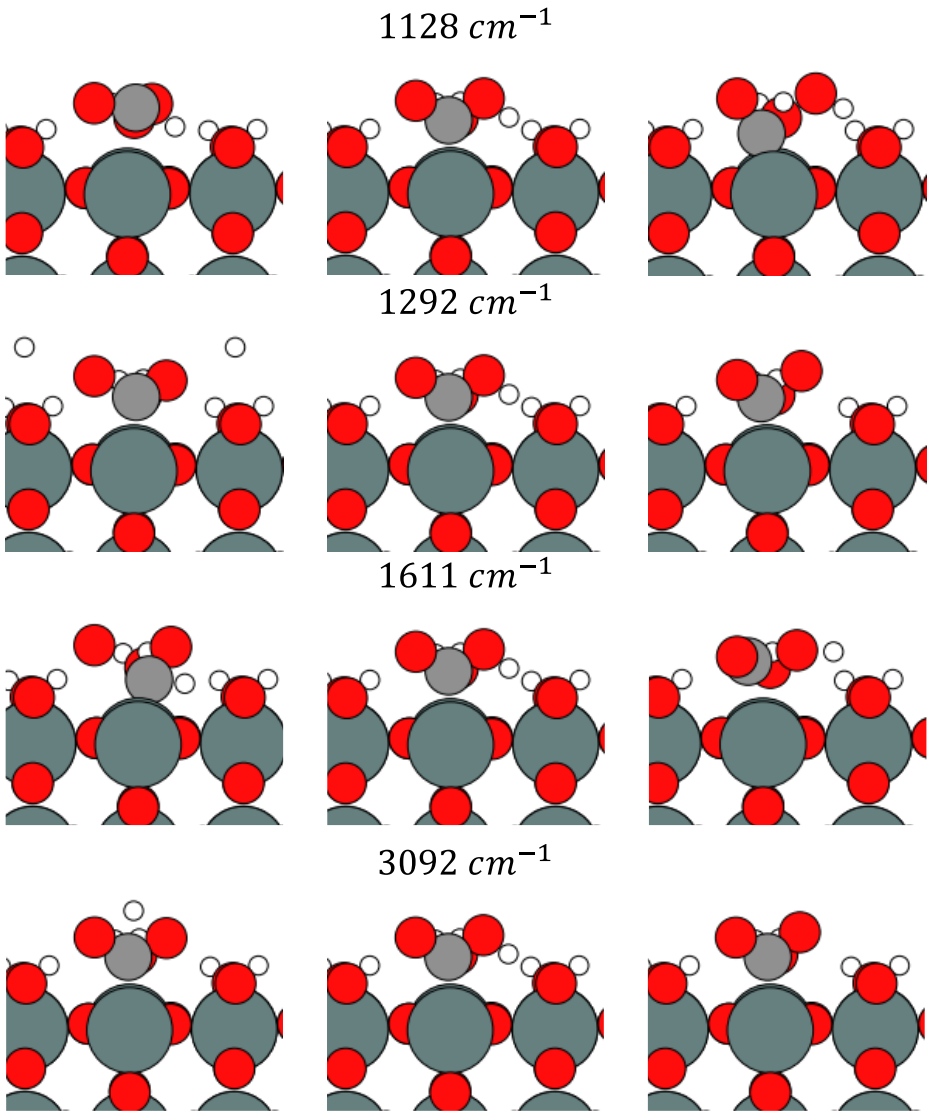

Figure S3.32: Visualization of vibrational modes for COOH on SnO_2 with one cus-water and one cus-vacancy

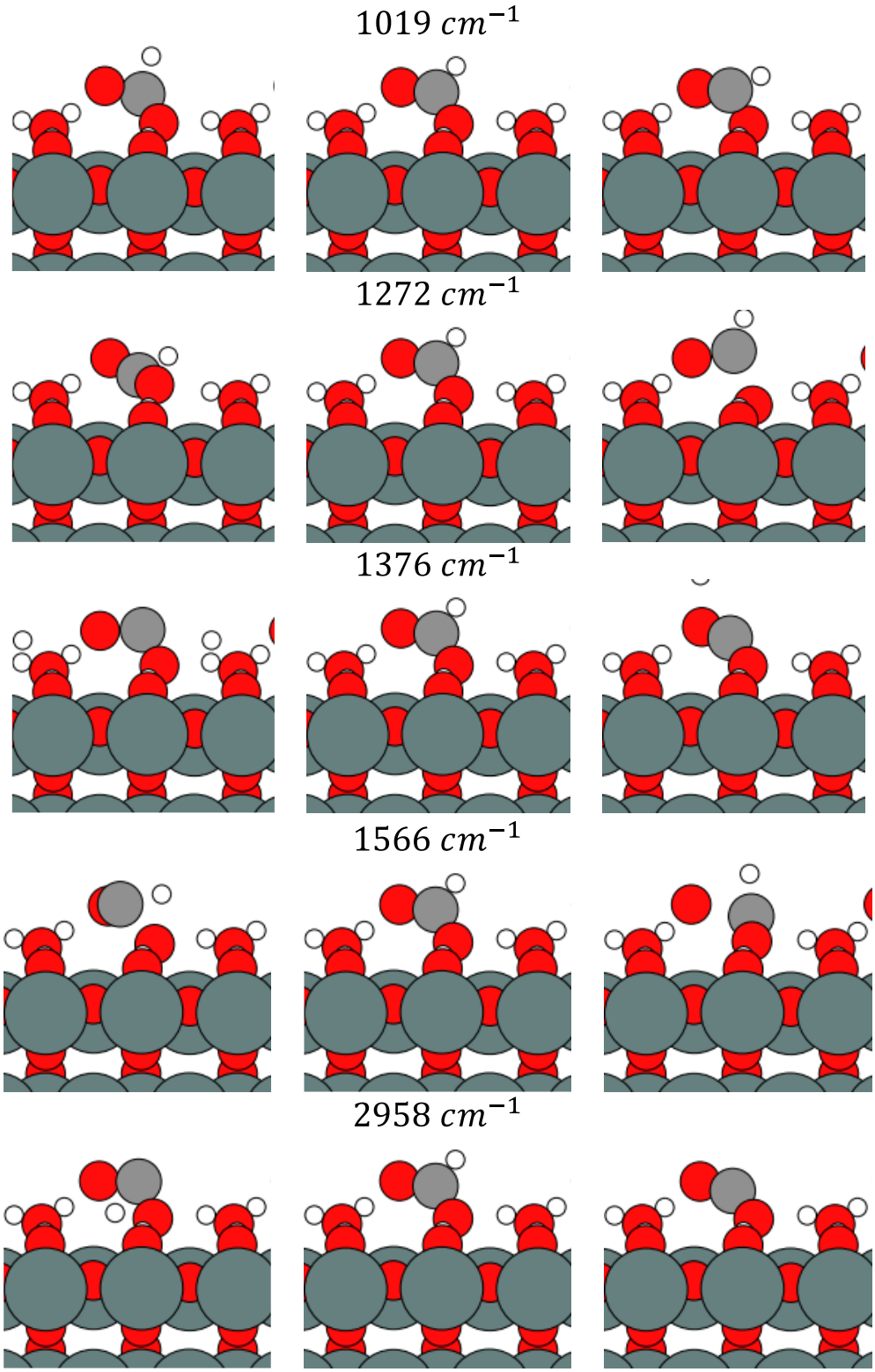

Figure S3.33: Visualization of vibrational modes for monodentate OCHO on SnO_2 with one cus-water and one cus-vacancy

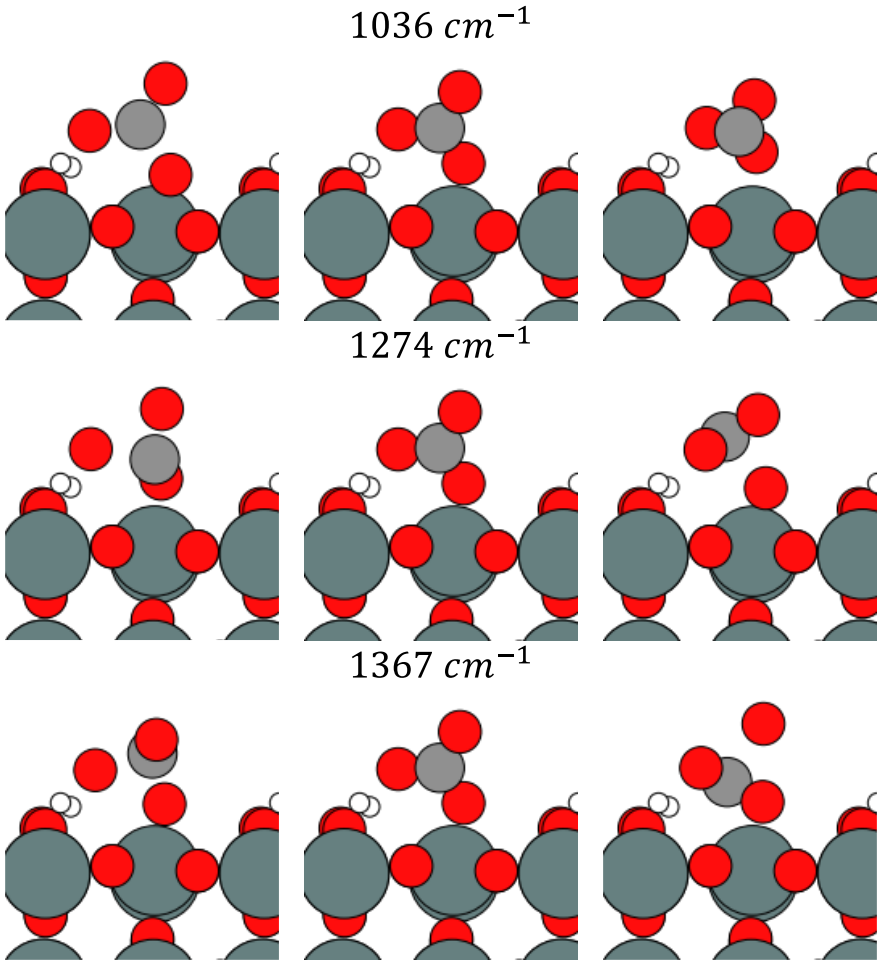

Figure S3.34: Visualization of vibrational modes for monodentate CO_3 on SnO_2 with no cus-water and two cus-vacancies

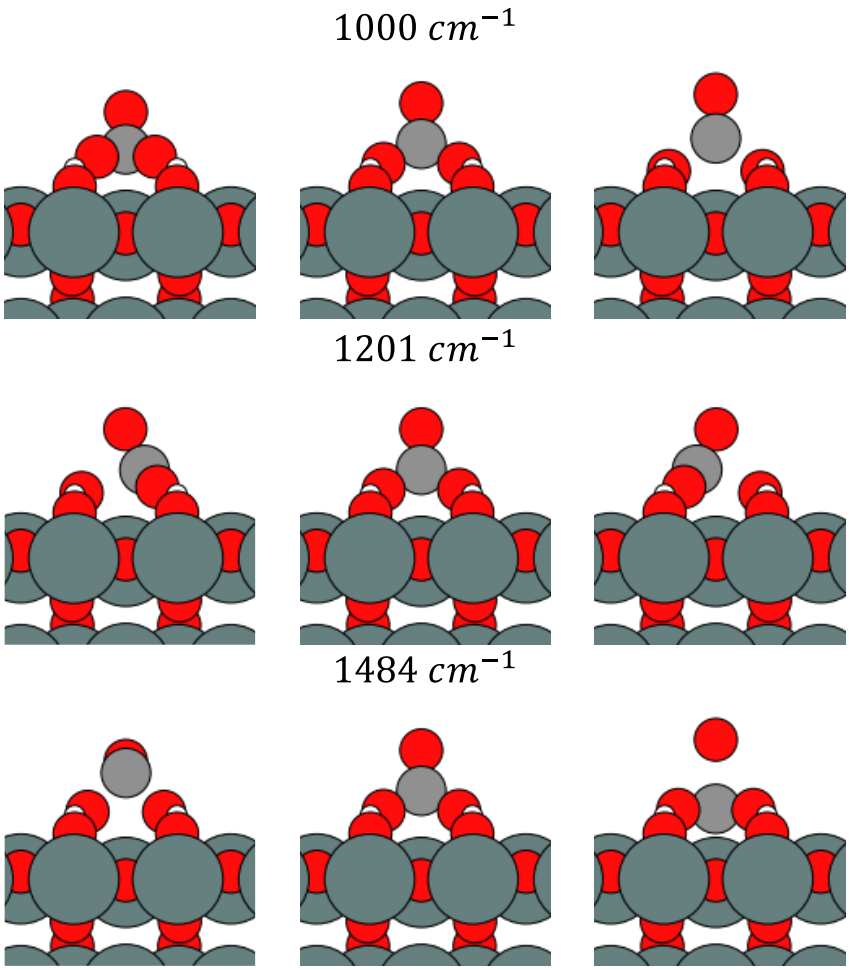

Figure S3.35: Visualization of vibrational modes for bidentate CO_3 on SnO_2 with no cus-water and two cus-vacancies

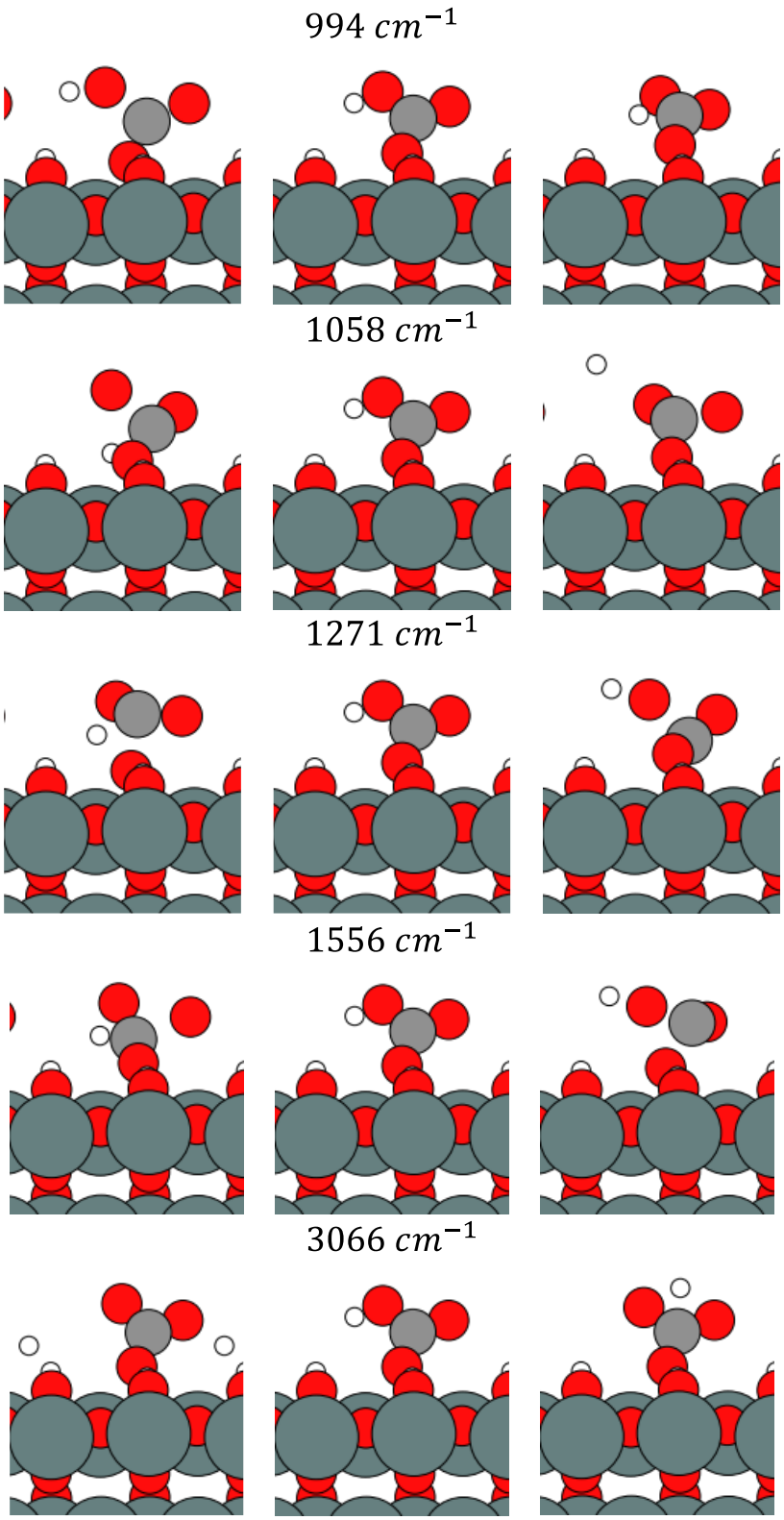

Figure S3.36: Visualization of vibrational modes for monodentate HCO_3 on SnO_2 with no cus-water and two cus-vacancies

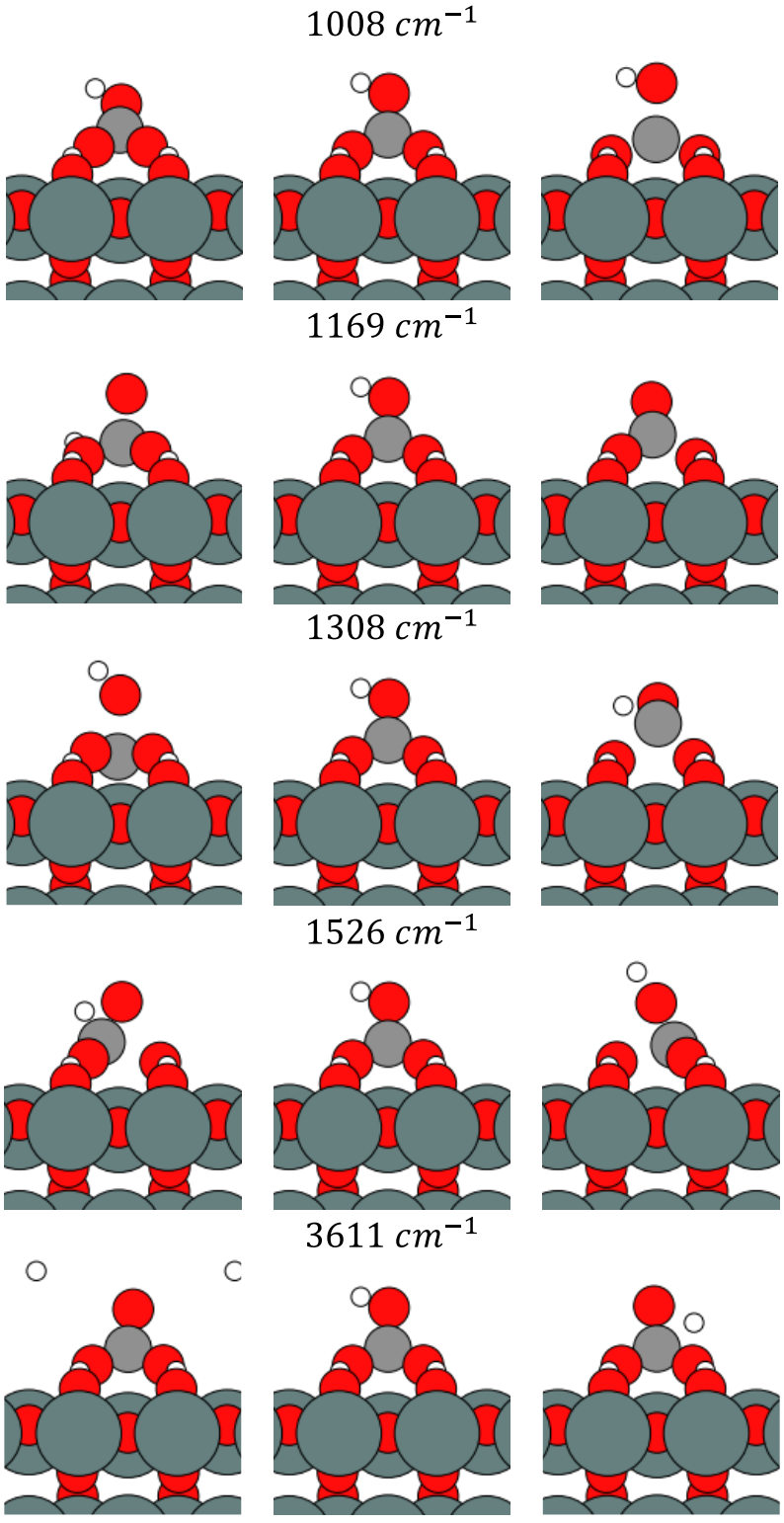

Figure S3.37: Visualization of vibrational modes for bidentate HCO_3 on SnO_2 with no cus-water and two cus-vacancies

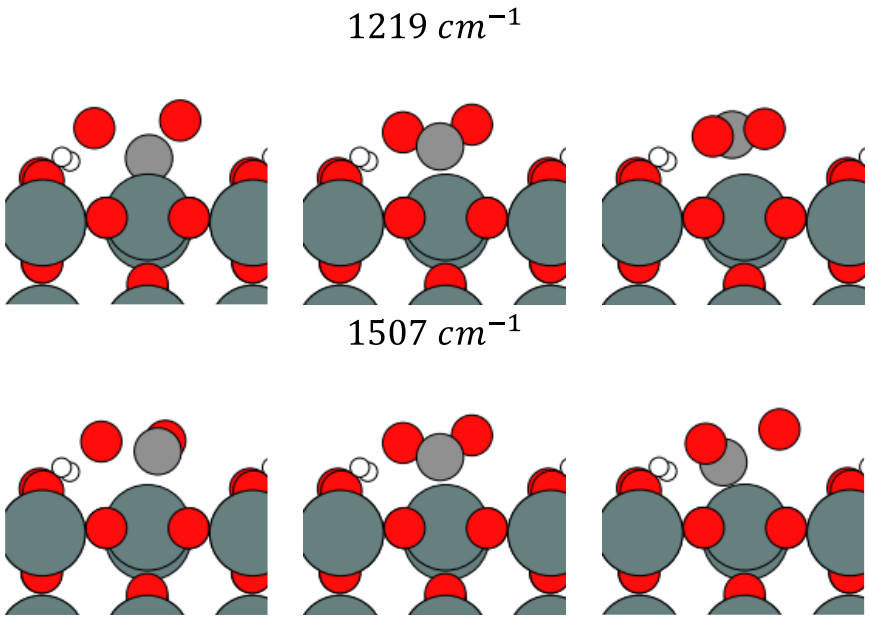

Figure S3.38: Visualization of vibrational modes for CO_2 bound through carbon on SnO_2 with no cus-water and two cus-vacancies

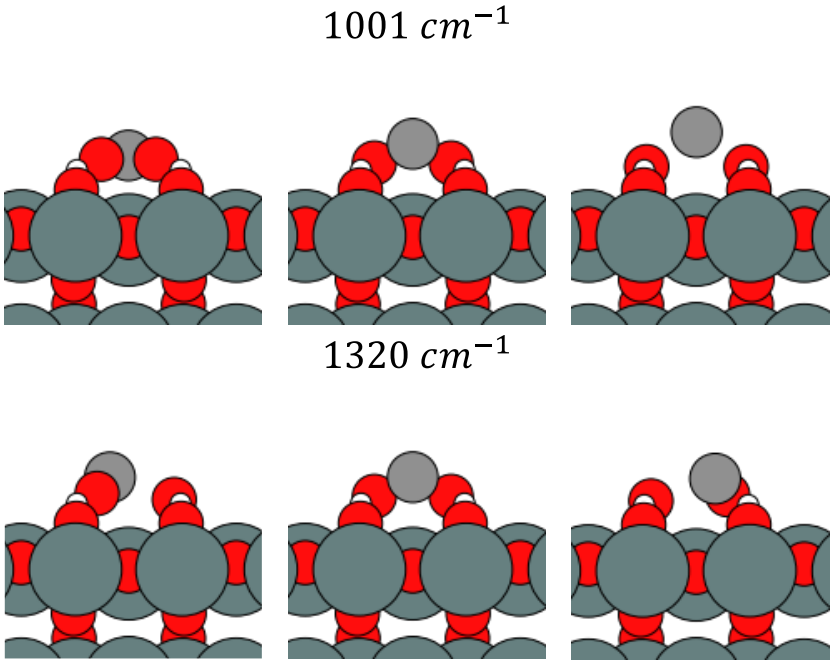

Figure S3.39: Visualization of vibrational modes for CO_2 bound through oxygens on SnO_2 with no cus-water and two cus-vacancies

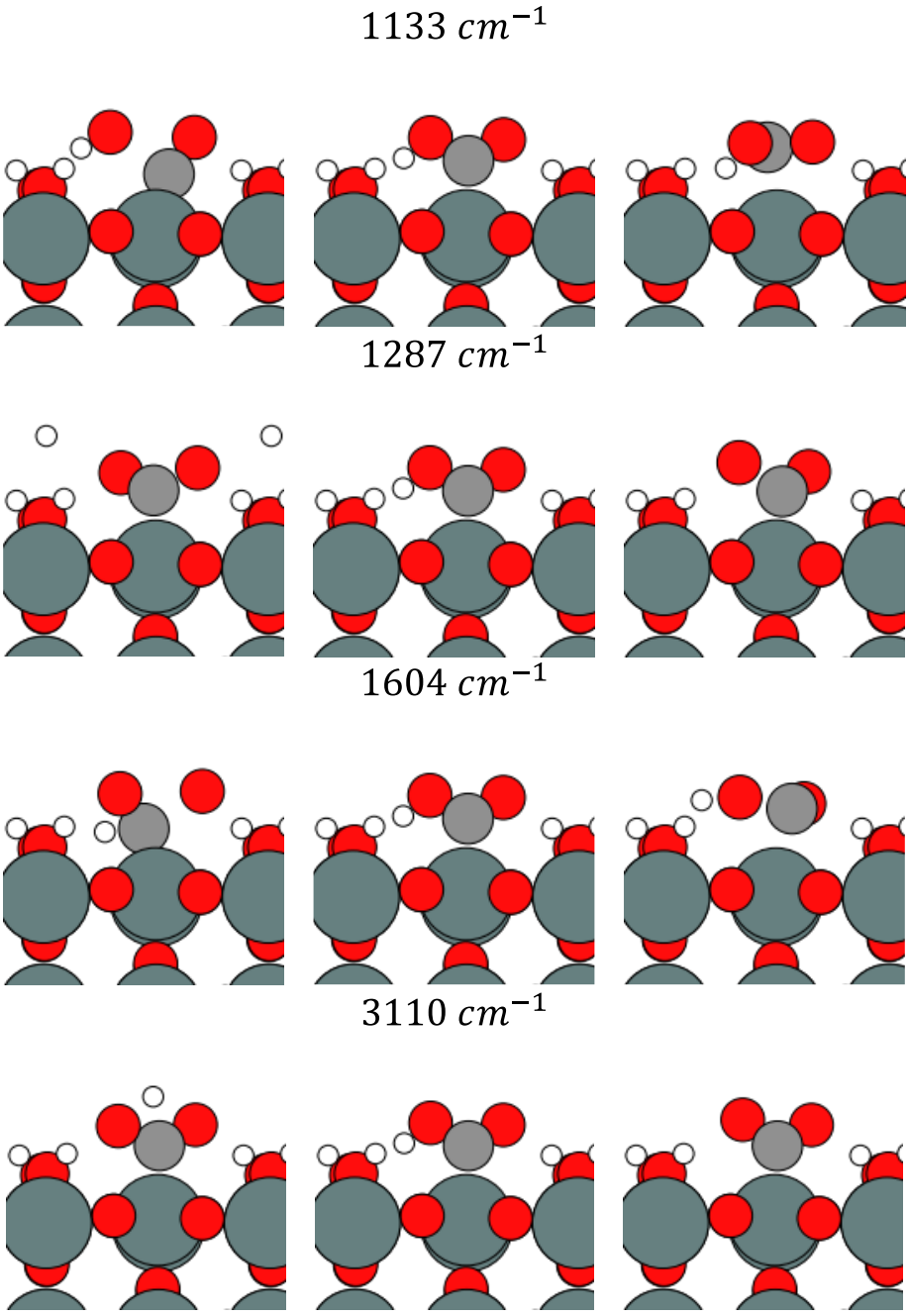

Figure S3.40: Visualization of vibrational modes for COOH on SnO_2 with no cus-water and two cus-vacancies

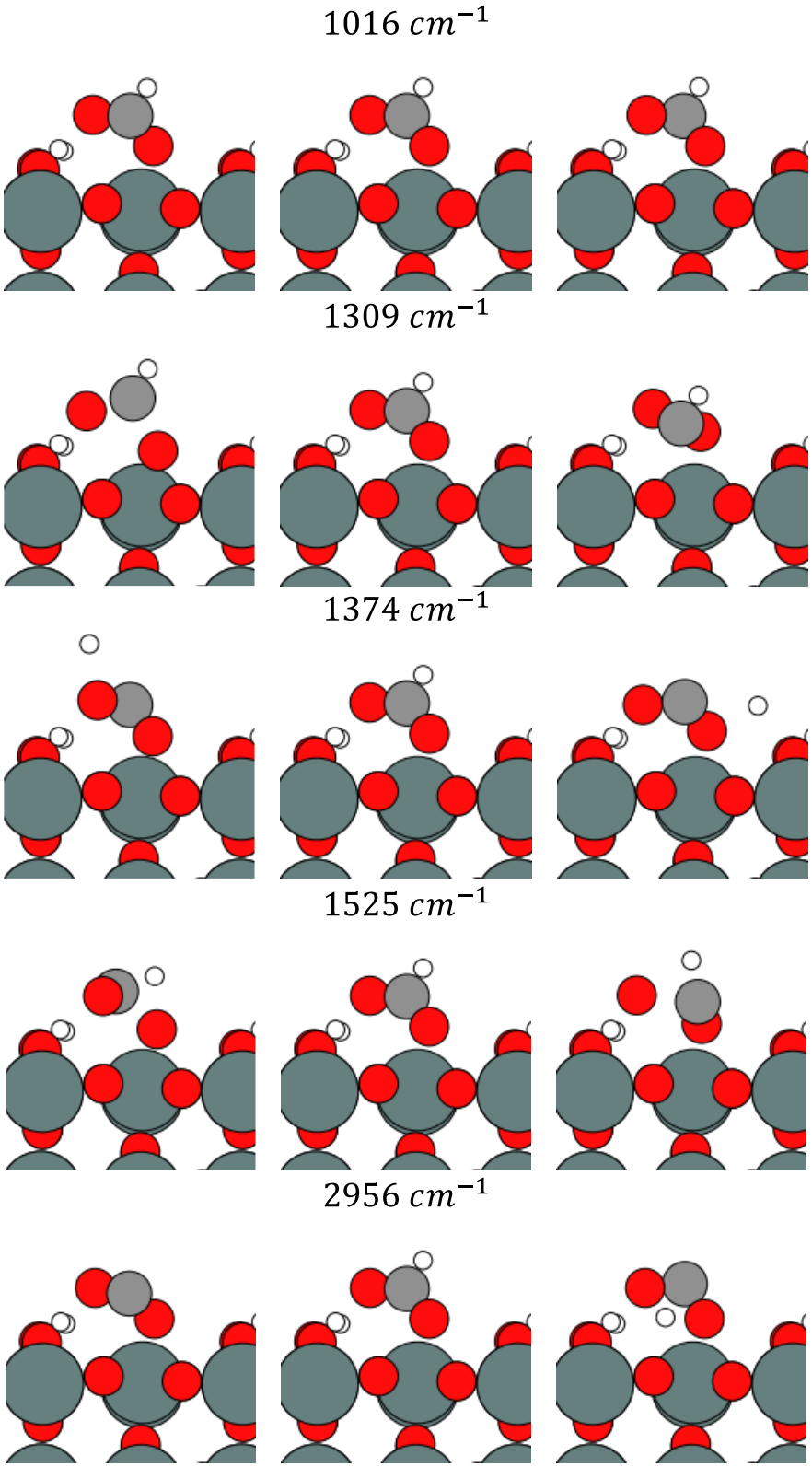

Figure S3.41: Visualization of vibrational modes for monodentate OCHO on SnO_2 with no cus-water and two cus-vacancies

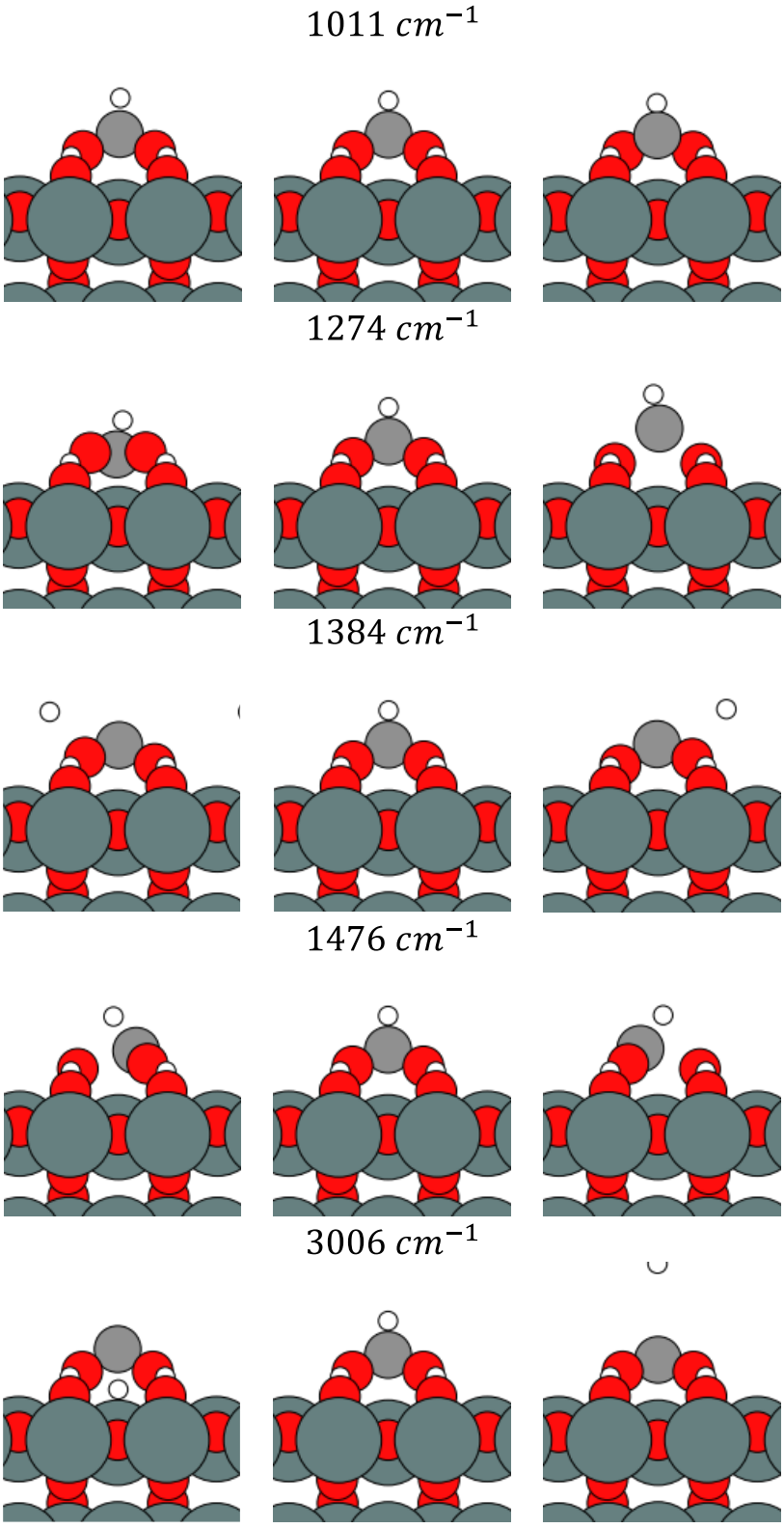

Figure S3.42: Visualization of vibrational modes for bidentate OCHO on SnO_2 with no cus-water and two cus-vacancies

Table S3.1 Calculated vibrational frequencies for all modes above 900 cm^{-1} for all adsorbates (units are cm^{-1}).

Surface	Adsorbate	0 V_{RHE}	-0.5 V_{RHE}	-1 V_{RHE}
Metallic Sn	CO_3 (mono)	1002	1047	1030
		1199	1230	1215
		1430	1421	1351
	CO_3 (bi)	999	1013	1010
		1232	1182	1233
		1464	1379	1348
	HCO_3 (mono)	975	954	877
		1164	1157	1113
		1269	1236	1257
		1531	1549	1575
		3714	3675	3773
	HCO_3 (bi)	1018	987	925
		1143	1190	1204
		1311	1260	1261
		1530	1550	1541
		3631	3655	3676
	CO_2 (carbon)	1098	1151	1172
		1489	1461	1398
	CO_2 (oxygens)	1230	1094	1028
		2192	1816	1282
	COOH	1012	996	965
		1180	1228	1158
		1633	1585	1577
		3543	3592	3411
	OCHO (mono)	1017	978	994
		1274	1295	1297
		1343	1341	1415
		1502	1492	1482
		2900	2859	2927
	OCHO (bi)	988	967	1110
		1265	1293	1267
		1334	1311	1308
		1513	1478	1443
		2963	2956	2831
SnO_2 – 1 cus-water	CO_3 (mono)	994	1002	1010
		1272	1266	1277
		1478	1437	1430
	HCO_3 (mono)	1013	1006	985
		1136	1147	1105
		1339	1326	1325
		1580	1568	1562

		3647	3652	3665
	CO_2 (carbon)	1249	1246	1278
		1487	1461	1442
	CO_2 (oxygens)	981	987	1038
		1474	1372	1329
	COOH	1137	1128	1118
		1283	1292	1318
		1623	1611	1593
		3192	3092	2963
	OCHO (mono)	1032	1019	1010
		1268	1272	1278
		1385	1376	1371
		1589	1566	1541
		2967	2958	2931
SnO_2 – 0 cus-water	CO_3 (mono)	1037	1036	1030
		1277	1274	1280
		1401	1367	1345
	CO_3 (bi)	993	1000	983
		1200	1201	1191
		1482	1484	1456
	HCO_3 (mono)	1009	994	995
		1070	1058	1053
		1282	1271	1313
		1613	1556	1606
		3060	3066	3026
	HCO_3 (bi)	1025	1008	1000
		1166	1169	1158
		1350	1308	1290
		1517	1526	1515
		3591	3611	3622
	CO_2 (carbon)	1202	1219	1228
		1547	1507	1475
	CO_2 (oxygens)	1000	1001	1040
		1422	1320	1233
	COOH	1146	1133	1109
		1289	1287	1289
		1611	1604	1598
		3178	3110	3034
	OCHO (mono)	1024	1016	1017
		1273	1309	1318
		1372	1374	1378
		1539	1525	1519
		2965	2956	2948
	OCHO (bi)	1009	1011	1003
		1282	1274	1278

	1392	1384	1387
	1480	1476	1454
	3014	3006	2959

Chapter 4: Cooperative Effects Associated with High Electrolyte Concentrations in Driving the Conversion of CO_2 to C_2H_4 on Copper

Reprint from: ChemRxiv. 2024, 14 June, Version 1, https://doi.org/10.26434/chemrxiv-2024-03mmk. The full-text version of this article may be viewed at: https://chemrxiv.org/engage/chemrxiv/article-details/6667d49512188379d8d1365f

In this work, I was in charge of the ATR-SEIRAS methodology, measurements acquisition, processing and analysis, and ATR-SEIRAS section writing and editing.

4.1 Abstract

Increasing the product selectivity and decreasing the cost of product separation is critical for large scale application of electrochemical CO_2 reduction (ECO_2R). We hypothesize that highly concentrated aqueous electrolytes can tune the microenvironment of the catalyst/electrolyte interface and improve product selectivity. Compared to a conventional electrolyte concentration of 1 M HCOOK, the use of a 7.1 M HCOOK electrolyte increases the FE ratio of C_2H_4/CO from 2.2 ± 0.3 to 18.3 ± 4.8 at -1.08 V vs RHE on a Cu gas diffusion electrode. Based on electrochemical analysis and AIMD simulation, the identity and concentration of the cation and anion play more important roles in controlling the CO_2R reaction pathway than the bulk CO_2 solubility and the bulk pH of electrolytes. *In-situ* ATR-SEIRAS suggests that, unlike 1 M HCOOK, the *CO-bridge binding mode on Cu is dominant in 7.1 M HCOOK electrolyte, which potentially results in less CO release and higher yield of C_2H_4. This study demonstrates that while we can tailor the electrolyte composition to shift product selectivity, the factors that control the product selectivity are numerous and cannot be distilled down into one correlated property-reactivity relationship. Thus, when CO_2R conditions are changed, care must be taken to understand their effects on the bulk electrolyte properties and the electrode-electrolyte interface.

4.2 Introduction

Electrochemical CO_2 reduction (ECO_2R) provides a promising pathway to produce chemical feedstocks and fuels using a carbon negative method, which is essential for realizing carbon neutrality.[170–176] Despite its intriguing impact on environmental protection, ECO2R suffers from drawbacks that prevent large-scale deployment.[177–179] Currently, there are a few startup companies targeting conversion of CO_2 to CO, HCOOH, C_2H_4 and other important chemical feedstock materials.[180–184] Among all the technical challenges, reducing the cost of product separation by improving the product selectivity of desired products is one of the obstacles that needs to be addressed.[185–188]

C_2H_4, EtOH, acetate and other C_{2+} products are fundamental chemical feedstock materials that are widely used in chemical industries and can be products of ECO_2R.[175,189] Interestingly, Cu is one of the only heterogeneous catalysts that can form C_{2+} products in ECO_2R.[27,190–196] Studies have been focused on improving the turnover rate and product selectivity of C_2H_4 and other C_{2+} products in ECO_2R. Specific effort has been made on tuning the microenvironment of the Cu/electrolyte interface to control product selectivity. For instance, strategies to tune the catalytic behavior of Cu metal have been pursued to control its affinity towards intermediates like adsorbed CO (*CO) to lower the C-C coupling energy barrier and inhibit competing reactions. These strategies include tuning the morphology of the electrode surface, modulating the oxidation state, controlling the exposed crystal facets, introducing Cu alloys (e.g. with Ag), or adjusting the interaction between deposited Cu with substrates.[197–203] Additionally, strategies to tune the electrode-electrolyte interface have been pursued that use surface modifiers like ionomer or organic additive films to improve the C_{2+} product turnover rate.[204–209] The films are thought to tune local pH, modify the mass transport of reactants and products, and adjust the interaction of reaction

intermediates. Moreover, implementing electrolyte chemistry and tuning the microenvironment of relevant species in solution is also critical to control the product distribution. The choice of solvent and supporting electrolyte can tune the electrolyte properties like pH, buffer capacity, CO_2 solubility, and the mass transport of CO_2, which all play important roles in determining the preference of multiple competing reaction pathway on Cu surface.[210–218]

By tuning the salt concentration, the properties of the electrolyte can be systematically varied. Water-in Salt Electrolyte (WiSE) is a type of highly concentrated aqueous electrolyte.[219,220] It was first introduced for achieving the goal of an aqueous battery owing to its wide electrochemical stability window and suitable conductivity.[221,222] The significantly increased salt solubility and decreased concentration of free water of WiSE compared to conventional low concentration electrolyte provides a pathway to tune the electrolyte for CO_2R. As a few studies have shown, applying WiSE for CO_2R can mitigate the unwanted HER reaction and control the product selectivity. The study by Zhang et al. demonstrated that applying LiTFSI WiSE on Au can inhibit HER while promoting CO formation.[223] Meanwhile, Ren et al. proposed that by controlling the surface electric field on electrocatalyst using WiSE, the CO_2R product selectivity can be controlled.[224] In another study, Zhang et al. suggested that the reason for $NaClO_4$ WiSE to promote C_{2+} product on Cu is due to the tuning of water activity as a result of the change of the salt concentration.[225] Employing WiSE on Cu for CO_2R alters the Cu/electrolyte interface in multiple ways as per the concentration of cation/anion, the pH, CO_2 mass transport and proton deliver processes all changed simultaneously. Therefore, understanding the effect of changes both in the bulk properties of the electrolyte and the interfacial properties is necessary for fully understanding the impact of WiSE on tuning CO_2R reaction pathway on Cu. Insight will enable the design of optimized WiSE/Cu system to further improve the yield of C_2H_4 and other valuable products.

In this study, we study the effect of electrolyte concentration on CO_2R of a HCOOK supporting electrolyte ranging from 1 M to 7.1 M with a Cu GDE. We find that the high salt concentrations increase the FE ratio of C_2H_4/CO from 2.2 ± 0.3 in the 1 M HCOOK control to 18.3 ± 4.8 in the 7.1 M HCOOK at -1.08 V vs RHE. The origin of the improved product selectivity towards C_2H_4 over CO is investigated from both the perspective of bulk electrolyte properties and interfacial effects at the electrode. As the concentration is increased from 1 M to 7.1 M, both the pH and the solubility of CO_2 are affected. We show, however, that the shift in these two bulk properties cannot fully account for the change in product selectivity. Experimental data supported by ab initio molecular dynamics (AIMD) calculations show that K^+ is an important cation in the 7.1 M electrolyte that is found to stabilize *CO on Cu and facilitate CO-CO coupling. The energy barrier of forming the *OCCO intermediate is lower in 7.1 M HCOOK than 1 M HCOOK, in line with the higher C_2H_4 yield in 7.1 M HCOOK. We also find that the anion can affect the selectivity of C_2H_4 with respect to CO at high electrolyte concentration. To gain more insight into the processes at the interface, the Cu-electrolyte interface is studied using in situ surface-sensitive attenuated reflectance surface enhanced infrared absorption spectroscopy (ATR-SEIRAS). ATR-SEIRAS shows a higher population of the bridge binding *CO ($*CO_B$) in electrolytes with higher salt concentration, highlighting the potential role of $*CO_B$ on Cu in 7.1 M HCOOK on C_2H_4/CO FE ratio. Through the analysis presented here, it becomes clear that the electrolyte concentration changes several factors that range not only from the changes to the bulk electrolyte properties, but also changes to the electrode-electrolyte interface that can affect the C_2H_4/CO ratio. These factors are intertwined, highlighting the complexity of the electrolyte formulation and also the CO_2 reduction reaction, and all come together to change the product distribution.

4.3 Methods

4.3.1 Materials

Potassium formate (HCOOK, ReagentPlus®, 99 %) and Potassium trifluoromethanesulfonate, (KOTf, 98 %) were purchased from Sigma Aldrich. Sodium formate (≥99.0% ACS) is obtained from VWR. Potassium hydroxide (99.98%, trace metal basis) is purchased from Acros Organics. Water was purified by a Nanopure Analytical Ultrapure Water System (Thermo Scientific) or a Milli-Q Advantage A10 Water Purification System (Millipore) with specific resistance of 18.2 MΩ·cm at 25 °C.

4.3.2 Preparation of Cu GDE and Cu plate electrode

A 300 nm thick Cu catalyst layer was deposited on a PTFE gas diffusion layer (Sterlitech, 0.45 micron) using Cu target obtained from Kurt J. Lesker (99.95 %, 2-inch diameter) in ATC Orion 8: Dielectric Sputter System. Cu foil electrode (99.999% trace metals basis, 1 mm thick, purchased from Sigma-Aldrich) was first mechanically polished then electrochemically polished in 1 M H_3PO_4 (85 wt. % in H2O, 99.99% trace metals basis, purchased from Sigma-Aldrich) under anodic potential for 5 min before electrolysis experiments.

4.3.3 Electrochemical measurements

The electrolysis cell is adapted from the stack flow cell developed by Kuhl et al. (REF, Energy Environ. Sci., 2012, 5, 7050) mentioned previously in literature. Electrochemical measurements were performed on a Biologic SP200 potentiostat under a N_2 atmosphere, using a slice of Cu GDE or Cu plate as the working electrode, leakless Ag/AgCl electrode (EDAQ) as the reference electrode, and Pt foil as the counter electrode with AEM Fumasep FAA-3-50 separating anode cell and cathode cell. The CO_2 or CO_2/Ar mix reactant gas is flowed to the back side of Cu

GDE or in electrolyte with Cu plate at a flow rate of 10 sccm. Catholyte and anolyte are circulated at 2.5 ml/min. Electrochemical impedance spectroscopy (EIS) was taken before every measurement to quantify the solution resistance (Rs) for IR correction. The applied potential with the Ag/AgCl scale ($E_{Ag/AgCl}$) RHE was converted to the reversible hydrogen electrode (RHE) scale (ERHE) with the following equation:

$$E_{RHE} = E_{Ag/AgCl} + 0.059 \times pH + 0.197 + I * Rs \text{ ; } \textbf{(eq 4.1)}$$

where i is the current during CO_2R electrolysis. For CO_2 concentration dependent experiment, the partial pressure of CO_2 was controlled by mixing CO_2 and Ar with specific flow rate. Gas mixture with different ratio of CO_2 was flow through the GDE in electrolysis as mentioned previously.

4.3.4 Product quantification

Reactant gas was flowed through the GDE flow cell or H-cell with the flow rate set as 10 sccm by an Alicat flow controller. The gasses passed the electrolysis cell is injected to GC/MS (Agilent 7880A Gas Chromatograph) with Ar as the carrier gas. H_2, CO, CH_4, C_2H_4 and C_2H_6 were detected by a thermal conductivity detector (TCD) and Flame Ionization detector (FID) and quantified based on calibration curve collected from standard gas samples. The liquid products were quantified by both HPLC (Thermo Scientific Ultimate 3000) and 1H NMR with water suppression technique and Dimethylsulfoxide as internal standard on a Bruker 400 MHz NMR.

4.3.5 Measurement of CO_2 solubility

Measurements of bulk electrolyte were taken using a Nicolet IS30 spectrometer with a VeeMAX^{TM} III (PIKE Technologies) ATR configuration chamber. A custom flow cell was used to allow constant replenishment of CO_2 saturated analyte over a Si ATR Crystal (PIKE Technologies).[226] Reservoirs of DI water, 1M HCOOK, and 7.1 M HCOOK were sparged with

CO_2 for 30 minutes prior to measurements and continually sparged with CO_2 while being pumped into the flow cell at 10 mL/min. 32 interferograms were measured for each analyte and the solubility of CO_2 was probed via the area of the asymmetric stretch vibration of CO_2 at 2343 cm^{-1}.[227] Measured CO_2 peak areas in 1 M and 7.1 M HCOOK were obtained by integrating the absorbance between 2333 and 2355 cm^{-1} and then normalized by the CO_2 peak area measured in DI water, which was set to 34 mM.

4.3.6 pH determination

The pH of low concentration electrolytes (≥1 M) is measured by Oakton pH 6+ Handheld Meter. To avoid misreading of the pH of high concentration electrolyte due to uncounted liquid junction potential, pH Test Strips from VWR Chemicals BDH® (pH range: 7.0 to 14.0, pH graduation: 0.5) and EEEE (pH range: 5.0 to 9.0, pH graduation: 0.5) were used to determine to pH value of 4.2 M, 7.1 M and 9.1 M HCOOK.

4.3.7 pH imaging with laser-scanning confocal microscopy

pH imaging experiments were performed with laser-scanning confocal microscopy (CLSM) in combination with the ratiometric fluorescent probe 8-Aminopyrene-1,3,6-trisulfonic acid trisodium salt (APTS) purchased from Millipore Sigma that acts as an excited-state fluorescence sensor of the local pH. APTS can directly sense local hydroxide activity and is sensitive to a pH range between 11.7 and 14. 200 μM APTS were dissolved in 1 M and 10 M CO_2-saturated HCOOK electrolyte, respectively. A custom-made electrochemical cell compatible with CLSM was used to map the local pH value at an applied potential of -1.7 V vs. Ag/AgCl as a function of time. The pH was mapped in an area of 443 μm x 443 μm with a resolution of 64 x 64 pixels parallel to the electrode surface. In the direction perpendicular to the electrode surface, the

pH was imaged over a range of 61 μm with a step size of 1 μm, starting a few microns below the surface. The pH value was averaged for each z-position and the plane with the highest average pH value was assumed to represent the pH at the position closest to the electrode surface since the pH increases as a function of proximity to the cathode surface.

4.3.8 *Ex situ* characterization of Cu GDE

X-ray photo-electron spectroscopy (XPS) data were collected using a Kratos AXIS Ultra spectrometer (Kratos Analytical, Manchester, UK) equipped with a monochromatic Al $K_{\alpha 1}$ X-ray source (1486.7 eV). Data were collected at pressures of ~$5x10^{-9}$ Torr. The electron-collection lens aperture was set to sample a 700x300 μm spot. The survey scan was collected with an analyzer pass energy of 40, with a step size of 1 eV and a dwell time of 100 ms. The element-specific scans were collected with an analyzer pass energy of 20, a step size of 0.05 eV, and a dwell time of 100 ms. The instrument energy scale and work function were calibrated using clean Au, Ag, and Cu standards. All spectra were collected with no external charge neutralization with the exception of the blank Cu GDE sample, which was collected with an electron gun charge neutralizer with a charge balance voltage of 1.5 V. The spectra were referenced with the adventitious carbon peak shifting to 284 eV. The instrument was operated by Vision Manager software version 2.2.10 revision 5. The XPS data were analyzed using CasaXPS software (CASA Software Ltd). (Acknowledgement: The XPS data were collected at the Molecular Materials Research Center in the Beckman Institute at Caltech. The authors thank Jake M. Evans for assistance with XPS data collection.) Powder X-ray Diffraction (PXRD) data were collected using a Rigaku SmartLab diffractometer (Cu K_{α}). The patterns of all samples and blank were collected using Bragg-Brentano geometry, from 10° to 60° 2θ with a step size of 0.03° and a rate of 10° per minute. Scanning

Electron Microscope (SEM) images were recorded with a NOVA NanoSEM 450 using 10 kV accelerating voltage and spot size of 3.

4.3.9 *In situ* ATR-SEIRAS

For in-situ ATR-FTIR measurements, a Nicolet 6700 FTIR spectrometer (Thermo Fisher Scientific) with VeeMAX^{TM} III (PIKE Technologies) ATR configuration chamber was used. The photoelectrochemical experiments were performed in a J1W Jackfish spectro-electrochemical cell (PIKE Technologies) with a PTFE/PEEK base, and IRUBIS Si(100) specialized 1 ATR element (single-bounce ATR crystal). Polycrystalline Au electrodes were chemically deposited (electroless deposition) based on previous works, which was first established and demonstrated by Osawa in 2002.[43] Each electrode was first deaired with argon for at least 2 minutes per ml of electrolyte, then cycled between 0.2 V – 1.75 V vs RHE using a gold mesh as a counter electrode for 10 cycles at 50 mV/s for surface cleaning and SEIRA activation.

Following Au SEIRA activation, Cu catalyst synthesis was conducted by electrodeposition via direct cathodic electro-reduction within a modified electrochemical ATR-FTIR cell. The cell assembly consists of the same base piece from the ATR-FTIR PTFE/PEEK with an in lab made acrylic top piece, which attaches to the PTFE/PEEK base and contains a bubbler, reference electrode, and counter electrode ports. The counter electrode was held in parallel to the working electrode directly above it. A graphite rod was used as the counter electrode and Ag/AgCl electrode was used as the reference electrode. As a precursor, 5.75 mM copper sulfate pentahydrate ($CuSO_4 \cdot 5H_2O$, 99.995% trace metals basis, Sigma-Aldrich) in 0.1 M Sulfuric acid (H_2SO_4 - Merck, Suprapur 96%), similar to Heyes et al.,[228] was used deposited at a potential bias of 59 mV vs RHE for a total charge of 44 mC/cm$^2_{geo}$. Post electrodeposition, electrocatalyst was rinsed with pH~9.2 KOH (Semiconductor grade pellets, 99.99% trace metals basis, Sigma-Aldrich) solution

3 times followed by 3 rinses with analyte (either 1 M or 7.1 M - HCOOK, ReagentPlus®, 99%, Sigma-Aldrich).

Prior to electrochemical (EC) ATR-SEIRAS experiments the analyte solution was deaired with argon for at least 2 minutes per ml of solution. After this, a potential bias was applied for 5 minutes to reduce the copper oxide, at the copper oxide reduction peak potential (~0 V vs RHE). For pH-controlled experiments, the solution was CO spurged for at least 2 minutes per ml of solution with continuous bubbling throughout the experiment. Then, a background spectrum was taken at 0.0 V vs RHE averaging over 32 interferograms followed by a potential step series with increments of -0.1 V between 0.0 V and -1.2 V vs RHE while collecting 32 interferograms at each potential step. For time evolution EC ATR-SEIRAS experiments, a background spectrum was taken at 0.2V vs RHE, averaging over 32 interferograms followed by a potential step to either -0.7 or -1.1 V vs RHE collecting 64 interferograms per time stamp. For CO_2 reduction time evolution experiments, the solution was CO_2 spurge for at least 2 minutes per ml of solution with continuous bubbling throughout the experiment. Lastly, for in situ CO_2RR EC ATR-SEIRAS experiments, a background spectrum was taken at 0.2 V vs RHE, averaging over 32 interferograms followed by a cyclic voltammetry (CV) sweep between 0.2 and -1.2 V vs RHE. During the CV, 17 interferograms were collected over the course of 10 seconds (10 mV intervals). Finally, data has been averaged out collecting 170 interferograms over 100 mV intervals.

4.3.10 Computational Methods

The initial structures were modeled using the CHARMM-GUI Nanomaterial Modeler.[229,230] Each model comprised one CO molecule and either one pair or ten pairs of K^+ and $HCOO^-$ ions, representing 1 M or 7.1 M concentrations, respectively, with 56 H_2O on top of 4 layers of $3\sqrt{2}\times3\sqrt{2}$ Cu(100). Classical molecular dynamics simulations were performed to

equilibrate the constructed systems using GROMACS[231] with a 2 fs timestep. We employed the CHARMM force field,[232] and the water molecules were described by the TIP3P model.[233] Initially, the constructed models were relaxed by steepest-descent energy minimization, followed by equilibration in the NVT ensemble (constant particles, constant volume, and 298 K temperature) for 100 ps, where positional restraints were applied on the CO molecule and the Cu layers with a force constant of 1 eV $Å^{-2}$. For each system, we additionally performed 10 ns NVT simulations at 298 K without any restraints for further equilibration. The temperature was controlled using a velocity-rescale thermostat with a damping constant of 1.0 ps,[234] and periodic boundary conditions were applied in all three directions.

The Vienna ab initio simulation package (VASP ver. 5.4.5)[235] was used for DFT calculations. Electron exchange and correlation were treated within the generalized gradient approximation (GGA)[133] in the form of the PBE functional, including the D3 correction for London Dispersion (van der Waals attraction).[236] The interaction between the ionic core and the valence electrons was described by the projector-augmented wave (PAW) method.[237] The plane-wave basis set was truncated with an energy cutoff of 500 eV and the Brillouin zone was sampled only at gamma point. The electronic structure was minimized until the total energy converges to 10^{-5} eV. Our model systems employed $3\sqrt{2}\times3\sqrt{2}$ Cu(100) with 4 Cu layers with the top layer equilibrated while the atoms of the other 3 layers were fixed. The system explicitly includes 1 and 10 K^+ and $HCOO^-$ pairs with 56 H_2O to mimic 1 M and 7.1 M HCOOK electrolyte, respectively (Figure S4.4). Finite temperature ab-initio molecular dynamics (AIMD) was, then, performed for 20 ps to equilibrate the systems at room temperature. The canonical ensembles (NVT) were equilibrated at 298 K using the Nose-Hoover thermostat[238,239] with 1 fs time step and 40 fs damping parameter.

The implicit electrolyte based on Poisson-Boltzmann model is included using VASPsol[240] to neutralize the system with some net charge (non-zero) for grand canonical dynamics. To prevent the fictitious implicit electrolyte inclusion in explicit solvent regime, we used SOLHYBRID (explicit-implicit solvent model)[241] which employs a modified shape function with parameter of σ_{SH} = 1 Å and α_{SH} = 10 %. This effectively removes the bound charge in the explicit region, as shown in Figure S4.5. For constant potential dynamics with a finite temperature, we used the TPOT routine[241] which guides the electrode to a target potential by varying the number of electrons. The number of electrons was optimized for each ionic step when the potential deviation was larger than a threshold of 0.01 V with a rate limit of 0.2 V/electron. This setup allows the system reach to the target potential within 200 fs (Figure S4.7).

To obtain the kinetic barrier of the CO dimerization step, a metadynamics simulation[242] was performed using the last atomic configuration and velocities from the > 15 ps equilibration at each electrochemical condition. The collective variable (CV) was defined as the atomic C distance of two surface-bound CO (CO*). The initial structures including the atomic configurations and velocities and predictor-corrector coordinates for the four systems, 1 M HCOOK (at 0 V vs RHE), 1 M HCOOK (at -1 V vs RHE), 7.1 M HCOOK (at 0 V vs RHE), 7.1 M HCOOK (at -1 V vs RHE) are provided (Figure S4.8). A time-dependent bias potential was applied with 20 fs time intervals using a Gaussian height (h) of 0.05 eV and width (w) of 0.10 eV. To prevent the two CO* from diffusing away from each other, a single Gaussian hill with h = 4.5 eV and w = 0.2 eV was applied to guide the metadynamics not to exceed the CV = 5 Å as a limit. The dynamics was stopped when the CV exceed the limit, which occurred after 25 ps. The potential energy surface (PES) was calculated by adding the Gaussian potential in a one-dimensional grid ranging from 1 Å to 7 Å with 1000 intervals.

The vibrational density of states (vDoS) was calculated using the 2PT method with the last 10 ps of trajectory from the room-temperature equilibration.[243]

The equilibration procedures in the presence of a single *CO using PBE-D3 leads to the vDoS of CO* stretching mode ranging from 1400~1550 cm^{-1}, which is much lower than experimental values.[244–246] This observation is attributed to the hollow CO preference of the PBE-D3 level of theory[247] due to a substantial π backdonation from Cu d-band to the 2π* orbital of CO, originating from the underestimated LUMO (2π*) level of CO molecule.[248] To address this issue, the rotationally variant DFT+U method has been proposed.[249] But, this method may encounter challenges in accurately describing the frustrated rotational motion of CO* during room temperature equilibration or the energy configuration along CO dimerization, as discussed later in this study. Alternatively, the hybrid functional incorporating a fraction of exact exchange can correctly predict the site preferences by mitigating the self-interaction.[250–252] However, the dynamics with this high level of theory is practically prohibitive even with the hybrid method with a periodic LCAO DFT code. Even so, the current level of theory furnishes valuable insights into surface adsorbate-electrolyte interactions at a computational cost suitable for full explicit dynamics.

4.4 Results and discussion

4.4.1 ECO_2R on Cu GDE with HCOOK electrolytes

Aqueous HCOOK is selected as the electrolyte to understand the role of increasing salt concentration on tuning the product selectivity of CO_2R on Cu electrocatalyst. The electrolyte salt is chosen due to the established role of K^+ in affecting CO_2R and varying the concentration allows for a study on the effect of [K^+] on CO_2R.[27,210,253] Later, we find that the HCOO is additionally an

important component. As the concentration of HCOOK is increased from 1 M to 7.1 M, the concentration of the anions and cations not only increases, but the concentration of water also decreases.[254] The nature of water in the solution changes as high concentrations force coordination of the water to the cations and anions, leaving less "free" water.

We originally hypothesized that the shift in water microenvironment would enable us to change the selectivity of CO_2R products just by changing the salt concentration. To test this hypothesis, electrochemical CO_2 reduction electrolysis is conducted at various HCOOK concentrations in water, up to 9.1 M, and the products are quantified using GC and HPLC. The cathode is a Cu gas diffusion electrode (GDE) fabricated by depositing a 300 nm thick Cu layer on a PTFE gas diffusion layer. Across all concentrations, the products of the reduction include H_2, CH_4, CO, C_2H_4, acetate, 1-propanol, and ethanol, consistent with previous reports of aqueous CO_2R on Cu GDE.[255–257] The quantification of products allows for the determination of the Faradaic efficiency (FE) of each product. Of specific interest here is the ratio of the C_{2+} products, namely C_2H_4, to CO which highlights the ability to form C_2 coupled products over CO. Figure 4.1a shows the ratio of the FE for C_2H_4 to CO as a function of electrolyte concentration and applied potential. As more negative potentials are reached, the amount of C_2H_4 generally increases relative to CO. Interestingly, the ratio of the FE of C_2H_4/CO is also a function of the electrolyte concentration. At the same applied potential with respect to the RHE scale, the FE ratio of C_2H_4/CO increases as the concentration of HCOOK electrolyte increases until 7.1 M HCOOK. Among all screening conditions, the optimal condition that shows highest C_2H_4/CO FE ratio (18.3 ± 4.8) is bias at -1.08 V vs RHE with 7.1 M HCOOK electrolyte. The FE associated with each product and the total current density at these conditions using both a 1 M and 7.1 M electrolyte is shown in Figure 4.1b. In addition to a favorable C_2H_4/CO ratio, the higher concentration electrolyte

also yields higher current densities (206.7 ± 23.5 mA/cm^2) and lower FE for parasitic H_2 evolution. The FE for C_2H_4 at these conditions is 43.0 ± 1.4%. To understand the mechanism that promotes product selectivity towards C_2H_4 over CO, we hereafter compare between 1 M and 7.1 M HCOOK

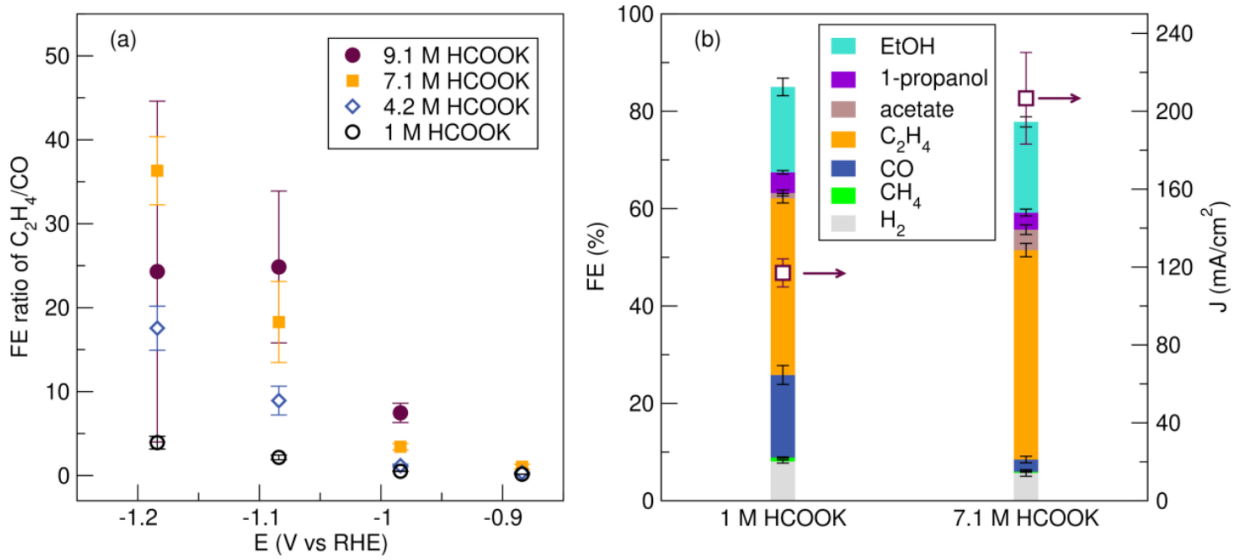

at -1.08 V vs RHE.

Figure 4.1: (a) FE ratio of C_2H_4/CO for electrochemical CO_2R on Cu GDE in 1 M, 4.2 M, 7.1 M, and 9.1 M HCOOK under different applied potentials. (b) Product distribution and total current density of electrochemical CO_2R electrolysis on Cu GDE in 1 M HCOOK and 7.1 M HCOOK at -1.08 V vs RHE.

4.4.2 [CO_2] effect

First, we address the bulk properties that change as the electrolyte concentration increases from 1 M to 7.1 M HCOOK and attempt to vary these properties to determine their effect on the C_2H_4/CO ratio. As the supporting electrolyte concentration increases, both the solubility of CO_2 and the mass transport of CO_2 will be affected, which could explain the C_2H_4/CO ratio shift.[210,258]

First, the solubility of CO_2 is measured in 1 M and 7.1 M HCOOK aqueous solutions by recording the asymmetric stretch mode of CO_2 at 2343 cm^{-1} using attenuated total reflectance –

infrared spectroscopy (ATR-IR). The peak area in these electrolytes shown in Figure S4.1 is compared to CO_2 saturated DI water to determine the amount of dissolved CO_2. The CO_2 solubility of 7.1 M HCOOK is determined to be 18 ± 1 mmol/L, while the CO_2 solubility for 1 M HCOOK is 36 ± 2 mmol/L. Lower CO_2 solubility could lead to less local [CO_2] on Cu during electrolysis which would limit the turnover rate of CO_2R and enhance HER. However, the lower CO_2 solubility of 7.1 M HCOOK results in neither lower CO_2R FE nor lower total current density. In fact, recent studies show that slightly lower CO_2 concentrations at GDE can yield higher FE for C_{2+} products.[259–262] We note, however, that it is difficult to correlate the solubility of a reactant to its reactivity at a GDE electrode.

To further probe the effect of [CO_2], the partial pressure of CO_2 delivered to the Cu GDE is tuned by mixing CO_2 and Ar at different ratios at -1.08 V vs RHE. The partial current density associated with H_2, CO, C_2H_4 is plotted vs. the relative [CO_2] in the gas stream in 1 M vs. 7.1 M HCOOK in Figure 4.2a and b, respectively. For both 1 M and 7.1 M HCOOK, as the ratio of CO_2 in the CO_2/Ar mixture increases from 5% to 100%, the partial current density of C_2H_4 and CO increases while the H_2 slightly decreases. Notably, in the 7.1 M HCOOK electrolyte, the partial current density of C_2H_4 increases much more than in the 1 M electrolyte. To gain insight into the selectivity of C_2H_4 vs. CO, the FE associated with each major product and the FE ratio is potted vs. [CO_2] in the gas stream in the 1 M and 7.1 M HCOOK electrolyte in Figure 4.2c and d, respectively. Above 25% CO_2, the FE of C_2H_4 is nearly constant while the FE of H_2 decreases in both electrolytes. The FE for CO in the 1 M electrolyte shows a maximum FE at 75% [CO_2]. The turning point at 75 % CO_2 may be due to the coverage of intermediates, the mass transport, and the competition between aqueous CO_2, $*CO_2^-$ and *CO.[259–261] Conversely, in the FE of CO trends similarly in the 7.1 M electrolyte, but the magnitude of the FE compared to the FE of C_2H_4 remains

very low. These factors result in a much higher FE ratio of C_2H_4/CO in the 7.1 M HCOOK electrolyte compared to the 1 M. The FE ratio of C_2H_4/CO generally decreases as the [CO_2] in the gas stream increases.

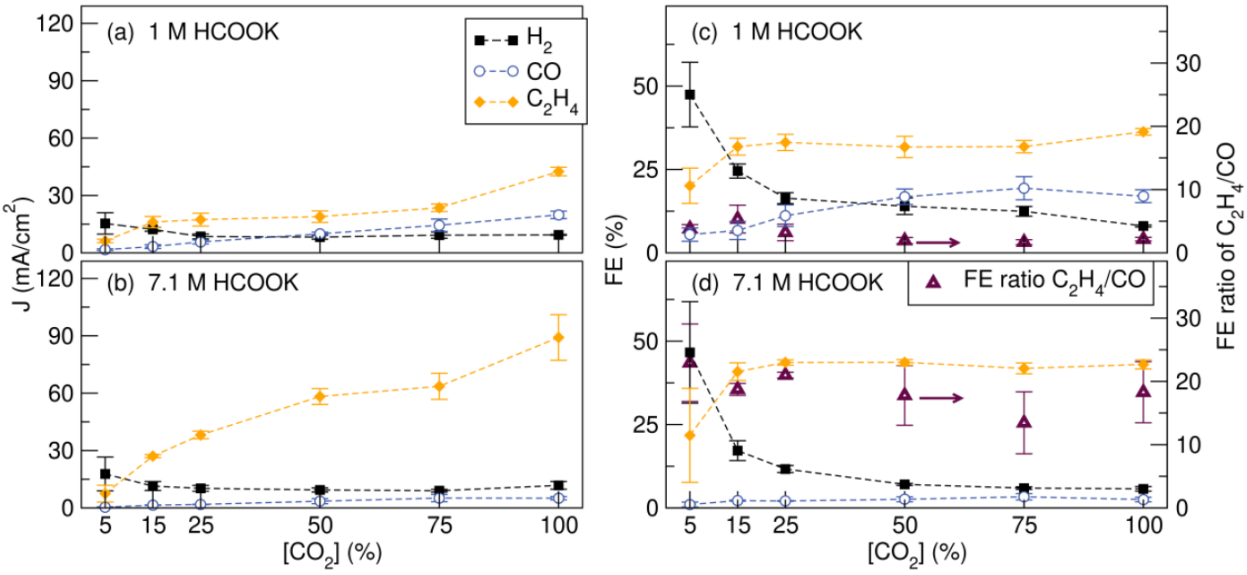

Figure 4.2: Partial current density of H_2, CO, and C_2H_4 obtained from CO_2R on a Cu GDE as a function of the ratio of CO_2 in CO_2/Ar mixture in the (a) 1 M HCOOK and (b) 7.1 M HCOOK electrolyte at -1.08 V vs RHE. The partial current density of H_2, CO, C_2H_4, and the FE ratio of C_2H_4/CO obtained from CO_2R on Cu GDE in (c) 1 M HCOOK and (d) 7.1 M HCOOK at -1.08 V vs RHE as a function of the ratio of CO_2 in CO_2/Ar mixture.

The FE ratio of C_2H_4/CO in 7.1 M HCOOK at all the [CO_2] are at least 3 times higher than the highest value measured in the 1 M HCOOK electrolyte. The highest partial current for C_2H_4 in 1 M HCOOK is reached at 100 % CO_2, which is similar to the partial current for C_2H_4 in 7.1 M HCOOK at only 25% [CO_2]. Thus, the reactivity of CO_2 is not dependent only on the solubility of CO_2 in the electrolyte at a GDE since the 7.1 M electrolyte has a 50% lower solubility for CO_2. The difference of CO_2 solubility between 1 M and 7.1 M HCOOK cannot explain the origin of the increased C_2H_4/CO FE ratio of 7.1 M HCOOK.

4.4.3 pH effect

Increasing the concentration of HCOOK electrolytes from 1 M to 7.1 M also increases the bulk pH. Though pH is difficult to measure in these high concentration electrolytes, especially using a pH probe, both a pH probe and pH paper suggest that the pH of 7.1 M HCOOK is approximately 9, which is higher than 1 M HCOOK (pH = 8). The change in bulk pH may change the product selectivity, as nearly all CO_2R products require proton transfers in their generation pathway, and the pH dependent carbonate-bicarbonate equilibrium also affects the local [CO_2]. A higher pH at the electrode surface is known to cause higher yields of C_2 products in CO_2R on Cu electrodes.[7,212,263,264] The current understanding of the CO_2R mechanism suggests that the rate determining step (RDS) for the C_2 products is C-C bond formation from *CO-*CO or *CO-*COH.[265–270] Though the C-C coupling process is a chemical reaction step which is pH independent, competing reaction pathways like the formation of CH_4 do involve proton transfer and are pH dependent. Higher pH inhibits CH_4 formation, which likely affects the *CO/*COH and possibly other surface species to indirectly promote C-C coupling.[271–273] In the system studied here, higher bulk pH of HCOOK could potentially be a key factor which determines the C_2H_4/CO FE ratio.

To understand the effect of the bulk pH, concentrated KOH (1 mol/L) is titrated into 1 M HCOOK to increase the pH to 9. Electrolysis experiments under the same conditions are conducted using 1 M HCOOK + KOH (pH = 9). Compared to 1 M HCOOK, the total current density is almost the same: 117.0 ± 10.1 mA/cm^2 for 1 M HCOOK + KOH (pH = 9) and 117 ± 7.2 mA/cm^2 for 1 M HCOOK. By increasing the bulk pH of 1 M HCOOK, the FE of C_2H_4 and the FE ratio of C_2H_4/CO only slightly increase from 36.3 ± 1.0 % and 2.2 ± 0.3 to 37.1 ± 1.7 % and 2.4 ± 0.2, respectively (Figure S4.2). These values are lower than that measured in the 7.1 M HCOOK, demonstrating

that the difference of the bulk pH between 1 M and 7.1 M HCOOK is not the key factor that controls the product selection profile, which is consistent with previous results showing that, under the conditions used in this study, bulk pH is not the key factor controlling the CO_2R reaction at the electrode/electrolyte interface.[274]

Though we can control the bulk pH value, the local pH at the electrode surface is significantly different from the bulk pH under CO_2R condition which will play a more significant role in the product profile. To further investigate the role of local pH, in situ confocal fluorescence microscopy is applied to measure the local/surface pH on a Cu GDE under electrolysis conditions.[275–277] By scanning the Z direction within a range of 60 μm of the GDE-electrolyte surface, the approximate location of the electrode-electrolyte interface can be determined. Then, the pH is measured at this location to yield a time dependent pH profile during the first 5 minutes of electrolysis in 1 M HCOOK and 7.1 M HCOOK at -1.08 V vs RHE. Both the pH and the current density during electrolysis are shown in Figure S4.3. Both electrolytes stabilize to a high surface pH, though the 7.1 M HCOOK yields a slightly higher local pH, which could cause shifts in product profiles. However, further work is required to accurately correlate the surface pH measured here with the local pH in the electrochemical double layer to elucidate its impact on product distribution.

4.4.4 Cation Effect

Besides local pH, the choice of electrolyte can also affect the microenvironment of the reaction sites. According to previous experimental and simulation studies, the major impacts of alkali cation can be described as: (1) stabilizing the reaction intermediates, (2) increasing the electric field in electrochemical double layer and (3) acting as a pH buffer agent at the electrode surface.[278–280] Cations that yield higher C_2 products trend as $Cs^+ > K^+ > Na^+ > Li^+$. Thus, K^+ is

suggested to promote C_2 products.[27,210,253] To determine if excess K^+ can account for the product selectivity shift, we select 7.1 M HCOONa electrolyte as a control. Compared to 7.1 M HCOOK, 7.1 M HCOONa decreases the total current density from 206.7 ± 23.5 mA/cm^2 to 56.2 ± 7.3 mA/cm^2 (Figure 4.3). Thus, the partial current density associated with each product also decreases

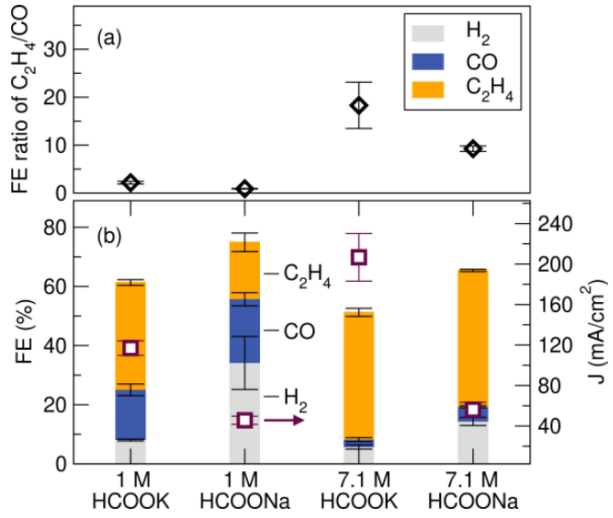

Figure 4.3: (a) FE ratio of C_2H_4/CO and (b) FE of H_2, CO, and C_2H_4 with the total current density obtained from CO_2R on Cu GDE in 1 M HCOOK, 1 M HCOONa, 7.1 M HCOOK, and 7.1 M HCOONa at -1.08 V vs RHE.

significantly. The FE of C_2H_4, CO, and H_2, however, increase in 7.1 M HCOONa electrolyte, but the FE ratio of C_2H_4/CO decreases by nearly two times. The lower current density along with the lower C_2H_4/CO FE ratio in 7.1 M HCOONa suggests that replacing K^+ with Na^+ inhibits the C-C coupling.

To highlight the effect of K^+ vs. Na^+, we compare the electrolysis results in 1 M HCOOK vs. 1 M HCOONa. Under the same conditions, 1 M HCOONa on Cu GDE dramatically promotes HER relative to the 1 M HCOOK, resulting in higher FE and partial current density for H_2. The total partial current density of C_2H_4 and CO drops by ~44 mA/cm^2 compared to the 1 M HCOOK.

Meanwhile, both the FE of C_2H_4 and the FE ratio of C_2H_4/CO decrease. These results suggest that K^+ plays an essential role in promoting the conversion of *CO to C_2H_4.

To understand whether the higher C_2H_4/CO selectivity in the HCOOK electrolytes can be attributed to the increased concentration of K^+, AIMD simulations are conducted to examine the interaction between *CO and K^+, followed by the impact of K^+ on *CO dimerization. First, the equilibrium configuration of the electrolyte-electrode interface is established. The Cu(100)/electrolyte system is equilibrated for 10 ns at 298 K after minimization through CHARMM FF (Figure S4.4). Along the 10 ns trajectory, four snapshots for 7.1 M HCOOK electrolyte system are taken. Those systems are further equilibrated for at least 20 ps with AIMD to get equilibrated potential energies (Figure S4.4). Then, to investigate the influence of K^+ on CO*, four different ensembles of the Cu(100)/7.1 M HCOOK electrolyte system in the presence of *CO are equilibrated (Figure S4.5 and S4.6) and the average energy over the last 10 ps is calculated. Figure 4.4b and Table S1 illustrate the relative energies with respect to the corresponding average distance between the oxygen of *CO and K^+. As the distance between *CO and K^+ decreases, the energy also decreases, indicating a significant stabilization of *CO in the presence of adjacent K^+. The explicit interaction results in a system stabilization of 0.5 eV, suggesting that a high molarity of K^+ could lead to increased coverage of *CO or may enhance the conversion of CO_2 to CO.

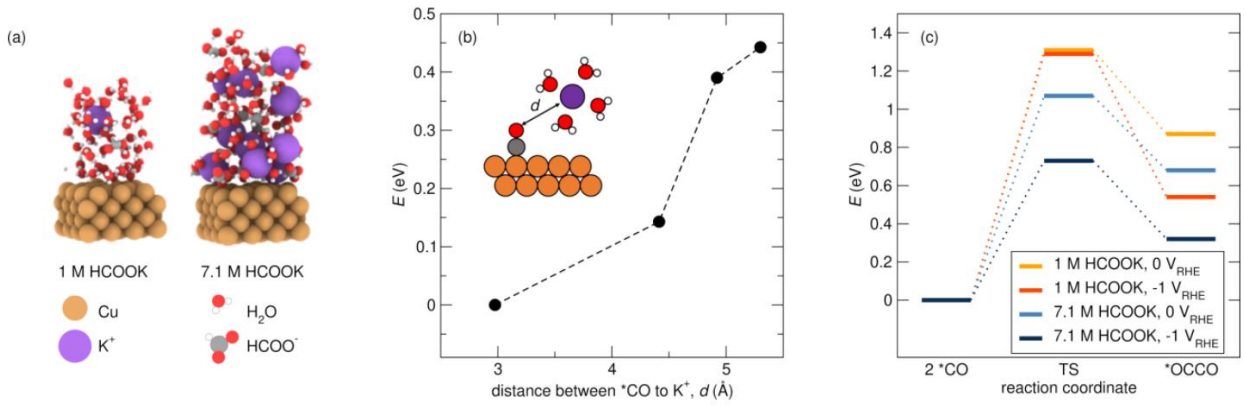

Figure 4.4: (a) Atomic representation of model systems including 1.0 M and 7.1 M HCOOK with Cu electrode. (b) Relative energies with respect to the average distance between CO* and K^+ for 7.1 M HCOOK/Cu. (c) Energy landscape for CO dimerization under different electrochemical conditions: 1 M / 7.1 M HCOOK at 0 V / -1 V vs RHE.

Previous work suggests that the CO binding must be optimal, not too strong or too weak, for C_{2+} product formation.[196] If *CO binds too weakly, the gas phase CO or formic acid (HCOOH) would be produced as a major product. Conversely, if it binds too strongly, the catalytic surface would be poisoned by *CO. To investigate whether the stabilization of *CO by K^+ leads to CO poisoning or facilitates further *CO-*CO coupling, we conduct metadynamics at room temperature for the CO dimerization step using grand canonical AIMD at fixed potentials of 0 V and -1 V vs RHE in the two different electrolyte concentrations. We construct a potential energy surface (PES) along the distance between two carbon atoms as a collective variable (CV). The time evolution of the CV and the obtained PES are displayed in Figure S4.8 and Figure 4.4c, respectively, and Table S2 summarizes those results. The reaction free energy of *CO dimerization in 1 M HCOOK can be reduced from 0.87 eV to 0.54 eV by increasing cathodic bias from 0 V to -1 V vs RHE. In 7.1 M HCOOK electrolyte, *CO dimerization is more favorable, decreasing from 0.68 eV to 0.32 eV with the same voltage drop. The corresponding kinetic barrier is also reduced

from 1.07 eV to 0.73 eV. Therefore, while a 1 V voltage drop increases the driving force for C-C coupling by 0.3 eV, the high molarity condition further facilitates it by an additional 0.2 eV.

The charge density difference plot (Figure S4.9) of the CO* dimer state (OCCO*) with and without the adjacent K^+ (dCO-K^+ = 3.1 Å) shows a strong electronic effect of K^+ for C-C coupling. It shows that the interfacial cation induces the charge (e^-) accumulation on C-C σ bond while it depletes in C-O σ orbital. These effects should reduce the activation barrier for C-C coupling. We also observe charge accumulation on the O pz orbital of CO* adjacent to the K^+, which might further facilitate its protonation to form OCCOH* the next step along the reduction pathway for forming the C2 products.[281] Our findings suggest that the higher K^+ concentration both stabilizes CO* and promotes CO dimerization.

4.4.5 Anion Effects

In addition, the anion can play a role in determining the CO_2R product profile due to specific adsorption on the electrode surface which can induce reconstruction (e.g., halide ion),[216,282,283] shifted buffer capacity that tunes local pH (like HCO_3^-, HPO_4^{2-}),[195,258,262,274] or interaction with surface adsorbed reaction intermediates.[215,216,284,285] To determine if the HCOO in particular has an effect on product selectivity in the 7.1 M electrolyte, first we characterize the surface of Cu GDE before and after electrolysis to evaluate the potential of anion adsorption and its impact on the Cu surface (Figure S4.10). The two regions of the XPS that are useful for characterizing HCOO are the O 1s and the C 1s regions. In the O 1s region, environments associated with both hydroxide and oxide are present due to the oxidized $Cu(OH)_2$ and Cu_2O/CuO species on the Cu electrode.[286–289] The Cu 2p region suggests the oxidized Cu is mostly Cu(I) due to the lack of satellite peaks characteristic of Cu(II).[287,289] Due to the inevitable air exposure for Cu GDE samples before *ex situ* XPS measurement, accurate quantification for the ratio of different

Cu species is not possible. Nonetheless, it is important to note that there is no significant difference in Cu oxidation state and Cu species on the GDE surface after electrolysis in 1 M HCOOK and 7.1 M HCOOK. Therefore, the shift in product profile is likely not due to the difference in the composition of the Cu GDE surface.

Although no anion adsorption is found via *ex situ* XPS, *in situ* HCOO adsorption under electrolysis condition is still possible. Therefore, we conduct *ex situ* X-ray diffraction (XRD) and scanning electron microscopy (SEM) to evaluate the potential Cu surface reconstruction. *Ex situ* XRD of the Cu GDE before and after electrolysis in 1 M and 7.1 M HCOOK shows no changes (Figure S4.11). However, though Cu reconstruction can penetrate 10-100 nm into the surface and the Cu layer on our GDE is only 300 nm thick, it could be that XRD is not sensitive enough to the surface to observe the reconstruction as it examines the entire 300 nm Cu film.[290–293] In fact, *ex situ* SEM shows that the morphology of the Cu GDE changes after electrolysis in both 1 M HCOOK and 7.1 M HCOOK, which may affect C_{2+} product yield (Figure S4.12).[290,292–295] The crystallite grains on the Cu surface become less defined after electrolysis in both electrolytes, however, after electrolysis in the 7.1 M HCOOK, the surface has smaller features that are likely small Cu crystallites that could introduce new active sites unique to the 7.1 M electrolyte. This Cu reconstruction could affect the product selectivity. Notably, the morphological change does not increase the electrochemically active surface area (ECSA) after electrolysis in both 1 M and 7.1 M HCOOK (Table S3). ECSA has been shown to shift product selectivity.[290,295] Characterization of Cu GDEs under operando condition could illustrate the role morphological evolution on product selectivity but it is out of scope of this study.

To further explore the role of $HCOO^-$, control CO_2R electrolysis experiments are conducted with potassium acetate (KOAc), another type of K^+ based high concentration electrolyte with

acetate as the anion. Although a mixture of $HCOO^-$/HCOOH or OAc^-/HOAc can be buffer electrolytes, both HCOOK and KOAc electrolytes should not have strong buffer capacity due to the limited amount of conjugated acid in both electrolytes. Therefore, KOAc is a reasonable choice to compare with HCOOK to analyze the role of HCOO in CO_2R. The total current density and FE associated with H_2, CO, and C_2H_4 as a result of CO_2R is measured in 1 M KOAc and is compared to 1 M HCOOK in Figure 4.5. Compared to 1 M HCOOK, no significant change in total current density or product distribution is observed with 1 M KOAc on Cu GDE, suggesting that the CO_2R

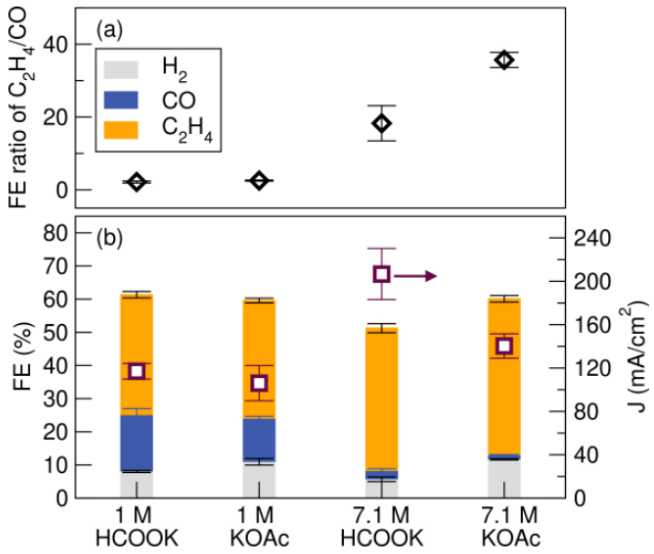

Figure 4.5: (a) FE ratio of C_2H_4/CO and (b) FE as well as the partial current density of H_2, CO and C_2H_4 obtained from CO_2R on Cu GDE in 1 M HCOOK, 1 M KOAc, 7.1 M HCOOK, and 7.1 M KOAc at -1.08 V vs RHE.

pathway is similar in both HCOO and OAc at low electrolyte concentration. Next, we compare 7.1 M KOAc with 7.1 M HCOOK electrolyte to determine if the difference between 7.1 M OAc vs. 7.1 M HCOO can affect the product distribution. Again, the current density and FE associated with products are shown in Figure 4.5. Compared to 7.1 M HCOOK, running electrolysis with 7.1 M KOAc decreases the total current density from 206.7 ± 23.5 mA/cm^2 to 140.3 ± 11.2 mA/cm^2 and

increases the FE ratio of C_2H_4/CO from 18.3 ± 4.8 to 35.7 ± 2.1. The major difference between 7.1 M HCOOK and 7.1 M KOAc is the choice of anion, and thus this result indicates that the role of anion on the product profile is not negligible. Looking back at the AIMD results, however, we do not observe strong electronic interactions of the anions near the surface and OCCO* (Figure S4.9b). Therefore, we postulate that HCOO in the outer Helmholtz plane (OHP) or diffusion layer might play an important role to modulate the reaction pathway which affects the C_2H_4/CO FE ratio.

4.4.6 Probing reaction intermediates on Cu experimentally

The above results suggest that both bulk electrolyte and electrode-electrolyte interface properties are important to control the product profile, however, all surface characterization we have discussed thus far has been limited to theoretical data. To further explore the Cu/HCOOK interface and adsorbed intermediates during ECO_2R experimentally, in situ electrochemical attenuated total reflection – surface enhanced infrared absorption spectroscopy (ATR-SEIRAS) measurements are performed. This technique can help reveal trends in activity and selectivity of adsorbed electrolyte species in a non-invasive approach.

4.4.6.1 Potential dependent in situ IR

ATR-SEIRAS measurements are limited to the use of a planar (Cu) electrode deposited on an ATR crystal to allow maximum surface enhancement of the IR optical signal. Therefore, it is important to note that the Cu cathode used in the ATR-SEIRAS experiments is in a different architecture than the gas diffusion electrodes used in the above experiments. In particular, the mass transport of CO_2 will be different between the two cells. In the GDE cell, the concentration of CO_2 near the electrode will be much higher as electrolysis proceeds compared to the planar Cu electrode in the ATR-SEIRAS cell, which will quickly consume CO_2 after cathodic bias is applied.

Therefore, we focus on analyzing and interpreting the ATR-SEIRAS results at short time scales after electrolysis starts to simulate the high concentration of CO_2 seen in the GDE experiments while the electrolyte is saturated with CO_2.

To determine the effect of CO_2 consumption on the surface speciation in the ATR-SEIRAS cell, we first observe the spectroscopic signal response as a function of time at a fixed potential bias during CO_2R. ATR-SEIRAS allows for IR vibrational modes associated with only those species at or near the surface of the Cu electrode to be detected. To highlight modes associated with species that arrive to the surface as a result of the applied potential, the initial IR spectrum measured at 0.2 V vs RHE is subtracted from those measured after polarization. The difference in the IR spectra are plotted as a function of time after polarization at -0.7 V vs RHE and -1.1 V vs. RHE in the 1 M HCOOK electrolyte in Figure 4.6a and b, respectively. We propose that comparing these two potentials could offer insights on a Cu GDE system since C_2 products are major CO_2R

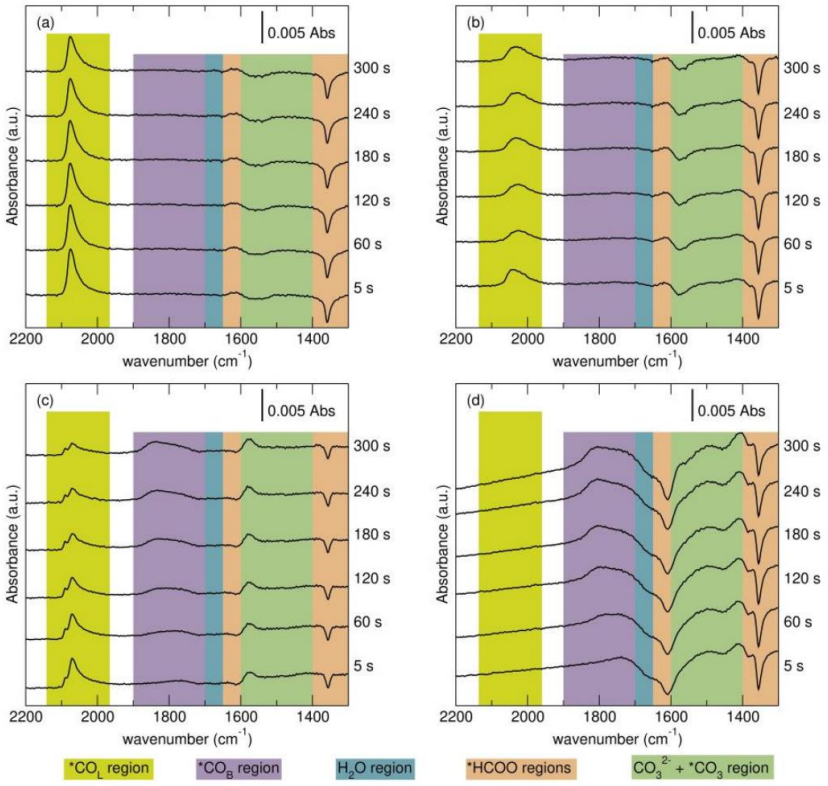

Figure 4.6: Time evolution CO_2RR ATR-SEIRAS experiment at a potential bias of (a) -0.7 V vs RHE, and (b) - 1.1 V vs RHE in 1 M HCOOK and at a potential bias of (c) -0.7 V vs RHE and (d) -1.1 V vs RHE in 7.1 M HCOOK.

products at -1.1 V vs RHE on Cu while C_1 products are dominant at -0.7 V vs RHE. In 1 M HCOOK, a strong positive peak is observed around 2070 cm^{-1}, a region associated with *CO binding atop to a Cu atom to yield a linear *CO, or $*CO_L$. The frequency range suggests that the $*CO_L$ is a mixture of CO adsorbed on an edge site and/or a defect site, which is termed the high frequency band (HFB). The asymmetric peak shape, which results in having a shoulder at a slightly lower frequencies (around 2058 cm^{-1}) suggests an additional type of $*CO_L$ associated with different Cu sites and is thus termed the low frequency band mode (LFB).[244] Because the signal is positive, it indicates that CO arrives at the surface of the electrode following cathodic polarization. No other *CO signals are observed regardless of the applied potential bias. The negative band around 1650 cm^{-1} corresponds to water bending mode.[24,296] The same $*CO_L$ mode appears at -1.1 V vs. RHE, however, the peak at -0.7 V vs RHE is more pronounced than the signal at -1.1 V vs RHE. Further, the $*CO_L$ observed at -1.1 V is comprised mainly of the lower frequency $*CO_L$, namely LFB. The ratio of the HFB/LFB as a function of time is discussed in more detail in the SI (Figure S13). In addition, negative bands are observed within 1420-1590 cm^{-1} at both potentials suggesting desorption of initially adsorbed species. The negative peak around 1380 cm^{-1} is assigned as *HCOO in a bidentate orientation since it is absent in a control IR measurement in 0.1 M $KHCO_3$ (Figure S4.14). In addition, a small peak appears around 1408 cm^{-1} only at -1.1 V vs RHE which we assigned to solution phase carbonate (Figure S4.15) species. This is most likely due to the increase in local pH under reducing conditions which results in a shift in equilibrium between bicarbonate and carbonate.[7] Finally, unlike the monotonic decay in $*CO_L$ signal response

at -0.7 V vs RHE, polarization at -1.1 V vs. RHE causes the $*CO_L$ peak to first decay over 60 seconds followed by a monotonic slow growth.

Different species and trends are observed in the time evolution ATR-SEIRAS in 7.1 M HCOOK during CO_2R (Figure 4.6c and d). First, a new mode is observed between 1790-1850 cm^{-1} associated with *CO between two Cu atoms, termed the bridge bound *CO or $*CO_B$.[244,297,298] The intensity of the $*CO_B$ grows regardless of potential bias with a faster $*CO_B$ accumulation rate at -1.1 V vs RHE. Similar to 1 M HCOOK, at -0.7 V vs RHE there is a monotonic decay in $*CO_L$. But, in this case, three $*CO_L$ peaks are apparent, with an additional peak at around 2089 cm^{-1} on top of the HFB and LFB. Due to its higher vibrational frequency, this feature most likely results from an adsorbed CO on an additional binding site involving *CO that is bound more weakly to a less coordinated surface site. This adsorbed CO species might exist in 1 M HCOOK but could be hindered by the HFB CO peak. We suspect that the slightly lower value for HFB CO in 7.1 relative to 1 M HCOOK is the result of slightly higher local pH due to higher current density at the same potential bias. It has been proposed by Rebstock et al. that this CO peak is related to the active site for CO_2R to CO.[299] However, their work was performed on Au in 0.1 M bicarbonate solution, and therefore the results might not be translatable to our system so further analysis is needed to compare the different effects of CO binding sites on product selectivity across different catalysts. Moreover, $*CO_L$ is not detected at -1.1 V vs RHE. In addition, an increase in solution phase carbonate (1408 cm^{-1}) and the loss of the water bending mode is recorded at -1.1 V vs RHE. Finally, a growth in the band around 1580 cm^{-1} at -0.7 V vs RHE likely originates from the adsorption of formate, bi/carbonate or CO_2R related species.

The ATR-SEIRAS data clearly show that *CO speciates differently in 1 M vs. 7.1 M HCOOK. In an attempt to directly correlate CO_2R products to the *CO species, we measure the

product distribution on a Cu plate electrode in an H-type electrochemical cell were conducted due to its similarity with the *in-situ* IR electrochemical cell. For both electrolytes, the total FE for CO_2R products is higher at -1.1 V vs RHE, but the major product is H_2 (Table S4). H_2 is the only significant product in both electrolytes at less negative potential (-0.7 V vs RHE), as well. Therefore, the formation of any *CO reduction product is significantly limited in both the 1 M and the 7.1 M HCOOK electrolytes, making it difficult to correlate surface speciation of *CO to product profiles directly. The 7.1 M HCOOK is particularly hindered by mass transport limitations, as it is more viscous than the 1 M electrolyte, leading to very small quantities of CH_4 and CO product formation in the H-cell. The 1 M electrolyte shows slightly more CH_4, CO, and some C_2H_4, but again the quantities are very small. According to Rebstock et al. when probing CO_2R on Au in 0.1 $MHCO_3$, the highest frequency $*CO_L$ peak was proposed to be related to the active site for CO formation.[299] However, due to the difference between the systems working with Cu in more concentrated solutions using HCOOK as a supporting electrolyte and due to the low CO_2R products according to the H-cell electrolysis, this might not be the case in our system so further investigation is needed. Considering the HFB/LFB ratio, according to Si Young Lee et al. HFB is proposed to be the active species for CO_2R to ethylene.[300] However, according to their results using Raman spectroscopy, there is an increase in HFB signal intensity at -1.1 V vs RHE. In addition, their work was done in 0.1 M $MHCO_3$ which is different than the system probed in our current study.

While the product selectivity profile is different in the GDE and H-cell electrolysis measurements, we attempted to simulate conditions seen in the GDE for further ATR-SEIRAS measurements. For example, in a GDE setup, a concentrated stream of CO_2 is constantly provided to the electrolyte and thus the diffusion layer is much thinner during electrolysis.[301] For the ATR-

SEIRAS cell, this condition will be most represented at early time points after starting electrolysis while the electrolyte is saturated with CO_2. Because the time resolution of the ATR-SEIRAS cell is on the order of seconds, we consider the earliest time point of 5 s to be most representative of the highest concentration CO_2 conditions which are closer to the GDE conditions. At moderate potentials (-0.7 V vs. RHE), only $*CO_L$ modes are observed at 1 M HCOOK while both $*CO_L$ and $*CO_B$ modes are observed at 7.1 M HCOOK. If we compare the potential at which C_2 products can form, -1.1 V vs. RHE, only $*CO_L$ modes are observed in the 1 M HCOOK electrolyte and only $*CO_B$ are observed in the 7.1 M HCOOK electrolyte. Previous results showed that the 7.1 M HCOOK electrolyte in the GDE cell has a much higher C_2H_4/CO product selectivity, and we see under similar conditions that $*CO_B$ is the only CO species observed at the Cu surface. Therefore, we suggest that the $*CO_B$ species is an important intermediate to promote C-C coupling reactions to yield C_2H_4. The $*CO_B$ grows fastest at -1.1 V vs RHE in 7.1 M HCOOK and is persistent on the surface (Figure S4.16) which might suggest that CO_B is poisoning the surface. However, the exact role of $*CO_B$ is still under debate.[297,302,303]

4.4.6.2 Mimicking the high current density local environment of a Cu GDE during SEIRAS

To further investigate the effect of *CO binding modes on the CO_2 to C_2H_4 reduction pathways, ATR-SEIRAS was measured under CO reduction conditions at both the as-prepared pH and the KOH adjusted pH (pH~12) for both electrolyte concentrations (Figure S4.17 a-d). CO is used *in lieu* of CO_2 to prevent the formation of carbonate/bicarbonate, which would shift the pH during electrolysis. Increasing the pH of electrolyte offers opportunities to correlate the reaction intermediates measured on Cu at the low current densities achieved in the ATR-SEIRAS batch cell to the ones recorded at the high current density obtained from the electrolysis on GDE. The SEIRAS experiments performed at high pH are meant to mimic the high local pH that develops

during CO_2R on a GDE when it increases current density from 10's to 100's of mA/cm^2. We note that pH 12 is close to the measured surface pH value discussed earlier, which allows us to assume similar local pH and surface adsorbed intermediates species at Cu GDE.

The ATR-SEIRAS spectra under these conditions are plotted as the potential is stepped from 0 V to -1.2 V vs. RHE using the 1 M HCOOK electrolyte at the as-prepared pH, 7.8, and at an adjusted pH of 11.9 in Figure S4.17a and b. As the cathodic bias is increased, a band around ~2000-2100 cm^{-1} corresponding to $*CO_L$[244,304] first appears then diminishes. The peak intensity is maintained to lower potentials in the pH ~7.8 electrolyte compared to the pH ~11.9 electrolyte. The same experiment is repeated in the 7.1 M HCOOK first at its as-prepared pH of ~9 and then at a KOH adjusted pH of ~11.9 (Figure S4.

17c and d). In 7.1 M HCOOK, in addition to a very weak $*CO_L$ peak, the presence of an additional *CO band at lower wavenumbers (1700-1900 cm^{-1}) indicates the formation of $*CO_B$,[244,298] similar to the results from time dependent in situ IR under CO_2 discussed previously. The peak area of $*CO_L$ in 1 M HCOOK is much higher than 7.1 M HCOOK. In both electrolytes, the $*CO_L$ peak emerges at around -0.1 V then diminishes at a more negative potential: -0.9 V for 1 M HCOOK and -0.5 V for 7.1 M HCOOK. The $*CO_B$ peak is observed only in 7.1 M HCOOK where it grows continuously as the applied potential is sweeping catholically with a stark shifting effect. By increasing the pH, the adsorbed CO intensity in both 1 M and 7.1 M HCOOK at native pH is higher than the related *CO peaks in the corresponding KOH adjusted electrolytes at pH 11.9. Because $*CO_B$ is not observed in the 1 M electrolyte at either pH and is observed in the 7.1 M electrolytes at both pHs, we can conclude that the emergence of $*CO_B$ in 7.1 M HCOOK is due to the increased HCOOK concentration and not to the higher pH caused by higher current densities.

It is important to note that the supporting electrolyte concentration does shift the *CO speciation. To test the hypothesis of the supporting electrolyte concentration being a key parameter for CO binding sites distribution during CO_2RR, we measured the ATR-SEIRAS spectral response to an increase in HCOOK concentration under fixed potential bias (Figure S4.18). In doing so, we observe a monotonic displacement between $*CO_L$ and $*CO_B$ as a function of the supporting electrolyte concentration. These results further affirm that the electrolyte concentration plays a major role in the binding sites distribution of adsorbed CO intermediates. Considering the OH stretching region (3000-3700 cm^{-1}) (Figure S4.16.b), we observe a transition from an increase in all water species (1 to 4 hydrogen bonding water species and K^+-H2O)[305,306] as well as non-hydrogen bond OH,[307] to a loss in all water species other than "Ice like" (4 hydrogen bonding water species) including non-hydrogen bond OH.

To correlate the surface speciation found in the ATR-SEIRAS measurements to the associated product distribution under similar conditions, the product distribution was measured for a planar Cu electrode during CO reduction in an H-cell. The results are tabulated in Table S5. Similar to the results of CO_2R on the planar Cu electrode discussed above, the major product in both electrolyte concentrations at both pHs is again H_2. At low pH conditions, the FE of C_2H_4 in 1 M HCOOK (pH 8) vs. that in 7.1 M HCOOK (pH 9) are very similar, 2.0 ± 0.2 % and 0.94 ± 0.06 %, respectively. The much lower peak area of $*CO_L$ in 7.1 M HCOOK compared to 1 M HCOOK is not correlated to lower yields of C_2H_4. Therefore, even with CO as a C source, we cannot directly corelate the peak area of $*CO_L$ or $*CO_B$ to CO_2R product distribution. At the higher pH condition (pH 12), the FE of C_2H_4 for both electrolyte concentrations is negligible (< 0.2 %), which is not in line with the product distribution measured with the GDE. Thus, even with a high pH that might be correlated with the large current densities measured on a GDE, the low solubility of CO in

aqueous electrolyte still limits the mass transport of CO, promoting HER instead. Thus, we cannot directly correlate the *CO speciation on the Cu planar electrode with the product profiles of a Cu GDE.

4.4.6.3 pH and cation concentration effects on adsorbed CO Stark tuning

Observing the change in vibrational frequency for the C-O stretching mode of *CO could shed insights on the electric field strength in the outer Helmholtz plane (OHP) within the electric double layer which is often referred to as stark tuning.[278,308] It has been previously shown that the electrolyte cation identity (i.e. valence charge and hydration shell radius) affects the CO_L Stark tuning via tuning the width of the OHP.[278,309] In addition, shifts in the vibrational frequency can also result from changes in *CO surface concentrations via dipole-dipole interactions and chemical shifts.[244,310,311] Attempts to deconvolute the apparent Stark tuning have been previously made,[312] but we are unable to isolate the contribution from the applied external electric field. Therefore, our discussion will focus only on the apparent Stark tuning. In addition, this discussion assumes no change in the most stable orientation of *CO species under the effect of applied potential bias, bulk pH value, electrolyte concentration, or changes in surface coverage.

In this work, we sample at least three data points to allow error statistics and reported the apparent Stark tuning using a linear fit (Figure S4.17e-h). In doing so, we find that within each experiment, the Stark tuning increases with an increase in binding energy to the surface, with the largest shift observed for the $*CO_B$ species, followed by the low frequency band (LFB) of $*CO_L$, and then the high frequency band (HFB) of $*CO_L$, (HFB-$*CO_L$ < LFB-$*CO_L$ < $*CO_B$). This is in line with the argument that enhanced π back donation accompanies with an increase in Cu-C coordination, in particular when comparing between $*CO_L$ and $*CO_B$ species where a higher overlap between the frontier orbitals of Cu and CO is suggested.[313–315] Interestingly, apart from a

single data point in 1 M HCOOK at pH 11.9 (Figure S4.17f), HFB-CO_L shows a lower population than LFB-*CO_L on the surface. Unlike CO_L, in 7.1 M HCOOK, *CO_B's apparent Stark tuning remains consistent regardless of the bulk pH value (Figure S4.17g,h). Finally, the non-linearity in Stark tuning, and the Stark tuning values for *CO_L between 1 M HCOOK and 7.1 M HCOOK suggest that concentration effects play a major role in the apparent Stark tuning.

As mentioned earlier, due to the concentration effect on the apparent Stark tuning, and since *CO_L is undetectable at higher overpotentials, we are unable to determine the external electric field component effect as a function of K^+ concentration. By comparing apparent Stark tuning of *CO_L within the potential range of (-0.2 V and -0.5 V vs RHE), it appears that there is an increase in the apparent Stark tuning as a function of bulk pH. In addition, the fact that we observed similar apparent Stark tuning in both 1 M HCOOK at pH 11.9 and 7.1 M HCOOK at pH 9.0, while considering an increase in the Stark tuning due to an increase in pH,[316] we suspect that an increase in K^+ concentration from 1 M to 7.1 M also increases the Stark tuning. The lack of linear Stark tunning region for *CO_L in 7.1 M HCOOK at pH 11.9 limits the opportunity to discuss its effect. Nonetheless, based on our results, we propose that both an increase in bulk pH, as well as K^+ concentration increases the apparent Stark tuning, resulting in the following order: 1 M HCOOK (pH 7.8) < 1 M HCOOK (pH 11.9) < 7.1 M HCOOK (pH 9.0) < 7.1M HCOOK (pH 11.9). Previously, it was proposed that when comparing different cations with different identity, an increase in Stark tuning results in an increase in CO_2R activity.[278,309] However, as mentioned above, it has been proposed by Lee et al. that HFB-*CO_L is a more active species for CO_2R to ethylene, while LFB-*CO_L is a more active site for CO formation.[300] They also demonstrated that HFB-*CO_L has a lower Stark tuning rate than LFB-*CO_L which is in agreement with our results discussed above (Figure S4.17e-g). In addition, it has been shown by Rebstock et al. on Au for

CO_2R to CO that the active site demonstrates an inverse Stark tuning.[299] However, further analysis at the potential range of interest is required since our analysis is done at lower overpotentials than the electrolysis results. In addition, to our current knowledge, the effect of highly concentrated electrolytes has not been explored previously.

4.4.6.4 Attempts to bridge the gap between in situ IR measurements and GDE electrolysis

Although the discrepancy observed between the cells used in in-situ ATR-SEIRAS and GDE electrolysis cannot be fully resolved, the ATR-SEIRAS measurements still provide valuable information about the *CO binding preference and the properties of $*CO_L$ and $*CO_B$ under different applied potentials, HCOOK concentrations, and bulk pHs. With the results from in-situ IR and electrolysis, we propose potential explanations to bridge the gap between in-situ IR measurements and CO_2R electrolysis product selectivity on Cu GDE.

The preference of $*CO_B$ on Cu in 7.1 M HCOOK, which results in strongly bound *CO on the surface, could be the reason for less free CO release compared to the 1 M HCOOK electrolyte under GDE conditions. In addition, the mass transport of CO_2 could affect the CO binding site distribution. With higher CO_2 supply rate at the Cu GDE surface, we can assume that more *CO forms on Cu vs. the condition in the H cell. Higher coverage of *CO (potentially both $*CO_L$ and $*CO_B$) may promote a higher C-C coupling rate and produce more C_2H_4. To test this hypothesis, we conducted CO_2R ATR-SEIRAS experiments by sparging the system with a nitrogen balanced 5% CO_2 stream for comparison to the 100% CO_2 stream used in the previous experiments under similar electrolyte concentrations (Figure S4.19). First, we observe that when sparging the electrolyte with 5% CO_2, the modes corresponding to *CO features are less intense. This could be the result of lower CO_2 availability. Importantly, while no $*CO_L$ is observed in 7.1 M HCOOK under 5 % CO_2 polarized between 0.2 to -1.2 V vs. RHE, $*CO_L$ is found on the Cu surface in 7.1

M HCOOK when switching the gas stream to 100 % CO_2 at moderate potentials, around -0.5 to -0.7 V vs. RHE. This suggests that at higher CO_2 mass transport rates, *CO_L is present and measurable on Cu in 7.1 M HCOOK even with the clear preference for the *CO_B. Although we do not have direct observation of the *CO binding mode on Cu GDE in this study, the higher CO_2 mass transport in the GDE likely results in more *CO as *CO_L compared to the H cell condition in 7.1 M HCOOK. The potential coupling between *CO_L with *CO_L or *CO_B could facilitate the conversion of *CO to C_2H_4. The overall results can lead to a higher FE ratio of C_2H_4/CO in 7.1 M HCOOK than 1 M HCOOK on the Cu GDE.

4.5 Conclusion

Herein, we find improved selectivity towards C_2H_4 over CO by simply increasing the electrolyte concentration from 1 M to 7.1 M HCOOK on a Cu GDE cathode. We find that both bulk properties of the electrolyte and shifts in speciation at the electrode-electrolyte interface all contribute to the shift in product selectivity. For bulk properties, experimental and simulation results show CO_2 solubility, bulk pH, and the choice and concentration of cation and anion can all change product selectivity. To probe the electrode/electrolyte microenvironment in an attempt to elucidate the CO_2R reaction pathway at the interface, simulations with explicit solvent provide insight into the effect of electrolyte concentration on the *CO and the C-C coupling reaction. Higher HCOOK concentrations allow for more stabilized *CO on Cu likely due to interactions with K^+ and leads to lowered reaction barriers for C-C coupling. Experimental characterization of surface species conducted with in situ ATR-SEIRAS reveals that *CO prefers *CO_B sites in the 7.1 M HCOOK vs. the preference for *CO_L sites in the 1 M HCOOK. However, the differences in cell configurations make it difficult to directly correlate the surface adsorbed species to the product profiles. *CO_B may act to suppress the release of CO and promote C_2H_4 formation, but more work

needs to be done to prove this correlation. However, *CO_B is certainly the most prominent *CO species in the high concentration electrolyte which strongly suggests that it is not inactive during CO_2R. Thus, this system proves that the intertwined and dynamic effects of various properties ranging from the bulk to the interface should be thoroughly investigated to try to understand CO_2R mechanisms. Although one property could be correlated, it does not mean it is the only property changing to affect a shift in product distribution.

4.6 Supporting Information

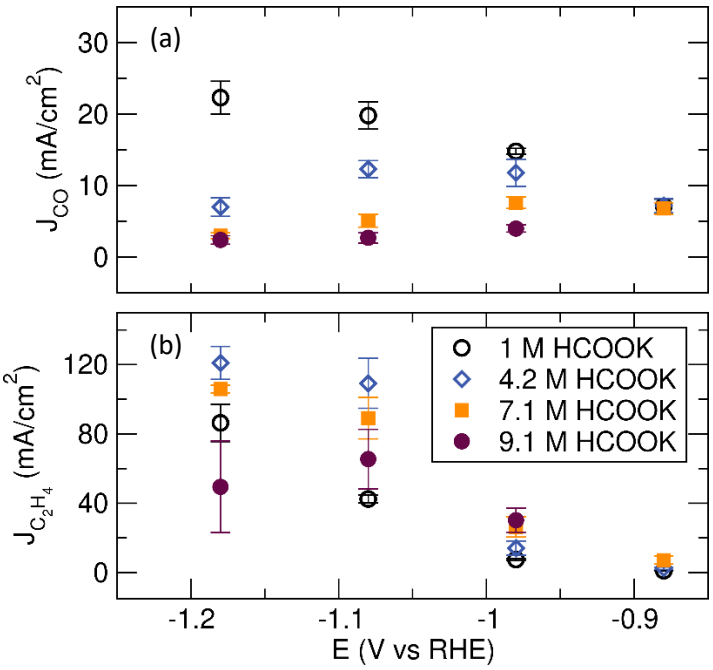

Figure S4.1: The partial current density for (a) CO and (b) C_2H_4 electrochemical CO_2R on Cu GDE in 1 M, 4.2 M, 7.1 M, and 9.1 M HCOOK under different applied potentials.

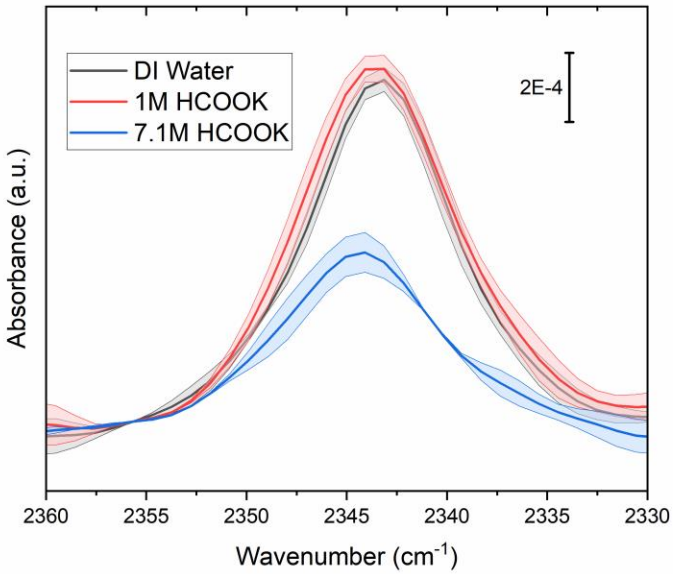

Figure S4.2 Aqueous CO_2 ATR-FTIR spectra for CO_2 saturated deionized water, 1 M HCOOK, and 7.1 M HCOOK.

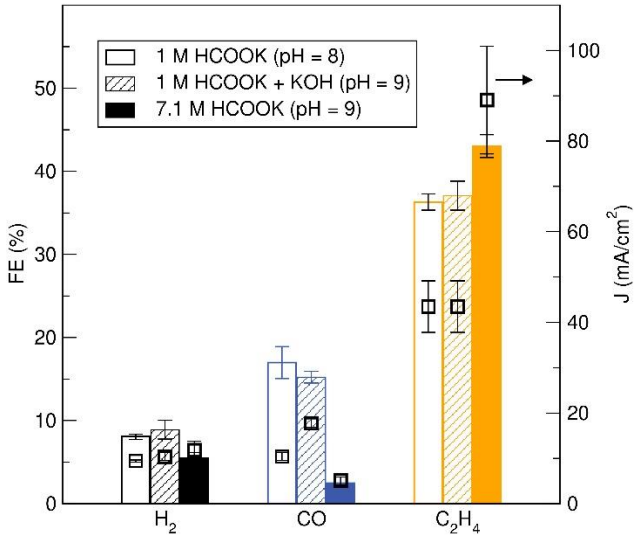

Figure S4.3: FE and partial current for H_2, CO and C_2H_4 produced on Cu GDE in 1 M HCOOK (pH = 8), 1 M HCOOK + KOH (pH = 9) and 7.1 M HCOOK (pH = 9) at -1.08 V vs RHE.

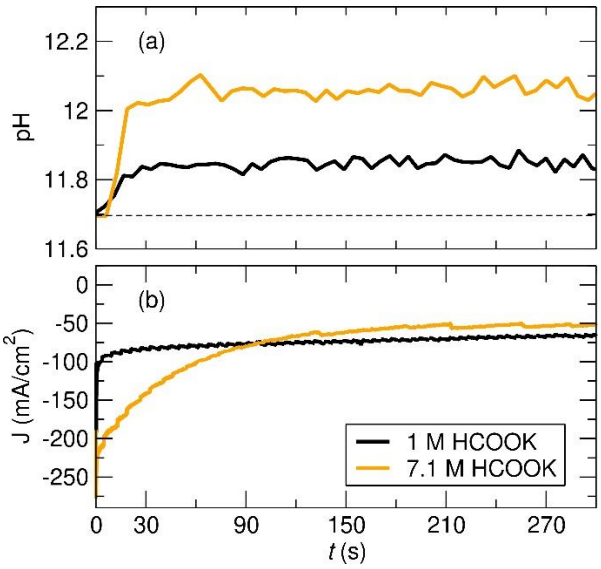

Figure S4.4: (a) pH around the Cu GDE surface and (b) total current density of Cu GDE as a function of time in 1 M HCOOK and 7.1 M HCOOK at -1.08 V vs RHE measured by in situ confocal fluorescence spectroscopy. The pH probe used in the experiments is sensitive to a pH range between 11.7 and 14. We note that the dye used to detect pH cannot measure pH below 11.7.

In both cases, once the negative potential is applied to the Cu GDE, the surface pH increases substantially and stabilizes after the first 30 s. We note that initially, the current density measured in the 7.1 M HCOOK is higher than the 1 M HCOOK, which is consistent with the electrolysis results, but the two electrolytes stabilize to around the same current density after 90 s. The discrepancy observed might be due to the different electrochemical cell setup used for electrolysis vs. confocal fluorescence spectroscopy measurements. In the latter setup, the catholyte is exposed to air and hosts the Pt counter electrode. The decay of current density can also be due to $KHCO_3/K_2CO_3$ salt formation which can cause GDE flooding or Cu electrode deactivation. Although the investigation of the origin of the current drop is still undergoing at this stage, it is important to note that higher local [OH-] is recorded for 7.1 M HCOOK (~10 mM) than 1 M HCOOK (6 mM) at the first 30 s, when the current density matches with the electrolysis experiment. Since we couldn't precisely determine the local pH in the double layer due to the resolution of our technique (~ 1 μm), we can only postulate that the slightly higher local pH on Cu

GDE in 7.1 M HCOOK (pH 12) compared with 1 M HCOOK (pH ~11.8) might lead to a higher FE ratio of C_2H_4/CO. Future work should be done to testify this assumption.

Table S4.1 The potential (*E* vs. SHE) applied for each experiment

E (*V* vs. RHE)	*E* (*V* vs. SHE)			
	1 M HCOOK	4.2 M HCOOK	7.1 M HCOOK	9.1 M HCOOK
-0.7	-1.44	-1.47	-1.5	-1.53
-1.1	-1.54	-1.57	-1.6	-1.63
-0.7	-1.64	-1.67	-1.7	-1.73
-1.1	-1.74	-1.77	-1.8	-1.83

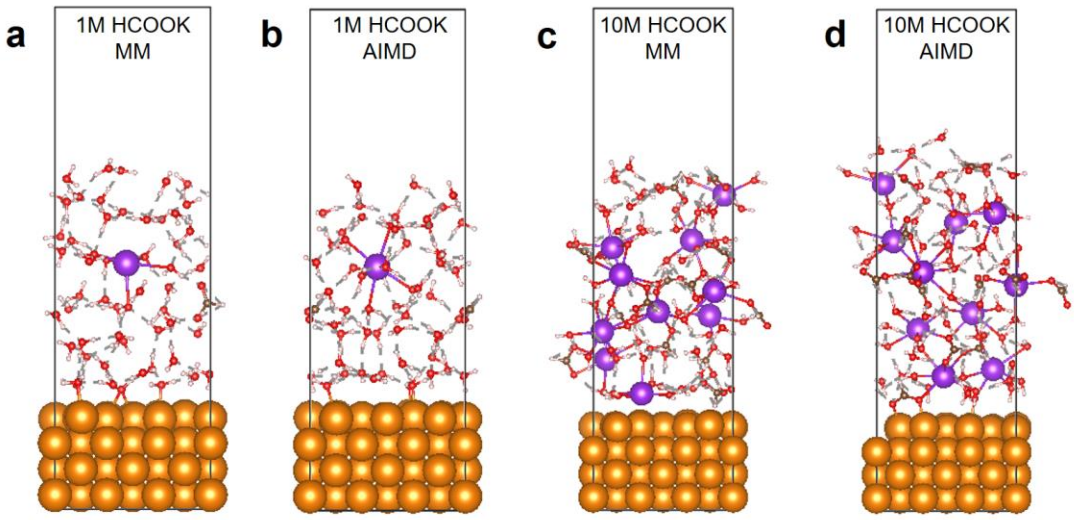

Figure S4.5: Equilibrated geometries at room temperature for Cu(100)/1 M HCOOK (56 H_2O + $HCOO^-$ + K^+) system from (a) CHARMM FF molecular mechanics (MM) (b) Ab-initio molecular dynamics (AIMD), and for Cu(100) + 7.1 M (10 mol/kg) HCOOK (56 H_2O + 10 $HCOO^-$ + 10 K^+) from (c) CHARMM FF MM and (d) AIMD.

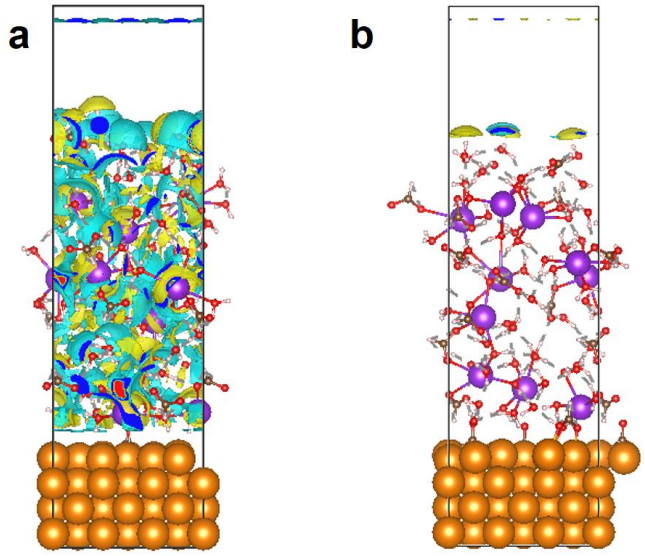

Figure S4.6: Bound charge density distribution for Cu(100)/7.1 M HCOOK system using (a) implicit solvation model (VASPsol) and (b) implicit-explicit solvation model (SOLHYBRID).

Table S4.2 Calculated relative potential energies with respect to the corresponding average distance (d [Å]) between the oxygen atom of *CO and K^+ for 7.1 M HCOOK on Cu.

d [Å]	ΔE[eV]
2.975941	0
4.413059	0.1429
4.920868	0.3901
5.300381	0.4425

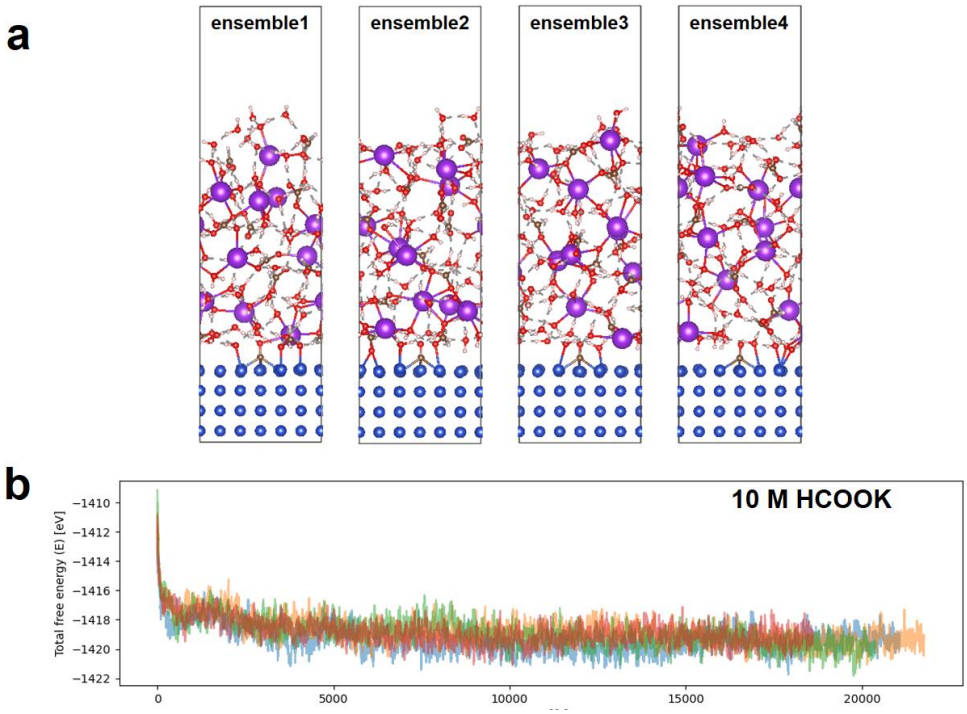

Figure S4.7: (a) Atomic geometries of four different ensembles of Cu(100)/7.1 M HCOOK electrolyte system after canonical AIMD equilibration. (b) Total free energy evolution of those four ensembles as a function of time during room temperature equilibration. The energy fluctuates within 4 eV window once the system reaches to the equilibrium.

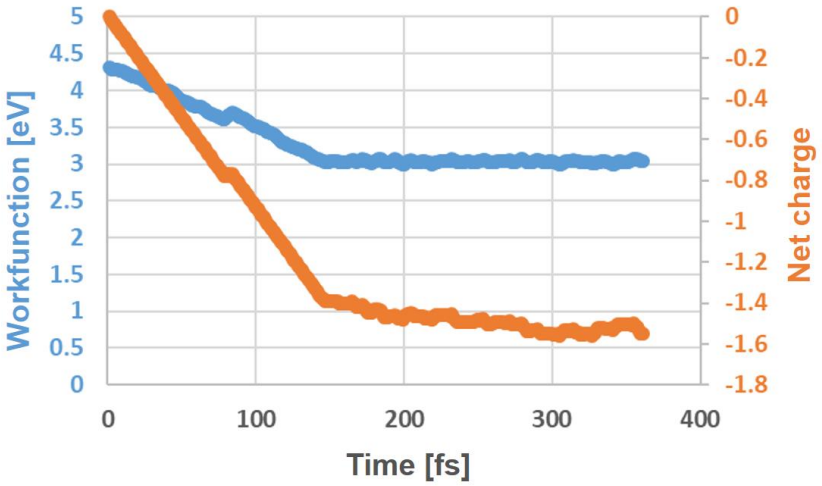

Figure S4.8: Initial few hundreds fs trajectory of grand canonical AIMD for an equilibration of Cu(100)/7.1 M HCOOK system using implicit-explicit solvation model (SOLHYBRID). The blue and orange lines denote the work function and net charge of the system. We equilibrated the systems for each electrochemical condition for at least 15 ps before the metadynamics calculation.

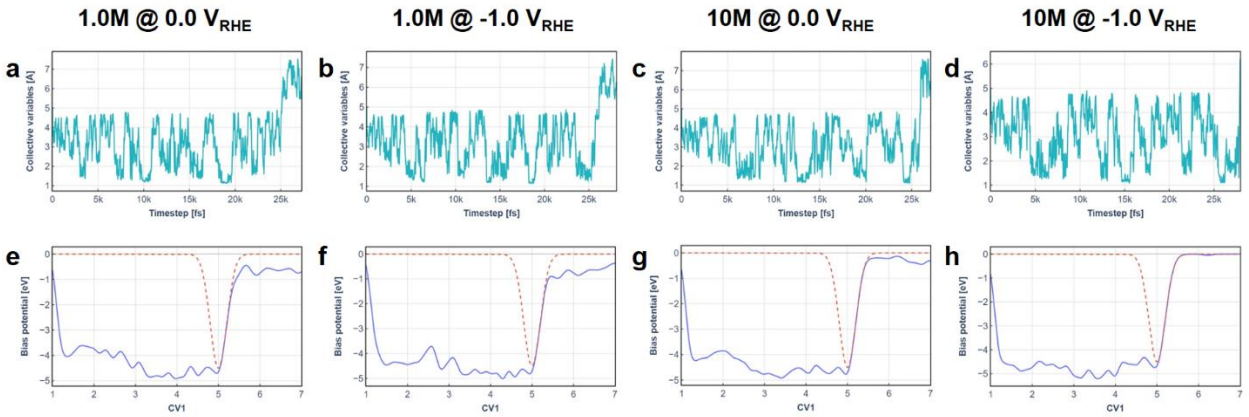

Figure S4.9: (a-d) The time evolution of the collective variables (CVs, C-C distance) at different electrochemical conditions during grand canonical ab-initio metadynamics at room temperature. (e-h) The dotted red line represents the penalty function and the solid blue line denotes corresponding potential energy landscape (sum of the Gaussian bias potentials and the penalty function) as a function of the CVs. A Gaussian potential, characterized by a height of 0.05 eV and a width of 0.10 eV, is applied every 20 fs.

Table S4.3 Reaction energy and kinetic barrier for CO dimerization under different electrochemical conditions from grand canonical ab-initio metadynamics.

Electrolyte	1 M HCOOK		7.1 M HCOOK	
Potential	0 V vs RHE	-1 V vs RHE	0 V vs RHE	-1 V vs RHE
Reaction energy	0.87 eV	0.54 eV	0.68 eV	0.32 eV
Activation barrier	1.31 eV	1.29 eV	1.07 eV	0.73 eV

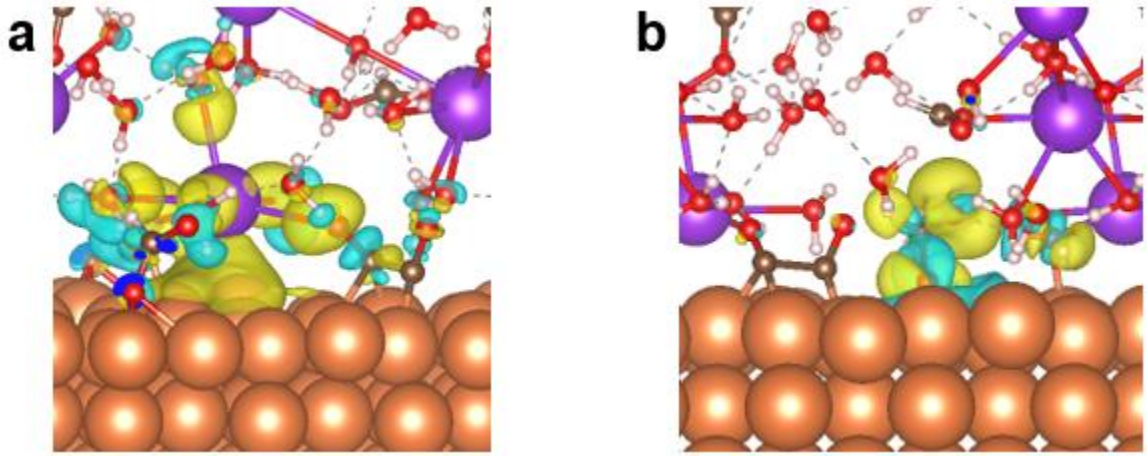

Figure S4.10: Charge redistribution by presence of (a) K^+ and (b) $HCOO^-$ at Cu(100)/7.1 M HCOOK interface. Yellow and blue isosurfaces represents the charge accumulation and depletion, respectively.

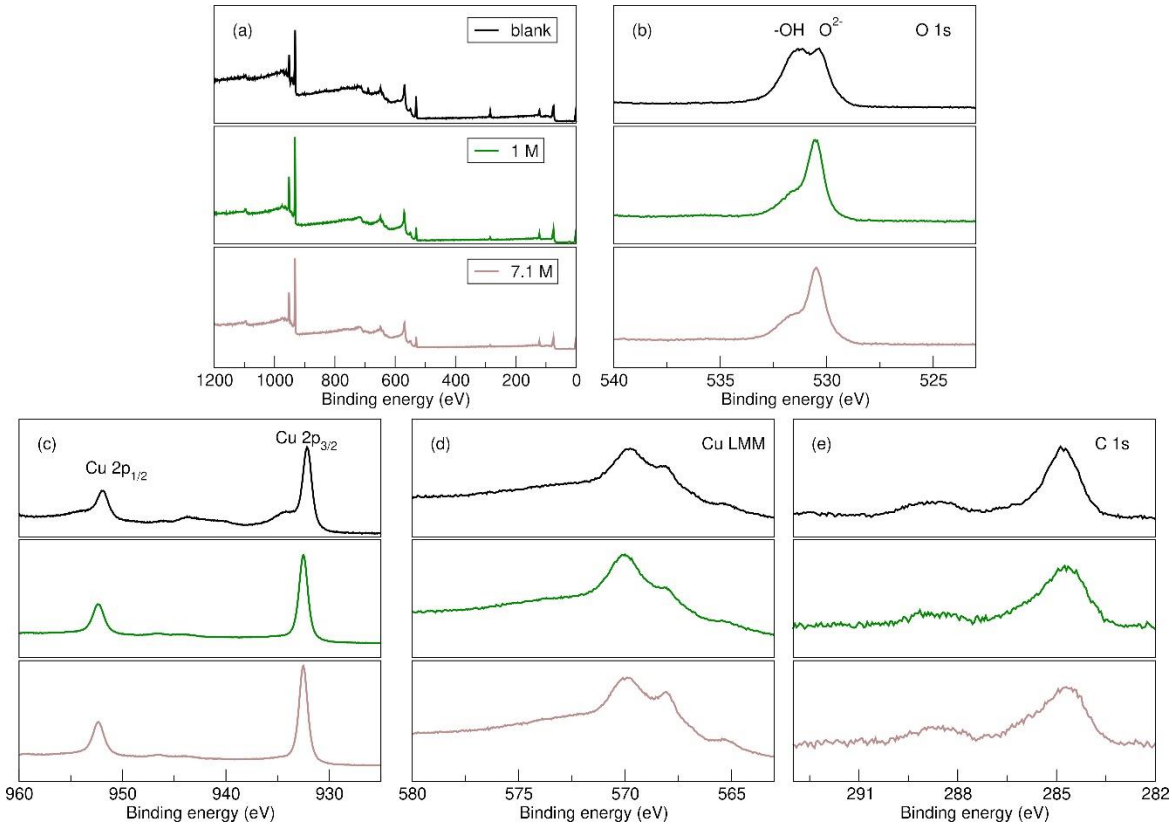

Figure S4.11: Normalized XPS spectra ((a) survey, (b) O 1s, (c) Cu 2p, (d) Cu LMM and (e) C 1s) of Cu GDE before electrolysis and after CO_2R electrolysis at -1.08 V vs RHE in 1 M HCOOK and 7.1 M HCOOK.

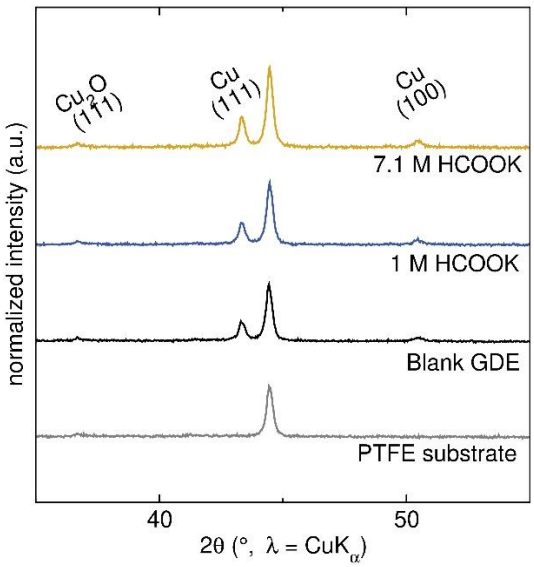

Figure S4.12: XRD patterns of the PTFE GDL substrate, the Cu GDE before electrolysis and after CO_2R electrolysis at -1.08 V vs RHE in 1 M HCOOK and 7.1 M HCOOK.

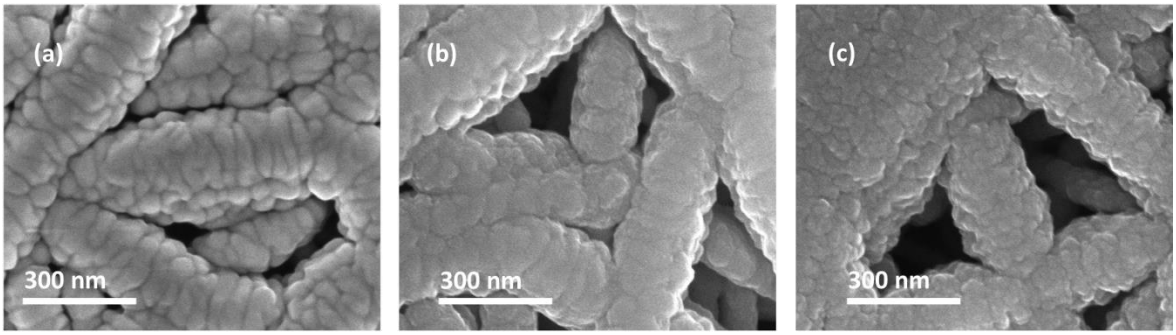

Figure S4.13: SEM images of Cu GDE before electrolysis (a) and after CO_2R electrolysis at -1.08 V vs RHE in 1 M HCOOK (b) and 7.1 M HCOOK (c).

Table S4.4 The electrochemically active surface area (ECSA) of Cu GDE CO_2R before and after 10 minutes electrolysis experiments at -1.08 V vs RHE in 1 M HCOOK and 7.1 M HCOOK.

	1 M (pre)	1 M (post)	7.1 M (pre)	7.1 M (post)
ECSA ($\mu F/cm^2$)	443 ± 45	442 ± 52	452 ± 31	374 ± 39

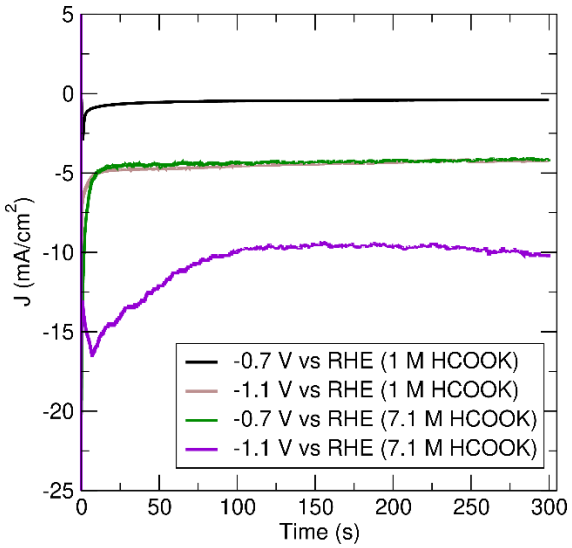

Figure S4.14: The current profile for the time evolution CO_2RR ATR-SEIRAS experiment under -0.7 V and -1.1 V for 1 M HCOOK and 7.1 M HCOOK, respectively.

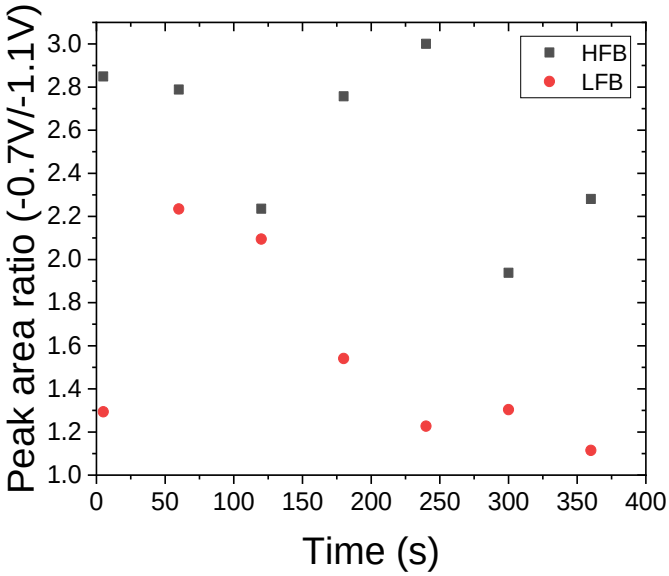

Figure S4.15: Peak area ratio of -0.7 V/-1.1 V vs RHE *CO_L mode during CO2R in 1 M HCOOK for HFB and LFB. From *CO_L peak area ratio analysis, it appears that the *CO_L -0.7 V/-1.1 V ratio for LFB converges to a value which approaches unity under the assumption of comparable ECSA (Measurement at each potential bias was taken on a fresh electrocatalyst). On the contrary, for HFB *CO_L, the ratio of -0.7 V/-1.1 V vs RHE is above 2 for the cell at -0.7 V vs. RHE. According to Gunathunge et al., HFB and LFB signal response rises from either step and terrace adsorbate species, or due to reversible surface reconstruction with increase in surface population which results in an increase in step edges density.[244,298,317] This implies that in both cases, the terrace adsorbed *CO_L population remains constant. Meanwhile, at -1.1 V vs RHE, the population of *CO_L on less coordinated Cu atoms is lower than -0.7 V vs RHE.

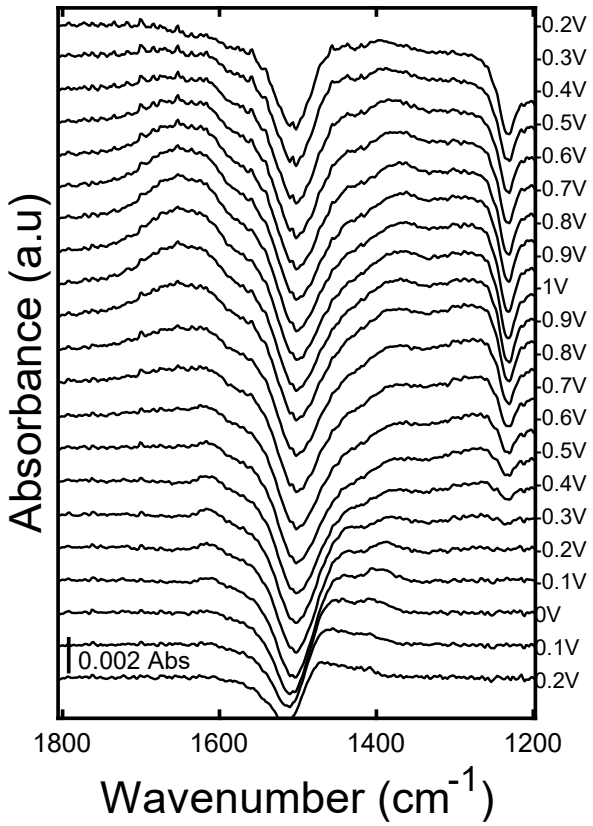

Figure S4.16: ATR-SEIRAS during CO_2R in 0.1 M $KHCO_3$ between 0.2 V and -1.0 V vs RHE.

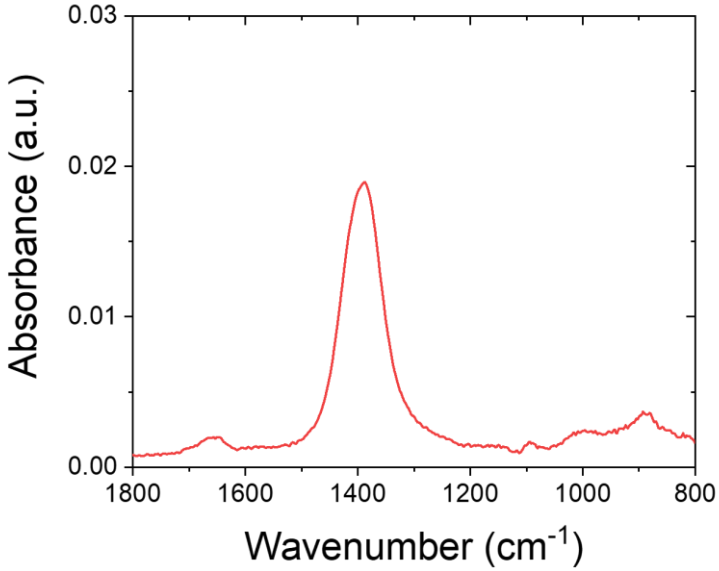

Figure S4.17: ATR-FTIR spectrum of aqueous 0.1 M CO_3^{2-} species.

Table S4.5 Product distribution of CO_2R on Cu plate electrode in H-cell in 1 M and 7.1 M HCOOK.

[HCOOK]	E (V vs RHE)	J (mA/cm^2)	FE (%) H_2	CH_4	CO	C_2H_4
1 M	-0.7	0.9 ± 0.1	73.2 ± 11.4	0	0	0.11
1 M	-1.1	3.7 ± 0.5	77.4 ± 4.8	0.52 ± 0.12	0.66 ± 0.18	0.35 ± 0.06
7.1 M	-0.7	1.7 ± 0.5	97.1	0	0	0
7.1 M	-1.1	15.3 ± 0.8	93.6 ± 1.4	0.02 ± 0.01	0.02 ± 0.01	0

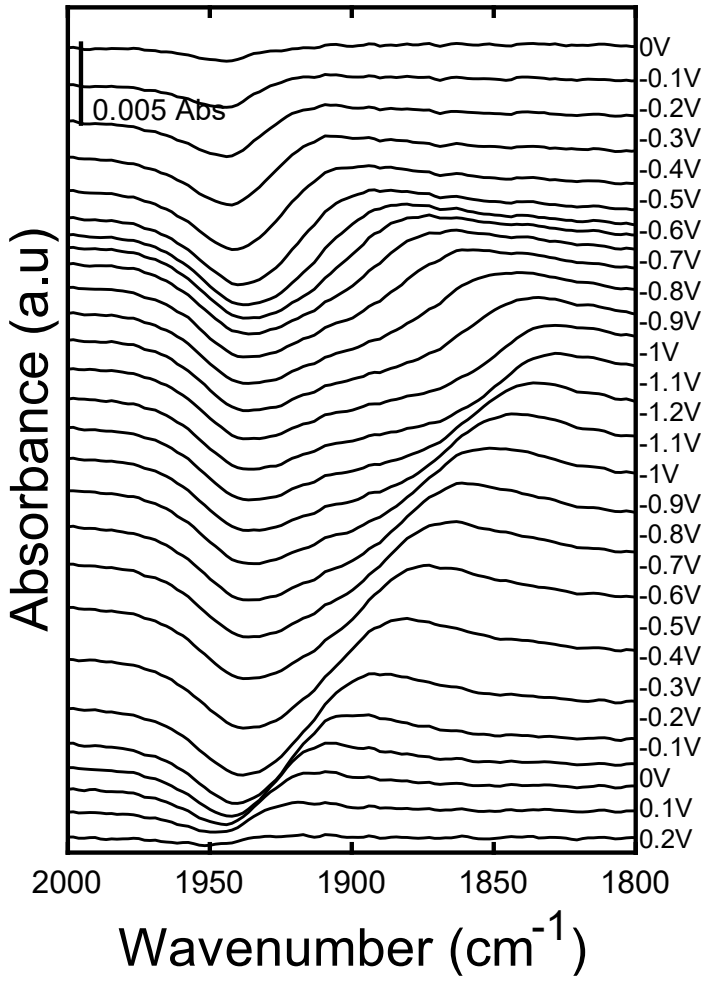

Figure S4.18: ATR-SEIRAS signal response to *CO_B during 2nd cycle of potential sweeping in 7.1 M HCOOK under CO_2.

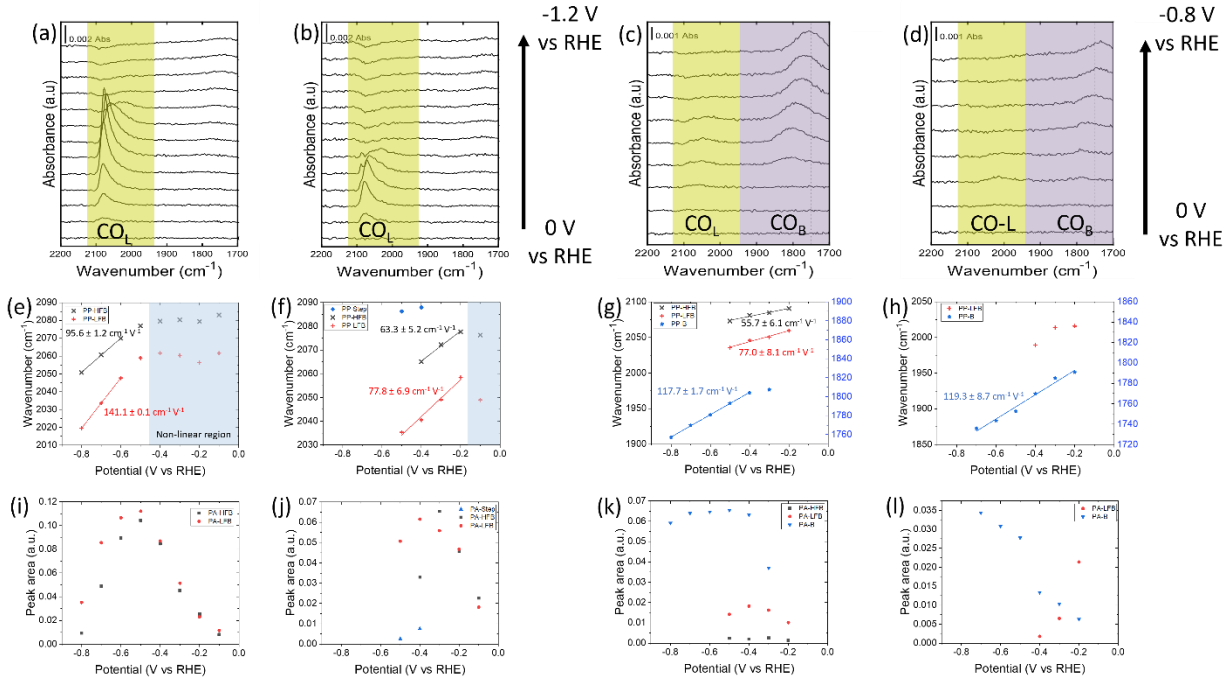

Figure S4.19: ATR-SEIRAS step scan during COR in 1 M HCOOK at (a) pH 7.8 and at (b) pH 11.9 (KOH titrated) between 0 and -1.2 V vs RHE. ATR-SEIRAS step scan during COR in 7.1 M HCOOK at (c) pH 9.0 and at (d) pH 11.9 between 0 and -0.8 V vs RHE. Adsorbed CO vibrational frequency (Step, HFB and LFB CO_L, and CO_B) as a function of potential in 1 M HCOOK at (e) pH 7.8 and at (f) pH 11.9 (KOH titrated), and in 7.1 M HCOOK at (g) pH 9.0, and at (h) pH 11.9 (KOH titrated). Adsorbed CO peak area as a function of potential in 1 M HCOOK at (i) pH 7.8 and at (j) pH 11.9, and in 7.1 M HCOOK at (k) pH 9.0 and at (l) pH 11.9.

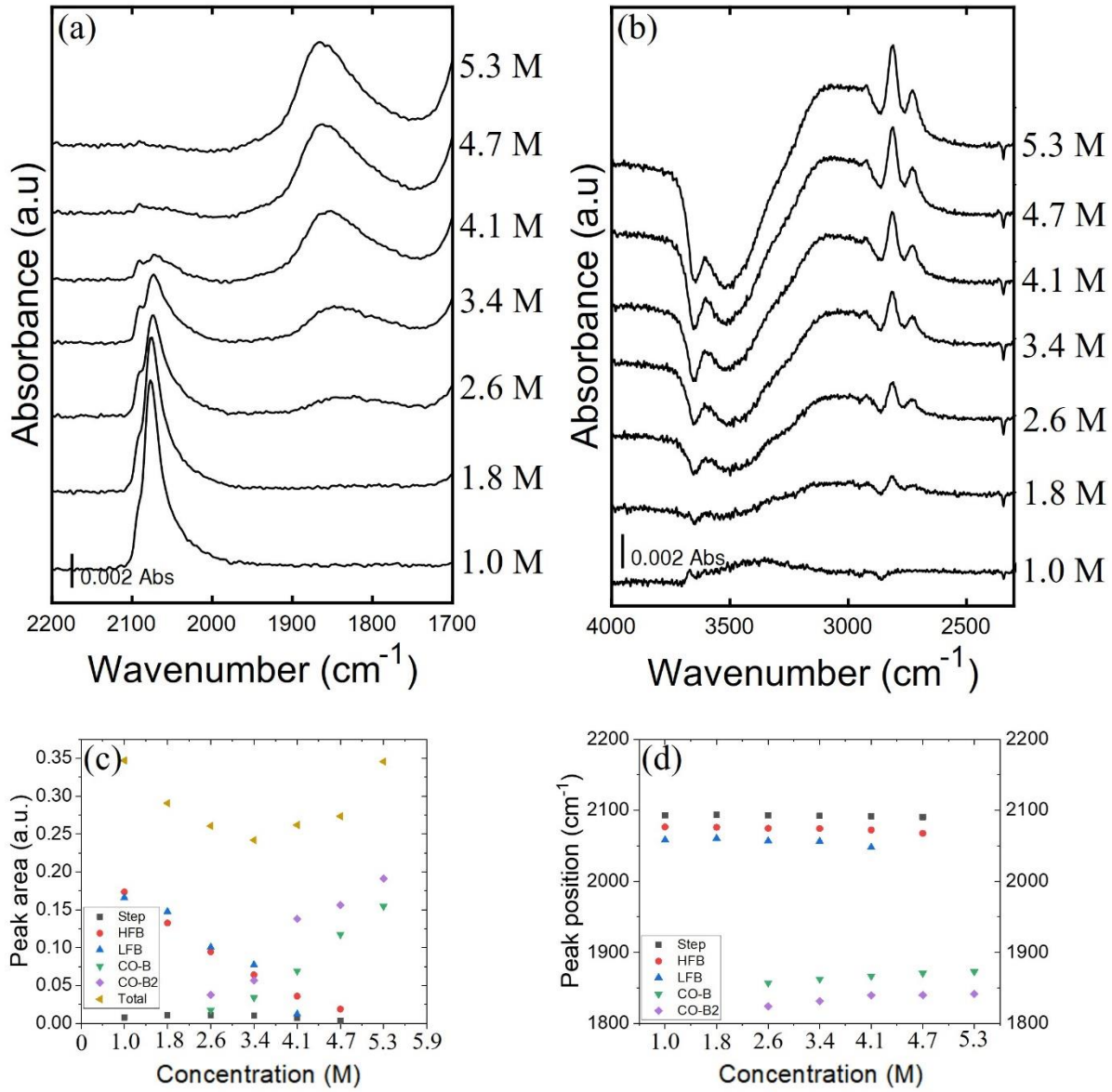

Figure S4.20: (a) Adsorbed CO ATR-SEIRAS signal response as a function of the supporting electrolyte concentration. (b) Dissolved CO_2 and OH stretching region signal response as a function of the supporting electrolyte concentration. (c) Peak area of adsorbed CO species as a function of the supporting electrolyte concentration. (d) Peak position of adsorbed CO species as a function of the supporting electrolyte concentration.

Table S4.6 Product analysis of ECOR on Cu plate for 1 M HCOOK and 7.1 M HCOOK.

	E (*V* vs. RHE)	J (mA/cm^2)	H_2 FE (%)	CH_4 FE (%)	C_2H_4 FE (%)
1 M (pH 8)	-1.0	-1.7 ± 0.5	81.3 ± 4.4	0.222 ± 0.105	2.003 ± 0.233
1 M (pH 12)	-1.0	-63.3 ± 9.9	83.9 ± 6.8	0.085 ± 0.017	0.012 ± 0.003
7.1 M (pH 9)	-1.0	-1.6 ± 0.2	86.9 ± 9.3	0	0.939 ± 0.055
7.1 M (pH 12)	-1.0	-18.4 ± 2.3	83.4 ± 1.8	0.101 ± 0.039	0.013 ± 0.013

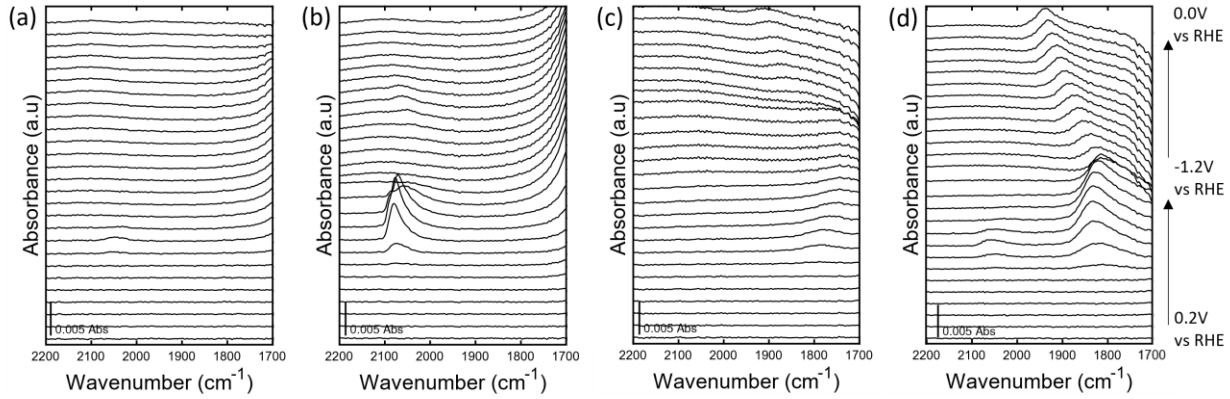

Figure S4.21: CO_2R ATR-SEIRAS experiment sweeping between 0.2 and -1.2 V vs RHE using (a) 5% CO_2 stream (CO_2 is balanced with N_2) in 1 M HCOOK, (b) 100 % CO_2 stream in 1 M HCOOK, (c) 5% CO_2 stream in 7.1 M HCOOK and (d) 100% CO_2 stream in 7.1 M HCOOK.

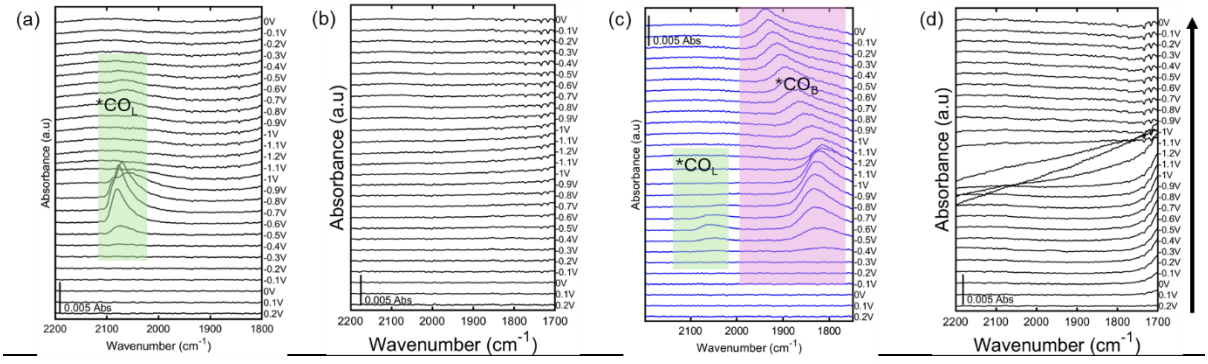

Figure S4.22: CO_2R ATR-SEIRAS experiment sweeping between 0.2 and -1.2 V vs RHE on (a) Cu and (b) Au/Si substrate in 1 M HCOOK, as well as on (c) Cu and (d) Au/Si substrate in 7.1 M HCOOK.

Chapter 5: Conclusion

5.1 Summary and Conclusions

To summarize, carbon emissions are a major concern due to their contribution to global warming. There is a continuous growth in the need for renewable energy solutions to address this issue. For example, CO_2RR to viable chemical derived from solar energy could support a sustainable alternative to current processes while minimizing fossil fuels energy CO_2 emissions. However, there is a need for technological improvements and method development in order to economically compete with current state of the art processes. One major component of interest is the catalyst-electrolyte interface, where electrochemical processes take place. Therefore, there is a need for the use and further development of spectro-electrochemical characterization methods such as ATR-SEIRAS which can monitor the catalyst-electrolyte microenvironment of electrochemical processes *in-situ*. Doing so, it is possible to gain insights on the different components affecting electrochemical CO_2RR, which could contribute to an improvement in performance of current electrolyzers.

In this project we have worked on the following goals. First, we have demonstrated a simple ans general approach for catalysts electrosynthesis methods for ATR-SEIRAS applications. In addition, we have devised an approach for ATR-SEIRAS signal response profile and initiated an investigation on the differences in spectral features using Sn thin films on CO_2RR, comparing metallic and oxide derived electrocatalysts. Second, we further investigated the fundamental CO_2 to formate electrochemical reaction as a case study for a 2-electron transfer reaction using computational GC-DFT models, validated by *in-situ* ATR-SEIRAS. Lastly, we demonstrated the complexity of the various effects on CO_2RR towards C_{2+} products on Cu based electrodes while further affirming experimental results using AIMD simulations. In addition, we worked towards

resolving the contribution of the different parameters and the sensitivity of CO_2RR to changes in each parameter.

5.2 Future Directions

In case of additional time for the PhD, as a direct future work of this project I propose the following ideas:

Further investigation of Sn based thin film electrocatalysts via additional characterization methods could support better understanding of their SEIRA performance (e.g., Infrared ellipsometry) and electronic structure (e.g., X-ray absorption spectroscopy). In addition, product distribution and degradation analysis during CO_2RR could support their relevance for implication in industry. These studies combined could also contribute to improved understanding of layered thin films. When considering CO_2RR in concentrated electrolytes using Cu as an electrocatalyst. In my opinion, the next step should involve studying spectroscopically the effect of bi/carbonate species and cation effect on CO binding site. This study could shed some insights on the system fundamentally.

In the bigger scheme of things and beyond direct follow up works, there is a lot of space for innovative contribution in the CO_2 capture and conversion domain. An interesting topic for investigation is the applicability of reactive CO_2 capture and conversion relative to a decoupled process. It appears that separate capture and conversion is more commercialized, as several companies are working on establishing this technology. However, is it viable to pursue reactive CO_2 capture and conversion at all, or efforts should be invested in elevating the technology readiness level of capture technologies. Second, split capture and conversion is currently more versatile than reactive capture and conversion with a growing promising field of direct ocean

capture via electrodialysis. Therefore, in the long run, I am curious about the feasibility and scalability of reactive ocean CO_2 capture and conversion as a platform to minimize CO_2 emissions contribution to global warming and ocean acidification.

This hypothetical work is interdisciplinary and requires multiple phases. First, there is a lot of room for research on understanding reactive capture and conversion for CO_2RR. This involves designer solvent molecules and their characterization. Second, understanding the performance of CO_2RR in the presence of contaminants from seawater and their interaction with different reactive capture sorbent molecules. Third, scaled up process performance relative to bench scale. Finally, technoeconomic feasibility and competitiveness relative to alternative solutions. Therefore, if I had more time to work in the ElectroBuffs group, I would highly consider research in this direction.

references

(1) Hoegh-Guldberg, O.; Jacob, D.; Taylor, M.; Guillén Bolaños, T.; Bindi, M.; Brown, S.; Camilloni, I. A.; Diedhiou, A.; Djalante, R.; Ebi, K.; Engelbrecht, F.; Guiot, J.; Hijioka, Y.; Mehrotra, S.; Hope, C. W.; Payne, A. J.; Pörtner, H.-O.; Seneviratne, S. I.; Thomas, A.; Warren, R.; Zhou, G. The Human Imperative of Stabilizing Global Climate Change at 1.5°C. *Science* **2019**, *365* (6459), eaaw6974. https://doi.org/10.1126/science.aaw6974.

(2) Calvin, K.; Dasgupta, D.; Krinner, G.; Mukherji, A.; Thorne, P. W.; Trisos, C.; Romero, J.; Aldunce, P.; Barrett, K.; Blanco, G.; Cheung, W. W. L.; Connors, S.; Denton, F.; Diongue-Niang, A.; Dodman, D.; Garschagen, M.; Geden, O.; Hayward, B.; Jones, C.; Jotzo, F.; Krug, T.; Lasco, R.; Lee, Y.-Y.; Masson-Delmotte, V.; Meinshausen, M.; Mintenbeck, K.; Mokssit, A.; Otto, F. E. L.; Pathak, M.; Pirani, A.; Poloczanska, E.; Pörtner, H.-O.; Revi, A.; Roberts, D. C.; Roy, J.; Ruane, A. C.; Skea, J.; Shukla, P. R.; Slade, R.; Slangen, A.; Sokona, Y.; Sörensson, A. A.; Tignor, M.; Van Vuuren, D.; Wei, Y.-M.; Winkler, H.; Zhai, P.; Zommers, Z.; Hourcade, J.-C.; Johnson, F. X.; Pachauri, S.; Simpson, N. P.; Singh, C.; Thomas, A.; Totin, E.; Arias, P.; Bustamante, M.; Elgizouli, I.; Flato, G.; Howden, M.; Méndez-Vallejo, C.; Pereira, J. J.; Pichs-Madruga, R.; Rose, S. K.; Saheb, Y.; Sánchez Rodríguez, R.; Ürge-Vorsatz, D.; Xiao, C.; Yassaa, N.; Alegría, A.; Armour, K.; Bednar-Friedl, B.; Blok, K.; Cissé, G.; Dentener, F.; Eriksen, S.; Fischer, E.; Garner, G.; Guivarch, C.; Haasnoot, M.; Hansen, G.; Hauser, M.; Hawkins, E.; Hermans, T.; Kopp, R.; Leprince-Ringuet, N.; Lewis, J.; Ley, D.; Ludden, C.; Niamir, L.; Nicholls, Z.; Some, S.; Szopa, S.; Trewin, B.; Van Der Wijst, K.-I.; Winter, G.; Witting, M.; Birt, A.; Ha, M.; Romero, J.; Kim, J.; Haites, E. F.; Jung, Y.; Stavins, R.; Birt, A.; Ha, M.; Orendain, D. J. A.; Ignon, L.; Park, S.; Park, Y.; Reisinger, A.; Cammaramo, D.; Fischlin, A.; Fuglestvedt, J. S.; Hansen, G.; Ludden, C.; Masson-Delmotte, V.; Matthews, J. B. R.; Mintenbeck, K.; Pirani, A.; Poloczanska, E.; Leprince-Ringuet, N.; Péan, C. *IPCC, 2023: Climate Change 2023: Synthesis Report. Contribution of Working Groups I, II and III to the Sixth Assessment Report of the Intergovernmental Panel on Climate Change [Core Writing Team, H. Lee and J. Romero (Eds.)]. IPCC, Geneva, Switzerland.*, First.; Intergovernmental Panel on Climate Change (IPCC), 2023. https://doi.org/10.59327/IPCC/AR6-9789291691647.

(3) Park, T.; Hashimoto, H.; Wang, W.; Thrasher, B.; Michaelis, A. R.; Lee, T.; Brosnan, I. G.; Nemani, R. R. What Does Global Land Climate Look Like at 2°C Warming? *Earths Future* **2023**, *11* (5), e2022EF003330. https://doi.org/10.1029/2022EF003330.

(4) Collins, M.; Knutti, R.; Arblaster, J.; Dufresne, J.-L.; Fichefet, T.; Gao, X.; Jr, W. J. G.; Johns, T.; Krinner, G.; Shongwe, M.; Weaver, A. J.; Wehner, M.; Allen, M. R.; Andrews, T.; Beyerle, U.; Bitz, C. M.; Bony, S.; Booth, B. B. B.; Brooks, H. E.; Brovkin, V.; Browne, O.; Brutel-Vuilmet, C.; Cane, M.; Chadwick, R.; Cook, E.; Cook, K. H.; Eby, M.; Fasullo, J.; Forest, C. E.; Forster, P.; Good, P.; Goosse, H.; Gregory, J. M.; Hegerl, G. C.; Hezel, P. J.; Hodges, K. I.; Holland, M. M.; Huber, M.; Joshi, M.; Kharin, V.; Kushnir, Y.; Lawrence, D. M.; Lee, R. W.; Liddicoat, S.; Lucas, C.; Lucht, W.; Marotzke, J.; Massonnet, F.; Matthews, H. D.; Meinshausen, M.; Morice, C.; Otto, A.; Patricola, C. M.; Philippon, G.; Rahmstorf, S.; Riley, W. J.; Saenko, O.; Seager, R.; Sedláček, J.; Shaffrey, L. C.; Shindell, D.; Sillmann, J.; Stevens, B.; Stott, P. A.; Webb, R.; Zappa, G.; Zickfeld, K.; Joussaume, S.; Mokssit, A.; Taylor, K.; Tett, S. Long-Term Climate Change: Projections, Commitments and Irreversibility.

(5) Guerra, O. J.; Almajed, H. M.; Smith, W. A.; Somoza-Tornos, A.; Hodge, B.-M. S. Barriers and Opportunities for the Deployment of CO2 Electrolysis in Net-Zero Emissions Energy Systems. *Joule* **2023**, *7* (6), 1111–1133. https://doi.org/10.1016/j.joule.2023.05.002.

(6) Almajed, H. M.; Kas, R.; Brimley, P.; Crow, A. M.; Somoza-Tornos, A.; Hodge, B.-M.; Burdyny, T. E.; Smith, W. A. Closing the Loop: Unexamined Performance Trade-Offs of Integrating Direct Air Capture with (Bi)Carbonate Electrolysis. *ACS Energy Lett.* **2024**, *9* (5), 2472–2483. https://doi.org/10.1021/acsenergylett.4c00807.
(7) Yang, K.; Kas, R.; Smith, W. A. In Situ Infrared Spectroscopy Reveals Persistent Alkalinity near Electrode Surfaces during CO 2 Electroreduction. *J. Am. Chem. Soc.* **2019**, *141* (40), 15891–15900. https://doi.org/10.1021/jacs.9b07000.
(8) Kas, R.; Ayemoba, O.; Firet, N. J.; Middelkoop, J.; Smith, W. A.; Cuesta, A. In-Situ Infrared Spectroscopy Applied to the Study of the Electrocatalytic Reduction of CO2: Theory, Practice and Challenges. *ChemPhysChem* **2019**, *20* (22), 2904–2925. https://doi.org/10.1002/cphc.201900533.
(9) Simonson, H.; Klein, W. E.; Henckel, D.; Verma, S.; Neyerlin, K. C.; Smith, W. A. Direct Measurement of Electrochemical Selectivity Gradients over a 25 Cm2 Copper Gas Diffusion Electrode. *ACS Energy Lett.* **2023**, *8* (9), 3811–3819. https://doi.org/10.1021/acsenergylett.3c01489.
(10) Jouny, M.; Luc, W.; Jiao, F. General Techno-Economic Analysis of CO2 Electrolysis Systems. *Ind. Eng. Chem. Res.* **2018**, *57* (6), 2165–2177. https://doi.org/10.1021/acs.iecr.7b03514.
(11) Digdaya, I. A.; Sullivan, I.; Lin, M.; Han, L.; Cheng, W.-H.; Atwater, H. A.; Xiang, C. A Direct Coupled Electrochemical System for Capture and Conversion of CO2 from Oceanwater. *Nat. Commun.* **2020**, *11* (1), 4412. https://doi.org/10.1038/s41467-020-18232-y.
(12) Sassenburg, M.; de Rooij, R.; Nesbitt, N. T.; Kas, R.; Chandrashekar, S.; Firet, N. J.; Yang, K.; Liu, K.; Blommaert, M. A.; Kolen, M.; Ripepi, D.; Smith, W. A.; Burdyny, T. Characterizing CO2 Reduction Catalysts on Gas Diffusion Electrodes: Comparing Activity, Selectivity, and Stability of Transition Metal Catalysts. *ACS Appl. Energy Mater.* **2022**, *5* (5), 5983–5994. https://doi.org/10.1021/acsaem.2c00160.
(13) Longo, S.; Cellura, M.; Guarino, F.; Ferraro, M.; Antonucci, V.; Squadrito, G. Chapter 6 - Life Cycle Assessment of Solid Oxide Fuel Cells and Polymer Electrolyte Membrane Fuel Cells: A Review. In *Hydrogen Economy*; Scipioni, A., Manzardo, A., Ren, J., Eds.; Academic Press, 2017; pp 139–169. https://doi.org/10.1016/B978-0-12-811132-1.00006-7.
(14) Liu, K.; Smith, W. A.; Burdyny, T. Introductory Guide to Assembling and Operating Gas Diffusion Electrodes for Electrochemical CO2 Reduction. *ACS Energy Lett.* **2019**, *4* (3), 639–643. https://doi.org/10.1021/acsenergylett.9b00137.
(15) Jouny, M.; Luc, W.; Jiao, F. High-Rate Electroreduction of Carbon Monoxide to Multi-Carbon Products. *Nat. Catal.* **2018**, *1* (10), 748–755. https://doi.org/10.1038/s41929-018-0133-2.
(16) Aftab, M.; Mansha, M. S.; Iqbal, T.; Farooq, M. Surface Plasmon Excitation: Theory, Configurations, and Applications. *Plasmonics* **2024**, *19* (4), 1701–1719. https://doi.org/10.1007/s11468-023-02095-2.
(17) *Materials Project - Pourbaix Diagram*. Materials Project. https://next-gen.materialsproject.org/pourbaix (accessed 2023-12-21).
(18) Persson, K. A.; Waldwick, B.; Lazic, P.; Ceder, G. Prediction of Solid-Aqueous Equilibria: Scheme to Combine First-Principles Calculations of Solids with Experimental Aqueous States. *Phys. Rev. B* **2012**, *85* (23), 235438. https://doi.org/10.1103/PhysRevB.85.235438.

(19) Singh, A. K.; Zhou, L.; Shinde, A.; Suram, S. K.; Montoya, J. H.; Winston, D.; Gregoire, J. M.; Persson, K. A. Electrochemical Stability of Metastable Materials. *Chem. Mater.* **2017**, *29* (23), 10159–10167. https://doi.org/10.1021/acs.chemmater.7b03980.
(20) Patel, A. M.; Nørskov, J. K.; Persson, K. A.; Montoya, J. H. Efficient Pourbaix Diagrams of Many-Element Compounds. *Phys. Chem. Chem. Phys.* **2019**, *21* (45), 25323–25327. https://doi.org/10.1039/C9CP04799A.
(21) Jain, A.; Ong, S. P.; Hautier, G.; Chen, W.; Richards, W. D.; Dacek, S.; Cholia, S.; Gunter, D.; Skinner, D.; Ceder, G.; Persson, K. A. Commentary: The Materials Project: A Materials Genome Approach to Accelerating Materials Innovation. *APL Mater.* **2013**, *1* (1), 011002. https://doi.org/10.1063/1.4812323.
(22) Nasirpouri, F. Electrodeposited Nanocrystalline Films and Coatings. In *Electrodeposition of Nanostructured Materials*; Nasirpouri, F., Ed.; Springer Series in Surface Sciences; Springer International Publishing: Cham, 2017; pp 261–288. https://doi.org/10.1007/978-3-319-44920-3_6.
(23) Schädle, T.; Pejcic, B.; Mizaikoff, B. Monitoring Dissolved Carbon Dioxide and Methane in Brine Environments at High Pressure Using IR-ATR Spectroscopy. *Anal. Methods* **2016**, *8* (4), 756–762. https://doi.org/10.1039/C5AY02744F.
(24) Mojet, B. L.; Ebbesen, S. D.; Lefferts, L. Light at the Interface: The Potential of Attenuated Total Reflection Infrared Spectroscopy for Understanding Heterogeneous Catalysis in Water. *Chem. Soc. Rev.* **2010**, *39* (12), 4643–4655. https://doi.org/10.1039/C0CS00014K.
(25) *Electrochemical Methods: Fundamentals and Applications, 2nd Edition | Wiley*. Wiley.com. https://www.wiley.com/en-kr/Electrochemical+Methods%3A+Fundamentals+and+Applications%2C+2nd+Edition-p-9780471043720 (accessed 2024-11-08).
(26) Hori, Y.; Kikuchi, K.; Suzuki, S. PRODUCTION OF CO AND CH4 IN ELECTROCHEMICAL REDUCTION OF CO2 AT METAL ELECTRODES IN AQUEOUS HYDROGENCARBONATE SOLUTION. *Chem. Lett.* **1985**, *14* (11), 1695–1698. https://doi.org/10.1246/cl.1985.1695.
(27) Nitopi, S.; Bertheussen, E.; Scott, S. B.; Liu, X.; Engstfeld, A. K.; Horch, S.; Seger, B.; Stephens, I. E. L.; Chan, K.; Hahn, C.; Nørskov, J. K.; Jaramillo, T. F.; Chorkendorff, I. Progress and Perspectives of Electrochemical CO $_2$ Reduction on Copper in Aqueous Electrolyte. *Chem. Rev.* **2019**, *119* (12), 7610–7672. https://doi.org/10.1021/acs.chemrev.8b00705.
(28) Hori, Y.; Wakebe, H.; Tsukamoto, T.; Koga, O. Electrocatalytic Process of CO Selectivity in Electrochemical Reduction of CO2 at Metal Electrodes in Aqueous Media. *Electrochimica Acta* **1994**, *39* (11), 1833–1839. https://doi.org/10.1016/0013-4686(94)85172-7.
(29) Yoon, J.; Kim, J.; Kim, C.; Jang, H.; Lee, J. MOF-Based Hybrids for Solar Fuel Production. *Adv. Energy Mater.* **2021**, *11*. https://doi.org/10.1002/aenm.202003052.
(30) 60 Years of PerkinElmer Innovation in Infrared Spectroscopy.
(31) Larkin, P. Chapter 3 - Instrumentation and Sampling Methods. In *Infrared and Raman Spectroscopy*; Larkin, P., Ed.; Elsevier: Oxford, 2011; pp 27–54. https://doi.org/10.1016/B978-0-12-386984-5.10003-5.
(32) Aroca, R. F.; Ross, D. J.; Domingo, C. Surface-Enhanced Infrared Spectroscopy. *Appl. Spectrosc.* **2004**, *58* (11), 324A-338A. https://doi.org/10.1366/0003702042475420.

(33) Gao, Y.; Aspnes, D. E.; Franzen, S. Classical Model of Surface Enhanced Infrared Absorption (SEIRA) Spectroscopy. *J. Phys. Chem. A* **2022**, *126* (2), 341–351. https://doi.org/10.1021/acs.jpca.1c08463.
(34) Andvaag, I. R.; Lins, E.; Burgess, I. J. An Effective Medium Theory Description of Surface-Enhanced Infrared Absorption from Metal Island Layers Grown on Conductive Metal Oxide Films. *J. Phys. Chem. C* **2021**, *125* (40), 22301–22311. https://doi.org/10.1021/acs.jpcc.1c06627.
(35) Maeda, K.; Domen, K. Photocatalytic Water Splitting: Recent Progress and Future Challenges. *J. Phys. Chem. Lett.* **2010**, *1* (18), 2655–2661. https://doi.org/10.1021/jz1007966.
(36) Burdyny, T.; Smith, W. A. CO 2 Reduction on Gas-Diffusion Electrodes and Why Catalytic Performance Must Be Assessed at Commercially-Relevant Conditions. *Energy Environ. Sci.* **2019**, *12* (5), 1442–1453. https://doi.org/10.1039/C8EE03134G.
(37) Zhang, H.; Wang, S.; Zhang, H.; Clark, J. H.; Cao, F. A Biomass-Derived Metal-Free Catalyst Doped with Phosphorus for Highly Efficient and Selective Oxidation of Furfural into Maleic Acid. *Green Chem.* **2021**, *23* (3), 1370–1381. https://doi.org/10.1039/D0GC04205F.
(38) Lucas, F. W. S.; Grim, R. G.; Tacey, S. A.; Downes, C. A.; Hasse, J.; Roman, A. M.; Farberow, C. A.; Schaidle, J. A.; Holewinski, A. Electrochemical Routes for the Valorization of Biomass-Derived Feedstocks: From Chemistry to Application. *ACS Energy Lett.* **2021**, 1205–1270. https://doi.org/10.1021/acsenergylett.0c02692.
(39) Román, A. M.; Hasse, J. C.; Medlin, J. W.; Holewinski, A. Elucidating Acidic Electro-Oxidation Pathways of Furfural on Platinum. *ACS Catal.* **2019**, *9* (11), 10305–10316. https://doi.org/10.1021/acscatal.9b02656.
(40) Lucas, F. W. S.; Fishler, Y.; Holewinski, A. Tuning the Selectivity of Electrochemical Levulinic Acid Reduction to 4-Hydroxyvaleric Acid: A Monomer for Biocompatible and Biodegradable Plastics. *Green Chem.* **2021**, *23* (22), 9154–9164. https://doi.org/10.1039/D1GC02826J.
(41) Zhao, S.; Li, S.; Guo, T.; Zhang, S.; Wang, J.; Wu, Y.; Chen, Y. Advances in Sn-Based Catalysts for Electrochemical CO2 Reduction. *Nano-Micro Lett.* **2019**, *11* (1), 62. https://doi.org/10.1007/s40820-019-0293-x.
(42) Baruch, M. F.; Pander, J. E.; White, J. L.; Bocarsly, A. B. Mechanistic Insights into the Reduction of CO 2 on Tin Electrodes Using in Situ ATR-IR Spectroscopy. *ACS Catal.* **2015**, *5* (5), 3148–3156. https://doi.org/10.1021/acscatal.5b00402.
(43) Miyake, H.; Ye, S.; Osawa, M. Electroless Deposition of Gold Thin Films on Silicon for Surface-Enhanced Infrared Spectroelectrochemistry. *Electrochem. Commun.* **2002**, *4* (12), 973–977. https://doi.org/10.1016/S1388-2481(02)00510-6.
(44) Wang, H.-F.; Yan, Y.-G.; Huo, S.-J.; Cai, W.-B.; Xu, Q.-J.; Osawa, M. Seeded Growth Fabrication of Cu-on-Si Electrodes for in Situ ATR-SEIRAS Applications. *Electrochimica Acta* **2007**, *52* (19), 5950–5957. https://doi.org/10.1016/j.electacta.2007.03.042.
(45) Shao, M. H.; Adzic, R. R. Electrooxidation of Ethanol on a Pt Electrode in Acid Solutions: In Situ ATR-SEIRAS Study. *Electrochimica Acta* **2005**, *50* (12), 2415–2422. https://doi.org/10.1016/j.electacta.2004.10.063.
(46) Delgado, J. M.; Orts, J. M.; Pérez, J. M.; Rodes, A. Sputtered Thin-Film Gold Electrodes for in Situ ATR-SEIRAS and SERS Studies. *J. Electroanal. Chem.* **2008**, *617* (2), 130–140. https://doi.org/10.1016/j.jelechem.2008.01.029.
(47) Berná, A.; Delgado, J. M.; Orts, J. M.; Rodes, A.; Feliu, J. M. In-Situ Infrared Study of the Adsorption and Oxidation of Oxalic Acid at Single-Crystal and Thin-Film Gold Electrodes: A

Combined External Reflection Infrared and ATR−SEIRAS Approach. *Langmuir* **2006**, *22* (17), 7192–7202. https://doi.org/10.1021/la060400l.
(48) Morhart, T. A.; Unni, B.; Lardner, M. J.; Burgess, I. J. Electrochemical ATR-SEIRAS Using Low-Cost, Micromachined Si Wafers. *Anal. Chem.* **2017**, *89* (21), 11818–11824. https://doi.org/10.1021/acs.analchem.7b03509.
(49) Delgado, J. M.; Orts, J. M.; Rodes, A. A Comparison between Chemical and Sputtering Methods for Preparing Thin-Film Silver Electrodes for in Situ ATR-SEIRAS Studies. *Electrochimica Acta* **2007**, *52* (14), 4605–4613. https://doi.org/10.1016/j.electacta.2006.12.045.
(50) Liang, S.; Guan, T.; Yin, S.; Krois, E.; Chen, W.; Everett, C. R.; Drewes, J.; Strunskus, T.; Gensch, M.; Rubeck, J.; Haisch, C.; Schwartzkopf, M.; Faupel, F.; Roth, S. V.; Cheng, Y.-J.; Müller-Buschbaum, P. Template-Induced Growth of Sputter-Deposited Gold Nanoparticles on Ordered Porous TiO2 Thin Films for Surface-Enhanced Raman Scattering Sensors. *ACS Appl. Nano Mater.* **2022**, *5* (5), 7492–7501. https://doi.org/10.1021/acsanm.2c01481.
(51) López-Lorente, A. I.; Picca, R. A.; Izquierdo, J.; Kranz, C.; Mizaikoff, B.; Di Franco, C.; Cárdenas, S.; Cioffi, N.; Palazzo, G.; Valentini, A. Ion Beam Sputtering Deposition of Silver Nanoparticles and TiOx/ZnO Nanocomposites for Use in Surface Enhanced Vibrational Spectroscopy (SERS and SEIRAS). *Microchim. Acta* **2018**, *185* (2), 153. https://doi.org/10.1007/s00604-018-2708-7.
(52) Nong, J.; Tang, L.; Lan, G.; Luo, P.; Li, Z.; Huang, D.; Shen, J.; Wei, W. Combined Visible Plasmons of Ag Nanoparticles and Infrared Plasmons of Graphene Nanoribbons for High-Performance Surface-Enhanced Raman and Infrared Spectroscopies. *Small* **2021**, *17* (1), 2004640. https://doi.org/10.1002/smll.202004640.
(53) Clarke, O. J. R.; Burgess, I. J. Electrodeposited Gold Nanodaggers on Conductive Metal Oxide Films Provide Substrates for Dual-Modality Surface Sensitive Vibrational Spectroscopy. *J. Phys. Chem. C* **2020**, *124* (24), 13356–13364. https://doi.org/10.1021/acs.jpcc.0c03351.
(54) Andvaag, I. R.; Morhart, T. A.; Clarke, O. J. R.; Burgess, I. J. Hybrid Gold–Conductive Metal Oxide Films for Attenuated Total Reflectance Surface Enhanced Infrared Absorption Spectroscopy. *ACS Appl. Nano Mater.* **2019**, *2* (3), 1274–1284. https://doi.org/10.1021/acsanm.8b02155.
(55) Guske, J. T.; Brown, J.; Welsh, A.; Franzen, S. Infrared Surface Plasmon Resonance of AZO-Ag-AZO Sandwich Thin Films. *Opt. Express* **2012**, *20* (21), 23215–23226. https://doi.org/10.1364/OE.20.023215.
(56) Sachet, E.; Losego, M. D.; Guske, J.; Franzen, S.; Maria, J.-P. Mid-Infrared Surface Plasmon Resonance in Zinc Oxide Semiconductor Thin Films. *Appl. Phys. Lett.* **2013**, *102* (5), 051111. https://doi.org/10.1063/1.4791700.
(57) Sachet, E.; Aspnes, D. E.; Maria, J.-P.; Franzen, S. Critical Test of the Interaction of Surface Plasmon Resonances with Molecular Vibrational Transitions. *J. Phys. Chem. A* **2020**, *124* (9), 1744–1753. https://doi.org/10.1021/acs.jpca.9b10835.
(58) Heyes, J.; Dunwell, M.; Xu, B. CO_2 Reduction on Cu at Low Overpotentials with Surface-Enhanced in Situ Spectroscopy. *J. Phys. Chem. C* **2016**, *120* (31), 17334–17341. https://doi.org/10.1021/acs.jpcc.6b03065.
(59) Xu, Q.; Berná, A.; Pobelov, I. V.; Rodes, A.; Feliu, J. M.; Wandlowski, T.; Kuzume, A. ATR-SEIRAS Study of CO Adsorption and Oxidation on Rh Modified Au(111-25nm) Film

Electrodes in 0.1M H2SO4. *Electrochimica Acta* **2015**, *176*, 1202–1213. https://doi.org/10.1016/j.electacta.2015.07.165.
(60) Aranzales, D.; Wijenberg, J. H. O. J.; Koper, M. T. M. Voltammetric Study of Tin Electrodeposition on Polycrystalline Gold from Sulfuric and Methanesulfonic Acid. *J. Electrochem. Soc.* **2019**, *166* (8), D283–D289. https://doi.org/10.1149/2.0211908jes.
(61) House, C. I.; Kelsall, G. H. Potential—pH Diagrams for the Sn/H2O□Cl System. *Electrochimica Acta* **1984**, *29* (10), 1459–1464. https://doi.org/10.1016/0013-4686(84)87028-0.
(62) Gamsjaeger, H.; Gajda, T.; Sangster, J.; Saxena, S. K.; Voigt, W.; Perrone, J. Chemical Thermodynamics Vol. 12 - Chemical Thermodynamics of Tin. **2012**, 108.
(63) Pu, S. D.; Gong, C.; Gao, X.; Ning, Z.; Yang, S.; Marie, J.-J.; Liu, B.; House, R. A.; Hartley, G. O.; Luo, J.; Bruce, P. G.; Robertson, A. W. Current-Density-Dependent Electroplating in Ca Electrolytes: From Globules to Dendrites. *ACS Energy Lett.* **2020**, *5* (7), 2283–2290. https://doi.org/10.1021/acsenergylett.0c01153.
(64) Walsh, F. C.; Low, C. T. J. A Review of Developments in the Electrodeposition of Tin. *Surf. Coat. Technol.* **2016**, *288*, 79–94. https://doi.org/10.1016/j.surfcoat.2015.12.081.
(65) Vequizo, J. J. M.; Wang, J.; Ichimura, M. Electrodeposition of SnO_2 Thin Films from Aqueous Tin Sulfate Solutions. *Jpn. J. Appl. Phys.* **2010**, *49* (12R), 125502. https://doi.org/10.1143/JJAP.49.125502.
(66) Patnaik, S. G.; Jadon, A.; Tran, C. C. H.; Estève, A.; Guay, D.; Pech, D. High Areal Capacity Porous Sn-Au Alloys with Long Cycle Life for Li-Ion Microbatteries. *Sci. Rep.* **2020**, *10* (1), 10405. https://doi.org/10.1038/s41598-020-67309-7.
(67) Santhi, K.; Rani, C.; Karuppuchamy, S. Synthesis and Characterization of a Novel SnO/SnO2 Hybrid Photocatalyst. *J. Alloys Compd.* **2016**, *662*, 102–107. https://doi.org/10.1016/j.jallcom.2015.12.007.
(68) Chandrashekar, S.; Nesbitt, N. T.; Smith, W. A. Electrochemical CO2 Reduction Over Bimetallic Au–Sn Thin Films: Comparing Activity and Selectivity against Morphological, Compositional, and Electronic Differences. *J. Phys. Chem. C* **2020**, *124* (27), 14573–14580. https://doi.org/10.1021/acs.jpcc.0c01894.
(69) Cushman, C. V.; Brüner, P.; Zakel, J.; Major, G. H.; Lunt, B. M.; Smith, N. J.; Grehl, T.; Linford, M. R. Low Energy Ion Scattering (LEIS). A Practical Introduction to Its Theory, Instrumentation, and Applications. *Anal Methods* **2016**, *8* (17), 3419–3439. https://doi.org/10.1039/C6AY00765A.
(70) Powell, C. X-Ray Photoelectron Spectroscopy Database XPS,Version 4.1, NIST Standard Reference Database 20, 1989. https://doi.org/10.18434/T4T88K.
(71) Moulder, J.; Stickle, W.; Sobol, W.; Bomben, K. D. Handbook of X-Ray Photoelectron Spectroscopy; 1992.
(72) Peters, S.; Peredkov, S.; Neeb, M.; Eberhardt, W.; Al-Hada, M. Size-Dependent XPS Spectra of Small Supported Au-Clusters. *Surf. Sci.* **2013**, *608*, 129–134. https://doi.org/10.1016/j.susc.2012.09.024.
(73) Yoon, Y.; Yan, B.; Surendranath, Y. Suppressing Ion Transfer Enables Versatile Measurements of Electrochemical Surface Area for Intrinsic Activity Comparisons. *J. Am. Chem. Soc.* **2018**, *140* (7), 2397–2400. https://doi.org/10.1021/jacs.7b10966.
(74) Vericat, C.; E. Vela, M.; C. Salvarezza, R. Self-Assembled Monolayers of Alkanethiols on Au(111): Surface Structures, Defects and Dynamics. *Phys. Chem. Chem. Phys.* **2005**, *7* (18), 3258–3268. https://doi.org/10.1039/B505903H.

(75) Worley, B. C.; Ricks, W. A.; Prendergast, M. P.; Gregory, B. W.; Collins, R.; Cassimus, J. J. Jr.; Thompson, R. G. Anodic Passivation of Tin by Alkanethiol Self-Assembled Monolayers Examined by Cyclic Voltammetry and Coulometry. *Langmuir* **2013**, *29* (42), 12969–12981. https://doi.org/10.1021/la402703w.
(76) Calvente, J. J.; Kováčová, Z.; Sanchez, M. D.; Andreu, R.; Fawcett, W. R. Desorption of Spontaneously Adsorbed and Electrochemically Readsorbed 2-Mercaptoethanesulfonate on Au(111). *Langmuir* **1996**, *12* (23), 5696–5703. https://doi.org/10.1021/la9601770.
(77) Jaffey, D. M.; Madix, R. J. Reactivity of Sulfur-Containing Molecules on Noble Metal Surfaces. 2. Tert-Butyl Thioalcohol on Au(110). *J. Am. Chem. Soc.* **1994**, *116* (7), 3012–3019. https://doi.org/10.1021/ja00086a034.
(78) Rouhana, L. L.; Moussallem, M. D.; Schlenoff, J. B. Adsorption of Short-Chain Thiols and Disulfides onto Gold under Defined Mass Transport Conditions: Coverage, Kinetics, and Mechanism. *J. Am. Chem. Soc.* **2011**, *133* (40), 16080–16091. https://doi.org/10.1021/ja2041833.
(79) Blanchette, Z.; Zhang, J.; Yazdi, S.; Griffin, M. B.; Schwartz, D. K.; Medlin, J. W. Investigating Deposition Sequence during Synthesis of Pd/Al $_2$ O $_3$ Catalysts Modified with Organic Monolayers. *Catal. Sci. Technol.* **2022**, *12* (7), 2306–2314. https://doi.org/10.1039/D1CY02131A.
(80) *Organic Chemistry*. https://www.pearson.com/content/one-dot-com/one-dot-com/us/en/higher-education/product.html (accessed 2023-02-28).
(81) Hiramatsu, N.; Kusa, F.; Imasaka, K.; Morichika, I.; Takegami, A.; Ashihara, S. Propagation Length of Mid-Infrared Surface Plasmon Polaritons on Gold: Impact of Morphology Change by Thermal Annealing. *J. Appl. Phys.* **2016**, *120* (17), 173103. https://doi.org/10.1063/1.4966934.
(82) Ramos, N. C.; Medlin, J. W.; Holewinski, A. Electrochemical Stability of Thiolate Self-Assembled Monolayers on Au, Pt, and Cu. *ACS Appl. Mater. Interfaces* **2023**, *15* (11), 14470–14480. https://doi.org/10.1021/acsami.3c01224.
(83) Boyd, S.; Kirkwood, J. Quantitative Analysis Using ATR-FTIR Spectroscopy - Application Note. **2011**.
(84) Aroca, R.; Price, B. A New Surface for Surface-Enhanced Infrared Spectroscopy: Tin Island Films. *J. Phys. Chem. B* **1997**, *101* (33), 6537–6540. https://doi.org/10.1021/jp971601o.
(85) Killian, M. M.; Villa-Aleman, E.; Sun, Z.; Crittenden, S.; Leverette, C. L. Dependence of Surface-Enhanced Infrared Absorption (SEIRA) Enhancement and Spectral Quality on the Choice of Underlying Substrate: A Closer Look at Silver (Ag) Films Prepared by Physical Vapor Deposition (PVD). *Appl. Spectrosc.* **2011**, *65* (3), 272–283. https://doi.org/10.1366/10-06176.
(86) Liu, H.; Su, Y.; Liu, Z.; Chuai, H.; Zhang, S.; Ma, X. Tailoring Microenvironment for Enhanced Electrochemical CO2 Reduction on Ultrathin Tin Oxide Derived Nanosheets. *Nano Energy* **2023**, *105*, 108031. https://doi.org/10.1016/j.nanoen.2022.108031.
(87) Moradzaman, M.; Mul, G. Infrared Analysis of Interfacial Phenomena during Electrochemical Reduction of CO $_2$ over Polycrystalline Copper Electrodes. *ACS Catal.* **2020**, *10* (15), 8049–8057. https://doi.org/10.1021/acscatal.0c02130.
(88) Hsu, J.; Eid, A. M.; Randall, C.; Houache, M. S. E.; Abu-Lebdeh, Y.; Al-Abadleh, H. A. Mechanistic In Situ ATR-FTIR Studies on the Adsorption and Desorption of Major Intermediates in CO2 Electrochemical Reduction on CuO Nanoparticles. *Langmuir* **2022**, *38* (48), 14789–14798. https://doi.org/10.1021/acs.langmuir.2c02445.

(89) Gankanda, A.; Cwiertny, D. M.; Grassian, V. H. Role of Atmospheric CO2 and H2O Adsorption on ZnO and CuO Nanoparticle Aging: Formation of New Surface Phases and the Impact on Nanoparticle Dissolution. *J. Phys. Chem. C* **2016**, *120* (34), 19195–19203. https://doi.org/10.1021/acs.jpcc.6b05931.
(90) Dunwell, M.; Lu, Q.; Heyes, J. M.; Rosen, J.; Chen, J. G.; Yan, Y.; Jiao, F.; Xu, B. The Central Role of Bicarbonate in the Electrochemical Reduction of Carbon Dioxide on Gold. *J. Am. Chem. Soc.* **2017**, *139* (10), 3774–3783. https://doi.org/10.1021/jacs.6b13287.
(91) Thornton, E. W.; Harrison, P. G. Tin Oxide Surfaces. Part 1.—Surface Hydroxyl Groups and the Chemisorption of Carbon Dioxide and Carbon Monoxide on Tin(IV) Oxide. *J. Chem. Soc. Faraday Trans. 1 Phys. Chem. Condens. Phases* **1975**, *71* (0), 461–472. https://doi.org/10.1039/F19757100461.
(92) Miki, A.; Ye, S.; Osawa, M. Surface-Enhanced IR Absorption on Platinum Nanoparticles: An Application to Real-Time Monitoring of Electrocatalytic Reactions. *Chem. Commun.* **2002**, No. 14, 1500–1501. https://doi.org/10.1039/B203392E.
(93) He, M.; Xu, B.; Lu, Q. Probing the Role of Surface Speciation of Tin Oxide and Tin Catalysts on CO2 Electroreduction Combining in Situ Raman Spectroscopy and Reactivity Investigations. *Chin. J. Catal.* **2022**, *43* (6), 1473–1477. https://doi.org/10.1016/S1872-2067(21)64014-7.
(94) Shkondin, E.; Takayama, O.; Panah, M. E. A.; Liu, P.; Larsen, P. V.; Mar, M. D.; Jensen, F.; Lavrinenko, A. V. Large-Scale High Aspect Ratio Al-Doped ZnO Nanopillars Arrays as Anisotropic Metamaterials. *Opt. Mater. Express* **2017**, *7* (5), 1606–1627. https://doi.org/10.1364/OME.7.001606.
(95) Babar, S.; Weaver, J. H. Optical Constants of Cu, Ag, and Au Revisited. *Appl. Opt.* **2015**, *54* (3), 477–481. https://doi.org/10.1364/AO.54.000477.
(96) Golovashkin, A. I.; Motulevich, G. P. Optical and Electrical Properties of Tin. *JETP* **1964**, *19*, 310–317.
(97) Overa, S.; Ko, B. H.; Zhao, Y.; Jiao, F. Electrochemical Approaches for CO2 Conversion to Chemicals: A Journey toward Practical Applications. *Acc. Chem. Res.* **2022**, *55* (5), 638–648. https://doi.org/10.1021/acs.accounts.1c00674.
(98) Monteiro, M. C. O.; Philips, M. F.; Schouten, K. J. P.; Koper, M. T. M. Efficiency and Selectivity of CO2 Reduction to CO on Gold Gas Diffusion Electrodes in Acidic Media. *Nat. Commun.* **2021**, *12* (1), 4943. https://doi.org/10.1038/s41467-021-24936-6.
(99) Singh, M. R.; Goodpaster, J. D.; Weber, A. Z.; Head-Gordon, M.; Bell, A. T. Mechanistic Insights into Electrochemical Reduction of CO2 over Ag Using Density Functional Theory and Transport Models. *Proc. Natl. Acad. Sci.* **2017**, *114* (42), E8812–E8821. https://doi.org/10.1073/pnas.1713164114.
(100) Somoza-Tornos, A.; Guerra, O. J.; Crow, A. M.; Smith, W. A.; Hodge, B.-M. Process Modeling, Techno-Economic Assessment, and Life Cycle Assessment of the Electrochemical Reduction of CO2: A Review. *iScience* **2021**, *24* (7), 102813. https://doi.org/10.1016/j.isci.2021.102813.
(101) Reutemann, W.; Kieczka, H. Formic Acid. In *Ullmann's Encyclopedia of Industrial Chemistry*; Wiley-VCH, Ed.; Wiley, 2011. https://doi.org/10.1002/14356007.a12_013.pub2.
(102) Parsons, R. Atlas of Electrochemical Equilibria in Aqueous Solutions. *J. Electroanal. Chem. Interfacial Electrochem.* **1967**, *13* (4), 471. https://doi.org/10.1016/0022-0728(67)80059-7.

(103) Lide, D. R. *CRC Handbook of Chemistry and Physics, 84th Edition*; Taylor & Francis, 2003.
(104) Deng, W.; Zhang, L.; Li, L.; Chen, S.; Hu, C.; Zhao, Z.-J.; Wang, T.; Gong, J. Crucial Role of Surface Hydroxyls on the Activity and Stability in Electrochemical CO2 Reduction. *J. Am. Chem. Soc.* **2019**, *141* (7), 2911–2915. https://doi.org/10.1021/jacs.8b13786.
(105) Chen, Y.; Vise, A.; Klein, W. E.; Cetinbas, F. C.; Myers, D. J.; Smith, W. A.; Deutsch, T. G.; Neyerlin, K. C. A Robust, Scalable Platform for the Electrochemical Conversion of CO2 to Formate: Identifying Pathways to Higher Energy Efficiencies. *ACS Energy Lett.* **2020**, *5* (6), 1825–1833. https://doi.org/10.1021/acsenergylett.0c00860.
(106) Hu, L.; Wrubel, J. A.; Baez-Cotto, C. M.; Intia, F.; Park, J. H.; Kropf, A. J.; Kariuki, N.; Huang, Z.; Farghaly, A.; Amichi, L.; Saha, P.; Tao, L.; Cullen, D. A.; Myers, D. J.; Ferrandon, M. S.; Neyerlin, K. C. A Scalable Membrane Electrode Assembly Architecture for Efficient Electrochemical Conversion of CO2 to Formic Acid. *Nat. Commun.* **2023**, *14* (1), 7605. https://doi.org/10.1038/s41467-023-43409-6.
(107) Chen, X.; Cavallo, L.; Huang, K.-W. Selectivity of Electrochemical CO2 Reduction on Metal Electrodes: The Role of the Surface Oxidized Layer. *ACS Catal.* **2023**, *13* (19), 13089–13100. https://doi.org/10.1021/acscatal.3c01970.
(108) Liu, Z.; Zong, X.; Vlachos, D. G.; Filot, I. A. W.; Hensen, E. J. M. A Computational Study of Electrochemical CO2 Reduction to Formic Acid on Metal-Doped SnO2. *Chin. J. Catal.* **2023**, *50*, 249–259. https://doi.org/10.1016/S1872-2067(23)64476-6.
(109) Liu, H.; Li, B.; Liu, Z.; Liang, Z.; Chuai, H.; Wang, H.; Lou, S. N.; Su, Y.; Zhang, S.; Ma, X. Ceria -Mediated Dynamic Sn0/Snδ+ Redox Cycle for CO2 Electroreduction. *ACS Catal.* **2023**, *13* (7), 5033–5042. https://doi.org/10.1021/acscatal.2c06135.
(110) Zhang, S.; Kang, P.; Meyer, T. J. Nanostructured Tin Catalysts for Selective Electrochemical Reduction of Carbon Dioxide to Formate. *J. Am. Chem. Soc.* **2014**, *136* (5), 1734–1737. https://doi.org/10.1021/ja4113885.
(111) Fang, L.; Lyu, X.; Xu, J. J.; Liu, Y.; Hu, X.; Reinhart, B. J.; Li, T. Operando X-Ray Absorption Spectroscopy Study of SnO2 Nanoparticles for Electrochemical Reduction of CO2 to Formate. *ACS Appl. Mater. Interfaces* **2022**, *14* (50), 55636–55643. https://doi.org/10.1021/acsami.2c17481.
(112) Dutta, A.; Kuzume, A.; Kaliginedi, V.; Rahaman, M.; Sinev, I.; Ahmadi, M.; Roldán Cuenya, B.; Vesztergom, S.; Broekmann, P. Probing the Chemical State of Tin Oxide NP Catalysts during CO2 Electroreduction: A Complementary *Operando* Approach. *Nano Energy* **2018**, *53*, 828–840. https://doi.org/10.1016/j.nanoen.2018.09.033.
(113) Jiang, Y.; Shan, J.; Wang, P.; Huang, L.; Zheng, Y.; Qiao, S.-Z. Stabilizing Oxidation State of SnO2 for Highly Selective CO2 Electroreduction to Formate at Large Current Densities. *ACS Catal.* **2023**, *13* (5), 3101–3108. https://doi.org/10.1021/acscatal.3c00123.
(114) Liu, L.-X.; Zhou, Y.; Chang, Y.-C.; Zhang, J.-R.; Jiang, L.-P.; Zhu, W.; Lin, Y. Tuning Sn3O4 for CO2 Reduction to Formate with Ultra-High Current Density. *Nano Energy* **2020**, *77*, 105296. https://doi.org/10.1016/j.nanoen.2020.105296.
(115) Dutta, A.; Kuzume, A.; Rahaman, M.; Vesztergom, S.; Broekmann, P. Monitoring the Chemical State of Catalysts for CO2 Electroreduction: An In Operando Study. *ACS Catal.* **2015**, *5* (12), 7498–7502. https://doi.org/10.1021/acscatal.5b02322.
(116) Chen, Y.; Kanan, M. W. Tin Oxide Dependence of the CO2 Reduction Efficiency on Tin Electrodes and Enhanced Activity for Tin/Tin Oxide Thin-Film Catalysts. *J. Am. Chem. Soc.* **2012**, *134* (4), 1986–1989. https://doi.org/10.1021/ja2108799.

(117) Feaster, J. T.; Shi, C.; Cave, E. R.; Hatsukade, T.; Abram, D. N.; Kuhl, K. P.; Hahn, C.; Nørskov, J. K.; Jaramillo, T. F. Understanding Selectivity for the Electrochemical Reduction of Carbon Dioxide to Formic Acid and Carbon Monoxide on Metal Electrodes. *ACS Catal.* **2017**, *7* (7), 4822–4827. https://doi.org/10.1021/acscatal.7b00687.
(118) Salvini, C.; Re Fiorentin, M.; Risplendi, F.; Raffone, F.; Cicero, G. Active Surface Structure of SnO2 Catalysts for CO2 Reduction Revealed by Ab Initio Simulations. *J. Phys. Chem. C* **2022**, *126* (34), 14441–14447. https://doi.org/10.1021/acs.jpcc.2c02583.
(119) Nørskov, J. K.; Rossmeisl, J.; Logadottir, A.; Lindqvist, L.; Kitchin, J. R.; Bligaard, T.; Jónsson, H. Origin of the Overpotential for Oxygen Reduction at a Fuel-Cell Cathode. *J. Phys. Chem. B* **2004**, *108* (46), 17886–17892. https://doi.org/10.1021/jp047349j.
(120) Lindgren, P.; Kastlunger, G.; Peterson, A. A. Electrochemistry from the Atomic Scale, in the Electronically Grand-Canonical Ensemble. *J. Chem. Phys.* **2022**, *157* (18), 180902. https://doi.org/10.1063/5.0123656.
(121) Tezak, C. R.; Singstock, N. R.; Alherz, A. W.; Vigil-Fowler, D.; Sutton, C. A.; Sundararaman, R.; Musgrave, C. B. Revised Nitrogen Reduction Scaling Relations from Potential-Dependent Modeling of Chemical and Electrochemical Steps. *ACS Catal.* **2023**, *13* (19), 12894–12903. https://doi.org/10.1021/acscatal.3c01978.
(122) Alsunni, Y. A.; Musgrave, C. B. Effect of Applied Potential on Metal Surfaces: Surface Energy, Wulff Shape and Charge Distribution. *Appl. Surf. Sci.* **2023**, *610*, 155147. https://doi.org/10.1016/j.apsusc.2022.155147.
(123) Alsunni, Y. A.; Alherz, A. W.; Musgrave, C. B. Electrocatalytic Reduction of CO2 to CO over Ag(110) and Cu(211) Modeled by Grand-Canonical Density Functional Theory. *J. Phys. Chem. C* **2021**, *125* (43), 23773–23783. https://doi.org/10.1021/acs.jpcc.1c07484.
(124) Brimley, P.; Almajed, H.; Alsunni, Y.; Alherz, A. W.; Bare, Z. J. L.; Smith, W. A.; Musgrave, C. B. Electrochemical CO2 Reduction over Metal-/Nitrogen-Doped Graphene Single-Atom Catalysts Modeled Using the Grand-Canonical Density Functional Theory. *ACS Catal.* **2022**, *12* (16), 10161–10171. https://doi.org/10.1021/acscatal.2c01832.
(125) Fishler, Y.; Leick, N.; Teeter, G.; Holewinski, A.; Smith, W. A. Layered Sn–Au Thin Films for Increased Electrochemical ATR-SEIRAS Enhancement. *ACS Appl. Mater. Interfaces* **2024**, *16* (15), 19780–19791. https://doi.org/10.1021/acsami.4c01525.
(126) Yan; Li, Q.-X.; Huo, S.-J.; Ma, M.; Cai, W.-B.; Osawa, M. Ubiquitous Strategy for Probing ATR Surface-Enhanced Infrared Absorption at Platinum Group Metal−Electrolyte Interfaces. *J. Phys. Chem. B* **2005**, *109* (16), 7900–7906. https://doi.org/10.1021/jp044085s.
(127) Wang, H.; Zhou, Y.-W.; Cai, W.-B. Recent Applications of *in Situ* ATR-IR Spectroscopy in Interfacial Electrochemistry. *Curr. Opin. Electrochem.* **2017**, *1* (1), 73–79. https://doi.org/10.1016/j.coelec.2017.01.008.
(128) Dunwell, M.; Yang, X.; Yan, Y.; Xu, B. Potential Routes and Mitigation Strategies for Contamination in Interfacial Specific Infrared Spectroelectrochemical Studies. *J. Phys. Chem. C* **2018**, *122* (43), 24658–24664. https://doi.org/10.1021/acs.jpcc.8b05634.
(129) Jerkiewicz, G. Applicability of Platinum as a Counter-Electrode Material in Electrocatalysis Research. *ACS Catal.* **2022**, *12* (4), 2661–2670. https://doi.org/10.1021/acscatal.1c06040.
(130) Topalov, A. A.; Katsounaros, I.; Auinger, M.; Cherevko, S.; Meier, J. C.; Klemm, S. O.; Mayrhofer, K. J. J. Dissolution of Platinum: Limits for the Deployment of Electrochemical Energy Conversion? *Angew. Chem. Int. Ed.* **2012**, *51* (50), 12613–12615. https://doi.org/10.1002/anie.201207256.

(131) Duan, Z.; Henkelman, G. Atomic-Scale Mechanisms of Electrochemical Pt Dissolution. *ACS Catal.* **2021**, *11* (23), 14439–14447. https://doi.org/10.1021/acscatal.1c02366.
(132) Sundararaman, R.; Letchworth-Weaver, K.; Schwarz, K. A.; Gunceler, D.; Ozhabes, Y.; Arias, T. A. JDFTx: Software for Joint Density-Functional Theory. *SoftwareX* **2017**, *6*, 278–284. https://doi.org/10.1016/j.softx.2017.10.006.
(133) Perdew, J. P.; Burke, K.; Ernzerhof, M. Generalized Gradient Approximation Made Simple. *Phys. Rev. Lett.* **1996**, *77* (18), 3865–3868. https://doi.org/10.1103/PhysRevLett.77.3865.
(134) Grimme, S.; Antony, J.; Ehrlich, S.; Krieg, H. A Consistent and Accurate Ab Initio Parametrization of Density Functional Dispersion Correction (DFT-D) for the 94 Elements H-Pu. *J. Chem. Phys.* **2010**, *132* (15), 154104. https://doi.org/10.1063/1.3382344.
(135) Garrity, K. F.; Bennett, J. W.; Rabe, K. M.; Vanderbilt, D. Pseudopotentials for High-Throughput DFT Calculations. *Comput. Mater. Sci.* **2014**, *81*, 446–452. https://doi.org/10.1016/j.commatsci.2013.08.053.
(136) Sundararaman, R.; Goddard, W. A., III. The Charge-Asymmetric Nonlocally Determined Local-Electric (CANDLE) Solvation Model. *J. Chem. Phys.* **2015**, *142* (6), 064107. https://doi.org/10.1063/1.4907731.
(137) Rhodes, K. J.; Meisner, R.; Kirkham, M.; Dudney, N.; Daniel, C. In Situ XRD of Thin Film Tin Electrodes for Lithium Ion Batteries. *J. Electrochem. Soc.* **2012**, *159* (3), A294. https://doi.org/10.1149/2.077203jes.
(138) Shieh, S. R.; Kubo, A.; Duffy, T. S.; Prakapenka, V. B.; Shen, G. High-Pressure Phases in ${\mathrm{SnO}}_{2}$ to 117 GPa. *Phys. Rev. B* **2006**, *73* (1), 014105. https://doi.org/10.1103/PhysRevB.73.014105.
(139) Haines, J.; Léger, J. M. X-Ray Diffraction Study of the Phase Transitions and Structural Evolution of Tin Dioxide at High Pressure:ffRelationships between Structure Types and Implications for Other Rutile-Type Dioxides. *Phys. Rev. B* **1997**, *55* (17), 11144–11154. https://doi.org/10.1103/PhysRevB.55.11144.
(140) Eckold, P.; Sellers, M. S.; Niewa, R.; Hügel, W. The Surface Energies of β-Sn — A New Concept for Corrosion and Whisker Mitigation. *Microelectron. Reliab.* **2015**, *55* (12, Part B), 2799–2807. https://doi.org/10.1016/j.microrel.2015.08.018.
(141) Oviedo, J.; Gillan, M. J. Energetics and Structure of Stoichiometric SnO2 Surfaces Studied by First-Principles Calculations. *Surf. Sci.* **2000**, *463* (2), 93–101. https://doi.org/10.1016/S0039-6028(00)00612-9.
(142) Tran, R.; Xu, Z.; Radhakrishnan, B.; Winston, D.; Sun, W.; Persson, K. A.; Ong, S. P. Surface Energies of Elemental Crystals. *Sci. Data* **2016**, *3* (1), 160080. https://doi.org/10.1038/sdata.2016.80.
(143) Hjorth Larsen, A.; Jørgen Mortensen, J.; Blomqvist, J.; Castelli, I. E.; Christensen, R.; Dułak, M.; Friis, J.; Groves, M. N.; Hammer, B.; Hargus, C.; Hermes, E. D.; Jennings, P. C.; Bjerre Jensen, P.; Kermode, J.; Kitchin, J. R.; Leonhard Kolsbjerg, E.; Kubal, J.; Kaasbjerg, K.; Lysgaard, S.; Bergmann Maronsson, J.; Maxson, T.; Olsen, T.; Pastewka, L.; Peterson, A.; Rostgaard, C.; Schiøtz, J.; Schütt, O.; Strange, M.; Thygesen, K. S.; Vegge, T.; Vilhelmsen, L.; Walter, M.; Zeng, Z.; Jacobsen, K. W. The Atomic Simulation Environment-a Python Library for Working with Atoms. *J. Phys. Condens. Matter Inst. Phys. J.* **2017**, *29* (27), 273002. https://doi.org/10.1088/1361-648X/aa680e.

(144) Lindan, P. J. D. Water Chemistry at the SnO2(110) Surface: The Role of Inter-Molecular Interactions and Surface Geometry. *Chem. Phys. Lett.* **2000**, *328* (4–6), 325–329. https://doi.org/10.1016/S0009-2614(00)00963-5.
(145) Lindan, P. J. D.; Harrison, N. M.; Gillan, M. J. Mixed Dissociative and Molecular Adsorption of Water on the Rutile (110) Surface. *Phys. Rev. Lett.* **1998**, *80* (4), 762–765. https://doi.org/10.1103/PhysRevLett.80.762.
(146) Zhang, C.; Lindan, P. J. D. Towards a First-Principles Picture of the Oxide–Water Interface. *J. Chem. Phys.* **2003**, *119* (17), 9183–9190. https://doi.org/10.1063/1.1614208.
(147) Whittaker, T.; Kumar, K. B. S.; Peterson, C.; Pollock, M. N.; Grabow, L. C.; Chandler, B. D. H2 Oxidation over Supported Au Nanoparticle Catalysts: Evidence for Heterolytic H2 Activation at the Metal–Support Interface. *J. Am. Chem. Soc.* **2018**, *140* (48), 16469–16487. https://doi.org/10.1021/jacs.8b04991.
(148) Chen, J.; Cheng, C.; Bai, Y.-M.; Liu, H.; Dong, C.; Du, X.-W. Identifying a Key Factor Determining Interfacial Electron Transfer in CO2 Reduction to Formate: Potential of Zero Charge. *J. Phys. Chem. C* **2023**, *127* (20), 9623–9630. https://doi.org/10.1021/acs.jpcc.3c01692.
(149) Evans, M. G.; Polanyi, M. Inertia and Driving Force of Chemical Reactions. *Trans. Faraday Soc.* **1938**, *34* (0), 11–24. https://doi.org/10.1039/TF9383400011.
(150) Bligaard, T.; Nørskov, J. K.; Dahl, S.; Matthiesen, J.; Christensen, C. H.; Sehested, J. The Brønsted–Evans–Polanyi Relation and the Volcano Curve in Heterogeneous Catalysis. *J. Catal.* **2004**, *224* (1), 206–217. https://doi.org/10.1016/j.jcat.2004.02.034.
(151) Liu, Z.-P.; Hu, P. General Trends in the Barriers of Catalytic Reactions on Transition Metal Surfaces. *J. Chem. Phys.* **2001**, *115* (11), 4977–4980. https://doi.org/10.1063/1.1403006.
(152) Quan, J.; Muttaqien, F.; Kondo, T.; Kozarashi, T.; Mogi, T.; Imabayashi, T.; Hamamoto, Y.; Inagaki, K.; Hamada, I.; Morikawa, Y.; Nakamura, J. Vibration-Driven Reaction of CO2 on Cu Surfaces via Eley–Rideal-Type Mechanism. *Nat. Chem.* **2019**, *11* (8), 722–729. https://doi.org/10.1038/s41557-019-0282-1.
(153) Domínguez-Flores, F.; Melander, M. M. Approximating Constant Potential DFT with Canonical DFT and Electrostatic Corrections. *J. Chem. Phys.* **2023**, *158* (14), 144701. https://doi.org/10.1063/5.0138197.
(154) Durst, J.; Siebel, A.; Simon, C.; Hasché, F.; Herranz, J.; Gasteiger, H. A. New Insights into the Electrochemical Hydrogen Oxidation and Evolution Reaction Mechanism. *Energy Environ. Sci.* **2014**, *7* (7), 2255–2260. https://doi.org/10.1039/C4EE00440J.
(155) Azizi, O.; Jafarian, M.; Gobal, F.; Heli, H.; Mahjani, M. G. The Investigation of the Kinetics and Mechanism of Hydrogen Evolution Reaction on Tin. *Int. J. Hydrog. Energy* **2007**, *32* (12), 1755–1761. https://doi.org/10.1016/j.ijhydene.2006.08.043.
(156) Wuttig, A.; Yoon, Y.; Ryu, J.; Surendranath, Y. Bicarbonate Is Not a General Acid in Au-Catalyzed CO2 Electroreduction. *J. Am. Chem. Soc.* **2017**, *139* (47), 17109–17113. https://doi.org/10.1021/jacs.7b08345.
(157) Shan, W.; Liu, R.; Zhao, H.; Liu, J. Bicarbonate Rebalances the *COOH/*OCO- Dual Pathways in CO2 Electrocatalytic Reduction: In Situ Surface-Enhanced Raman Spectroscopic Evidence. *J. Phys. Chem. Lett.* **2022**, *13* (31), 7296–7305. https://doi.org/10.1021/acs.jpclett.2c01372.
(158) Monteiro, M. C. O.; Mirabal, A.; Jacobse, L.; Doblhoff-Dier, K.; Barton, S. C.; Koper, M. T. M. Time-Resolved Local pH Measurements during CO2 Reduction Using Scanning

Electrochemical Microscopy: Buffering and Tip Effects. *JACS Au* **2021**, *1* (11), 1915–1924. https://doi.org/10.1021/jacsau.1c00289.
(159) Webb, J. D.; Gedvilas, L. M.; Crandall, R. S.; Iwaniczko, E.; Nelson, B. P.; Mahan, A. H.; Reedy, R.; Matson, R. J. Anisotropy in Hydrogenated Amorphous Silicon Films as Observed Using Polarized Ftir-Atr Spectroscopy. *MRS Proc.* **1999**, *557*, 311. https://doi.org/10.1557/PROC-557-311.
(160) Pennathur, A. K.; Tseng, C.; Salazar, N.; Dawlaty, J. M. Controlling Water Delivery to an Electrochemical Interface with Surfactants. *J. Am. Chem. Soc.* **2023**, *145* (4), 2421–2429. https://doi.org/10.1021/jacs.2c11503.
(161) Ge, W.; Chen, Y.; Fan, Y.; Zhu, Y.; Liu, H.; Song, L.; Liu, Z.; Lian, C.; Jiang, H.; Li, C. Dynamically Formed Surfactant Assembly at the Electrified Electrode–Electrolyte Interface Boosting CO2 Electroreduction. *J. Am. Chem. Soc.* **2022**, *144* (14), 6613–6622. https://doi.org/10.1021/jacs.2c02486.
(162) Jiang, T.-W.; Qin, X.; Ye, K.; Zhang, W.-Y.; Li, H.; Liu, W.; Huo, S.; Zhang, X.-G.; Jiang, K.; Cai, W.-B. An Interactive Study of Catalyst and Mechanism for Electrochemical CO2 Reduction to Formate on Pd Surfaces. *Appl. Catal. B Environ.* **2023**, *334*, 122815. https://doi.org/10.1016/j.apcatb.2023.122815.
(163) Cao, C.; Ma, D.-D.; Gu, J.-F.; Xie, X.; Zeng, G.; Li, X.; Han, S.-G.; Zhu, Q.-L.; Wu, X.-T.; Xu, Q. Metal–Organic Layers Leading to Atomically Thin Bismuthene for Efficient Carbon Dioxide Electroreduction to Liquid Fuel. *Angew. Chem. Int. Ed.* **2020**, *59* (35), 15014–15020. https://doi.org/10.1002/anie.202005577.
(164) Vijay, S.; Kastlunger, G.; Chan, K.; Nørskov, J. K. Limits to Scaling Relations between Adsorption Energies? *J. Chem. Phys.* **2022**, *156* (23), 231102. https://doi.org/10.1063/5.0096625.
(165) Liu, F.; Ren, X.; Zhao, J.; Wu, H.; Wang, J.; Han, X.; Deng, Y.; Hu, W. Inhibiting Sulfur Dissolution and Enhancing Activity of SnS for CO2 Electroreduction via Electronic State Modulation. *ACS Catal.* **2022**, *12* (21), 13533–13541. https://doi.org/10.1021/acscatal.2c02617.
(166) Li, K.; Xu, J.; Zheng, T.; Yuan, Y.; Liu, S.; Shen, C.; Jiang, T.; Sun, J.; Liu, Z.; Xu, Y.; Chuai, M.; Xia, C.; Chen, W. In Situ Dynamic Construction of a Copper Tin Sulfide Catalyst for High-Performance Electrochemical CO2 Conversion to Formate. *ACS Catal.* **2022**, *12* (16), 9922–9932. https://doi.org/10.1021/acscatal.2c02627.
(167) Atrak, N.; Tayyebi, E.; Skúlason, E. Insight into Catalytic Active Sites on TiO2/RuO2 and SnO2/RuO2 Alloys for Electrochemical CO2 Reduction to CO and Formic Acid. *ACS Catal.* **2023**, *13* (8), 5491–5501. https://doi.org/10.1021/acscatal.3c00450.
(168) Kim, C.; Bui, J. C.; Luo, X.; Cooper, J. K.; Kusoglu, A.; Weber, A. Z.; Bell, A. T. Tailored Catalyst Microenvironments for CO2 Electroreduction to Multicarbon Products on Copper Using Bilayer Ionomer Coatings. *Nat. Energy* **2021**, *6* (11), 1026–1034. https://doi.org/10.1038/s41560-021-00920-8.
(169) Baruch, M. F.; Pander, J. E.; White, J. L.; Bocarsly, A. B. Mechanistic Insights into the Reduction of CO2 on Tin Electrodes Using in Situ ATR-IR Spectroscopy. *ACS Catal.* **2015**, *5* (5), 3148–3156. https://doi.org/10.1021/acscatal.5b00402.
(170) Resasco, J.; Bell, A. T. Electrocatalytic CO2 Reduction to Fuels: Progress and Opportunities. *Trends Chem.* **2020**, *2* (9), 825–836. https://doi.org/10.1016/j.trechm.2020.06.007.

(171) Fan, L.; Xia, C.; Yang, F.; Wang, J.; Wang, H.; Lu, Y. Strategies in Catalysts and Electrolyzer Design for Electrochemical CO2 Reduction toward C2+ Products. *Sci. Adv.* **2020**, *6* (8), eaay3111. https://doi.org/10.1126/sciadv.aay3111.
(172) Xia, R.; Overa, S.; Jiao, F. Emerging Electrochemical Processes to Decarbonize the Chemical Industry. *JACS Au* **2022**, *2* (5), 1054–1070. https://doi.org/10.1021/jacsau.2c00138.
(173) Grim, R. G.; Huang, Z.; Guarnieri, M. T.; Ferrell, J. R.; Tao, L.; Schaidle, J. A. Transforming the Carbon Economy: Challenges and Opportunities in the Convergence of Low-Cost Electricity and Reductive CO2 Utilization. *Energy Environ. Sci.* **2020**, *13* (2), 472–494. https://doi.org/10.1039/C9EE02410G.
(174) Masel, R. I.; Liu, Z.; Yang, H.; Kaczur, J. J.; Carrillo, D.; Ren, S.; Salvatore, D.; Berlinguette, C. P. An Industrial Perspective on Catalysts for Low-Temperature CO2 Electrolysis. *Nat. Nanotechnol.* **2021**, *16* (2), 118–128. https://doi.org/10.1038/s41565-020-00823-x.
(175) Huang, Z.; Grim, R. G.; Schaidle, J. A.; Tao, L. The Economic Outlook for Converting CO2 and Electrons to Molecules. *Energy Environ. Sci.* **2021**, *14* (7), 3664–3678. https://doi.org/10.1039/D0EE03525D.
(176) Sheehan, S. W.; Buonsanti, R. Deriving Value from CO2: From Catalyst Design to Industrial Implementation. *Chem Catal.* **2021**, *1* (4), 751–753. https://doi.org/10.1016/j.checat.2021.08.010.
(177) Zhang, S.; Fan, Q.; Xia, R.; Meyer, T. J. CO2 Reduction: From Homogeneous to Heterogeneous Electrocatalysis. *Acc. Chem. Res.* **2020**, *53* (1), 255–264. https://doi.org/10.1021/acs.accounts.9b00496.
(178) Liang, S.; Altaf, N.; Huang, L.; Gao, Y.; Wang, Q. Electrolytic Cell Design for Electrochemical CO2 Reduction. *J. CO2 Util.* **2020**, *35*, 90–105. https://doi.org/10.1016/j.jcou.2019.09.007.
(179) Goldman, M.; Prajapati, A.; Duoss, E.; Baker, S.; Hahn, C. Bridging Fundamental Science and Applied Science to Accelerate CO2 Electrolyzer Scale-Up. *Curr. Opin. Electrochem.* **2023**, *39*, 101248. https://doi.org/10.1016/j.coelec.2023.101248.
(180) *Twelve | The Carbon Transformation Company™*. Twelve. https://www.twelve.co (accessed 2024-11-09).
(181) *AIR COMPANY | Carbon Technology Leader for a Decarbonized Future*. AIR COMPANY. https://www.aircompany.com/ (accessed 2024-11-09).
(182) *Converting Carbon. Storing Energy. - OCOchem*. https://ocochem.com/ (accessed 2024-11-09).
(183) *Dioxycle | Rethinking emissions and displacing fossil fuels*. https://dioxycle.com/ (accessed 2024-11-09).
(184) *Oxylus Energy - A circular economy for a zero-emission Earth*. Oxylus Energy. https://oxylusenergy.com/ (accessed 2024-11-09).
(185) Xia, C.; Zhu, P.; Jiang, Q.; Pan, Y.; Liang, W.; Stavitski, E.; Alshareef, H. N.; Wang, H. Continuous Production of Pure Liquid Fuel Solutions via Electrocatalytic CO2 Reduction Using Solid-Electrolyte Devices. *Nat. Energy* **2019**, *4* (9), 776–785. https://doi.org/10.1038/s41560-019-0451-x.
(186) Alerte, T.; Edwards, J. P.; Gabardo, C. M.; O'Brien, C. P.; Gaona, A.; Wicks, J.; Obradović, A.; Sarkar, A.; Jaffer, S. A.; MacLean, H. L.; Sinton, D.; Sargent, E. H. Downstream of the CO2 Electrolyzer: Assessing the Energy Intensity of Product Separation. *ACS Energy Lett.* **2021**, *6* (12), 4405–4412. https://doi.org/10.1021/acsenergylett.1c02263.

(187) Nabil, S. K.; McCoy, S.; Kibria, M. G. Comparative Life Cycle Assessment of Electrochemical Upgrading of CO2 to Fuels and Feedstocks. *Green Chem.* **2021**, *23* (2), 867–880. https://doi.org/10.1039/D0GC02831B.
(188) Moore, T.; Oyarzun, D. I.; Li, W.; Lin, T. Y.; Goldman, M.; Wong, A. A.; Jaffer, S. A.; Sarkar, A.; Baker, S. E.; Duoss, E. B.; Hahn, C. Electrolyzer Energy Dominates Separation Costs in State-of-the-Art CO2 Electrolyzers: Implications for Single-Pass CO2 Utilization. *Joule* **2023**, *7* (4), 782–796. https://doi.org/10.1016/j.joule.2023.03.015.
(189) De Luna, P.; Hahn, C.; Higgins, D.; Jaffer, S. A.; Jaramillo, T. F.; Sargent, E. H. What Would It Take for Renewably Powered Electrosynthesis to Displace Petrochemical Processes? *Science* **2019**, *364* (6438), eaav3506. https://doi.org/10.1126/science.aav3506.
(190) Chen, Y.; Miao, R. K.; Yu, C.; Sinton, D.; Xie, K.; Sargent, E. H. Catalyst Design for Electrochemical CO2 Reduction to Ethylene. *Matter* **2024**, *7* (1), 25–37. https://doi.org/10.1016/j.matt.2023.12.008.
(191) Karapinar, D.; Creissen, C. E.; Rivera de la Cruz, J. G.; Schreiber, M. W.; Fontecave, M. Electrochemical CO2 Reduction to Ethanol with Copper-Based Catalysts. *ACS Energy Lett.* **2021**, *6* (2), 694–706. https://doi.org/10.1021/acsenergylett.0c02610.
(192) Heenen, H. H.; Shin, H.; Kastlunger, G.; Overa, S.; Gauthier, J. A.; Jiao, F.; Chan, K. The Mechanism for Acetate Formation in Electrochemical CO(2) Reduction on Cu: Selectivity with Potential, pH, and Nanostructuring. *Energy Environ. Sci.* **2022**, *15* (9), 3978–3990. https://doi.org/10.1039/D2EE01485H.
(193) Chen, J.; Wang, T.; Li, Z.; Yang, B.; Zhang, Q.; Lei, L.; Feng, P.; Hou, Y. Recent Progress and Perspective of Electrochemical CO2 Reduction towards C2-C5 Products over Non-Precious Metal Heterogeneous Electrocatalysts. *Nano Res.* **2021**, *14* (9), 3188–3207. https://doi.org/10.1007/s12274-021-3335-x.
(194) Garza, A. J.; Bell, A. T.; Head-Gordon, M. Mechanism of CO2 Reduction at Copper Surfaces: Pathways to C2 Products. *ACS Catal.* **2018**, *8* (2), 1490–1499. https://doi.org/10.1021/acscatal.7b03477.
(195) Hori, Y.; Murata, A.; Takahashi, R. Formation of Hydrocarbons in the Electrochemical Reduction of Carbon Dioxide at a Copper Electrode in Aqueous Solution. *J. Chem. Soc. Faraday Trans. 1 Phys. Chem. Condens. Phases* **1989**, *85* (8), 2309–2326. https://doi.org/10.1039/F19898502309.
(196) Bagger, A.; Ju, W.; Varela, A. S.; Strasser, P.; Rossmeisl, J. Electrochemical CO2 Reduction: A Classification Problem. *ChemPhysChem* **2017**, *18* (22), 3266–3273. https://doi.org/10.1002/cphc.201700736.
(197) Luc, W.; Fu, X.; Shi, J.; Lv, J.-J.; Jouny, M.; Ko, B. H.; Xu, Y.; Tu, Q.; Hu, X.; Wu, J.; Yue, Q.; Liu, Y.; Jiao, F.; Kang, Y. Two-Dimensional Copper Nanosheets for Electrochemical Reduction of Carbon Monoxide to Acetate. *Nat. Catal.* **2019**, *2* (5), 423–430. https://doi.org/10.1038/s41929-019-0269-8.
(198) Gao, D.; Arán-Ais, R. M.; Jeon, H. S.; Roldan Cuenya, B. Rational Catalyst and Electrolyte Design for CO2 Electroreduction towards Multicarbon Products. *Nat. Catal.* **2019**, *2* (3), 198–210. https://doi.org/10.1038/s41929-019-0235-5.
(199) Lin, Y.-R.; Lee, D. U.; Tan, S.; Koshy, D. M.; Lin, T. Y.; Wang, L.; Corral, D.; Avilés Acosta, J. E.; Zamora Zeledon, J. A.; Beck, V. A.; Baker, S. E.; Duoss, E. B.; Hahn, C.; Jaramillo, T. F. Vapor-Fed Electrolyzers for Carbon Dioxide Reduction Using Tandem Electrocatalysts: Cuprous Oxide Coupled with Nickel-Coordinated Nitrogen-Doped Carbon. *Adv. Funct. Mater.* **2022**, *32* (28), 2113252. https://doi.org/10.1002/adfm.202113252.

(200) Rasouli, A. S.; Wang, X.; Wicks, J.; Dinh, C.-T.; Abed, J.; Wu, F.-Y.; Hung, S.-F.; Bertens, K.; Huang, J. E.; Sargent, E. H. Ga Doping Disrupts C-C Coupling and Promotes Methane Electroproduction on CuAl Catalysts. *Chem Catal.* **2022**, *2* (4), 908–916. https://doi.org/10.1016/j.checat.2022.03.016.
(201) Wu, Y.; Chen, C.; Yan, X.; Wu, R.; Liu, S.; Ma, J.; Zhang, J.; Liu, Z.; Xing, X.; Wu, Z.; Han, B. Enhancing CO2 Electroreduction to CH4 over Cu Nanoparticles Supported on N-Doped Carbon. *Chem. Sci.* **2022**, *13* (28), 8388–8394. https://doi.org/10.1039/D2SC02222B.
(202) De Gregorio, G. L.; Burdyny, T.; Loiudice, A.; Iyengar, P.; Smith, W. A.; Buonsanti, R. Facet-Dependent Selectivity of Cu Catalysts in Electrochemical CO2 Reduction at Commercially Viable Current Densities. *ACS Catal.* **2020**, *10* (9), 4854–4862. https://doi.org/10.1021/acscatal.0c00297.
(203) Tomboc, G. M.; Choi, S.; Kwon, T.; Hwang, Y. J.; Lee, K. Potential Link between Cu Surface and Selective CO2 Electroreduction: Perspective on Future Electrocatalyst Designs. *Adv. Mater.* **2020**, *32* (17), 1908398. https://doi.org/10.1002/adma.201908398.
(204) Akter, T.; Pan, H.; Barile, C. J. Tandem Electrocatalytic CO2 Reduction inside a Membrane with Enhanced Selectivity for Ethylene. *J. Phys. Chem. C* **2022**, *126* (24), 10045–10052. https://doi.org/10.1021/acs.jpcc.2c01663.
(205) Ozden, A.; Li, F.; García de Arquer, F. P.; Rosas-Hernández, A.; Thevenon, A.; Wang, Y.; Hung, S.-F.; Wang, X.; Chen, B.; Li, J.; Wicks, J.; Luo, M.; Wang, Z.; Agapie, T.; Peters, J. C.; Sargent, E. H.; Sinton, D. High-Rate and Efficient Ethylene Electrosynthesis Using a Catalyst/Promoter/Transport Layer. *ACS Energy Lett.* **2020**, *5* (9), 2811–2818. https://doi.org/10.1021/acsenergylett.0c01266.
(206) Huang, M.; Gong, S.; Wang, C.; Yang, Y.; Jiang, P.; Wang, P.; Hu, L.; Chen, Q. Lewis-Basic EDTA as a Highly Active Molecular Electrocatalyst for CO2 Reduction to CH4. *Angew. Chem. Int. Ed.* **2021**, *60* (42), 23002–23009. https://doi.org/10.1002/anie.202110594.
(207) Banerjee, S.; Gerke, C. S.; Thoi, V. S. Guiding CO2RR Selectivity by Compositional Tuning in the Electrochemical Double Layer. *Acc. Chem. Res.* **2022**, *55* (4), 504–515. https://doi.org/10.1021/acs.accounts.1c00680.
(208) Nie, W.; Heim, G. P.; Watkins, N. B.; Agapie, T.; Peters, J. C. Organic Additive-Derived Films on Cu Electrodes Promote Electrochemical CO2 Reduction to C2+ Products Under Strongly Acidic Conditions. *Angew. Chem. Int. Ed.* **2023**, *62* (12), e202216102. https://doi.org/10.1002/anie.202216102.
(209) Han, Z.; Kortlever, R.; Chen, H.-Y.; Peters, J. C.; Agapie, T. CO2 Reduction Selective for C≥2 Products on Polycrystalline Copper with N-Substituted Pyridinium Additives. *ACS Cent. Sci.* **2017**, *3* (8), 853–859. https://doi.org/10.1021/acscentsci.7b00180.
(210) König, M.; Vaes, J.; Klemm, E.; Pant, D. Solvents and Supporting Electrolytes in the Electrocatalytic Reduction of CO2. *iScience* **2019**, *19*, 135–160. https://doi.org/10.1016/j.isci.2019.07.014.
(211) Moura de Salles Pupo, M.; Kortlever, R. Electrolyte Effects on the Electrochemical Reduction of CO2. *ChemPhysChem* **2019**, *20* (22), 2926–2935. https://doi.org/10.1002/cphc.201900680.
(212) Deng, B.; Huang, M.; Zhao, X.; Mou, S.; Dong, F. Interfacial Electrolyte Effects on Electrocatalytic CO2 Reduction. *ACS Catal.* **2022**, *12* (1), 331–362. https://doi.org/10.1021/acscatal.1c03501.

(213) Marcandalli, G.; Monteiro, M. C. O.; Goyal, A.; Koper, M. T. M. Electrolyte Effects on CO2 Electrochemical Reduction to CO. *Acc. Chem. Res.* **2022**, *55* (14), 1900–1911. https://doi.org/10.1021/acs.accounts.2c00080.
(214) Shin, S.-J.; Choi, H.; Ringe, S.; Won, D. H.; Oh, H.-S.; Kim, D. H.; Lee, T.; Nam, D.-H.; Kim, H.; Choi, C. H. A Unifying Mechanism for Cation Effect Modulating C1 and C2 Productions from CO2 Electroreduction. Research Square May 4, 2022. https://doi.org/10.21203/rs.3.rs-1589012/v1.
(215) Verma, S.; Lu, X.; Ma, S.; Masel, R. I.; Kenis, P. J. A. The Effect of Electrolyte Composition on the Electroreduction of CO2 to CO on Ag Based Gas Diffusion Electrodes. *Phys. Chem. Chem. Phys.* **2016**, *18* (10), 7075–7084. https://doi.org/10.1039/C5CP05665A.
(216) Varela, A. S.; Ju, W.; Reier, T.; Strasser, P. Tuning the Catalytic Activity and Selectivity of Cu for CO2 Electroreduction in the Presence of Halides. *ACS Catal.* **2016**, *6* (4), 2136–2144. https://doi.org/10.1021/acscatal.5b02550.
(217) Tomisaki, M.; Kasahara, S.; Natsui, K.; Ikemiya, N.; Einaga, Y. Switchable Product Selectivity in the Electrochemical Reduction of Carbon Dioxide Using Boron-Doped Diamond Electrodes. *J. Am. Chem. Soc.* **2019**, *141* (18), 7414–7420. https://doi.org/10.1021/jacs.9b01773.
(218) Yoo, J. M.; Ingenmey, J.; Salanne, M.; Lukatskaya, M. R. Anion Effect in Electrochemical CO2 Reduction: From Spectators to Orchestrators. *J. Am. Chem. Soc.* **2024**. https://doi.org/10.1021/jacs.4c10661.
(219) Suo, L.; Borodin, O.; Gao, T.; Olguin, M.; Ho, J.; Fan, X.; Luo, C.; Wang, C.; Xu, K. "Water-in-Salt" Electrolyte Enables High-Voltage Aqueous Lithium-Ion Chemistries. *Science* **2015**, *350* (6263), 938–943. https://doi.org/10.1126/science.aab1595.
(220) Amiri, M.; Bélanger, D. Physicochemical and Electrochemical Characterization of Salt-in-Water and Water-in-Salt Potassium and Lithium Acetate Electrolytes. *J. Mater. Chem. A* **2021**, *9* (42), 24012–24023. https://doi.org/10.1039/D1TA07214E.
(221) Zhao, Y.; Hu, X.; Stucky, G. D.; Boettcher, S. W. Thermodynamic, Kinetic, and Transport Contributions to Hydrogen Evolution Activity and Electrolyte-Stability Windows for Water-in-Salt Electrolytes. *J. Am. Chem. Soc.* **2024**, *146* (5), 3438–3448. https://doi.org/10.1021/jacs.3c12980.
(222) Xiao, D.; Zhang, L.; Li, Z.; Dou, H.; Zhang, X. Design Strategies and Research Progress for Water-in-Salt Electrolytes. *Energy Storage Mater.* **2022**, *44*, 10–28. https://doi.org/10.1016/j.ensm.2021.09.035.
(223) Dong, Q.; Zhang, X.; He, D.; Lang, C.; Wang, D. Role of H2O in CO2 Electrochemical Reduction As Studied in a Water-in-Salt System. *ACS Cent. Sci.* **2019**, *5* (8), 1461–1467. https://doi.org/10.1021/acscentsci.9b00519.
(224) Ren, W.; Xu, A.; Chan, K.; Hu, X. A Cation Concentration Gradient Approach to Tune the Selectivity and Activity of CO2 Electroreduction. *Angew. Chem. Int. Ed.* **2022**, *61* (49), e202214173. https://doi.org/10.1002/anie.202214173.
(225) Zhang, H.; Gao, J.; Raciti, D.; Hall, A. S. Promoting Cu-Catalysed CO2 Electroreduction to Multicarbon Products by Tuning the Activity of H2O. *Nat. Catal.* **2023**, 1–11. https://doi.org/10.1038/s41929-023-01010-6.
(226) Avilés Acosta, J. E.; Lin, J. C.; Un Lee, D.; Jaramillo, T. F.; Hahn, C. Electrochemical Flow Reactor Design Allows Tunable Mass Transport Conditions for Operando Surface Enhanced Infrared Absorption Spectroscopy. *ChemCatChem* **2023**, *15* (15), e202300520. https://doi.org/10.1002/cctc.202300520.

(227) Falk, M.; Miller, A. G. Infrared Spectrum of Carbon Dioxide in Aqueous Solution. *Vib. Spectrosc.* **1992**, *4* (1), 105–108. https://doi.org/10.1016/0924-2031(92)87018-B.
(228) Heyes, J.; Dunwell, M.; Xu, B. CO2 Reduction on Cu at Low Overpotentials with Surface-Enhanced in Situ Spectroscopy. *J. Phys. Chem. C* **2016**, *120* (31), 17334–17341. https://doi.org/10.1021/acs.jpcc.6b03065.
(229) Jo, S.; Kim, T.; Iyer, V. G.; Im, W. CHARMM-GUI: A Web-Based Graphical User Interface for CHARMM. *J. Comput. Chem.* **2008**, *29* (11), 1859–1865. https://doi.org/10.1002/jcc.20945.
(230) Choi, Y. K.; Kern, N. R.; Kim, S.; Kanhaiya, K.; Afshar, Y.; Jeon, S. H.; Jo, S.; Brooks, B. R.; Lee, J.; Tadmor, E. B.; Heinz, H.; Im, W. CHARMM-GUI Nanomaterial Modeler for Modeling and Simulation of Nanomaterial Systems. *J. Chem. Theory Comput.* **2022**, *18* (1), 479–493. https://doi.org/10.1021/acs.jctc.1c00996.
(231) Abraham, M. J.; Murtola, T.; Schulz, R.; Páll, S.; Smith, J. C.; Hess, B.; Lindahl, E. GROMACS: High Performance Molecular Simulations through Multi-Level Parallelism from Laptops to Supercomputers. *SoftwareX* **2015**, *1*, 19–25. https://doi.org/10.1016/j.softx.2015.06.001.
(232) Lee, J.; Cheng, X.; Jo, S.; MacKerell, A. D.; Klauda, J. B.; Im, W. CHARMM-GUI Input Generator for NAMD, Gromacs, Amber, Openmm, and CHARMM/OpenMM Simulations Using the CHARMM36 Additive Force Field. *Biophys. J.* **2016**, *110* (3), 641a. https://doi.org/10.1016/j.bpj.2015.11.3431.
(233) Jorgensen, W. L.; Chandrasekhar, J.; Madura, J. D.; Impey, R. W.; Klein, M. L. Comparison of Simple Potential Functions for Simulating Liquid Water. *J. Chem. Phys.* **1983**, *79* (2), 926–935. https://doi.org/10.1063/1.445869.
(234) Bussi, G.; Donadio, D.; Parrinello, M. Canonical Sampling through Velocity Rescaling. *J. Chem. Phys.* **2007**, *126* (1), 014101. https://doi.org/10.1063/1.2408420.
(235) Kresse, G.; Furthmüller, J. Efficient Iterative Schemes for Ab Initio Total-Energy Calculations Using a Plane-Wave Basis Set. *Phys. Rev. B* **1996**, *54* (16), 11169–11186. https://doi.org/10.1103/PhysRevB.54.11169.
(236) Johnson, E. R.; Becke, A. D. A Post-Hartree-Fock Model of Intermolecular Interactions: Inclusion of Higher-Order Corrections. *J. Chem. Phys.* **2006**, *124* (17), 174104. https://doi.org/10.1063/1.2190220.
(237) Blöchl, P. E. Projector Augmented-Wave Method. *Phys. Rev. B* **1994**, *50* (24), 17953–17979. https://doi.org/10.1103/PhysRevB.50.17953.
(238) Nosé, S. A Unified Formulation of the Constant Temperature Molecular Dynamics Methods. *J. Chem. Phys.* **1984**, *81* (1), 511–519. https://doi.org/10.1063/1.447334.
(239) Hoover, W. G. Canonical Dynamics: Equilibrium Phase-Space Distributions. *Phys. Rev. A* **1985**, *31* (3), 1695–1697. https://doi.org/10.1103/PhysRevA.31.1695.
(240) Mathew, K.; Kolluru, V. S. C.; Mula, S.; Steinmann, S. N.; Hennig, R. G. Implicit Self-Consistent Electrolyte Model in Plane-Wave Density-Functional Theory. *J. Chem. Phys.* **2019**, *151* (23), 234101. https://doi.org/10.1063/1.5132354.
(241) Le, D. An Explicit-Implicit Hybrid Solvent Model for Grand Canonical Simulations of the Electrochemical Environment. ChemRxiv March 27, 2023. https://doi.org/10.26434/chemrxiv-2023-z2n4n.
(242) Laio, A.; Parrinello, M. Escaping Free-Energy Minima. *Proc. Natl. Acad. Sci.* **2002**, *99* (20), 12562–12566. https://doi.org/10.1073/pnas.202427399.

(243) Lin, S.-T.; Maiti, P. K.; Goddard, W. A. I. Two-Phase Thermodynamic Model for Efficient and Accurate Absolute Entropy of Water from Molecular Dynamics Simulations. *J. Phys. Chem. B* **2010**, *114* (24), 8191–8198. https://doi.org/10.1021/jp103120q.
(244) Gunathunge, C. M.; Li, J.; Li, X.; Waegele, M. M. Surface-Adsorbed CO as an Infrared Probe of Electrocatalytic Interfaces. *ACS Catal.* **2020**, *10* (20), 11700–11711. https://doi.org/10.1021/acscatal.0c03316.
(245) Wuttig, A.; Liu, C.; Peng, Q.; Yaguchi, M.; Hendon, C. H.; Motobayashi, K.; Ye, S.; Osawa, M.; Surendranath, Y. Tracking a Common Surface-Bound Intermediate during CO2-to-Fuels Catalysis. *ACS Cent. Sci.* **2016**, *2* (8), 522–528. https://doi.org/10.1021/acscentsci.6b00155.
(246) Roiaz, M.; Falivene, L.; Rameshan, C.; Cavallo, L.; Kozlov, S. M.; Rupprechter, G. Roughening of Copper (100) at Elevated CO Pressure: Cu Adatom and Cluster Formation Enable CO Dissociation. *J. Phys. Chem. C* **2019**, *123* (13), 8112–8121. https://doi.org/10.1021/acs.jpcc.8b07668.
(247) Feibelman, P. J.; Hammer, B.; Nørskov, J. K.; Wagner, F.; Scheffler, M.; Stumpf, R.; Watwe, R.; Dumesic, J. The CO/Pt(111) Puzzle. *J. Phys. Chem. B* **2001**, *105* (18), 4018–4025. https://doi.org/10.1021/jp002302t.
(248) Kresse, G.; Gil, A.; Sautet, P. Significance of Single-Electron Energies for the Description of CO on Pt(111). *Phys. Rev. B* **2003**, *68* (7), 073401. https://doi.org/10.1103/PhysRevB.68.073401.
(249) Gajdoš, M.; Hafner, J. CO Adsorption on Cu(1 1 1) and Cu(0 0 1) Surfaces: Improving Site Preference in DFT Calculations. *Surf. Sci.* **2005**, *590* (2), 117–126. https://doi.org/10.1016/j.susc.2005.04.047.
(250) Hu, Q.-M.; Reuter, K.; Scheffler, M. Towards an Exact Treatment of Exchange and Correlation in Materials: Application to the ``CO Adsorption Puzzle'' and Other Systems. *Phys. Rev. Lett.* **2007**, *98* (17), 176103. https://doi.org/10.1103/PhysRevLett.98.176103.
(251) Stroppa, A.; Termentzidis, K.; Paier, J.; Kresse, G.; Hafner, J. CO Adsorption on Metal Surfaces: A Hybrid Functional Study with Plane-Wave Basis Set. *Phys. Rev. B* **2007**, *76* (19), 195440. https://doi.org/10.1103/PhysRevB.76.195440.
(252) Chen, Z.; Liu, Z.; Xu, X. Accurate Descriptions of Molecule-Surface Interactions in Electrocatalytic CO2 Reduction on the Copper Surfaces. *Nat. Commun.* **2023**, *14* (1), 936. https://doi.org/10.1038/s41467-023-36695-7.
(253) Murata, A.; Hori, Y. Product Selectivity Affected by Cationic Species in Electrochemical Reduction of CO2 and CO at a Cu Electrode. *Bull. Chem. Soc. Jpn.* **1991**, *64* (1), 123–127. https://doi.org/10.1246/bcsj.64.123.
(254) Liu, T.; Tang, L.; Luo, H.; Cheng, S.; Liu, M. A Promising Water-in-Salt Electrolyte for Aqueous Based Electrochemical Energy Storage Cells with a Wide Potential Window: Highly Concentrated HCOOK. *Chem. Commun.* **2019**, *55* (85), 12817–12820. https://doi.org/10.1039/C9CC05927J.
(255) Lees, E. W.; Mowbray, B. A. W.; Parlane, F. G. L.; Berlinguette, C. P. Gas Diffusion Electrodes and Membranes for CO2 Reduction Electrolysers. *Nat. Rev. Mater.* **2022**, *7* (1), 55–64. https://doi.org/10.1038/s41578-021-00356-2.
(256) Nguyen, T. N.; Dinh, C.-T. Gas Diffusion Electrode Design for Electrochemical Carbon Dioxide Reduction. *Chem. Soc. Rev.* **2020**, *49* (21), 7488–7504. https://doi.org/10.1039/D0CS00230E.

(257) Rabiee, H.; Ge, L.; Zhang, X.; Hu, S.; Li, M.; Yuan, Z. Gas Diffusion Electrodes (GDEs) for Electrochemical Reduction of Carbon Dioxide, Carbon Monoxide, and Dinitrogen to Value-Added Products: A Review. *Energy Environ. Sci.* **2021**, *14* (4), 1959–2008. https://doi.org/10.1039/D0EE03756G.
(258) Möller, T.; Thanh, T. N.; Wang, X.; Ju, W.; Jovanov, Z.; Strasser, P. The Product Selectivity Zones in Gas Diffusion Electrodes during the Electrocatalytic Reduction of CO2. *Energy Environ. Sci.* **2021**, *14* (11), 5995–6006. https://doi.org/10.1039/D1EE01696B.
(259) Tan, Y. C.; Lee, K. B.; Song, H.; Oh, J. Modulating Local CO2 Concentration as a General Strategy for Enhancing C−C Coupling in CO2 Electroreduction. *Joule* **2020**, *4* (5), 1104–1120. https://doi.org/10.1016/j.joule.2020.03.013.
(260) Song, H.; Song, J. T.; Kim, B.; Tan, Y. C.; Oh, J. Activation of C2H4 Reaction Pathways in Electrochemical CO2 Reduction under Low CO2 Partial Pressure. *Appl. Catal. B Environ.* **2020**, *272*, 119049. https://doi.org/10.1016/j.apcatb.2020.119049.
(261) Li, J.; Wang, Z.; McCallum, C.; Xu, Y.; Li, F.; Wang, Y.; Gabardo, C. M.; Dinh, C.-T.; Zhuang, T.-T.; Wang, L.; Howe, J. Y.; Ren, Y.; Sargent, E. H.; Sinton, D. Constraining CO Coverage on Copper Promotes High-Efficiency Ethylene Electroproduction. *Nat. Catal.* **2019**, *2* (12), 1124–1131. https://doi.org/10.1038/s41929-019-0380-x.
(262) Moradzaman, M.; Mul, G. Optimizing CO Coverage on Rough Copper Electrodes: Effect of the Partial Pressure of CO and Electrolyte Anions (pH) on Selectivity toward Ethylene. *J. Phys. Chem. C* **2021**, *125* (12), 6546–6554. https://doi.org/10.1021/acs.jpcc.0c10792.
(263) Henckel, D. A.; Counihan, M. J.; Holmes, H. E.; Chen, X.; Nwabara, U. O.; Verma, S.; Rodríguez-López, J.; Kenis, P. J. A.; Gewirth, A. A. Potential Dependence of the Local pH in a CO2 Reduction Electrolyzer. *ACS Catal.* **2021**, *11* (1), 255–263. https://doi.org/10.1021/acscatal.0c04297.
(264) Monteiro, M. C. O.; Koper, M. T. M. Measuring Local pH in Electrochemistry. *Curr. Opin. Electrochem.* **2021**, *25*, 100649. https://doi.org/10.1016/j.coelec.2020.100649.
(265) Yao, K.; Li, J.; Wang, H.; Lu, R.; Yang, X.; Luo, M.; Wang, N.; Wang, Z.; Liu, C.; Jing, T.; Chen, S.; Cortés, E.; Maier, S. A.; Zhang, S.; Li, T.; Yu, Y.; Liu, Y.; Kang, X.; Liang, H. Mechanistic Insights into OC–COH Coupling in CO2 Electroreduction on Fragmented Copper. *J. Am. Chem. Soc.* **2022**, *144* (31), 14005–14011. https://doi.org/10.1021/jacs.2c01044.
(266) Sandberg, R. B.; Montoya, J. H.; Chan, K.; Nørskov, J. K. CO-CO Coupling on Cu Facets: Coverage, Strain and Field Effects. *Surf. Sci.* **2016**, *654*, 56–62. https://doi.org/10.1016/j.susc.2016.08.006.
(267) Xiao, H.; Cheng, T.; Goddard, W. A. I.; Sundararaman, R. Mechanistic Explanation of the pH Dependence and Onset Potentials for Hydrocarbon Products from Electrochemical Reduction of CO on Cu (111). *J. Am. Chem. Soc.* **2016**, *138* (2), 483–486. https://doi.org/10.1021/jacs.5b11390.
(268) Pérez-Gallent, E.; Figueiredo, M. C.; Calle-Vallejo, F.; Koper, M. T. M. Spectroscopic Observation of a Hydrogenated CO Dimer Intermediate During CO Reduction on Cu(100) Electrodes. *Angew. Chem. Int. Ed.* **2017**, *56* (13), 3621–3624. https://doi.org/10.1002/anie.201700580.
(269) Xiao, H.; Goddard, W. A.; Cheng, T.; Liu, Y. Cu Metal Embedded in Oxidized Matrix Catalyst to Promote CO2 Activation and CO Dimerization for Electrochemical Reduction of CO2. *Proc. Natl. Acad. Sci.* **2017**, *114* (26), 6685–6688. https://doi.org/10.1073/pnas.1702405114.

(270) Kim, Y.; Park, S.; Shin, S.-J.; Choi, W.; Min, B. K.; Kim, H.; Kim, W.; Hwang, Y. J. Time-Resolved Observation of C–C Coupling Intermediates on Cu Electrodes for Selective Electrochemical CO2 Reduction. *Energy Environ. Sci.* **2020**, *13* (11), 4301–4311. https://doi.org/10.1039/D0EE01690J.

(271) Wang, L.; Nitopi, S. A.; Bertheussen, E.; Orazov, M.; Morales-Guio, C. G.; Liu, X.; Higgins, D. C.; Chan, K.; Nørskov, J. K.; Hahn, C.; Jaramillo, T. F. Electrochemical Carbon Monoxide Reduction on Polycrystalline Copper: Effects of Potential, Pressure, and pH on Selectivity toward Multicarbon and Oxygenated Products. *ACS Catal.* **2018**, *8* (8), 7445–7454. https://doi.org/10.1021/acscatal.8b01200.

(272) Hori, Y.; Takahashi, R.; Yoshinami, Y.; Murata, A. Electrochemical Reduction of CO at a Copper Electrode. *J. Phys. Chem. B* **1997**, *101* (36), 7075–7081. https://doi.org/10.1021/jp970284i.

(273) Dinh, C.-T.; Burdyny, T.; Kibria, M. G.; Seifitokaldani, A.; Gabardo, C. M.; García de Arquer, F. P.; Kiani, A.; Edwards, J. P.; De Luna, P.; Bushuyev, O. S.; Zou, C.; Quintero-Bermudez, R.; Pang, Y.; Sinton, D.; Sargent, E. H. CO2 Electroreduction to Ethylene via Hydroxide-Mediated Copper Catalysis at an Abrupt Interface. *Science* **2018**, *360* (6390), 783–787. https://doi.org/10.1126/science.aas9100.

(274) Varela, A. S.; Kroschel, M.; Reier, T.; Strasser, P. Controlling the Selectivity of CO2 Electroreduction on Copper: The Effect of the Electrolyte Concentration and the Importance of the Local pH. *Catal. Today* **2016**, *260*, 8–13. https://doi.org/10.1016/j.cattod.2015.06.009.

(275) Welch, A. J.; Fenwick, A. Q.; Böhme, A.; Chen, H.-Y.; Sullivan, I.; Li, X.; DuChene, J. S.; Xiang, C.; Atwater, H. A. Operando Local pH Measurement within Gas Diffusion Electrodes Performing Electrochemical Carbon Dioxide Reduction. *J. Phys. Chem. C* **2021**, *125* (38), 20896–20904. https://doi.org/10.1021/acs.jpcc.1c06265.

(276) Böhme, A.; Bui, J. C.; Fenwick, A. Q.; Bhide, R.; Feltenberger, C. N.; Welch, A. J.; King, A. J.; Bell, A. T.; Weber, A. Z.; Ardo, S.; Atwater, H. A. Direct Observation of the Local Microenvironment in Inhomogeneous CO2 Reduction Gas Diffusion Electrodes via Versatile pOH Imaging. *Energy Environ. Sci.* **2023**, *16* (4), 1783–1795. https://doi.org/10.1039/D2EE02607D.

(277) Dolmanan, S. B.; Böhme, A.; Fan, Z.; King, A. J.; Fenwick, A. Q.; Handoko, A. D.; Leow, W. R.; Weber, A. Z.; Ma, X.; Khoo, E.; Atwater, H. A.; Lum, Y. Local Microenvironment Tuning Induces Switching between Electrochemical CO2 Reduction Pathways. *J. Mater. Chem. A* **2023**, *11* (25), 13493–13501. https://doi.org/10.1039/D3TA02558F.

(278) Ringe, S.; Clark, E. L.; Resasco, J.; Walton, A.; Seger, B.; Bell, A. T.; Chan, K. Understanding Cation Effects in Electrochemical CO2 Reduction. *Energy Environ. Sci.* **2019**, *12* (10), 3001–3014. https://doi.org/10.1039/C9EE01341E.

(279) Monteiro, M. C. O.; Dattila, F.; Hagedoorn, B.; García-Muelas, R.; López, N.; Koper, M. T. M. Absence of CO2 Electroreduction on Copper, Gold and Silver Electrodes without Metal Cations in Solution. *Nat. Catal.* **2021**, *4* (8), 654–662. https://doi.org/10.1038/s41929-021-00655-5.

(280) Park, D.; Jung, Y. Atomic-Scale Understanding of Alkali Metal Cation Effects on Electro-Catalytic Reactions. *Chem Catal.* **2024**, *4* (2). https://doi.org/10.1016/j.checat.2023.100823.

(281) Cheng, T.; Xiao, H.; Goddard, W. A. Full Atomistic Reaction Mechanism with Kinetics for CO Reduction on Cu(100) from Ab Initio Molecular Dynamics Free-Energy Calculations at 298 K. *Proc. Natl. Acad. Sci.* **2017**, *114* (8), 1795–1800. https://doi.org/10.1073/pnas.1612106114.

(282) Gao, D.; Scholten, F.; Roldan Cuenya, B. Improved CO2 Electroreduction Performance on Plasma-Activated Cu Catalysts via Electrolyte Design: Halide Effect. *ACS Catal.* **2017**, *7* (8), 5112–5120. https://doi.org/10.1021/acscatal.7b01416.
(283) Gao, D.; Sinev, I.; Scholten, F.; Arán-Ais, R. M.; Divins, N. J.; Kvashnina, K.; Timoshenko, J.; Roldan Cuenya, B. Selective CO2 Electroreduction to Ethylene and Multicarbon Alcohols via Electrolyte-Driven Nanostructuring. *Angew. Chem. Int. Ed.* **2019**, *58* (47), 17047–17053. https://doi.org/10.1002/anie.201910155.
(284) Yuan, T.; Wang, T.; Zhang, G.; Deng, W.; Cheng, D.; Gao, H.; Zhao, J.; Yu, J.; Zhang, P.; Gong, J. The Effect of Specific Adsorption of Halide Ions on Electrochemical CO2 Reduction. *Chem. Sci.* **2022**, *13* (27), 8117–8123. https://doi.org/10.1039/D2SC02689A.
(285) Huang, Y.; Ong, C. W.; Yeo, B. S. Effects of Electrolyte Anions on the Reduction of Carbon Dioxide to Ethylene and Ethanol on Copper (100) and (111) Surfaces. *ChemSusChem* **2018**, *11* (18), 3299–3306. https://doi.org/10.1002/cssc.201801078.
(286) Biesinger, M. C. Advanced Analysis of Copper X-Ray Photoelectron Spectra. *Surf. Interface Anal.* **2017**, *49* (13), 1325–1334. https://doi.org/10.1002/sia.6239.
(287) Martin, L.; Martinez, H.; Poinot, D.; Pecquenard, B.; Cras, F. L. *Comprehensive X-ray Photoelectron Spectroscopy Study of the Conversion Reaction Mechanism of CuO in Lithiated Thin Film Electrodes*. ACS Publications. https://doi.org/10.1021/jp3119633.
(288) Jiang, P.; Prendergast, D.; Borondics, F.; Porsgaard, S.; Giovanetti, L.; Pach, E.; Newberg, J.; Bluhm, H.; Besenbacher, F.; Salmeron, M. Experimental and Theoretical Investigation of the Electronic Structure of Cu2O and CuO Thin Films on Cu(110) Using x-Ray Photoelectron and Absorption Spectroscopy. *J. Chem. Phys.* **2013**, *138* (2), 024704. https://doi.org/10.1063/1.4773583.
(289) Biesinger, M. C.; Lau, L. W. M.; Gerson, A. R.; Smart, R. St. C. Resolving Surface Chemical States in XPS Analysis of First Row Transition Metals, Oxides and Hydroxides: Sc, Ti, V, Cu and Zn. *Appl. Surf. Sci.* **2010**, *257* (3), 887–898. https://doi.org/10.1016/j.apsusc.2010.07.086.
(290) Wang, L.; Nitopi, S.; Wong, A. B.; Snider, J. L.; Nielander, A. C.; Morales-Guio, C. G.; Orazov, M.; Higgins, D. C.; Hahn, C.; Jaramillo, T. F. Electrochemically Converting Carbon Monoxide to Liquid Fuels by Directing Selectivity with Electrode Surface Area. *Nat. Catal.* **2019**, *2* (8), 702–708. https://doi.org/10.1038/s41929-019-0301-z.
(291) Wang, X.; Klingan, K.; Klingenhof, M.; Möller, T.; Ferreira de Araújo, J.; Martens, I.; Bagger, A.; Jiang, S.; Rossmeisl, J.; Dau, H.; Strasser, P. Morphology and Mechanism of Highly Selective Cu(II) Oxide Nanosheet Catalysts for Carbon Dioxide Electroreduction. *Nat. Commun.* **2021**, *12* (1), 794. https://doi.org/10.1038/s41467-021-20961-7.
(292) Yang, Y.; Louisia, S.; Yu, S.; Jin, J.; Roh, I.; Chen, C.; Fonseca Guzman, M. V.; Feijóo, J.; Chen, P.-C.; Wang, H.; Pollock, C. J.; Huang, X.; Shao, Y.-T.; Wang, C.; Muller, D. A.; Abruña, H. D.; Yang, P. Operando Studies Reveal Active Cu Nanograins for CO2 Electroreduction. *Nature* **2023**, *614* (7947), 262–269. https://doi.org/10.1038/s41586-022-05540-0.
(293) Grosse, P.; Yoon, A.; Rettenmaier, C.; Herzog, A.; Chee, S. W.; Roldan Cuenya, B. Dynamic Transformation of Cubic Copper Catalysts during CO2 Electroreduction and Its Impact on Catalytic Selectivity. *Nat. Commun.* **2021**, *12* (1), 6736. https://doi.org/10.1038/s41467-021-26743-5.
(294) Arán-Ais, R. M.; Rizo, R.; Grosse, P.; Algara-Siller, G.; Dembélé, K.; Plodinec, M.; Lunkenbein, T.; Chee, S. W.; Cuenya, B. R. Imaging Electrochemically Synthesized Cu2O

Cubes and Their Morphological Evolution under Conditions Relevant to CO2 Electroreduction. *Nat. Commun.* **2020**, *11* (1), 3489. https://doi.org/10.1038/s41467-020-17220-6.

(295) Kas, R.; Yang, K.; Bohra, D.; Kortlever, R.; Burdyny, T.; Smith, W. A. Electrochemical CO2 Reduction on Nanostructured Metal Electrodes: Fact or Defect? *Chem. Sci.* **2020**, *11* (7), 1738–1749. https://doi.org/10.1039/C9SC05375A.

(296) Elderderi, S.; Leman-Loubière, C.; Wils, L.; Henry, S.; Bertrand, D.; Byrne, H. J.; Chourpa, I.; Enguehard-Gueiffier, C.; Munnier, E.; Elbashir, A. A.; Boudesocque-Delaye, L.; Bonnier, F. ATR-IR Spectroscopy for Rapid Quantification of Water Content in Deep Eutectic Solvents. *J. Mol. Liq.* **2020**, *311*, 113361. https://doi.org/10.1016/j.molliq.2020.113361.

(297) Bai, H.; Cheng, T.; Li, S.; Zhou, Z.; Yang, H.; Li, J.; Xie, M.; Ye, J.; Ji, Y.; Li, Y.; Zhou, Z.; Sun, S.; Zhang, B.; Peng, H. Controllable CO Adsorption Determines Ethylene and Methane Productions from CO2 Electroreduction. *Sci. Bull.* **2021**, *66* (1), 62–68. https://doi.org/10.1016/j.scib.2020.06.023.

(298) Gunathunge, C. M.; Ovalle, V. J.; Li, Y.; Janik, M. J.; Waegele, M. M. Existence of an Electrochemically Inert CO Population on Cu Electrodes in Alkaline pH. *ACS Catal.* **2018**, *8* (8), 7507–7516. https://doi.org/10.1021/acscatal.8b01552.

(299) Rebstock, J. A.; Zhu, Q.; Baker, L. R. Comparing Interfacial Cation Hydration at Catalytic Active Sites and Spectator Sites on Gold Electrodes: Understanding Structure Sensitive CO2 Reduction Kinetics. *Chem. Sci.* **2022**, *13* (25), 7634–7643. https://doi.org/10.1039/D2SC01878K.

(300) Lee, S. Y.; Kim, J.; Bak, G.; Lee, E.; Kim, D.; Yoo, S.; Kim, J.; Yun, H.; Hwang, Y. J. Probing Cation Effects on *CO Intermediates from Electroreduction of CO2 through Operando Raman Spectroscopy. *J. Am. Chem. Soc.* **2023**, *145* (42), 23068–23075. https://doi.org/10.1021/jacs.3c05799.

(301) Nesbitt, N. T.; Burdyny, T.; Simonson, H.; Salvatore, D.; Bohra, D.; Kas, R.; Smith, W. A. Liquid–Solid Boundaries Dominate Activity of CO2 Reduction on Gas-Diffusion Electrodes. *ACS Catal.* **2020**, *10* (23), 14093–14106. https://doi.org/10.1021/acscatal.0c03319.

(302) Zhan, C.; Dattila, F.; Rettenmaier, C.; Bergmann, A.; Kühl, S.; García-Muelas, R.; López, N.; Cuenya, B. R. Revealing the CO Coverage-Driven C–C Coupling Mechanism for Electrochemical CO2 Reduction on Cu2O Nanocubes via Operando Raman Spectroscopy. *ACS Catal.* **2021**, *11* (13), 7694–7701. https://doi.org/10.1021/acscatal.1c01478.

(303) Chou, T.-C.; Chang, C.-C.; Yu, H.-L.; Yu, W.-Y.; Dong, C.-L.; Velasco-Vélez, J.-J.; Chuang, C.-H.; Chen, L.-C.; Lee, J.-F.; Chen, J.-M.; Wu, H.-L. Controlling the Oxidation State of the Cu Electrode and Reaction Intermediates for Electrochemical CO2 Reduction to Ethylene. *J. Am. Chem. Soc.* **2020**, *142* (6), 2857–2867. https://doi.org/10.1021/jacs.9b11126.

(304) Ovalle, V. J.; Waegele, M. M. Impact of Electrolyte Anions on the Adsorption of CO on Cu Electrodes. *J. Phys. Chem. C* **2020**, *124* (27), 14713–14721. https://doi.org/10.1021/acs.jpcc.0c04037.

(305) Mohandas, N.; Narayanan, T. N.; Cuesta, A. Tailoring the Interfacial Water Structure by Electrolyte Engineering for Selective Electrocatalytic Reduction of Carbon Dioxide. *ACS Catal.* **2023**, *13* (13), 8384–8393. https://doi.org/10.1021/acscatal.3c01223.

(306) Wang, Y.-H.; Zheng, S.; Yang, W.-M.; Zhou, R.-Y.; He, Q.-F.; Radjenovic, P.; Dong, J.-C.; Li, S.; Zheng, J.; Yang, Z.-L.; Attard, G.; Pan, F.; Tian, Z.-Q.; Li, J.-F. In Situ Raman Spectroscopy Reveals the Structure and Dissociation of Interfacial Water. *Nature* **2021**, *600* (7887), 81–85. https://doi.org/10.1038/s41586-021-04068-z.

(307) Ataka, K.; Yotsuyanagi, T.; Osawa, M. Potential-Dependent Reorientation of Water Molecules at an Electrode/Electrolyte Interface Studied by Surface-Enhanced Infrared Absorption Spectroscopy. *J. Phys. Chem.* **1996**, *100* (25), 10664–10672. https://doi.org/10.1021/jp953636z.

(308) Bhattacharyya, D.; E. Videla, P.; Cattaneo, M.; S. Batista, V.; Lian, T.; P. Kubiak, C. Vibrational Stark Shift Spectroscopy of Catalysts under the Influence of Electric Fields at Electrode–Solution Interfaces. *Chem. Sci.* **2021**, *12* (30), 10131–10149. https://doi.org/10.1039/D1SC01876K.

(309) Malkani, A. S.; Li, J.; Oliveira, N. J.; He, M.; Chang, X.; Xu, B.; Lu, Q. Understanding the Electric and Nonelectric Field Components of the Cation Effect on the Electrochemical CO Reduction Reaction. *Sci. Adv.* **2020**, *6* (45), eabd2569. https://doi.org/10.1126/sciadv.abd2569.

(310) Sartin, M. M.; Yu, Z.; Chen, W.; He, F.; Sun, Z.; Chen, Y.-X.; Huang, W. Effect of Particle Shape and Electrolyte Cation on CO Adsorption to Copper Oxide Nanoparticle Electrocatalysts. *J. Phys. Chem. C* **2018**, *122* (46), 26489–26498. https://doi.org/10.1021/acs.jpcc.8b08541.

(311) Woodruff, D. P.; Hayden, B. E.; Prince, K.; Bradshaw, A. M. Dipole Coupling and Chemical Shifts in IRAS of CO Adsorbed on Cu(110). *Surf. Sci.* **1982**, *123* (2), 397–412. https://doi.org/10.1016/0039-6028(82)90336-3.

(312) Chang, X.; Xiong, H.; Xu, Y.; Zhao, Y.; Lu, Q.; Xu, B. Determining Intrinsic Stark Tuning Rates of Adsorbed CO on Copper Surfaces. *Catal. Sci. Technol.* **2021**, *11* (20), 6825–6831. https://doi.org/10.1039/D1CY01090E.

(313) Gameel, K. M.; Sharafeldin, I. M.; Abourayya, A. U.; Biby, A. H.; Allam, N. K. Unveiling CO Adsorption on Cu Surfaces: New Insights from Molecular Orbital Principles. *Phys. Chem. Chem. Phys.* **2018**, *20* (40), 25892–25900. https://doi.org/10.1039/C8CP04253E.

(314) Blyholder, G. Molecular Orbital View of Chemisorbed Carbon Monoxide. *J. Phys. Chem.* **1964**, *68* (10), 2772–2777. https://doi.org/10.1021/j100792a006.

(315) Banerji, L. C.; Jang, H.; Gardner, A. M.; Cowan, A. J. Studying the Cation Dependence of CO2 Reduction Intermediates at Cu by in Situ VSFG Spectroscopy. *Chem. Sci.* **2024**. https://doi.org/10.1039/D3SC05295H.

(316) Uddin, J.; Anderson, A. B. Trends with Coverage and pH in Stark Tuning Rates for CO on Pt(1 1 1) Electrodes. *Electrochimica Acta* **2013**, *108*, 398–403. https://doi.org/10.1016/j.electacta.2013.06.088.

(317) Gunathunge, C. M.; Li, X.; Li, J.; Hicks, R. P.; Ovalle, V. J.; Waegele, M. M. Spectroscopic Observation of Reversible Surface Reconstruction of Copper Electrodes under CO2 Reduction. *J. Phys. Chem. C* **2017**, *121* (22), 12337–12344. https://doi.org/10.1021/acs.jpcc.7b03910.